

Calibration and Monitoring for the Borexino Solar Neutrino Experiment

Dissertation submitted to the
Faculdade de Ciências da Universidade de Lisboa
for the degree of Ph.D. in Physics
by

José Carvalho Maneira

Advisors:

Prof. Amélia Maio

Prof. Gianpaolo Bellini (University of Milan)

Lisbon, November 2001

To my parents and my brother.

*"The first question I ask myself
when something doesn't seem to be beautiful
is why do I think it's not beautiful.
And very shortly you discover that there is no reason."*

John Cage

Summary

One of the major open issues in Elementary Particle Physics today, the phenomenon of Neutrino Oscillations is a natural consequence of a non-zero neutrino mass and a non-diagonal leptonic mixing matrix. Even if the Standard Model extension to accommodate neutrino oscillations is relatively trivial, a non-zero neutrino mass and mixing is widely considered as a doorway for the Unified Theory of the fundamental interactions. In fact, Super Symmetry naturally explains small neutrino masses through the well-known “see-saw” mechanism. From the experimental point of view, neutrino oscillations are a privileged way of studying the neutrino mass spectrum, since small mass splittings can lead to large and measurable phase differences between interfering quantum-mechanical amplitudes.

This is particularly true for Solar Neutrino Experiments, since the large distance between source and detector (1.5×10^{11} m) allows for a good sensitivity to very small mass differences (down to about 10^{-11} eV²), not available with the present accelerator and reactor experiments. In fact, the first indication for the possibility of Neutrino Oscillations came from the first measurements of Solar Neutrinos, more than thirty years ago. This hypothesis has been increasingly strengthened by the addition of successive results, from measurements of both Solar and Atmospheric Neutrinos.

The experimental constraints on the neutrino mass and mixing parameters have been obtained through the combined analysis of the complementary results from experiments with different potentialities. The Borexino experiment is conceived according to this perspective, since it is aimed at the real-time measurement of the ⁷Be neutrino flux, a high rate (46 events/day), low energy (0.86 MeV) component of the solar neutrino spectrum for which only indirect, integrated measurements are available up to now. The Physics potential of such a measurement relies on the fact that the ⁷Be component is monoenergetic so the oscillation patterns are not smoothed by averaging over the energy spectrum and on its low energy, where the presently allowed oscillation solutions predict large rate differences.

The main goal of the Borexino experiment, presently in its final installation phase at the Gran Sasso underground laboratory (LNGS) in Italy, is the detection of ^7Be solar neutrinos, requiring both a low energy threshold (250 keV) and a very low level of background from natural radioactivity in the detector materials (10^{-16} g/g of ^{238}U and ^{232}Th). In order to achieve this, the active detector target will be made of liquid scintillator, pseudocumene with PPO as fluor. However, the use of the scintillation technique limits the data analysis, since it does not allow any directional signature for neutrino events, and their identification is statistical, based on the energy spectrum shape analysis. Therefore, the challenging experimental measurement in Borexino requires precise energy and time calibrations, an accurate control of the background rejection cuts and excellent detector stability.

The aim of the work presented in this thesis was to supply the Borexino experiment with the calibration tools necessary to interpret the data and extract the Physics of Neutrino Oscillations. The priority was given to the design, testing, construction and installation of the different calibration systems, but a significant effort was also dedicated to the development of software tools for the energy spectrum analysis and ^7Be neutrino identification.

The calibration and monitoring systems, face the same challenge that drives some of the most crucial aspects of the Borexino design: to reach and maintain the lowest radioactivity levels ever achieved in any large scale underground detector. This fact limits the mass of any permanent calibration devices in the detector and the risk of radioactive contamination puts significant constraints on the access to the active scintillator volume and on the use of radioactive sources. The strategy followed was to develop non-invasive monitoring systems based on the coupling of optical fibers to lasers and a system to position a radioactive γ source (^{228}Th - 200 μCi) in an external region. The calibration and monitoring operations will be scheduled according to the radioactive contamination risk, each step being carried

out only if the required accuracy was not obtained with the preceding ones. Naturally, the calibration with internal radioactive sources, and in particular, long-lived ones, is the last step in the operational schedule.

This thesis is organized in six Chapters. Chapter 1 introduces the Physics of Solar Neutrinos and Neutrino Oscillations, while Chapter 2 describes the goals and design of the Borexino experiment. The design and tests of the Calibration and Monitoring systems are presented in Chapters 3 to 5, while Chapter 6 discusses the sensitivity of Borexino to ^7Be Solar Neutrino Physics. The work of the author includes Chapters 3, 4 and 6 and half of Chapter 5.

Chapter 3 presents the system for time and charge calibration of the 2200 photomultipliers (PMTs) that detect the light produced in the liquid scintillator. The system is based on the illumination of all the 2200 PMTs with a common light source -- a diode laser -- through a two-stage fiber splitting system, so that each PMT is illuminated by one fiber. We present the requirements, guidelines and design of the system, as well as the results from a prototype of the complete optical chain, built and operated in realistic conditions. From these results and further tests of the final system, now almost fully installed, we expect that all the Borexino PMTs will be illuminated with a low intensity, fast, light pulse, allowing a charge calibration at the single-photoelectron level and a time calibration with a 0.5 ns accuracy. These will be relevant, for an accurate energy measurement and event position reconstruction respectively.

Chapter 4 presents the two systems for the optical calibration of the scintillator and buffer liquid. The first of these systems is internal to the active volume and uses absorption and re-emission of ultraviolet laser pulses in the scintillator to measure its optical properties and mimic charged particle scintillation events. We describe the goals and design of the system, as well as the results of preliminary tests with a single photoelectron counting setup. We confirmed that, if the wavelength is low enough (below 300 nm), it will excite primarily the solvent and the fast component of the scintillation decay time is the same as for charged

particles. This allows us to use laser sources to measure the time distribution of the actual scintillation pulses, necessary for position reconstruction and external background rejection.

The second optical calibration system is external to the active volume and it will use a set of light beams in different directions in order to study the stability of the attenuation/scattering length of the buffer liquid and scintillator, that has a strong impact on the efficiency of the internal background rejection cut. The feasibility of this method, in which laser beams are carried to the detector by optical fibers, was tested in the Two Liquid Test Tank (TLTT), a 7 m³ tank built in LNGS for a long-term test of 50 PMTs in realistic conditions, i.e., immersed in the pseudocumene. The time distributions of PMT signals from different zones were used to distinguish between direct, reflected and scattered light and obtain control parameters. Independent measurements of the pseudocumene attenuation length confirmed the sensitivity of these parameters to the transparency changes of the liquid. The design and configuration of the light beam for the final system, now installed, was optimized by means of further tests and Monte Carlo simulations, so we expect to have a good accuracy for the attenuation length monitoring.

Chapter 5 presents the systems for calibrations with internal and external radioactive sources. We present the hardware design and the Monte Carlo feasibility studies for a system based on a radioactive γ source placed in a region outside the active detector volume, in order to minimize any detector contamination risk. In order to be sensitive to the ± 3.5 % yearly variation of the solar neutrino flux, we need to monitor the counting rate in one of the internal shells of the scintillator volume with an accuracy of 1 %. From our calculations and source insertion design, this can be accomplished with a 200 μCi ^{228}Th source in a short time (a 2 hour run). For completion, we present also the internal source system, designed by our collaborators.

Chapter 6 presents a study of the Borexino sensitivity to ^7Be solar neutrinos, focusing on the last step of the data processing, that is the energy spectrum

analysis, since the identification of the ^7Be neutrino signal is ultimately done by the recognition of its characteristic “Compton-like” edge. In the energy spectrum study, analytic functions based on the theoretical cross-sections and the detector resolution were used to describe both the neutrino and the background energy distributions. The goal of this strategy is to complement the detailed description of all the expected shapes with a flexible approach that allows the method to better adapt itself to unexpected and not easily reproducible effects.

The expected data were generated by Monte Carlo simulations. We studied the sensitivity to ^7Be neutrinos for different oscillation scenarios, and its dependence on the internal background rate. We also considered the effect of several “disturbing conditions” on the neutrino identification: secular equilibrium breaking in the ^{238}U and ^{232}Th chains; degradation of the scintillator/buffer liquid transparency and consequent loss of background rejection efficiency; quenching of low-energy electrons and consequent distortion of the γ -rays energy scale. All these effects can distort the energy spectrum, preventing the neutrino signal to be recognized. However, the calibration systems provide the tools to correct these possible sources of “systematic error”, contributing to re-establishing the good sensitivity of the analysis.

We concluded that a good knowledge of the energy spectrum shapes of both signal and background components is more critical than a good signal-background ratio. If the internal background cut efficiencies are not well known, the analysis of the spectrum without cuts is preferred, because less biased.

If the scintillator contamination level is 2×10^{-16} g/g (twice the design goal), and any energy spectrum distortions are corrected by means of adequate calibrations, the expected sensitivity to the ^7Be neutrino signal should allow a good discrimination between the Small Mixing Angle (SMA) and the Large Mixing Angle (LMA) oscillation solutions of the Solar Neutrino Problem. After one year of data-taking, if the SMA solution is correct, LMA can be excluded at the level of 3.8σ , and if the LMA solution is correct, SMA can be excluded at 1.2σ . The difference between the LMA oscillation solution and the no-oscillation case will be even higher. In addition, if the detector is monitored for stability at a 1 % level

with a period of some hours (for the day-night asymmetry check) as well as some months (for the seasonal variation check), the Vacuum and LOW oscillation solutions should be well identified by means of their characteristic time variations.

In conclusion, we can say that Borexino has the potential sensitivity to distinguish between the presently allowed oscillation scenarios, as long as the background rate does not exceed twice of the design value, and the detector's stability and efficiencies are calibrated and monitored according to the requirements for the identification of the ^7Be solar neutrinos.

Resumo

Um dos principais temas em aberto da Física de Partículas Elementares, o fenómeno das Oscilações de Neutrinos é uma consequência natural de uma massa não-nula do neutrino e de uma matriz de mistura leptónica não diagonal. embora a extensão do Modelo Standard para acomodar as oscilações de neutrinos seja relativamente trivial, a massa não-nula do neutrino é largamente considerada como uma “porta de entrada” para a Teoria Unificada das Interações Fundamentais. A Super-Simetria explica naturalmente pequenas massas de neutrinos através do conhecido mecanismo “see-saw”. Do ponto de vista experimental, as oscilações de neutrinos constituem um modo privilegiado de estudar o espectro de massa dos neutrinos, pois pequenas diferenças de massa podem levar a grandes e mensuráveis diferenças de fase entre amplitudes quânticas em interferência.

As experiências de Neutrinos Solares são potencialmente as mais adequadas para este tipo de medições pois a grande distância entre a fonte e o detector (1.5×10^{11} m) permite uma boa sensibilidade a diferenças de massa muito pequenas (até cerca de 10^{-11} eV²), o que não é possível com as actuais experiências actuais em aceleradores e reactores. De facto, a primeira indicação do fenómeno das Oscilações de neutrinos foi fornecida pelas primeiras medições de Neutrinos Solares, há mais de 30 anos. Esta hipótese tem sido cada vez mais fortalecida com os resultados das experiências sucessivas, a partir de medições quer de Neutrinos Solares, quer de Neutrinos Atmosféricos. Os constrangimentos experimentais às massas dos neutrinos e aos parâmetros de mistura foram obtidos através da análise combinada de resultados complementares de experiências com diferentes potencialidades. A experiência Borexino é concebida de acordo com esta perspectiva, visto que o seu objectivo é a medição em tempo-real do fluxo de neutrinos do ⁷Be, uma componente do espectro de neutrinos solares com elevada taxa de contagens (46 eventos/dia) e baixa energia (0.86 MeV), da qual apenas foram efectuadas medições integradas e indirectas. O potencial de Física de uma medição deste tipo reside no facto de a componente do ⁷Be ser monoenergética, e

portanto os padrões de oscilação não são suavizados ao integrar sobre o espectro de energia, e também no facto de se preverem grandes diferenças de taxa de contagens a baixas energias, nas soluções de oscilações actualmente permitidas pelos resultados experimentais.

O objectivo principal da experiência Borexino, actualmente na sua fase final de instalação no Laboratório Nacional (subterrâneo) do Gran Sasso (LNGS) em Itália, é a detecção dos neutrinos solares do ^7Be , o que requer não só um baixo limiar de energia (250 keV), mas também um baixo nível de fundo devido à radioactividade natural dos materiais do detector (10^{-16} g/g de ^{238}U e ^{232}Th). Para o conseguir, o alvo activo do detector é constituído por cintilador liquido, pseudocumene dopado com PPO. No entanto, o uso da técnica de cintilação limita a análise de dados, pois não permite nenhuma assinatura direcciona para os eventos de neutrinos, e a sua identificação é baseada na análise da forma do espectro de energia. Consequentemente, o desafio experimental que Borexino defronta requer calibrações precisas em energia e tempo, um controlo detalhado dos cortes para rejeição de fundo e uma excelente estabilidade do detector.

A meta a alcançar com o trabalho apresentado nesta tese foi providenciar à experiência Borexino os instrumentos de calibração necessários para interpretar os dados e extrair a Física das Oscilações de Neutrinos. Foi dada prioridade ao projecto, teste, construção e instalação dos diferentes sistemas de calibração, mas um esforço significativo também foi dedicado ao desenvolvimento de instrumentos de software para a análise do espectro de energia e a identificação dos neutrinos do ^7Be .

Os sistemas de calibração e controlo defrontam o mesmo desafio que rege alguns dos aspectos mais cruciais do design de Borexino: atingir e manter os mais baixos níveis de radioactividade alguma vez alcançados em detectores subterrâneos de grande escala. Este facto limita a massa de todo e qualquer aparelho de calibração permanente no detector e o risco de contaminação radioactiva coloca constrangimentos significativos ao acesso ao volume activo de cintilador e ao uso de fontes radioactivas. A estratégia seguida foi o desenvolvimento de sistemas de

controlo não invasivos baseados no acoplamento de fibras ópticas a lasers e de um sistema de posicionamento de uma fonte γ radioactiva (^{228}Th – 200 μCi) numa região externa ao cintilador. As operações de calibração e controlo serão programadas de acordo com o risco de contaminação radioactiva, sendo cada passo executado só no caso de a precisão necessária não ter sido atingida com os métodos precedentes. Naturalmente, a calibração com fontes radioactivas internas e, em particular, de vida-média elevada, é o último passo no programa operacional.

A tese está organizada em seis Capítulos. No Capítulo 1 é feita uma introdução à Física dos Neutrinos Solares e às Oscilações de Neutrinos, enquanto que no Capítulo 2 se descrevem os objectivos e o design da experiência Borexino. O projecto e os testes dos sistemas de Calibração e Controlo são apresentados nos Capítulos 3 a 5, enquanto no Capítulo 6 se discute a sensibilidade de Borexino à Física dos Neutrinos Solares do ^7Be . O trabalho do autor está essencialmente descrito nos Capítulos 3, 4 e 6 e grande parte do Capítulo 5.

O Capítulo 3 apresenta o sistema para a calibração em tempo e carga dos 2200 fotomultiplicadores (PMTs) que detectam a luz produzida no cintilador liquido. O sistema é baseado na iluminação de todos os 2200 PMTs com a mesma fonte de luz – um laser a diódo – através de um sistema de multiplexagem de fibras a dois estádios, de modo a que cada PMT seja iluminado por uma fibra. São apresentados os requisitos e o design do sistema, bem como os resultados de um protótipo da cadeia óptica completa, utilizado em condições realistas. A partir destes resultados e de testes sucessivos do sistema final, actualmente em fase final de instalação, prevê-se que todos os PMTs de Borexino sejam iluminados com impulsos luminosos rápidos e de baixa intensidade, permitindo a calibração em carga ao nível de um foto-electrão e a calibração em tempo com uma precisão de 0.5 ns. A calibração eficaz dos PMTs será relevante para uma medição precisa da energia e reconstrução da posição dos eventos.

No Capítulo 4 são apresentados os dois sistemas para a calibração óptica do cintilador e do líquido de buffer. O primeiro dos sistemas é colocado internamente ao volume activo e usa a absorção e re-emissão de impulsos laser ultravioleta no cintilador para medir as suas propriedades ópticas e simular eventos de cintilação devidos a partículas carregadas. São descritos os objectivos e design do sistema, bem como os resultados de testes preliminares com uma instalação de detecção no regime de um foto-electrão. Foi confirmado que, se o comprimento de onda é suficientemente baixo (< 300 nm), o impulso luminoso excita principalmente o solvente e a componente rápida da distribuição temporal de cintilação é a mesma que no caso de partículas carregadas. Daí o uso de fontes laser para medição da distribuição temporal dos eventos de cintilação no detector final, necessária para a reconstrução da posição e rejeição do ruído de fundo externo.

O segundo sistema de calibração é colocado externamente ao volume activo e usa um conjunto de feixes de luz em diferentes direcções para estudo da estabilidade do comprimento de atenuação/dispersão do líquido de buffer e do cintilador, que tem um forte impacto na eficiência do corte de rejeição dos eventos de ruído de fundo interno. A viabilidade deste método, no qual feixes laser são direccionados até ao detector através de fibras ópticas, foi testada na “Two-Liquid Test Tank”, um tanque de 7 m^3 construído no LNGS para um teste de 50 PMTs em condições realistas, i.e., imersos em pseudocumene. As distribuições temporais dos sinais de PMTs colocados em diferentes zonas foram usados para distinguir entre luz directa, reflectida e dispersa, e para obter parâmetros de controlo da transparência do líquido. Medições independentes do comprimento de atenuação do pseudocumene confirmaram a sensibilidade destes parâmetros a mudanças na transparência. A configuração do feixe de luz para o sistema final, já instalado, foi optimizada através de testes adicionais e simulações Monte Carlo, prevendo-se portanto uma precisão do controlo do comprimento de atenuação da ordem de 5%.

No Capítulo 5 descrevem-se os sistemas para calibração com fontes radioactivas internas e externas. São apresentados o projecto dos aparelhos e os estudos de viabilidade por simulações Monte Carlo de um sistema baseado numa fonte γ radioactiva colocada numa região fora do volume activo de cintilador, de forma a

minimizar os riscos de contaminação do detector. Para poder medir a variação anual do fluxo de neutrinos solares de $\pm 3.5 \%$, é necessário controlar a taxa de contagens numa das regiões internas do volume de cintilador com uma precisão de 1% . A partir dos cálculos efectuados e do projecto para o sistema de inserção das fontes, esta meta pode ser atingida com uma fonte de ^{228}Th de actividade $200 \mu\text{Ci}$ num intervalo de tempo de aproximadamente 2 horas.

De modo a completar o quadro dos sistemas de calibração com fontes radioactivas, é também apresentado o sistema de inserção de fontes internas, projectado pelos nossos colaboradores.

No Capítulo 6 é apresentado um estudo da sensibilidade de Borexino aos neutrinos solares do ^7Be , centrado no último passo do processamento dos dados, i.e., a análise do espectro de energia, dado que a identificação do sinal de neutrinos do ^7Be é feita, através do reconhecimento do seu limiar característico “de tipo Compton”. No estudo dos espectros, a descrição das distribuições de energia do sinal de neutrinos e do ruído de fundo foi efectuada usando funções analíticas baseadas nas secções eficazes teóricas e na resolução do detector. O objectivo desta estratégia é complementar a descrição detalhada de todas as formas esperadas com um método flexível que permita uma melhor adaptação a efeitos não esperados ou dificilmente reproductíveis.

As distribuições de dados esperadas foram obtidas a partir de simulações Monte Carlo. Foi realizado o estudo da sensibilidade aos neutrinos do ^7Be em diferentes cenários de oscilações, e a sua dependência com a taxa de contagens do ruído de fundo interno. Foi também considerado o efeito de varias situações de distorção do espectro na identificação dos neutrinos: rotura do equilíbrio secular nas cadeias radioactivas do ^{238}U e ^{232}Th , degradação da transparência do cintilador e líquido de buffer com a resultante perda de eficiência na rejeição do ruído de fundo, e finalmente “quenching” de electrões de baixa energia e consequente distorção da escala de energia da radiação γ .

Concluiu-se que o conhecimento das formas do espectro de energia de ambas as componentes, sinal e ruído de fundo, é mais crítico do que uma razão sinal/ruído

elevada: se as eficiências dos cortes do ruído de fundo interno não são bem conhecidas, é preferível a análise do espectro sem cortes, pois este é menos distorcido.

Se o nível de contaminação do cintilador for 2×10^{-16} g/g (o dobro do requisito de projecto), e as distorções do espectro de energia forem corrigidas através de calibrações adequadas, a sensibilidade aos neutrinos do ^7Be deverá permitir uma boa discriminação entre as soluções de oscilação Pequeno Ângulo de Mistura (SMA) e Grande Ângulo de Mistura (LMA). Após um ano de tomada de dados, se a solução SMA for correcta, a LMA pode ser excluída ao nível de 3.8σ , e se a solução LMA for correcta, a SMA pode ser excluída ao nível de 1.2σ . A diferença entre a solução de oscilação LMA e o caso em que não haja oscilações será ainda maior. Além disso, se a estabilidade do detector for controlada ao nível de 1 %, seja por períodos de algumas horas (para verificar uma possível assimetria dia-noite), seja por períodos de alguns meses (para verificar possíveis variações sazonais), as soluções do Vácuo e LOW poderão ser bem identificadas através das variações temporais previstas para o sinal de neutrinos.

Concluindo, podemos afirmar que Borexino apresenta a sensibilidade potencial para distinguir entre as soluções de oscilações actualmente permitidas pelos resultados experimentais, desde que a taxa de ruído de fundo não supere o dobro do valor de design, e que a estabilidade e as eficiências do detector sejam calibradas e controladas segundo os requisitos exigidos para a identificação do sinal de neutrinos do ^7Be .

Table of Contents

<i>Summary</i>	v
<i>Resumo</i>	xi
<i>Table of Contents</i>	xvii
Chapter 1 · Solar Neutrino Physics	1
1.1 Introduction	1
1.2 The Solar Model	2
1.3 Solar Neutrino Experiments	8
1.3.1 The Chlorine experiment	9
1.3.2 The Gallium experiments	9
1.3.3 Water Cerenkov detectors	10
1.3.4 Heavy Water Cerenkov detector	12
1.4 The Solar Neutrino Problem	13
1.4.1 Astrophysical solutions	15
1.5 Neutrino Oscillations	16
1.5.1 Oscillations in vacuum	16
1.5.2 Oscillations in matter	19
1.6 Status and outlook	24
Chapter 2 · The Borexino Experiment	29
2.1 Overview	29
2.2 The detector	31
2.2.1 Scintillator	32
2.2.2 Nylon Vessels	38
2.2.3 Stainless Steel Sphere and Pseudocumene Buffer	40
2.2.4 Photomultipliers	42
2.2.5 Muon Detector and Water Buffer	44
2.3 Auxiliary Systems	45
2.3.1 Fluid Handling Systems	45
2.3.2 Scintillator Purification Systems	45
2.3.3 Additional Purification Systems	47
2.3.4 Electronics and DAQ	48
2.3.5 Event simulation and reconstruction codes	49
2.3.5.1 Generation	49
2.3.5.2 Tracking	51
2.3.5.3 Reconstruction	52

2.4	<i>The Counting Test Facility (CTF)</i>	54
2.4.1	CTF Design	54
2.4.2	CTF Results	56
2.4.3	CTF Upgrades	59
2.5	<i>Solar Neutrino Physics in Borexino</i>	60
2.5.1	Neutrino cross sections	60
2.5.2	Interaction rates in different oscillation scenarios	61
2.5.3	Time variations	65
2.6	Background	68
2.6.1	External background	69
2.6.1.1	Sources	69
2.6.1.2	Expected γ rates in the scintillator	72
2.6.2	Internal background	75
2.6.2.1	Rejection methods	75
2.6.2.2	Expected rates	77
Chapter 3 · Calibration of the Photomultipliers		81
3.1	<i>Low intensity light detection with photomultipliers</i>	82
3.1.1	Charge response	83
3.1.2	Time resolution	86
3.1.3	The PMTs for Borexino	87
3.2	System design	88
3.2.1	Requirements	88
3.2.2	The CTF experience	90
3.2.3	Structure and components	91
3.2.3.1	Light Source	91
3.2.3.2	External fibers	92
3.2.3.3	Light-transmitting feedthrough	93
3.2.3.4	Internal fibers	94
3.3	Preliminary feasibility tests	95
3.3.1	Light transmission in the fiber multiplexing chain	95
3.3.1.1	Results	96
3.3.1.2	Implications for Borexino	97
3.3.2	Compliance of the materials with the standards of the experiment	99
3.4	Complete prototype test	100
3.4.1	The Two-Liquid Test Tank	100
3.4.2	The fiber system	102
3.4.3	Electronics and DAQ	105
3.4.4	Data analysis	106
3.4.4.1	Time Calibration	106
3.4.4.2	Charge calibration	109
3.5	Comissioning of the final system	111

3.5.1	Quality control of the feed-throughs	111
3.5.2	Quality control of the fiber bundles	112
3.5.3	Cleanliness	113
3.5.4	Installation	114

Chapter 4 · Optical Calibration of the Scintillator and the Buffer Liquid ..119

4.1	Overview	119
4.2	Internal system	121
4.2.1	Goals and requirements	121
4.2.2	Scintillation light production	122
4.2.2.1	Excitation by charged particles	123
4.2.2.2	Excitation with ultraviolet light	128
4.2.3	System design	128
4.2.3.1	Lasers	129
4.2.3.2	Fibers	130
4.2.4	Experimental tests	132
4.2.4.1	Overview	132
4.2.4.2	Description of the experimental setup	132
4.2.4.3	Experimental results	136
4.3	External systems	140
4.3.1	Light propagation in PC+PPO	141
4.3.2	Monitoring strategy	144
4.3.3	Radial beams system	145
4.3.3.1	Design	145
4.3.3.2	Experimental test in the TLTT	147
4.3.4	Oblique beams system	155
4.3.4.1	Goals and requirements	155
4.3.4.2	Design	157
4.3.4.3	Light beam profiles	161
4.3.5	Monte Carlo simulations of the expected performance	167
4.3.5.1	Simulation of the radial beams	167
4.3.5.2	Simulation of the oblique beams	169

Chapter 5 · Calibration with radioactive sources.....173

5.1	Internal sources	174
5.1.1	Types of sources	174
5.1.2	Insertion and positioning mechanisms	175
5.2	External source monitoring	178
5.2.1	Monte Carlo simulations of the expected performance	179
5.2.2	Design of the insertion system	182

Chapter 6 · Sensitivity of Borexino to ⁷Be solar Neutrinos.....185

6.1.1	General Approach	185
6.1.2	Neutrino energy spectrum	187
6.1.3	Background description	190
6.2	Sensitivity of the ⁷Be neutrino energy spectrum fit	192
6.2.1	Global fits	193
6.2.2	Signal/Background issues	196
6.2.2.1	Secular equilibrium breaking	196
6.2.2.2	Scintillator radiopurity and neutrino oscillation solutions	199
6.2.3	Calibration issues	203
6.2.3.1	PC transparency and Pulse-Shape discrimination	203
6.2.3.2	Energy scale correction for β/γ quenching	208
6.3	Conclusions	213
Appendix		217
References		223
Acknowledgements		221

Solar Neutrino Physics

1.1 Introduction

Nuclear fusion reactions provide the energy source that sustain the luminosity of most stars, and namely the Sun. The fusion of four hydrogen nuclei into a helium nucleus is the result of a series of reactions, that include neutrino-emitting weak processes. The individual reactions may include heavier nuclei as catalysts, but the overall reaction balance can be represented by:

$$4p \rightarrow \alpha + 2e^+ + 2\nu_e \quad \text{Eq. 1.1}$$

The mass excess is 24.7 MeV, but the e^+ annihilation produces 2 MeV. Since only a small fraction of the kinetic energy is carried by the neutrinos, the total neutrino flux is proportional to the Sun luminosity:

$$\Phi(\nu_e) = 2 \frac{L_\odot}{26.7 \text{ MeV}} \frac{1}{4\pi D^2} = 6.6 \times 10^{10} \nu_e \text{ cm}^{-2} \text{ s}^{-1} \quad \text{Eq. 1.2}$$

where L_\odot is the Sun luminosity ($2.4 \cdot 10^{39} \text{ MeVs}^{-1}$) and D is the Earth-Sun distance ($1.5 \cdot 10^{11} \text{ m}$). However, the neutrinos can be produced in different reactions at different energies, so the calculation of their individual fluxes requires detailed models of the Sun. The interaction length of a typical optical photon in solar matter is 1 cm, while for neutrinos, it is 20 orders of magnitude higher. Therefore with neutrinos one can probe directly the core of the Sun while the electromagnetic radiation we receive on Earth comes only from the Photosphere (the outer layer of the Sun). This was the motivation for the first solar neutrino

experiment: to submit the theories of stellar evolution and solar models to a direct test.

The long-standing solar neutrino problem was initially the discrepancy between the measured ν_e capture rate in ^{37}Cl (the Chlorine experiment) and the rate predicted by solar models. Later, when more experiments measured solar neutrinos with different targets, the inconsistency could be appreciated also independently of the solar model predictions. This was the first indication for neutrino oscillations, opening the way for Physics beyond the Standard Electroweak Model.

1.2 The Solar Model

The study of the Sun contributed largely to the development of the Physics of stellar evolution, simply because we know more about it than any other star. Until the late 1800's, it was believed that the energy of the stars was produced in chemical reactions or gravitational contraction. However, the energy that can be produced through these processes is not enough to account for the Sun luminosity, integrated over its age, estimated through geological considerations. Such kind of evidence is impossible to obtain outside the Solar system. This paradox would not be solved until the development of Nuclear Physics in the 1920's and 1930's.

In 1939 Hans Bethe proposed the idea that thermonuclear reactions can fuel the Sun over its estimated lifetime of 5 billion years [1]. The theory was based on the fusion of four hydrogen nuclei into a helium nucleus, a process that releases the energy of 26.7 MeV and that should be possible in a region of very high temperatures, such as the Sun's core. Bethe discussed two reaction sequences - the proton-proton (pp) chain and the carbon-nitrogen-oxygen (CNO) cycle – that result both in the fusion of four protons into a helium nucleus, the difference being mainly the role of the carbon, nitrogen, oxygen and fluorine nuclei as catalysts in the CNO cycle. While Bethe thought the CNO cycle to be dominant, modern solar models now assign 98% of the solar energy production to the pp chain.

Figure 1.1 shows a scheme of the pp chain reactions and Table 1.1 list the neutrino-emitting reactions of both sequences. There are, overall, eight reactions producing neutrinos, with energies up to 18.8 MeV, but only 1% of the emitted neutrinos have energies above 1 MeV. Neutrinos from ${}^7\text{Be}$ decay and the pep reaction are mono-energetic while all other sources have a continuous spectrum.

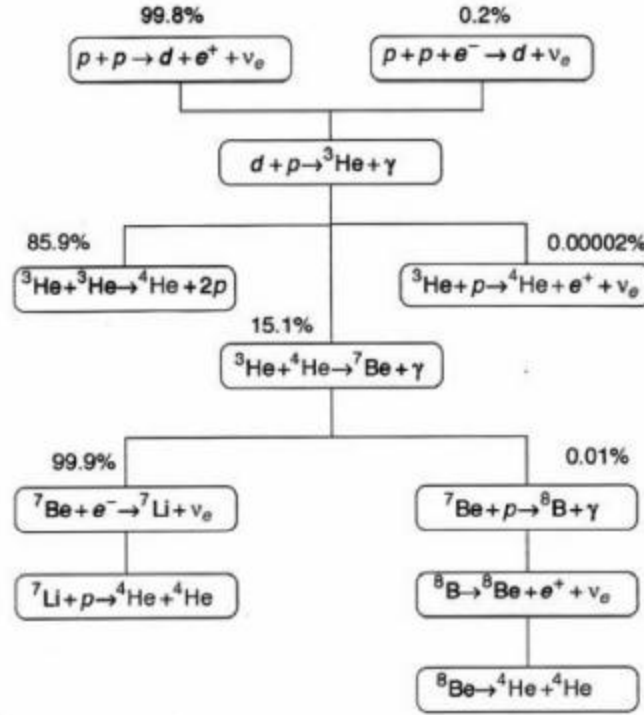


Figure 1.1 The proton-proton (pp) chain of nuclear fusion reactions in the Sun. The % values indicated are the branching ratio of each reaction.

Reaction	Neutrino source	E_n [MeV]	$\langle q_{ne} \rangle$ [MeV]
$p + p \rightarrow {}^2\text{H} + e^+ + \nu_e$	pp	0.420	0.265
$p + e^- + p \rightarrow {}^2\text{H} + \nu_e$	pep	1.442	1.442
${}^7\text{Be} + e^- \rightarrow {}^7\text{Li} + \nu_e$	${}^7\text{Be}$	0.862 (90 %)	0.862
		0.383 (10 %)	0.383
${}^8\text{B} \rightarrow {}^8\text{Be} + e^+ + \nu_e$	${}^8\text{B}$	15	6.71
${}^3\text{He} + p \rightarrow \alpha + e^+ + \nu_e$	hep	18.8	9.27
${}^{13}\text{N} \rightarrow {}^{13}\text{C} + e^+ + \nu_e$	${}^{13}\text{N}$	1.199	0.707
${}^{15}\text{O} \rightarrow {}^{15}\text{N} + e^+ + \nu_e$	${}^{15}\text{O}$	1.732	0.996
${}^{17}\text{F} \rightarrow {}^{17}\text{O} + e^+ + \nu_e$	${}^{17}\text{F}$	1.740	0.999

Table 1.1 Neutrino-emitting reactions in the Sun, from the pp chain and the CNO cycle (last three rows). Neutrino sources with a \pm sign before the energy value emit a continuous spectrum. The other sources (pep and ${}^7\text{Be}$) emit monoenergetic lines. $\langle q_{\nu e} \rangle$ is the average neutrino energy.

Luminosity	$3.86 \cdot 10^{33} \text{ erg s}^{-1}$
Mass	$1.99 \cdot 10^{30} \text{ kg}$
Radius	$6.96 \cdot 10^8 \text{ m}$
Oblateness [$R_{\text{equator}}/R_{\text{polar}}-1$]	$<2 \cdot 10^{-5}$
Age	$4.55 \cdot 10^9 \text{ yr}$

Table 1.2 Main properties of the Sun.

Since the pp reaction is at the base of the pp chain, the pp neutrino flux is connected directly to the Sun luminosity, but for all the other neutrino sources, detailed models describing the conditions inside the Sun are necessary. The Solar Models are essentially solutions of the stellar evolution equations using the known properties of luminosity, mass, radius and age as boundary conditions (listed in Table 1.2) and cross sections for nuclear reactions, element abundances and radiative absorption coefficients as input data. Since the oblateness is very small, the Sun is assumed to be spherical

The underlying assumptions of the solar models can be summarized as follows:

- **Hydrostatic equilibrium.** Gravitational attraction is balanced by thermal and radiation pressures.
- **Energy transport.** The energy is transported from the solar core to the surface by radiation and convection only, neglecting the contribution of acoustic or gravitational waves. This results in a large central region dominated by photon diffusion with a convective zone near the surface.
- **Energy generation.** The Sun is a Main Sequence star¹ so the energy is generated only by the hydrogen-burning nuclear reactions of the pp chain and CNO cycle. Helium-burning and gravitational energy generation are present only in late, turbulent phases of the life of a star. The rates of the fusion reactions are calculated by averaging the cross sections

¹ This designation refers to a region in the color-luminosity (or Hertzsprung-Russell) diagram where stars in their stable, hydrogen-burning phase are represented.

$$s(E) = \frac{S(E)}{E} \exp\left(-\frac{2pZ_1Z_2e^2}{\hbar v}\right) \quad \text{Eq. 1.3}$$

over Maxwell-Boltzmann velocity distributions, where v is the relative velocity of the nuclei with atomic number Z_1 and Z_2 [2]. At the temperatures of the solar core, the product of the exponential factor (known as Gamow penetration factor) by the exponential from the Maxwell-Boltzmann distribution peaks sharply at about 20 keV (the Gamow peak). The $S(E)$ factor is expected to vary smoothly and, at the low solar energies, its value is usually obtained by extrapolation from laboratory measurements at higher energies. In recent years, progress has been made with underground experiments, and measurements in low energy region of the Gamow peak have been performed [3], essentially confirming the previous extrapolations.

The system of equations that describe these assumptions is solved iteratively until the model agrees with the correct boundary conditions. The results of the model are the radial distributions of temperature, density and pressure, the composition of the Photosphere, the frequency spectrum for acoustic oscillations of the Sun's surface and the solar neutrino spectra and fluxes.

Different solar models have been published by several authors [2, 4]. The models based on the generally accepted physical assumptions are essentially in agreement. Other models (called non-standard) have changed the assumptions or introduced *ad hoc* input parameters in order to predict a lower neutrino capture rate in the Chlorine experiment. Hereafter, we will consider the model recently published by Bahcall and Pinsonneault [5] as the Standard Solar Model (SSM), referred as BP2000.

The fluxes of each individual source, as predicted by the BP2000 model, are listed in Table 1.3 and the correspondent energy spectra are shown in Figure 1.2, only for the pp chain neutrino sources.

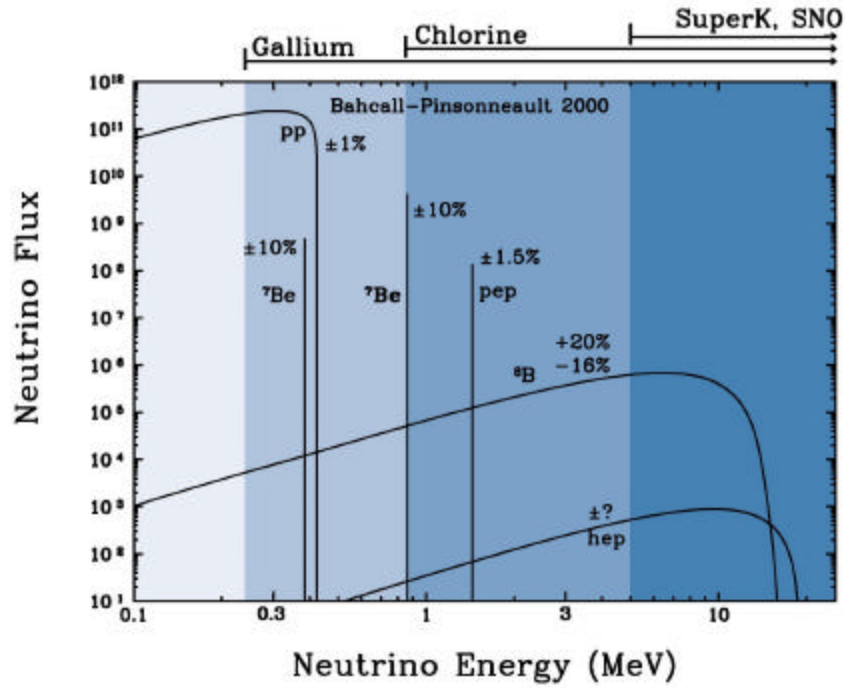


Figure 1.2 Energy spectrum of the pp chain solar neutrinos according to the BP2000 solar model. The errors for the flux prediction of each source are indicated.

Source	Flux [$10^{10} \text{ cm}^{-2} \text{ s}^{-1}$]	Cl rate [SNU]	Ga rate [SNU]
pp	$5.96(1.00^{+0.01}_{-0.01})$	0.0	69.6
pep	$1.40 \cdot 10^{-2}(1.00^{+0.015}_{-0.015})$	0.22	2.8
hep	$9.3 \cdot 10^{-7}$	0.0	0.0
^7Be	$4.82 \cdot 10^{-1}(1.00^{+0.10}_{-0.10})$	1.15	34.4
^8B	$5.15 \cdot 10^{-4}(1.00^{+0.20}_{-0.16})$	5.9	12.4
^{13}N	$5.56 \cdot 10^{-2}(1.00^{+0.21}_{-0.17})$	0.1	3.7
^{15}O	$4.88 \cdot 10^{-2}(1.00^{+0.25}_{-0.19})$	0.4	6.0
^{17}F	$5.73 \cdot 10^{-4}(1.00^{+0.25}_{-0.25})$	0.0	0.1
Total		$7.7^{+1.3}_{-1.1}$	129^{+9}_{-7}

Table 1.3 – Neutrino fluxes predicted by the BP2000 solar standard model. The last two columns show the predicted capture rate in the Chlorine and Gallium experiments, measured in Solar Neutrino Units (SNU), equivalent to 10^{-36} captures per target atom per second.

1.3 Solar Neutrino Experiments

The difficulties of neutrino detection are directly connected to the very low cross sections of interaction with matter. Solar neutrino detection presents additional problems with respect to reactor and accelerator experiments: much lower rates, high background from natural radioactivity at low energies, impossibility of background subtraction with “beam-off” or “reactor-off” runs. Consequently, all solar neutrino detectors have large masses, are built with low radioactivity materials and located in deep underground laboratories, for cosmic ray shielding.

The first attempts for detecting solar neutrinos have been made by F. Reines, T. L. Jenkins et al. [6, 7, 8, 9] with liquid scintillator and heavy water detectors, that could be considered precursors of Borexino and SNO, respectively. However, the sensitivity of these detectors was limited by background problems, as it happened also with the geochemical experiments that look for an integrated neutrino capture rate by precisely measuring isotopic abundances in suitable deep underground mineral ores. For more detail, see the report of Raymond Davis Jr. in [10].

The next sections will briefly focus on the six experiments that have detected solar neutrinos. Essentially, these are of two types:

- Radiochemical experiments based on neutrino capture reactions by specific isotopes. The reaction products can be chemically separated from the target mass and its radioactive decay can be detected in low background proportional counters. These experiments are able to measure only a total capture rate above a threshold, without any information on the neutrino energy spectrum.
- Real-time experiments detecting the Cerenkov light produced in the detector, supplying information about the energy, direction and time of neutrino interactions. The limitation of the Cerenkov detectors is the high energy threshold that restricts their sensitivity to ^8B neutrinos.

1.3.1 The Chlorine experiment

The Chlorine detector [11], operated since 1968 by Raymond Davis, Jr. and collaborators in the Homestake Gold Mine in Lead, South Dakota (USA), at a water equivalent depth of 4200 m (mwe), for almost two decades was the only operating solar neutrino experiment.

The detection reaction is the inverse β process

$$\nu_e + {}^{37}\text{Cl} \rightarrow e^- + {}^{37}\text{Ar}. \quad \text{Eq. 1.4}$$

The experimental method consists on counting the radioactive ${}^{37}\text{Ar}$ atoms produced by neutrino capture on ${}^{37}\text{Cl}$ atoms in the form of 615 tons of C_2Cl_4 (2.2×10^{30} atoms). After 1 to 3 months of exposure, the ${}^{37}\text{Ar}$ atoms are removed from the detector tank by circulating helium, and loaded into small proportional chambers. The ${}^{37}\text{Ar}$ electron capture decays ($\tau_{1/2} = 35$ d) are counted for about eight months by detecting the 2.82 keV Auger electrons. The SSM prediction for the neutrino capture rate in the Chlorine experiment is given in Table 1.3 as:

$$R_{\text{th}} = 7.7^{+1.2}_{-1.0} \text{ SNU},^2 \quad \text{Eq. 1.5}$$

where 5.9 SNU come from ${}^8\text{B}$ neutrinos and 1.15 SNU from ${}^7\text{Be}$ neutrinos. The measured counting rate, averaged over 25 years of data-taking (1970-1995), is roughly one third of the predicted value [12]:

$$R = [2.56 \pm 0.16] \text{ SNU}.$$

1.3.2 The Gallium experiments

The energy threshold of the neutrino capture reaction on ${}^{71}\text{Ga}$,

$$\nu_e + {}^{71}\text{Ga} \rightarrow e^- + {}^{71}\text{Ge} \quad \text{Eq. 1.6}$$

is 233 keV, low enough to allow the detection of pp solar neutrinos. We recall here the SSM prediction for neutrino capture rate in the Gallium experiments:

² The Solar Neutrino Unit (SNU) is equivalent to 10^{-36} neutrino captures per target atom per second.

$$R_{\text{th}} = 129_{-7}^{+9} \text{ SNU}$$

Of this rate, 70 SNU come from pp neutrinos, 34 SNU from ^7Be neutrinos and 12 SNU from ^8B neutrinos.

The reaction in Eq. 1.6 is used by the SAGE, GALLEX and GNO [13,14,15] experiments that, as the Chlorine experiment, also use the radiochemical method, so the ^{71}Ge atoms are periodically extracted from the target and its electron capture decay ($\tau_{1/2} = 11.4 \text{ d}$) measured in low background proportional counters.

The SAGE experiment is located in the Baksan Neutrino Observatory, in the Northern Caucasus, Russia, with an overhead shielding of 4700 mwe. Its target consists of 60 tons of pure metallic gallium.

The GALLEX experiment is located in Hall A of the Gran Sasso Underground Laboratory, in Italy, with a minimum shielding of 1400 m of rock, or 3800 mwe. Its target contains 30 tons of Ga in the form of GaCl_3 , so the chemical procedures for the extraction of ^{71}Ge are different from SAGE. GALLEX took data from 1991 to 1997 and GNO, which is essentially the continuation of GALLEX, started again in 1998. In the next years GNO projects to increase its mass from 30 tons to 100 tons.

The measured neutrino capture rates are:

$$\text{SAGE: } R = [67.2_{-7.0}^{+7.2} (\text{stat.})_{-3.0}^{+3.5} (\text{sys.})] \text{ SNU}$$

$$\text{GALLEX: } R = [77.5 \pm 6.2 (\text{stat.})_{-4.7}^{+4.3} (\text{sys.})] \text{ SNU}$$

$$\text{GNO: } R = [65.8_{-9.6}^{+10.2} (\text{stat.})_{-3.6}^{+3.4} (\text{sys.})] \text{ SNU}$$

The measured rates are about 54 % of the predicted rate, confirming the depletion scenario seen by the Chlorine experiment.

1.3.3 Water Cerenkov detectors

Kamiokande and its successor experiment, Super-Kamiokande, use water as sensitive target mass and exploit the neutrino-electron elastic scattering reaction

$$\nu + e^- \rightarrow \nu + e^- \quad \text{Eq. 1.7}$$

for the solar neutrino detection.

The experimental method consists of using photomultiplier tubes (PMTs) to observe the Cerenkov light produced by the fast recoil electrons crossing the water. The background imposes a high energy threshold for the study of the recoil electrons, 7.5 MeV in Kamiokande and 6.5 MeV in Super-Kamiokande. This limits the observable neutrino sources to ^8B and hep neutrinos. However, water Cerenkov detectors have several advantages with respect to the radiochemical experiment:

- They are sensitive, even if with a lower cross section, to neutrinos with flavours other than ν_e ;
- They can measure the energy of the recoil electron, providing information on the neutrino energy spectrum;
- They record the time of the event, allowing the study of the neutrino flux time variations;
- They can provide direct evidence for the solar origin of the neutrino events due to the high directionality of the Cerenkov light.

Both detectors are located in the Kamioka mine, 300 km west from Tokio, Japan, at a depth of 1 km (2700 mwe). The Kamiokande experiment had a fiducial mass of 680 tons of water and 948 photomultipliers. It started in 1983, but solar neutrino data-taking began in 1986, after the addition of a muon anticounter and improved electronics. In 1994, the detector was shut down and replaced by a large scale upgraded version, Super-Kamiokande, that started data-taking in April 1996. Super-Kamiokande has a fiducial mass of 22.5 kilotons of water and 11000 photomultiplier tubes.

The ^8B neutrino flux measured in Kamiokande [16], taking into account the whole data sample of 2079 days is:

$$\Phi(^8\text{B}) = [2.80 \pm 0.19 \text{ (stat.)} \pm 0.33 \text{ (sys.)}] \times 10^6 \text{ cm}^{-2}\text{s}^{-1},$$

which, compared to the predicted value, amounts to (see Table 1.3):

$$\Phi(^8\text{B})_{\text{exp}}/\Phi(^8\text{B})_{\text{theor}} = 0.54 \pm 0.08.$$

Mainly due to its higher mass, SuperKamiokande greatly increased the precision of this measurement. The latest published value [17], that takes into account a data sample of 1258 days, is:

$$\Phi(^8\text{B}) = [2.32 \pm 0.03 \text{ (stat.) } {}^{+0.08}_{-0.07} \text{ (sys.)}] \times 10^6 \text{ cm}^{-2}\text{s}^{-1} \quad \text{Eq. 1.8}$$

Compared to BP2000 prediction, the measured flux gives:

$$\Phi(^8\text{B})_{\text{exp}}/\Phi(^8\text{B})_{\text{theor}} = 0.451 \pm 0.005 \text{ (stat.) } {}^{+0.016}_{-0.014} \text{ (sys.)}$$

Due to the high statistics, SuperKamiokande is also sensitive to the shape of the ^8B signal energy spectrum. The measured spectrum is consistent with the ^8B neutrino spectrum as predicted by the SSM, with no energy-dependent distortions.

The seasonal variation of the flux is also consistent with that expected from the eccentricity of the Earth's orbit. However, there is a discrepancy between the flux measured during the day and during the night:

$$\frac{\Phi_n - \Phi_d}{\Phi_n + \Phi_d} = 0.033 \pm 0.022 \text{ (stat.) } {}^{+0.013}_{-0.012} \text{ (syst.)} \quad \text{Eq. 1.9}$$

showing a weak departure from 0 at about 1.3σ .

1.3.4 Heavy Water Cerenkov detector

The Sudbury Neutrino Observatory (SNO) [18] is located in INCO's Creighton mine near Sudbury, Ontario (Canada) and has been taking data since November 1999 (online since May 1999). The detector consists of a 1000 tons heavy water (D_2O) target observed by 9700 photomultipliers, contained by a spherical acrylic vessel, and shielded by 3 m of ultrapure normal (H_2O) water. The use of heavy water as target in SNO allows the detection of neutrinos through their capture on deuterium nuclei, in addition to neutrino-electron elastic scattering:

- $\nu_x + e^- \rightarrow \nu_x + e^-$
- $\nu_e + d \rightarrow e^- + p + p$
- $\nu_x + d \rightarrow \nu_x + p + n$

The capability of distinction between charged and neutral current reactions allows the measurement of the flavor content of the ^8B solar neutrino flux. Electrons are detected by the Cerenkov effect, and the neutrons produced in the neutral current reaction are thermalized and captured by protons, yielding a 2.2 MeV gamma ray. Its electron shower is detected by Cerenkov effect.

In order to increase the neutron detection efficiency, two different methods are planned: to detect the 8.6 MeV gamma ray from neutron capture in chlorine in NaCl added to the heavy water and to use ^3He filled proportional chambers placed inside the acrylic vessel.

The SNO collaboration has published [19] the measurement of solar neutrinos by the charged current reaction and the elastic scattering reaction. The measurements by the neutral current reaction are ongoing.

$$\Phi^{CC}(\mathbf{n}_e) = 1.75 \pm 0.07(\text{stat.})^{+0.12}_{-0.11}(\text{sys.}) \pm 0.05(\text{theor.}) \times 10^6 \text{ cm}^{-2} \text{ s}^{-1} \quad \text{Eq. 1.10}$$

$$\Phi^{ES}(\mathbf{n}_x) = 2.39 \pm 0.34(\text{stat.})^{+0.16}_{-0.14}(\text{sys.}) \times 10^6 \text{ cm}^{-2} \text{ s}^{-1} \quad \text{Eq. 1.11}$$

Comparison of $\Phi^{CC}(\mathbf{n}_e)$ with $\Phi^{ES}(\mathbf{n}_x)$ as measured with high precision by SuperKamiokande (Eq. 1.8) yields a 3.3σ difference and provides a strong indication for a non-electron flavor active component of the solar neutrino flux. From these values, the total flux of active ^8B neutrinos is determined to be $5.44 \pm 0.99 \times 10^6 \text{ cm}^{-2} \text{ s}^{-1}$, in close agreement with the solar model predictions.

1.4 The Solar Neutrino Problem

The central fact of the Solar Neutrino Problem is that the difference between the measured and predicted solar neutrino detection rates is significantly larger than the experimental and theoretical uncertainties. The accumulation of data from the several experiments expanded the solar neutrino problem to an inconsistency between neutrino rates measured with different energy thresholds.

This is illustrated in Figure 1.3, that shows the measured rates in blue and the predicted rates for each solar neutrino source in different colors. If we take the ^8B flux measured by the water Cerenkov detectors to predict the rate in the Chlorine detector, a higher value than the measured rate is obtained, forcing the ^7Be

neutrinos into a non-physical negative contribution. This is difficult to explain, without assuming an energy spectrum distortion by non-standard Neutrino Physics.

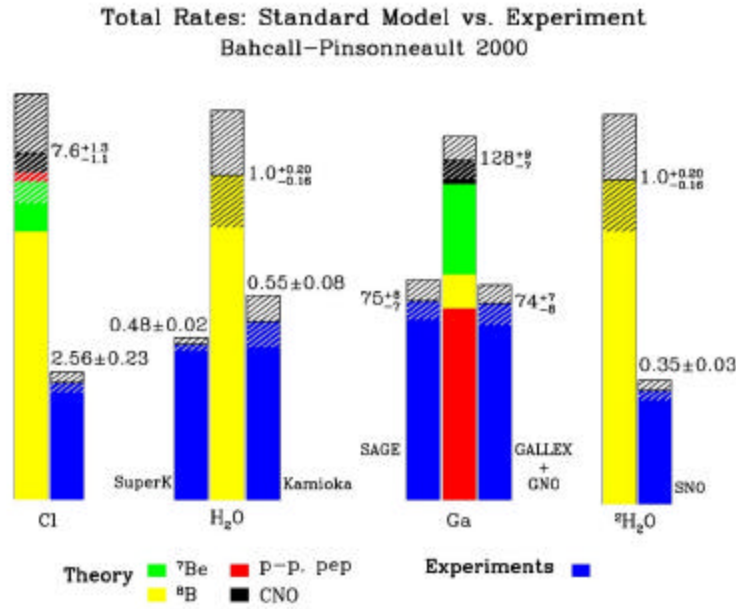


Figure 1.3 Comparison of the Standard Solar Model predictions with the total rates in the six solar neutrino experiments. From [20].

A second experimental inconsistency comes from the rate measured by the Gallium detectors, that is all accounted for by the pp neutrinos, leaving no space for the large expected contribution from ^{7}Be neutrinos. The inconsistency lies in the fact that the ^{8}B isotope that emits the neutrinos observed in the water Cerenkov detectors cannot be formed in the Sun without the ^{7}Be isotope. This is usually referred to as the $^{7}\text{Be}/^{8}\text{B}$ paradox.

Finally, there is the SNO charged current measurement of the ^{8}B neutrino flux, incompatible with the electron scattering measurement in SuperKamiokande, unless we admit a non-electron flavor component of the solar neutrino flux.

1.4.1 Astrophysical solutions

Several authors have proposed [21] different solar models based on non-standard physical assumptions or input parameters in order to reduce the predicted Chlorine rate. A summary of the predictions for the ${}^7\text{Be}$ and ${}^8\text{B}$ neutrino fluxes by non-standard solar models is shown in Figure 1.4. While some models predict a ${}^8\text{B}$ flux near to the measured value, none of them is capable of explaining the strong suppression of the ${}^7\text{Be}$ neutrinos, inferred from a combined fit of all the experimental data. So the ${}^7\text{Be}/{}^8\text{B}$ paradox strongly disfavors astrophysical solutions of the Solar Neutrino Problem.

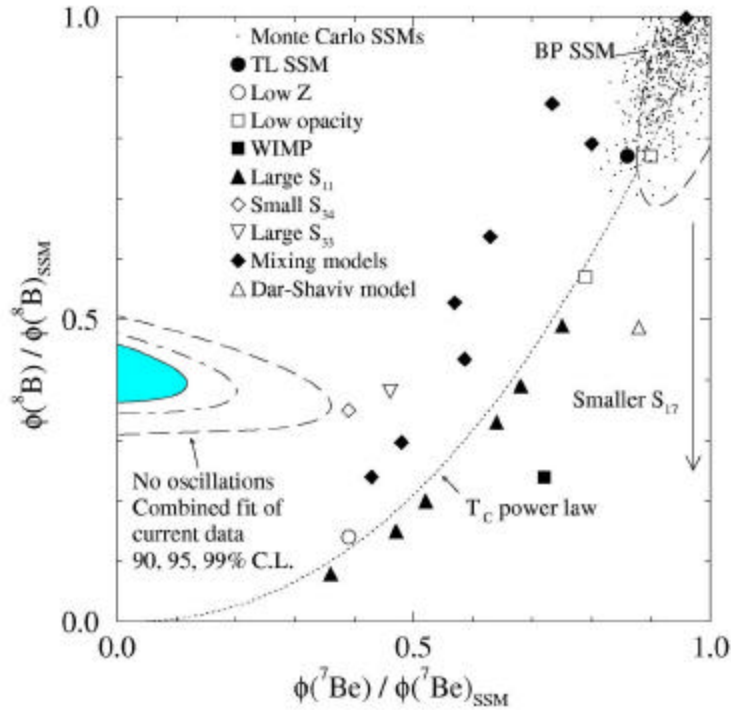


Figure 1.4 Predicted fluxes of ${}^8\text{B}$ and ${}^7\text{Be}$ neutrinos for several non-standard solar models, compared to the values obtained from a combined fit of the experimental measurements (indicated in the left part of the plot). From [21].

Solar Models can also be tested by comparing their predictions for the sound speed inside the Sun with the radial distributions calculated from the helioseismic activity precision observations made by several experiments [5]. The agreement between the measurements and the predictions of the BP2000 standard model is at

the level of 0.1 % rms, while the non-standard model predictions are off by at least 9%.

1.5 Neutrino Oscillations

In 1968, Pontecorvo[22] first made the suggestion that, along their travel to the Earth, the electron neutrinos produced in the Sun could oscillate into muon neutrinos, that cannot be detected in the Chlorine experiment. However, in order to explain the measured solar neutrino suppression by a factor of three, the model required the “fine-tuning” of the parameters, and a large flavour mixing, that seemed unnatural by analogy with the quark sector.

In 1985, Mikheyev and Smirnov [23,24], following the framework of Wolfenstein [25], proposed an elegant mechanism that, through the enhancement of flavour conversion in matter, produced large ν_e suppressions even with small mixing and in a vast parameter region. This mechanism, known as the MSW effect, is now widely considered as the most likely solution for the solar neutrino problem.

1.5.1 Oscillations in vacuum

We call $|\nu_i\rangle$, with $i=1, \dots, 3$ the neutrinos states with definite masses m_i , the eigenstates of the free-field Hamiltonian. The origin of the mass term comes from either the introduction of right-handed neutrino fields, giving rise to Dirac mass terms, or from an extension of the Higgs sector, allowing Majorana mass terms. However, we will not discuss the underlying differences, since the oscillation probabilities are insensitive to the Dirac or Majorana character of the neutrino fields³.

The $|\nu_i\rangle$ states are not necessarily the same as the neutrino states of definite flavour, that is, those that describe neutrinos ν_e , ν_μ and ν_τ produced together with the charged leptons e^+ , μ^+ and τ^+ in the decay of the W^+ boson. Since the $|\nu_i\rangle$ and

³ If neutrinos are described by Majorana fields, the particle is its own anti-particle. The opposite happens in the Dirac case.

$|\nu_\alpha\rangle$ states, with $\alpha = e, \mu, \tau$, are the orthogonal basis for the general neutrino states, they are related by a 3×3 unitary matrix,

$$|\mathbf{n}_a\rangle = \sum_i U_{ai} |\mathbf{n}_i\rangle \quad \text{Eq. 1.12}$$

The matrix U is the leptonic mixing matrix, also called the MNS (Maki-Nakagawa-Sakata) matrix. The analogous matrix in the quark sector is the well-known CKM (Cabbibo-Kobayashi-Maskawa) matrix.

It can be shown [26] that the oscillation probabilities in a three-neutrino scenario can be reduced to two-neutrino oscillation probabilities if two of the neutrino mass eigenstates are nearly degenerate, that is, if one of the mass splittings $\Delta m^2 = m_i^2 - m_j^2$ between m_1 , m_2 and m_3 is much smaller than the other two. As will be discussed ahead, the experimental evidence for neutrino oscillations from solar and atmospheric neutrinos give strong indications for this scenario, with $\Delta m_{atmosf}^2 \approx 10^{-3} \text{ eV}^2$ and $\Delta m_{solar}^2 \approx 10^{-5} \text{ eV}^2$.

So, with only a relative loss of generality, we consider only two-neutrino oscillation scenarios from now on and we can relate the flavor and mass basis by:

$$\begin{aligned} |\mathbf{n}_e\rangle &= \cos \theta |\mathbf{n}_1\rangle + \sin \theta |\mathbf{n}_2\rangle \\ |\mathbf{n}_\mu\rangle &= -\sin \theta |\mathbf{n}_1\rangle + \cos \theta |\mathbf{n}_2\rangle \end{aligned} \quad \begin{array}{l} \text{Eq.} \\ 1.13 \end{array}$$

where θ is called the mixing angle in vacuum. In a simplified approach (neglecting spin), the time evolution of an arbitrary neutrino state $|\nu(t)\rangle$ is given by Schrödinger's equation, so after a time t the flavor eigenstates have evolved into

$$\begin{aligned} |\mathbf{n}_e(t)\rangle &= \cos \theta e^{-iE_1 t} |\mathbf{n}_1\rangle + \sin \theta e^{-iE_2 t} |\mathbf{n}_2\rangle \\ |\mathbf{n}_\mu(t)\rangle &= -\sin \theta e^{-iE_1 t} |\mathbf{n}_1\rangle + \cos \theta e^{-iE_2 t} |\mathbf{n}_2\rangle \end{aligned} \quad \begin{array}{l} \text{Eq.} \\ 1.14 \end{array}$$

Since they have different masses, the components of eigenstates 1 e 2 have picked up different phases and the states are no longer pure $|\nu_e\rangle$ and $|\nu_\mu\rangle$. Using Eq. 1.13 and Eq. 1.14, we can calculate the probability for a neutrino created at time 0 as ν_e to be detected at time t still as a ν_e , also called survival probability.

$$P(\mathbf{n}_e \rightarrow \mathbf{n}_e) = \left| \langle \mathbf{n}_e | \mathbf{n}_e(t) \rangle \right|^2 = 1 - \sin^2 2\mathbf{q} \sin^2 \left(\frac{E_2 - E_1}{2} t \right) \quad \text{Eq. 1.15}$$

Assuming that both states are created with the same momentum p , for relativistic neutrinos, we have

$$E_i = \sqrt{p^2 + m_i^2} \approx p + \frac{m_i^2}{2p} \quad \text{Eq. 1.16}$$

Since, in natural units, $t \approx R$, where R is the distance traveled in time t , we can write the oscillation probabilities in a more convenient way:

$$\begin{aligned} P(\mathbf{n}_e \rightarrow \mathbf{n}_e) &= 1 - \sin^2 2\mathbf{q} \sin^2 \left(\frac{pR}{L_v} \right) \\ P(\mathbf{n}_e \rightarrow \mathbf{n}_m) &= \left| \langle \mathbf{n}_e | \mathbf{n}_m(t) \rangle \right|^2 = \sin^2 2\mathbf{q} \sin^2 \left(\frac{pR}{L_v} \right) \end{aligned} \quad \text{Eq. 1.17}$$

where we have introduced the oscillation length in vacuum L_v :

$$L_v = \frac{4pE}{\Delta m^2} \quad \text{Eq. 1.18}$$

From these equations, we can appreciate the oscillatory character of the flavour conversion in vacuum, with the parameter $\sin^2 2\theta$ assuming the role of an amplitude and the parameter Δm^2 assuming the role of a frequency.

A flavor conversion of $P(\mathbf{n}_e \rightarrow \mathbf{n}_e) \leq 5$, large enough to explain the experimental results (can be obtained in the vacuum oscillation scenario if the following conditions are fulfilled:

- $\sin^2 2\theta$ must be large, at least 0.5;
- the mass splitting Δm^2 between the oscillating neutrinos must be related to the Earth-Sun distance R and the neutrino energy E by

$$k + \frac{1}{2} = \frac{R\Delta m^2}{4pE} \quad \text{Eq. 1.19}$$

with k integer.

If k is large, the phase varies quickly with R and E and so, on average over the region of production of the solar neutrinos, the survival probability is $\frac{1}{2}$ on the

entire spectrum. If k is small, the phase varies slowly enough with R and E so that there can be a strong conversion at energies below 1 MeV, and a weaker conversion above that, which could explain the ${}^7\text{Be}/{}^8\text{B}$ paradox. In this case, the variation of the Earth-Sun distance due to the Earth orbit eccentricity would cause large seasonal variations of the observed neutrino rate.

From a theoretical point of view, the scenario for oscillations in vacuum is not preferred, since it requires a flavor mixing angle much larger for leptons than for quarks, and a fine-tuned coincidence between the neutrino energies and mass splittings and the Earth-Sun distance.

1.5.2 Oscillations in matter

The propagation of neutrinos in matter is affected by coherent forward scattering through the weak interaction. While neutrinos of all flavors can exchange Z bosons, only electron neutrinos can elastic scatter off electrons by exchanging W bosons. In the flavor basis the term for Z exchange will be proportional to the identity matrix and contribute to an overall phase in the neutrino state so we can neglect it. However the term for W exchange singles out the ν_e states and significantly changes the mass matrix.

It is useful to go back to the vacuum case and write the matrix for the squared mass in the basis of ν_e, ν_μ :

$$M_{vac}^2 = \frac{1}{2}(m_1^2 + m_2^2) \begin{bmatrix} 1 & 0 \\ 0 & 1 \end{bmatrix} + \frac{1}{2}(m_2^2 - m_1^2) \begin{bmatrix} -\cos 2q & \sin 2q \\ \sin 2q & \cos 2q \end{bmatrix} \quad \text{Eq. 1.20}$$

For the propagation in matter the extra term in the Hamiltonian is

$$H_{fs} = \frac{G_F}{\sqrt{2}} \bar{n}_e g_1 (1 + g_5) n_e \bar{e} g^I (1 + g_5) e \quad \text{Eq. 1.21}$$

where G_F is the Fermi constant of weak interactions. Since the electrons are at rest this is equivalent to a potential energy

$$V = \sqrt{2} G_F N_e \quad \text{Eq. 1.22}$$

where N_e is the number of electrons per unit volume.

Neglecting the small term V^2 , the energy and momentum of ν_e are related by

$$p^2 + m^2 = (E - V)^2 = E^2 - 2EV \quad \text{Eq. 1.23}$$

so this is the effect of the potential V is equivalent to adding the term $2\sqrt{2}G_F N_e E$ to the matrix M_{vac}^2 . In this way, we obtain the mass squared matrix in matter:

$$M_{Mat}^2 = \frac{1}{2} \begin{pmatrix} m_1^2 + m_2^2 + 2\sqrt{2}G_F N_e E & 0 \\ 0 & 1 \end{pmatrix} + \frac{1}{2} \begin{bmatrix} 2\sqrt{2}G_F N_e E - \Delta m^2 \cos 2q & \Delta m^2 \sin 2q \\ \Delta m^2 \sin 2q & -2\sqrt{2}G_F N_e E + \Delta m^2 \cos 2q \end{bmatrix} \quad \text{Eq. 1.24}$$

The eigenstates of this matrix are

$$\begin{aligned} |\mathbf{n}_{1m}\rangle &= \cos \mathbf{q}_m |\mathbf{n}_e\rangle - \sin \mathbf{q}_m |\mathbf{n}_m\rangle \\ |\mathbf{n}_{2m}\rangle &= \sin \mathbf{q}_m |\mathbf{n}_e\rangle + \cos \mathbf{q}_m |\mathbf{n}_m\rangle \end{aligned} \quad \text{Eq. 1.25}$$

and the eigenvalues are

$$m_{im}^2 = \frac{1}{2} \left(m_1^2 + m_2^2 + 2\sqrt{2}G_F N_e E \right) \pm \frac{1}{2} \Delta m^2 \frac{\sin 2q}{\sin 2q_m} \quad \text{Eq. 1.26}$$

where the $+$ sign corresponds to $|\nu_{2m}\rangle$ and the $-$ sign to $|\nu_{1m}\rangle$ and θ_m , the mixing angle in matter, is given by

$$\sin 2q_m = \frac{\Delta m^2 \sin 2q}{\sqrt{\left(2\sqrt{2}G_F N_e E - \Delta m^2 \cos 2q\right)^2 + \left(\Delta m^2 \sin^2 2q\right)^2}} \quad \begin{array}{l} \text{Eq.} \\ 1.2 \\ 7 \end{array}$$

This equation presents a resonance since, even for a small vacuum mixing angle θ , there can be a large mixing in matter, with $\sin 2\theta_m \sim 1$. For a given neutrino energy there is a resonant electron density given by

$$N_{e,res} = \frac{1}{2\sqrt{2}G_F} \cos 2\theta \frac{\Delta m^2}{E}$$

Eq.
1.2
8

at which the mixing is maximal.

Assuming, for simplicity, a small vacuum mixing angle the dependence of the mass eigenstates on the density of the medium can be distinguished in three cases:

- $N_e \ll N_{e,res}$. Well below resonance, the masses and the mixing angles are close to the vacuum values, so $|v_{1m}\rangle \sim |v_e\rangle$ and $|v_{2m}\rangle \sim |v_\mu\rangle$.
- $N_e = N_{e,res}$. At resonance $\theta_m = \pi/4$ and the flavor mixing is maximal. The difference between the mass of the two eigenstates reaches a minimum of $\Delta m^2 \sin 2\theta$.
- $N_e \gg N_{e,res}$. Far above the resonance, $\theta_m \sim \pi/2$, and the mass eigenstates are switched with respect to the vacuum, i.e., $|v_{1m}\rangle \sim |v_\mu\rangle$ and $|v_{2m}\rangle \sim |v_e\rangle$.

This is shown schematically in Figure 1.5, that represents the dependence of the mass eigenvalues m_{1m} and m_{2m} on the electron density of the medium.

In order to appreciate the full potential of matter oscillations, let us consider what happens inside the Sun, that is a medium with varying electron density. Suppose that Δm^2 and the energy E of a neutrino are such that the resonant density, given by Eq. 1.28, is lower than the electron density in the center of the Sun. Since $\rho_c \sim 150 \text{ g/cm}^3$, this gives a condition $E/\Delta m^2 > 5 \text{ MeV}/10^{-4} \text{ eV}^2$. In this case, the electron neutrino will be created inside the Sun predominantly in the state $|v_{2m}\rangle$. Its mass eigenvalue is shown by the upper curve in Figure 1.5. At some point in its travel towards the surface, the neutrino will cross a region where the electron density has the resonance value. In the adiabatic condition, the electron density changes sufficiently slowly so that the eigenstate rotates rapidly enough to “follow the variation of the eigenvalue” and there will not be transitions from one eigenstate to another.

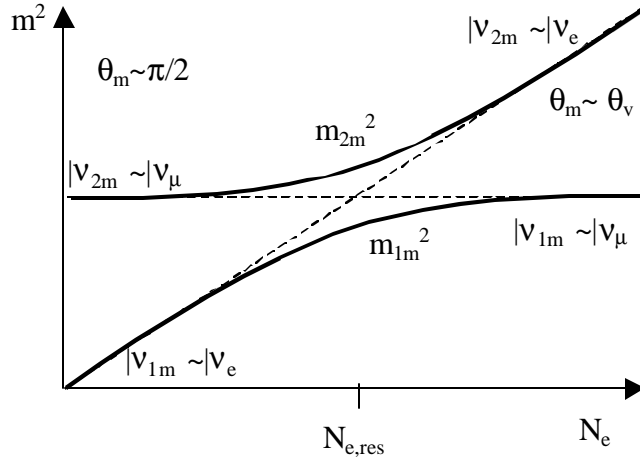


Figure 1.5 Schematic representation of the MSW effect. The solid lines represent the masses of the matter eigenstates $|v_{1m}\rangle$ and $|v_{2m}\rangle$ in function of the electron density N_e and the dashed lines their asymptotic behavior at $N_e \rightarrow 0$ and $N_e \rightarrow \infty$.

Consequently, the mass will still be given by the upper curve in Figure 1.5 and the neutrino will emerge from the Sun still as $|v_{2m}\rangle$ that, in vacuum, is mostly $|v_\mu\rangle$. The survival probability for electron neutrinos is given by

$$P(\mathbf{n}_e \rightarrow \mathbf{n}_e)_{adiab} = \frac{1}{2} (1 + \cos 2\mathbf{q} \cos 2\mathbf{q}_{m,0}) \approx \sin^2 \mathbf{q} \quad \text{Eq. 1.29}$$

where $\theta_{m,0}$ is the matter mixing angle evaluated at time 0, when the neutrino is produced. This equation expresses the remarkable feature of the MSW effect, i.e., that the flavor conversion is larger for small mixing angles.

The oscillation length in matter, defined as for the vacuum cases as the phase difference between the mass eigenstates, is:

$$L_m = \frac{2p}{|E_2 - E_1|} \cong \frac{4pE}{\Delta m^2} \frac{\sin 2\mathbf{q}_m}{\sin 2\mathbf{q}} \quad \text{Eq. 1.30}$$

This spatial width of the resonance is defined as the distance over which the change in electron density causes the eigenvalues to separate by an amount equal to the difference at resonance. According to ref. [27], it can be written as

$$dr = 2 \tan 2\mathbf{q} \left[-\frac{1}{N_e} \frac{dN_e}{dr} \right]_{res}^{-1} \quad \text{Eq. 1.31}$$

The adiabatic condition may be explicated by requiring that L_m should be smaller than δr . Using the solar model to obtain $\frac{dN_e}{dr}$, this may be written in a convenient way for numerical calculations [2]:

$$E < 5 \times 10^4 \text{ MeV} \frac{\sin^2 2q}{\cos 2q} \frac{\Delta m^2}{10^{-4} \text{ eV}^2} \quad \begin{array}{l} \text{Eq.} \\ 1.3 \\ 2 \end{array}$$

For example, for $\sin^2 2\theta < 4 \times 10^{-4}$ and $\Delta m^2 > 10^{-5} \text{ eV}^2$, the adiabatic condition will be fulfilled for neutrinos with energies below 2 MeV.

Outside that parameter range (Eq. 1.32), there can be transitions between the mass eigenstates at the resonant density, and so the survival probability for ν_e will be:

$$P(\mathbf{n}_e \rightarrow \mathbf{n}_e) = |\langle \mathbf{n}_e | \mathbf{n}_e(t) \rangle|^2 = \frac{1}{2} + \cos 2q \cos 2q_m \left(\frac{1}{2} - P_{\text{jump}} \right) \quad \text{Eq. 1.33}$$

where P_{jump} is the Landau-Zener probability for level crossing given by:

$$P_{\text{jump}} = \exp \left(- \frac{p^2 dr}{2L_{\text{mres}}} \right) \quad \text{Eq. 1.34}$$

In this case, the conversion will not be total, but can still be significant for the solar neutrino problem. The MSW effect thus predicts several scenarios of flavour conversion. According to the values of $\sin^2 2\theta$ and Δm^2 , the flavor conversion can happen predominantly at high energies, affecting the ^8B neutrino spectrum or at low energies, suppressing the ^7Be neutrinos, and solving the $^7\text{Be}/^8\text{B}$ paradox.

Neutrino oscillations in matter can also happen in a significant way inside the Earth. Neutrinos generated as ν_e in Sun core and converted into ν_μ on their way to the surface, can be converted back into ν_e in the Earth core. So the experiments on Earth would measure a higher neutrino interaction rate at night. The measurement of a significant day-night asymmetry would be a strong signature for the MSW effect.

1.6 Status and outlook

The solar neutrino flux predictions are robust, since the Standard Solar Models have been thoroughly confirmed by the helioseismological observations. Moreover, the Solar Neutrino Problem is not solved even if the flux predictions are not considered: a combined analysis [28] of all the data to undistorted neutrino energy spectra fails at the level of 4σ . So, the most likely explanation for the Solar Neutrino Problem is an energy-dependent flavor conversion of the neutrinos on their way from the Sun to the Earth.

Several authors have performed global analyses of all the solar neutrino data, including the SuperKamiokande day and night spectral information, taking into account two-flavor neutrino oscillations in vacuum and in matter (see references [29,30,31] for recent analyses including all the available data). They all agree that data are well described if flavour oscillations do take place, but the specific mechanism has not yet been identified.

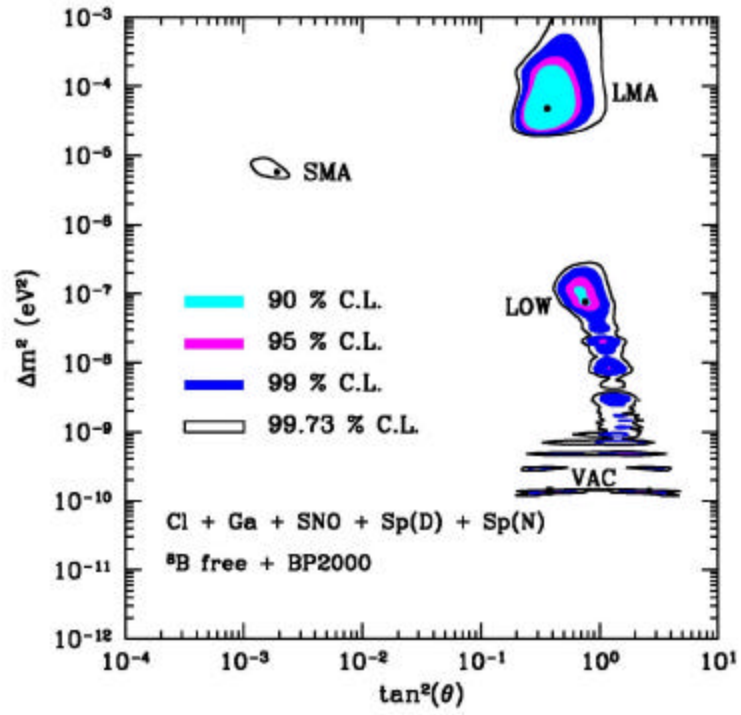


Figure 1.6 Confidence level (C.L.) contour plot of the neutrino oscillation solutions allowed by the present data. From [29].

Scenario	$\Delta m^2/\text{eV}^2$	$\tan^2\theta$	f_B	f_{hep}	χ^2_{min}
LMA	$4.8 \cdot 10^{-5}$	0.36	1.10	3	29.6
VAC	$1.4 \cdot 10^{-10}$	0.38	0.53	7	31.4
LOW	$7.6 \cdot 10^{-8}$	0.76	0.82	3	33.9
SMA	$5.7 \cdot 10^{-6}$	$1.9 \cdot 10^{-3}$	1.08	5	39.6

Table 1.4 Best-fit values of the parameters Δm^2 , $\tan^2\theta$, f_B and f_{hep} from the free flux analysis of the solar neutrino data. The fit has 38 degrees of freedom. From [29].

Figure 1.6 shows the contour plots of the allowed solutions in the space of the oscillation parameters Δm^2 and $\tan^2\theta$, from an analysis in which the flux of ${}^8\text{B}$ and hep neutrinos were left as free parameters⁴. In order to represent Δm^2 as a positive-definite quantity, the mixing angle representation with $\tan^2\theta$ is used instead of $\sin^2 2\theta$ in order to include also the negative region, corresponding to $\pi/4 < \theta < \pi/2$.

There is a solution for vacuum oscillations – VAC and three allowed solutions for oscillations in matter, LMA (large mixing angle), SMA (small mixing angle) and LOW (low mass). The best fit values of the oscillation parameters and the free neutrino fluxes are shown in Table 1.4. f_{B} and f_{hep} are the fluxes of ${}^8\text{B}$ and hep neutrinos in units of the BP2000 predicted value.

The most favored solution is inside the LMA region. The VAC solution provides a good fit of the data, as long as the ${}^8\text{B}$ flux is half of the SSM predicted value, showing a 2.5σ discrepancy. Also the LOW solution provides a good fit of the data, and the value for the ${}^8\text{B}$ flux is within 1σ of the SSM prediction. The SMA solution, that previously supplied the best fit point, is now more disfavoured because of the undistorted ${}^8\text{B}$ spectrum measured by SuperKamiokande, in contrast with the strong distortions predicted in the SMA solution. In fact, if a full consistency with the SSM is required, then only the LMA and LOW solutions are still allowed.

Additional evidence for neutrino oscillations was obtained in 1998 by the SuperKamiokande experiment through the observation of neutrinos produced in cosmic ray atmospheric showers [32]. SuperKamiokande observed a strong suppression of ν_{μ} events with respect to ν_e , and the dependence of the observed rate with the distance traveled by the ν_{μ} (shown in Figure 1.7) is consistent with $\nu_{\mu}-\nu_{\tau}$ oscillations with $\sin 2\theta \approx 1$ and $\Delta m^2 \approx 3.2 \times 10^{-3} \text{ eV}^2$. Since this value is at least 2 orders of magnitude higher than the Δm^2 value that explains the solar neutrino

⁴ The SSM prediction for the hep component is very poorly known and for the ${}^8\text{B}$ component is given with an error of 20 %.

problem (Table 1.4), solar neutrino oscillations must be predominantly between ν_e and ν_μ .

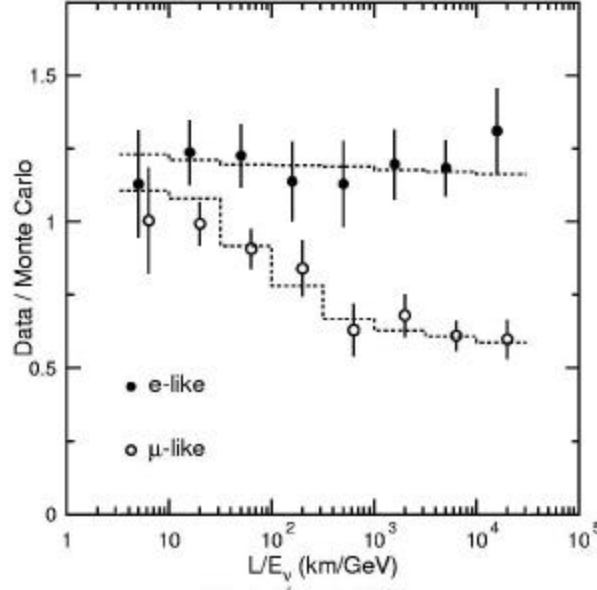


Figure 1.7 Ratio of observed and predicted atmospheric neutrino event rate, in Super-Kamiokande.

The atmospheric neutrino measurements in SuperKamiokande and the solar neutrino measurements in SNO have provided evidence for the phenomenon of neutrino oscillations. However, at least for solar neutrinos, the specific mechanism for the flavour conversion is not yet identified. We still do not know if the oscillations are happening in vacuum or in matter and the order of magnitude of the parameters involved ($10^{-10} \text{ eV}^2 < \Delta m^2 < 5 \times 10^{-5} \text{ eV}^2$ and $1.9 \times 10^{-3} < \tan^2 \theta < 0.76$).

In order to answer these questions, new measurements of solar neutrinos are still needed. In the near future, different measurements are expected – increased statistics in SuperKamiokande (possible better definition of the day-night asymmetry?), the measurement of the total ^8B flux through neutral currents in SNO, and the measurement of the ^7Be neutrinos in Borexino.

From the point of view of neutrino oscillations, the measurement of the ${}^7\text{Be}$ neutrinos has two strong features:

- The energy of ${}^7\text{Be}$ neutrinos is below 1 MeV, where no real-time measurements are available, and distinguishing features are predicted by the presently allowed scenarios. In the LOW solution, day-night asymmetries of up to 20 % can be observed. In the SMA solution, an almost complete ν_e suppression is expected in the ${}^7\text{Be}$ energy region, yielding a rate that is less than $\frac{1}{4}$ of the SSM and less than $\frac{1}{2}$ of the LMA solution.
- Since ${}^7\text{Be}$ neutrinos are monoenergetic, the strong energy dependence of the oscillation probabilities are not averaged through a continuous spectrum. In particular, strong seasonal variations are expected in the vacuum solution and the measurement in Borexino has the potential to cover almost completely this allowed region.

The Borexino Experiment

In this Chapter, we present the Borexino experiment and its main Physics goals, including the description of the detector components and auxiliary systems, the design and most important results of the Counting Test Facility (CTF), the Borexino prototype. In addition, we discuss the expected backgrounds and show the potential impact that the Borexino solar neutrino measurements can have on Neutrino oscillation Physics.

2.1 Overview

The experimental approach to solar neutrino flux measurements has been twofold: radiochemical experiments with low energy thresholds and real-time experiments with a high energy threshold. These approaches were complementary and supplied different milestones in the Solar Neutrino Physics:

- the pioneering first detection of solar neutrinos by the Chlorine experiment
- the lowest energy threshold in the Gallium experiments;
- the high-statistics, real-time measurement of ^8B neutrinos in Kamiokande and SuperKamiokande;
- the recent charged current measurement by the SNO detector, giving strong evidence for neutrino oscillations as the responsible for the 30-year long solar neutrino problem.

However, low energy solar neutrinos still have not been detected directly and their suppression is only extrapolated from the integrated rates and from the high energy measurements. In addition, the measurements done up to date still do not allow the full discrimination between the several oscillation solutions. The

solution of the solar neutrino problem will be complete only when the low energy region of the solar neutrino spectrum is covered by direct measurements. The Borexino experiment is specifically designed to address this task by detecting the 866 keV ^7Be solar neutrino line and measuring its time variations.

Borexino is presently in construction at the Gran Sasso National Laboratories (LNGS) in central Italy, under a rock shielding of 3800 mwe. The main institutions responsible for Borexino come from Italy, U.S.A. and Germany, but the collaboration also includes people from Russia, France, Hungary, Poland, Canada and Portugal.

In the original proposal by R. Raghavan, Borex would be a detector for neutral and charged current interactions of ^8B solar neutrinos on ^{11}B nuclei. The name of the project derived from the use of a Boron compound, trimethylborate, as the liquid scintillator. The design for Borex required a very large fiducial mass, of about 1000 tons, and Borexino was planned as a “small-scale” prototype.

However, it was realized that, as long as the low energy background could be reduced, the smaller mass of Borexino would be sufficient to detect the more intense flux from ^7Be neutrinos. The ^7Be neutrino detection did not require boron, so the scintillator changed to pseudocumene, and the focus of the experiment became the reduction of all the possible backgrounds, in particular the unshieldable intrinsic scintillator contamination.

The Counting Test Facility (CTF), a 5-ton prototype detector, was built and operated in Gran Sasso in order to test the most crucial aspects of the Borexino design, in particular the scintillator radiopurity, for which the required level was orders of magnitude below the sensitivity of the methods available at the time. On the basis of the results from CTF, the construction of Borexino in Hall C of the LNGS started in 1996.

The detection reaction for ^7Be solar neutrinos in Borexino is elastic scattering off electrons:

$$\boldsymbol{n} + e^- \rightarrow \boldsymbol{n} + e^- \quad \text{Eq. 2.1}$$

in an active target consisting of 300 tons of liquid scintillator. This reaction proceeds via neutral and charged current interactions, so it is sensitive not only to electron-neutrinos (ν_e), but also to muon- or tau-neutrinos (ν_μ, ν_τ).

The scintillation light produced by the recoil electrons is detected by an array of photomultipliers. The high light yield of the liquid scintillation technique allows the detection in Borexino of electrons with energies as low as a few tens of keV. However, the low energy background limits the effective threshold for the neutrino-recoiled electrons at 250 keV.

The separation of signal and background relies on the identification of the Compton-like edge in the recoil electron energy spectrum at 665 keV due to the fact that ^7Be neutrinos are monoenergetic. No event-by-event neutrino signature is possible in Borexino and the fluorescence light production is not directional, so the signal extraction from the background must be made statistically. This constraint makes the accuracy of the background control the main priority of the Borexino experiment. In fact, Borexino is the large volume underground experiment with the most challenging background requirements. For a signal/noise ratio of 1, a maximum background rate of 0.5 events/day/ton or 5×10^{-8} Bq/kg in the energy range 250-800 keV is required.

2.2 The detector

The design of Borexino was driven by the balanced optimization of three main parameters:

- *Signal/noise ratio.* The effort for a low background in Borexino focused on the reduction of the naturally occurring radioactive contaminants in the scintillator and the other detector materials and to the shielding of the active volume by means of a detector structure (shown in Figure 2.1) based on a succession of increasingly pure shells. It also led to the inclusion in the detector of a muon veto system and to the addition of a

light quencher to the buffer liquid, in order to make it a really passive shield.

- *Solar neutrinos statistics.* Given the low cross sections for neutrino interactions, maximization of the count rate leads to increase the target mass as much as possible. If the background rates will allow it, the fiducial mass employed in the analysis can, in principle, be larger than the design goal of 100 tons.
- *Light collection efficiency.* An optimum light collection efficiency maximizes energy resolution, fundamental for the recognition of the ^7Be neutrino edge, position resolution and particle identification efficiency, important for background discrimination. This was a major requirement in the choice of the scintillator, that should maximize the light yield and minimize the attenuation, the nylon vessels, that must be as transparent as possible and of the PMTs, with a large collection area, further improved by the use of optical concentrators.

The following paragraphs give a brief description of the fundamental detector components. For a detailed description of the goals and design of Borexino, see ref.[³³].

The structure of the detector is shown schematically in Figure 2.1. The active liquid scintillator target is contained in a thin nylon vessel and surrounded by a shielding (buffer) liquid. A stainless steel sphere serves as support structure for the PMTs and contains both the scintillator and the buffer liquid. A water buffer provides the last shielding shell, as well as the active volume for the muon detector.

2.2.1 Scintillator

The active target of the Borexino detector consists of 300 tons of organic liquid scintillator in which the solvent is 1,2,4 trimethylbenzene (pseudocumene, PC) and the solute is 2,5 diphenyloxazole (PPO) at a concentration of 1.5 g/l. Table 2.1 reports some of the Physical properties of pseudocumene.

The scintillator has been extensively studied, both in laboratory tests and in a multi-ton scale in the Counting Test Facility at Gran Sasso. Detailed reports on the CTF have been published [³⁴, ³⁵, ³⁶, ³⁷]. An outline of the main features and results is given in section 2.3.4. Results of the early studies on the radiopurity of organic liquid scintillators can be found in references [³⁸, ³⁹, ⁴⁰]. Laboratory measurements of the optical properties of PC+PPO are described in references [⁴¹, ⁴², ⁴³, ⁴⁴].

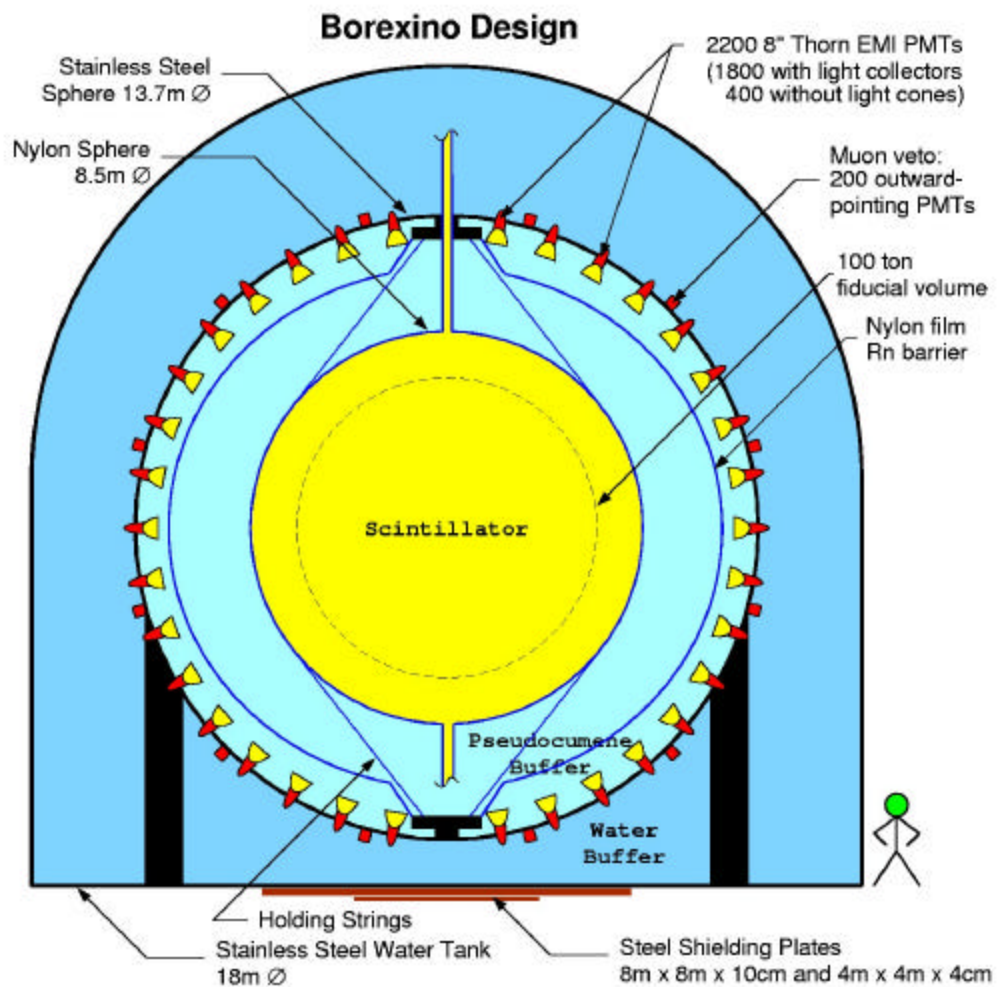


Figure 2.1 Scheme of the Borexino design.

Chemical name	1,2,4-trimethylbenzene
Molecular structure	$C_6H_3(CH_3)_3$
Molecular weight	120.2
Density	0.876
Index of refraction	1.505
Water solubility	57 mg/l at 20 °C
Flash point	48 °C

Table 2.1 Summary of Physical properties of pseudocumene

The solar neutrino rate in Borexino in the recoil electron energy window of 250-800 keV (the “neutrino window”) is 0.5 events per day and per ton of target material, assuming SSM fluxes. The background in this energy region comes essentially from the decays of the naturally radioactive contaminants of the scintillator itself, such as the isotopes in the ^{238}U and ^{232}Th chains. The best certified high-purity materials and the most sensitive measurements by mass spectrometry reach contamination levels of ppt (parts-per-trillion, 10^{-12} g/g), while, in order to have a signal/noise ratio of 1, the scintillator for Borexino must reach a contamination level of 10^{-16} g/g. This is the reason why up to now the only real time observations of solar neutrinos have been made in the energy region above 6 MeV, where this background is absent.

The method of concentrating impurities by analysing distillation residues was able to push the sensitivity down to 10^{-15} g/g, still an order of magnitude short of the design goal. Using tracers to track impurity removal through the distillation of contaminated samples, purification efficiencies of about 10 orders of magnitude were measured. These results supported the hypothesis that essentially non-polar liquids could be highly purifiable from metallic impurities. The radiopurity results from CTF confirmed this assumption, reaching contamination levels of the same order of magnitude of the Borexino design goals.

The contamination of the scintillator with ^{14}C constitutes a special case because the carbon atoms are constituents of the organic molecule themselves. The β -spectrum of ^{14}C ($E_{\text{max}}=156$ keV, $\tau_{1/2}=5700$ years), significantly overlaps a large fraction of the ^7Be neutrino signal, due to the limited energy resolution. A measurement of the ^7Be neutrino signal is feasible above an effective energy threshold of 250 keV, given a $^{14}\text{C}/^{12}\text{C}$ fraction of about 10^{-18}

($\sim 10^4$ events/day,ton). Very low levels of ^{14}C contamination are expected in liquid scintillators because of the petrochemical origin, but before CTF the most sensitive limit on any material was $^{14}\text{C}/^{12}\text{C} < 10^{-15}$, three orders of magnitude higher than the required level. The high sensitivity of the CTF allowed the measurement of the ^{14}C scintillator contamination, giving a value of

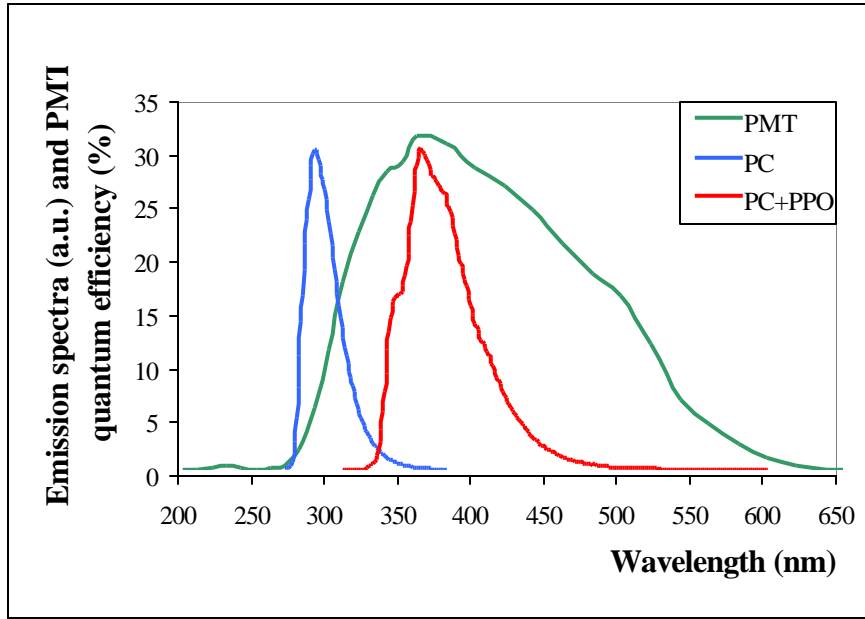


Figure 2.2 Emission spectra of pseudocumene (PC) and PC+PPO. Quantum efficiency of the photomultipliers.

$^{14}\text{C}/^{12}\text{C}=2\times 10^{-18}$. In order to ensure the compliance with the Borexino background requirements, the detector filling campaign includes ^{14}C screening tests in CTF. Scintillator batches with a $^{14}\text{C}/^{12}\text{C}$ level above 3×10^{-18} will be rejected. The fundamental optical properties of the scintillator are listed in Table 2.2 and its emission spectrum is shown in Figure 2.2, that shows also the quantum efficiency of the photomultipliers.

The primary excitation efficiency, i.e., the fraction of incident energy converted to electronic excitation energy depends on the solvent only and is of the order of 5 %, corresponding to an average fluorescence yield of about 10^4 optical photons/MeV [44,⁴⁵]. However, the fraction of excitation energy converted into scintillation photons – the fluorescence quantum efficiency – increases from 40 % to 82 % with the addition of PPO to the pseudocumene. In addition, the emission

Fluorescence yield	1.2×10^4 photons/MeV
Fluorescence quantum efficiency PPO (pure PC)	0.82 (0.40)
Emission range	340-450 nm (peak at 370 nm)
Absorption length (380 nm)	5.1 m
Fluorescence decay time – fast component	3.5 ns (5.5 ns)
Alpha quenching factor	$Q(E) = 20.3 - 1.3 E \text{ [MeV]}$

Table 2.2 Summary of photophysical properties of the PC+PPO (1.5 g/l) scintillator mixture.

spectrum is shifted to higher wavelengths, where it can match the quantum efficiency of the photomultipliers. PPO molecules partly self-absorb its own emitted light, but since the PPO fluorescence quantum efficiency is high (82 %), most of it is re-emitted after some delay. The net result is an effective increase of the decay time, from 3.5 ns in laboratory samples, to 5.5 ns in large volumes (measured in CTF).

The absorption length of optical photons in the scintillator (5 m at the scintillation peak) is low compared to the typical values in ultrapure water (50 m or more), but it still allows the direct propagation of light through the distances characteristic of the Borexino detector geometry.

In the energy range of most α particle emissions in the ^{238}U and ^{232}Th chains – 4 to 9 MeV – the factor of scintillation quenching with respect to β or γ particles ranges from 10 to 15. In this way, the β -equivalent energy of the α -decays lies within the neutrino window causing, in fact, the highest rate background. However, the signal quenching mechanism also results in long scintillation times and therefore, the pulse shapes of α and β events are substantially different, as can be seen in Figure 2.3. The fluorescence decay time profile can be described by a sum of exponential components:

$$F(t) = \sum_i \frac{q_i}{\tau_i} e^{-\frac{t}{\tau_i}} \quad \text{Eq. 2.2}$$

where the time constants τ_i and the weights q_i of each component for α and β excitations are listed in Table 2.3. The values of the time constants are similar for

α and β particles, but the weights of the longer time components are larger for a particle excitation. These differences can be used to tag α and β events, by means of the ratio of the integrated pulse tail (above a given time threshold) versus the total pulse charge. If β -type events can be due to neutrino-recoiled electrons or radioactive background, an α event is surely background, so its identification increases the signal-noise ratio.

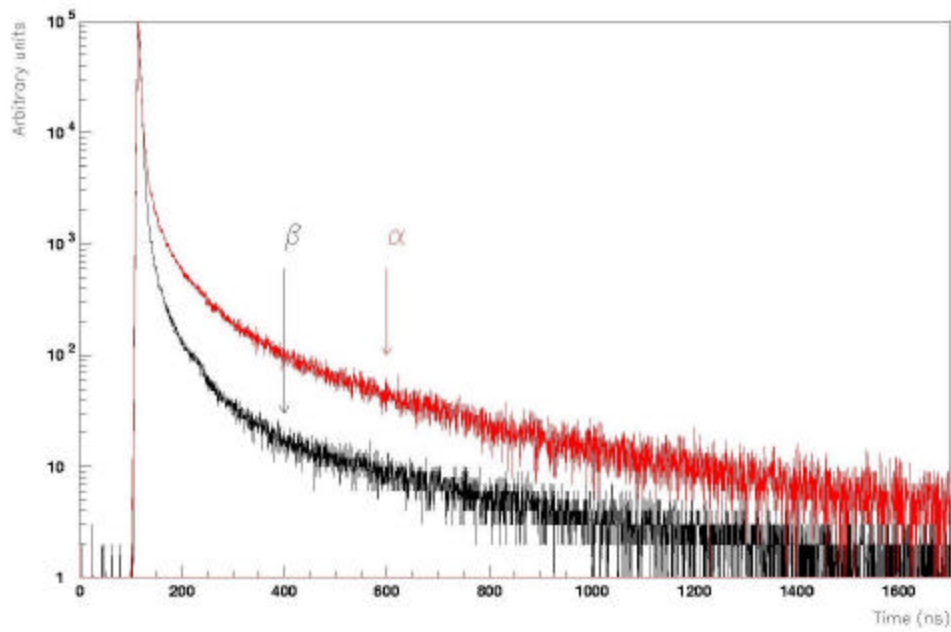


Figure 2.3 Time distributions for scintillation pulses due to α and β excitations.

Excitation	Time constant (τ_i)	Light fraction (q_i)
$\beta - \gamma$	3.57 ns	89.5 %
	17.6 ns	6.3%
	59.5 ns	4.2 %
α	3.25 ns	63.0 %
	13.5 ns	17.8 %
	60.0 ns	11.9 %
	279.1 ns	7.3 %

Table 2.3 Fluorescence decay times: breakdown in exponential components. From [37].

2.2.2 Nylon Vessels

The containment system of the liquid scintillator is one of the most challenging components of Borexino, due to the various severe constraints the material must meet:

- the lowest radioactive contamination levels of all the detector materials, excluding only the scintillator itself;
- chemical compatibility with aromatic liquids, like pseudocumene;
- mechanical integrity for several years, in presence of a buoyant force due to a 0.1% density difference between the scintillator and buffer liquid;
- optical transparency, with a haze (fraction of light scattered above a certain angle) not larger than a few %;
- effectiveness as a barrier against ^{222}Rn diffusion from the buffer liquid into the scintillator.

Table 2.4 lists the most relevant properties of the nylon vessel for Borexino. The ^{222}Rn barrier factor is the ratio between the concentrations inside and outside the vessel and it is calculated from measurements of the diffusivity of Rn in the nylon.

Vessel diameter	8.5 m
Film thickness	125 μm
Nylon type	Nylon-6
^{238}U content	1.7+/-0.2 ppt
^{232}Th content	3.6+/-0.5 ppt
^{222}Rn barrier factor	$<10^{-7}$
Transmittance (366 nm)	98.3+/-0.6 %
Haze (>3.5)	0.28+/-0.04 %
Maximum load (operating load)	40 Mpa (2 Mpa)

Table 2.4 Summary of the most relevant properties of the inner nylon vessel for Borexino. Data from [46].

A major concern in the vessel design is the contamination by ^{222}Rn . Being a noble gas, Radon is highly volatile and is easily released from any material that contains ^{226}Ra , a long-lived isotope of the ^{238}U radioactive chain. Its half-life of 3.8 days is long enough to allow it to diffuse for several meters in liquids. The 125 μm thick

nylon vessel acts naturally as a barrier against Radon diffusion, but since it is so thin, special care was devoted to finding a material with low diffusivity. The deposition of ^{210}Pb , a long-lived radon daughter, on the vessel walls can also cause a permanent background source in Borexino. To avoid this, the vessel fabrication is done in a controlled clean room environment, where a specially designed radon filter was installed [^{47, 48}].

The CTF data have shown that γ rays from the Radon contamination in the buffer liquid can be a major source of external background (see Section 2.3.4). A second nylon vessel will be installed outside the inner vessel in order to insulate it from ^{222}Rn and other impurities that might otherwise diffuse into the vicinity of the sensitive volume from the outer regions of the detector, especially the photomultipliers. The outer vessel will be made with the same nylon film as the inner vessel, but with a 11 diameter. Figure 2.4 shows the prototypes of both vessels, assembled together for a gas filling test at Princeton University.



Figure 2.4 Prototype of the inner and outer vessel during a gas filling test.

2.2.3 Stainless Steel Sphere and Pseudocumene Buffer

A buffer liquid layer with 2.3 m thickness shields the scintillator from external γ rays, mainly due to radioactivity in the photomultipliers. The use of a Stainless Steel Sphere (SSS) to contain the buffer liquid allows it to match the density of the scintillator. This creates a neutral buoyancy condition for the nylon vessel in which its mechanical stress is minimized. So the buoyant force that is produced due to the density difference between the scintillator ($\rho=0.87$) and water is placed on the SSS and not on the nylon vessel.

The design required the SSS to hold the positive buoyant force of 1300 m³ of PC in water (about 170 tons), but also to support its full weight even in the absence of water in the external tank. Its diameter is 13.7 m and the thickness varies from 8 mm in the upper hemisphere, 10 mm in the equatorial region and 12 mm on the lower hemisphere. The SSS is supported around the equator by 20 legs welded to the floor of the Water Tank. The SSS serves also as support structure for the 2200 PMTs. In Figure 2.5 a scheme of the Stainless Steel Sphere is shown inside the Water Tank. Each point on the sphere surface is a PMT port. One cable per each cluster of 80 PMTs is shown.

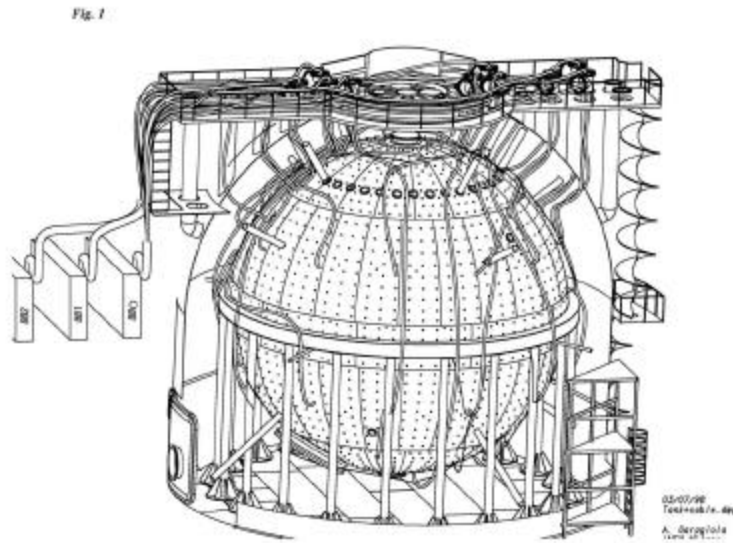


Figure 2.5 Stainless Steel Sphere inside the Water Tank. The SSS support structure, the PMT ports and cables are shown.

The choice for the buffer liquid was PC, since it is used as solvent of the scintillator mixture. Another major advantage of a PC buffer is its low intrinsic radiopurity, so that a PC buffer has a low impact on the external background. Besides the density match, the choice of PC as buffer liquid also allows the matching of the index of refraction of both liquids. This eliminates reflection and refraction at the interface, making the light propagation in the detector easier to understand and analyze.

In order to suppress the undesired fluorescence of the buffer liquid, due to γ radiation from the PMTs, a light quenching substance will be added to the PC. In fact, without PPO, PC is a much less efficient liquid scintillator, not only due to a reduced fluorescence quantum efficiency, but mainly to the poor match between its emission spectrum and the PMT sensitivity. However there is some overlap and the photons reaching the scintillator are absorbed by the PPO molecules and reemitted with the same wavelength spectrum as events from within the inner vessel (a process with 82 % of efficiency). Since the background rate due to gamma events from the PMTs is 5 orders of magnitude higher in the buffer region than in the scintillator, scintillation from a pure PC buffer could result in a rather large background.

Monte Carlo simulations [^{49,50}] predict a trigger rate of 12 Hz from these events, almost as much as the dominant ¹⁴C background at 20 Hz. Most of this background has a low visible energy, and the part above the 250 keV threshold would be largely recognizable through its time distributions, but the residual background would still be at about 350 ev/day (a factor 7 larger than the expected ⁷Be neutrino rate), so its simple elimination by means of a quencher adds an important safety factor. On the basis of its chemical stability, good light quenching efficiency and good transparency for the PC+PPO scintillation light, dimethylphtalate (DMP) was chosen for quencher of the Borexino buffer liquid [⁵¹]. A quenching factor of about 20 for the fluorescence light is obtained at the planned concentration of 5 g/l. This has no effect on the detected Cerenkov light since the DMP absorption bands are far from the wavelength region of PMT sensitivity. The compound also has acceptable radiopurity standards and good compatibility with PC and nylon.

2.2.4 Photomultipliers

The scintillation light in Borexino will be detected by an array of 2214 photomultipliers (PMTs) mounted on the Stainless Steel Sphere. The PMT model is ETL 9351, with a 20 cm diameter photocathode and its selection was based on the following requirements:

- Low radioactivity glass. The radioactivity content of the specially commissioned Schott glass bulbs is 3×10^{-8} g/g of ^{238}U , 1×10^{-8} g/g of ^{232}Th , and 2×10^{-5} of K_{nat} , about 10 times better than normal glass. Even with these values, the PMTs are still the source of the largest external γ background.
- A low time jitter of 1 ns, lower than the PC/PPO scintillation decay time of 3.5 ns, is important for time resolution and position reconstruction.
- A high quantum efficiency (see Figure 2.2), with a peak value of 32 % at 420 nm, is important for a good energy resolution.
- The low after-pulse frequency of 2.5 % prevents distortions of the pulse tail measurements for α/β discrimination.
- A low dark noise rate of 1 kHz, to avoid instrumental background.

All the PMTs have a mu-metal sheet to shield the Earth magnetic field, that has a significant effect on the gain and time resolution of the PMTs. The voltage dividers are designed to allow a single cable to carry both the signal and the operating high-voltage. In order to avoid ground loops, the PMTs are electrically decoupled from the Stainless Steel Sphere through the use of polymer (Viton) O-rings instead of metallic ones for the sealing. A large R&D effort was put into finding the best materials to seal the PMT bulb to the stainless steel can, while guaranteeing the safe and reliable operation of the PMT during several years immersed in pseudocumene. A milestone on the PMT sealing campaign was the successful testing of 50 PMTs in the Two-Liquid Test Tank, in which 49 PMTs were operated for 4 months without failure in a PC/water environment realistically mimicking the definitive situation in Borexino.

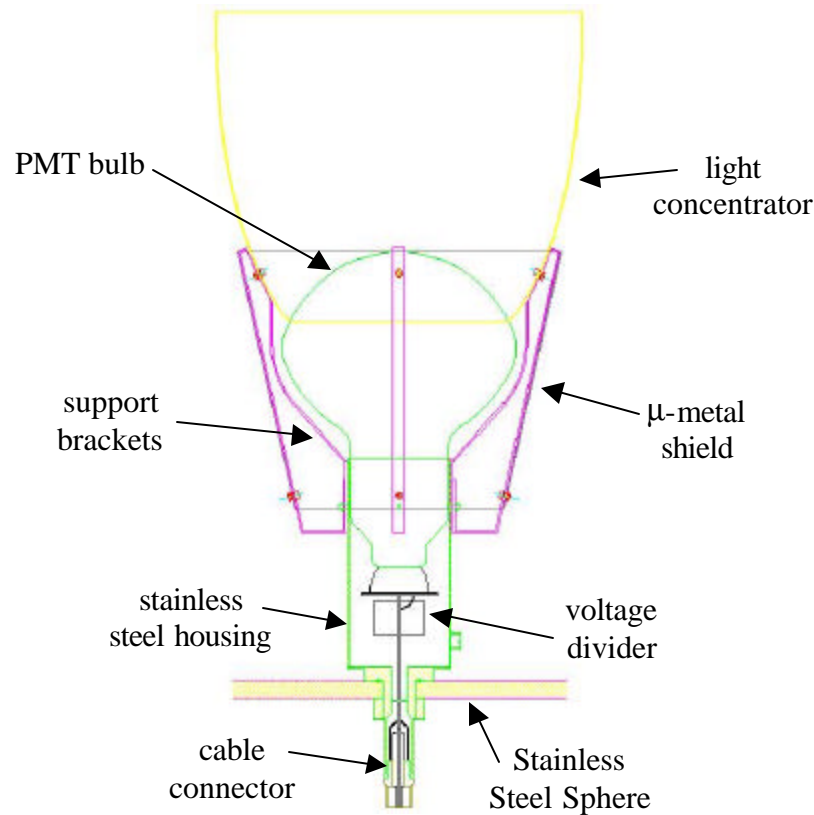


Figure 2.6 Photomultiplier assembly scheme.

In order to increase the light collection efficiency, 1800 PMTs will be coupled to optical concentrators made of anodized aluminum, as shown in Figure 2.6. The 400 PMTs without any concentrator are a part of the muon detector (see ahead). The shape of the concentrators is based on the “Compound Parabolic Concentrator (CPC)” design (see, for instance, [52]), built in such a way to send all the photons with an incidence angle lower than 44° in the direction of the photomultiplier window, reflecting back all the others. This direction corresponds to photons coming from the edge of the inner vessel, plus a 5° tolerance to misalignment, so the concentrator is effectively rejecting light not coming from the solid angle region of the inner vessel. Taking into account the aperture diameter of 32 cm and a reflectivity of 90%, averaged over the scintillator emission spectrum, the effective light collection area of the PMT is increased by a factor 2.4. So the total fraction of solid angle covered by the 2214 PMTs is 32 %.

2.2.5 *Muon Detector and Water Buffer*

The underground location of the Gran Sasso laboratory suppresses the cosmic muon flux by six orders of magnitude, but the surviving rate is still about $1 \text{ hr}^{-1} \text{ m}^{-2}$, or 4500 events/day in Borexino. Muons crossing the scintillator produce intense light pulses, easily recognizable because of their high energy, but the experience with CTF has shown that the Cerenkov light from muons crossing the buffer region produces background at low energies, in the neutrino window. In addition, muon interactions in the detector produce radioactive nuclides the decay of which can be detected as background events. Two strategies are employed to reduce the muon background to a level lower than 0.5 events/day:

- Increase the solid angle of the light acceptance of 400 PMTs mounted on the internal part of the SSS, by using them without the light concentrators. This improves the collection efficiency for the Cerenkov photons produced by the muons in the buffer region. Selection criteria for the identification of muons will be provided by the time distributions and hit patterns: photons from a muon track crossing the buffer will have longer mean times and hit more PMTs without concentrators than a scintillation event inside the inner vessel.
- Turn the water buffer into a Cerenkov detector by mounting 200 PMTs on the outer surface of the SSS. This detector will produce veto triggers, signaling the passage of muons even in the absence of a prompt signal from the internal detector. In this way, delayed events due to radio-nuclides produced in muon interactions can also be recognized.

The muon veto detection medium and outermost shielding layer for Borexino, the Water Buffer, is contained in the external tank, a stainless steel domed cylinder with 18 m diameter and 16.5 m high. In order to shield the detector against γ -rays and neutrons from the rock, the water buffer is at least 2 m thick except just below the SSS. To compensate the reduced shielding in this region, 15 cm steel plates were installed under the tank. In order to increase the Cerenkov light collection efficiency for the muon veto, the outer wall of the SSS and the inner wall of the

External Tank will be covered with sheets of highly reflecting material (Tyvek). To improve optical transparency, the water will be supplied by a purification plant (see Section 2.3.3).

2.3 Auxiliary Systems

2.3.1 *Fluid Handling Systems*

The fluid handling systems are required to perform a variety of tasks:

- Prepare and store the scintillator mixture of PC and PPO;
- Purify the scintillator and eventually the buffer liquid (see next Section);
- Produce high-purity water (see Section 2.3.3);
- Produce high-purity nitrogen to use in scintillator and water purification.
- Fill the Borexino Stainless Steel Sphere with 1300 tons of pseudocumene, divided by the nylon vessels in 3 regions: the inner vessel, the inner and the outer buffer;
- Fill the Borexino External Tank with 2000 tons of pure water;
- Fill CTF with 4 tons of scintillator and 1000 tons of pure water (see Section 2.3.4);

The main components of the fluid handling systems are the scintillator, water and nitrogen purification plants, the scintillator storage tanks, the filling stations and the interconnection tubing. In order to maintain a high purity level, and to avoid ^{222}Rn and ^{85}Kr contamination from the air, the systems are made from electro-polished stainless steel, use high quality valves and fittings, and are leak-checked with helium. There are four storage tanks with a capacity for 100 tons of pseudocumene each. The extra tank can be used for a faster batch purification of the scintillator prior to the filling.

2.3.2 *Scintillator Purification Systems*

The Scintillator Purification System for Borexino includes different plants implementing methods targeted at the reduction of different types of radioactive contaminants. The plants can be used independently or combined, for pre-filling or for online purification.

- A nitrogen counter-current stripping column to remove dissolved gas impurities, such as ^{222}Rn and ^{85}Kr .
- A vacuum distillation unit, to remove low volatility and non ionic contaminants, such as dust particles and degraded solvent molecules.
- A water extraction unit, to remove ionic impurities, such as the metals in the ^{238}U and ^{232}Th chains, and potassium.
- A silicagel column chromatography unit, for the same purpose.
- Filtration systems, to remove suspended dust particles larger than 50 nm.

Table 2.5 lists the radiopurity requirements for the different isotopes and the strategy or purification method used to achieve them.

Isotope	Source	Typical Concent.	Tolerable level	Strategy
^{14}C	Cosmogenic (from ^{14}N)	$\frac{^{14}\text{C}}{^{12}\text{C}} \leq 10^{-12}$	$\frac{^{14}\text{C}}{^{12}\text{C}} \leq 10^{-18}$	Petroleum derivative (old carbon)
^7Be	Cosmogenic (from ^{12}C)	$3 \times 10^{-2} \text{ Bq/ton}$	$< 10^{-6} \text{ Bq/ton}$	Underground storage, Distillation
^{222}Rn	Air, Emanation from materials	100 atoms/ cm^3 in air	1 atom/ton in scintillator	Nitrogen stripping
^{238}U ^{232}Th	Dust, Organometallic compounds (?)	$2 \times 10^{-5} \text{ g/g}$ in dust	$< 10^{-16} \text{ g/g}$ in scintillator	Distillation, Water extraction, Silicagel column chromatography
^{40}K	Dust or contaminant in fluor	$2 \times 10^{-6} \text{ g/g}$ in dust	$< 10^{-13} \text{ g/g}$ in scintillator $< 10^{-11} \text{ g/g}$ in fluor	Water extraction of fluor solution
^{85}Kr , ^{39}Ar , ^{42}Ar	Air	1 Bq/m^3 in air		Nitrogen stripping

Table 2.5 Radiopurity requirements for the Borexino scintillator. From [42].

2.3.3 Additional Purification Systems

The purification of the liquid scintillator and the operation of the Borexino and CTF detectors require dedicated systems to purify water and nitrogen.

In Borexino and CTF, ultra-pure water is used as a γ and neutron radiation shield. This water buffer is also used as an active target to the muon veto system. In CTF, the direct contact of the water with the scintillator containment vessel puts very stringent requirements on its purity. In addition, ultra-pure water is used in the water extraction scintillator purification unit and in the cleaning of all detector material (PMTs, cables, optical fibers) during the installation phase.

The water purification system [⁵³], operating in Gran Sasso since the installation of CTF in 1994, processes the Gran Sasso lab “raw” water by reverse osmosis, continuous deionization, ultrafiltration, ion exchange and nitrogen stripping. Table 2.6 shows the radiopurity requirements and measured contamination levels of the purified water. For Borexino, the requirements are easily met, while for CTF, there is still room for improvement in what concerns the ^{222}Rn contamination.

Contaminant	Requirements		Measured contamination	
	Borexino	CTF	“raw” water	Purified water
^{238}U , ^{232}Th [g/g]	10^{-10}	10^{-13}	10^{-10}	$3 \cdot 10^{-14}$
K_{nat} [g/g]	10^{-7}	10^{-10}	10^{-7}	$<5 \cdot 10^{-11}$
^{222}Rn [Bq/m ³]	1	10^{-3}	10^4	$<3 \cdot 10^{-3}$

Table 2.6 Requirements for Borexino and CTF and measured values of the radioactive contamination of the “raw” and purified water. Data from [⁵⁴].

Ultra-pure nitrogen is used in the scintillator and water purification processes, essentially to reduce the ^{222}Rn contamination. In addition, nitrogen is also used during the detector operation to keep the scintillator saturated under an inert gas blanket. This is needed in order to accommodate small volume changes without increasing the mechanical stresses of the containment vessels and to maintain the scintillator free of oxygen (that quenches the scintillation light).

The high purity nitrogen is produced by charcoal column purification of the liquid N_2 prior to evaporation. The system [⁵⁵] produces nitrogen with a ^{222}Rn

contamination of $1 \mu\text{Bq/m}^3$, the necessary level in order to reach the required scintillator contamination of 1 atom/ton.

2.3.4 *Electronics and DAQ*

The basic observable quantities in Borexino are the energy and the photon time distribution of the events. These are obtained from the amplitude and time of all the photomultiplier signals, measured according to a trigger condition.

The electronics system that reads and stores the information from the photomultipliers was designed according to the following requirements:

- A good pulse height resolution, optimized in particular for single photo-electron pulses, guaranteeing at the same time a large dynamic range, in order to allow the measurement of higher energy neutrino signals, up to about 20 MeV (an average of 4 photo-electrons per PMT).
- A good time resolution of less than 0.5 ns, important for position reconstruction and pulse-shape discrimination between α and β events. The modules are designed to be sensitive to the time of successive hits in the same PMT.
- Generation of a trigger signal, programmable according to different hit conditions.
- Distinction between successive interactions of single particles in the detector, with time delays as short as 100 ns. This capability is a fundamental tool for the recognition of internal background events from the radioactive chains of ^{238}U and ^{232}Th .

The signal from the PMTs is AC coupled to a front-end card [⁵⁶] that performs noise filtering, pre-amplification, shaping and integration of the input signal. It provides both a linear response used for time measurement and a voltage signal proportional to the total charge. Each front-end board provides also an analog sum of 12 linear output signals that extend the dynamic range of the system to about 30 MeV by means of a flash ADC system. The outputs of the front end cards are sent to a specially designed VME card that performs the analog to digital conversion of the charge signal with 8 bits resolution, measures the time of the

linear signal with 0.4 ns resolution, computes the sum of recorded hits in time window of 60 ns (used for triggering), and stores the whole information in a dual port random access memory. The data-acquisition (DAQ) software that reads these data is custom made, with a web-based user interface, and runs on the Linux operating system.

The outer muon veto PMTs are read with a different front-end system that performs a charge -to-time conversion of each signal after a linear pre-amplification. The converted signal is sent to time digitizers which are read by their own processor.

2.3.5 Event simulation and reconstruction codes

The study of the expected neutrino signal and background in Borexino is done in three steps:

1. Monte Carlo simulation of the particle interactions in the scintillator;
2. Monte Carlo simulation of the light production, propagation and detection;
3. Reconstruction of the event position.

This section describes the working principles and assumptions behind each step.

2.3.5.1 Generation

The interaction of solar neutrinos and ionising particles from several radioactive decays in Borexino is handled by the GENEB code (Generation of Neutrinos and Background) [⁵⁷,⁵⁸]. Muons are handled by a different code.

The incident neutrino energy is generated from a random choice based on the SSM predicted shapes. The neutrino flavor can be changed from electron to other flavors (muon and tau are not distinguished) according to the survival probability predicted in several neutrino oscillation scenarios.

Solar neutrinos are detected in Borexino via ν - e^- scattering, producing recoil electrons with energies up to 16 MeV (end-point of the hep neutrino spectrum). The energy of the recoil electrons is generated from the differential cross section for neutrino-electron scattering, considering the contributions from charged and

neutral current interactions (see Section 2.5.1). For non-electron flavor neutrinos, only the neutral current is considered.

The background from the ^{238}U and ^{232}Th radioactive chains is generated from random choices of the decay modes, based on their branching ratio. The several hundred decay modes of the 24 isotopes are listed in tables built from reference [59], specifying the branching ratio, particle type, number and energy. Decay modes with a branching ratio lower than 0.5 % are not considered.

Alpha particles have a high ionization density, so we consider their energy to be completely deposited in the generation point.

This is not the case for electrons and γ -rays with energies up to a few MeV, since they cause electromagnetic showers and so their energy deposits cannot be considered pointlike. The propagation of electron and γ showers is handled in GENEB by means of EGS4 routines [60].

The processes that are taken into account for the propagation of gamma rays in EGS4 are:

- Photoelectric effect $\gamma N \rightarrow e^- N^*$
- Compton scattering $\gamma e^- \rightarrow \gamma e^-$
- Pair production $\gamma (N) \rightarrow e^- e^+ (N)$

EGS4 simulates the propagation of γ rays until they reach the cutoff energy of 5 keV. In the energy window of the ^7Be neutrino recoil electrons (250 keV-800 keV) the dominant process is Compton scattering. In pseudocumene, the average dimension of a shower produced by a 1 MeV γ ray is 40 cm.

The processes considered for the propagation of electrons and positrons are:

- Möller scattering $e^- e^- \rightarrow e^- e^-$
- Bhabha scattering $e^+ e^- \rightarrow e^+ e^-$
- Elastic scattering from atoms $e^\pm N \rightarrow e^\pm N$
- Ionization $e^\pm N \rightarrow e^\pm N^* e^-$
- Positron annihilation $e^+ e^- \rightarrow \gamma\gamma$
- Bremsstrahlung $e^\pm (N) \rightarrow e^\pm \gamma (N)$

In the energy range of interest for Borexino, the dominant processes are Möller scattering and elastic scattering from atoms. Since the average electron path length of 1 cm (at 1 MeV) can be considered negligible, if the electron does not produce a Bremsstrahlung photon until it reaches the cutoff energy of 10 keV, the energy deposit is considered pointlike. In addition to the energy and position of the energy deposits, GENEB can also store the information about direction and speed of the relativistic electrons, in order to allow the simulation of Cerenkov light production.

2.3.5.2 Tracking

The tracking code [61] simulates the conversion of the excitation and ionization energy deposited by charged particles in the scintillator into optical photons. The path of each of the optical photons in the detector is tracked up to their detection in the PMTs or its absorption in the detector materials or surfaces. The tracking procedure takes into account the following processes and data:

- Scintillation light production, according to the known light yield, decay times, and emission spectrum of PC+PPO;
- Cerenkov light production, based upon the data on position and direction of the relativistic electrons, stored by GENEB;
- Absorption and reemission in the scintillator;
- Elastic scattering in the scintillator and buffer liquid;
- Diffusion on the nylon vessels;
- Reflection on the detector surfaces (SSS, light concentrators);
- Detection on the PMT, according to its quantum efficiency.

The most relevant parameters used in the simulation of Borexino are summarized in Table 2.7. For the complete scintillator emission spectrum and PMT quantum efficiency, see Figure 2.2. The full breakdown of the scintillation decay time in exponential components, was given in Eq. 2.2 and Table 2.3, for α and β particles. The phenomena of light absorption and re-emission, as well as elastic scattering, will be specifically discussed in Chapter 4. The spectra of absorption length and elastic scattering interaction length are presented in Figure 4.2.

From the Tracking simulations, we obtain the detector resolution. Electron interactions in the scintillator produce light pulses with, on average 386 detected photoelectrons per MeV of deposited energy. The energy resolution is 5 % at 1 MeV and is found to be inversely proportional to \sqrt{E} .

Liquid Scintillator	
Radius of spherical volume	4.25 m
Fluorescence yield	1.2×10^4 photons/MeV
α quenching factor	$Q(E) = 20.3 - 1.3 E$ [MeV]
Emission spectrum	340-450 nm (peak at 370 nm)
Decay time (main component)	3.5 ns
Absorption length (380 nm)	5.1 m
Re-emission probability (PPO qu. eff.)	82 %
Elastic scattering interaction length (380 nm)	4.1 m
Refractive index	1.505
Photomultipliers	
Total number	2214
Distance from center	6.52 m
Cathode diameter	19 cm
Quantum efficiency (average)	20 %
Practical coefficient	60 %
Light concentrators	
Total number	1844
Diameter	31.4 cm
Length	23 cm
Reflection coefficient (inside)	90 %
Reflection coefficient (outside)	75 %
Stainless Steel Sphere	
Radius	6.85 m
Reflection coefficient - specular	4 %
Reflection coefficient - diffuse	36 %

Table 2.7 Most relevant parameters of the Borexino detector, used in the tracking simulation.

2.3.5.3 Reconstruction

The time distributions of the PMT signals are used to reconstruct the position of the scintillation events. The algorithm works by comparing the measured time distribution of any event, with a reference distribution taken at the center in order to isolate the time-of-flight shape, characteristic of each position. In the spherical

symmetry of Borexino, the time-of-flight differences of the photons coming from the center cancel out and the resulting photon arrival time distribution depends only on fixed parameters, such as the decay time of the scintillator, the light propagation in the detector and the PMT time jitter. This distribution, that we shall refer to it as the **probability density function** of the photons' arrival time (pdf), is the fundamental tool of the position reconstruction algorithm.

The reconstructed position is obtained by minimizing the difference between the pdf and the measured time distribution, subtracted by the photon time-of-flight. In practice, the algorithm uses the MINUIT package to find the maximum of the likelihood function:

$$L(\vec{r}_{ev}, t_{ev}) = \prod_i pdf\left(t_i - t_{ev} - \frac{n}{c} |\vec{r}_i - \vec{r}_{ev}|\right). \quad \text{Eq. 2.3}$$

The product is extended over all the hit PMTs. Their coordinates are given by \vec{r}_i and the time at which they produced a signal by t_i . t_{ev} and \vec{r}_{ev} are the space-time coordinates of the scintillation event.

The **pdf** is presently obtained from Monte Carlo simulations, that use as input the distributions for the scintillation decay time measured in laboratory (Table 2.3). When Borexino is operative, the pdf will also be measured with the help of calibration sources, as in CTF.

Figure 2.7 shows the position resolution for simulated events with different distributions inside the detector. The resolution is roughly proportional to the square root of the energy and, except for points far from the center ($r=4$ m). At 1 MeV, the resolution is about 9 cm.

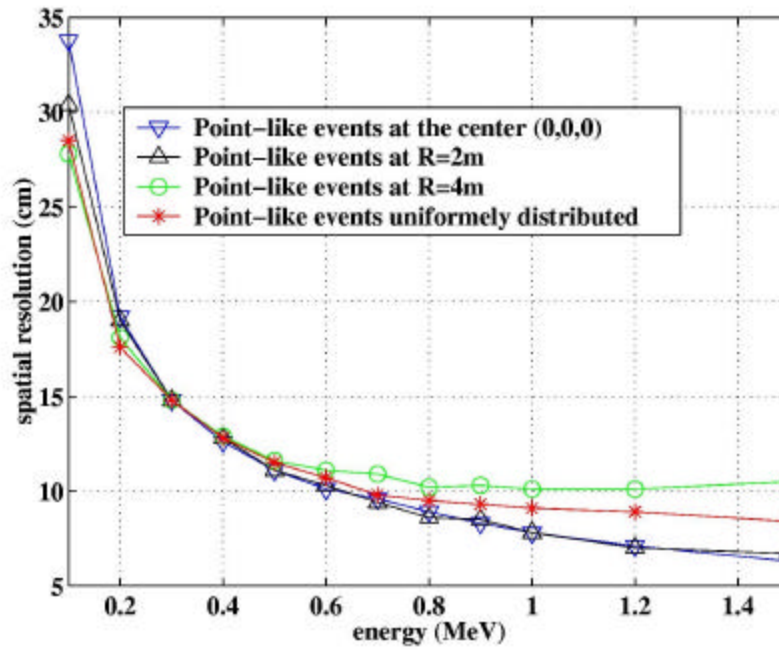


Figure 2.7 Spatial resolution of Borexino.

2.4 The Counting Test Facility (CTF)

When Borexino was first proposed, direct radiopurity measurements in scintillators were only possible for small samples and at sensitivities many orders of magnitude above the requirements for solar neutrino detection. The CTF is a prototype of the Borexino detector, designed to confirm experimentally the belief that organic liquid scintillators could be obtained with adequate purity. Promising results in view of Borexino have been achieved, since the scintillator showed an intrinsic activity at a level consistent with or below an equilibrium amount of $5 \cdot 10^{-16}$ g(U or Th)/g(scintillator), after standard purification methods, and a $^{14}\text{C}/^{12}\text{C}$ ratio of about 10^{-18} . In addition, many design features of the Borexino design were tested and optimized in the CTF detector, especially for what concerns the thin nylon vessel and the scintillator purification systems.

2.4.1 CTF Design

The CTF detector, shown in Figure 2.8, is based on an unsegmented 4.8 m^3 liquid scintillator volume composed of pseudocumene as solvent and PPO as solute at

the concentration of 1.5 g/l. The scintillator contained in a 0.5 mm thick nylon vessel (inner vessel, IV) in the center of an array of 100 PMTs detecting the scintillation pulses. The PMTs are coupled to CPC light concentrators, so that the total optical coverage is 20%. The IV is shielded from neutrons originating in the rock and γ -rays from the PMTs by 1000 t of ultra-pure water, contained in a cylindrical tank (11m \times 10m). CTF is also installed in the Hall C of the Gran Sasso underground laboratory, at a water-equivalent depth of 3800 m.

The ancillary systems for CTF include scintillator, water and nitrogen purification systems, a PMT calibration system based on the distribution of laser pulses through a bundle of optical fibers (see Chapter 3) and a mechanism for the insertion of calibration sources in the IV (see Chapter 5).

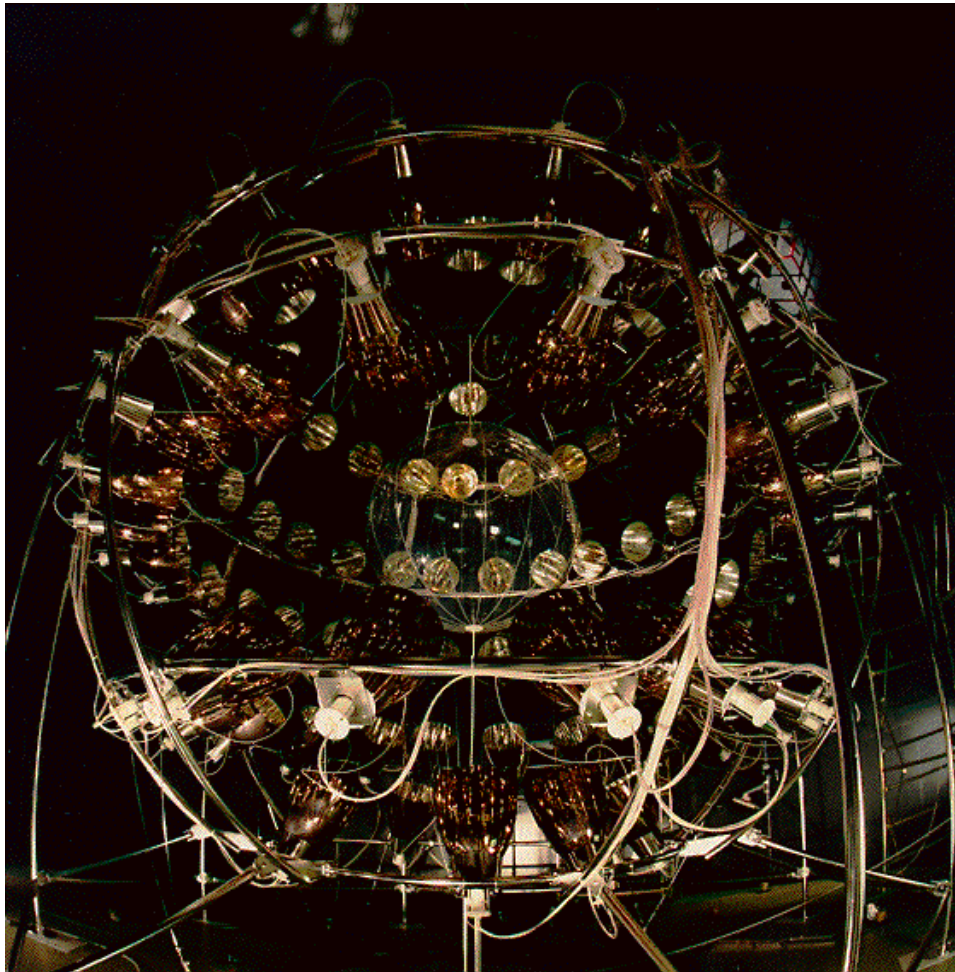


Figure 2.8 View of the CTF detector.

2.4.2 CTF Results

The first period of detector operation and data-taking (CTF-I) was carried out from January 1995 to July 1997. The most relevant tests performed in this phase were the measurement of the coincidence and single events rate, the use of the scintillator purification systems and the performance of calibration studies with radioactive sources. Only the main results will be summarized here so, for more detailed descriptions of the detector and the data analysis, we refer to the published articles [^{34, 35, 36, 37}].

- **Detector resolution.** The scintillation light yield in CTF was 300 photoelectrons/MeV. This leads to an energy resolution of 9% and a position resolution of 12 cm, at the energy of the ²¹⁴Po line – 751 keV.
- **¹⁴C.** The CTF low energy spectrum, shown in Figure 2.9, was normalized between 70 keV and 150 keV to the expected ¹⁴C spectral shape, obtained from Monte Carlo simulations, giving a ¹⁴C concentration in the liquid scintillator of:

$$\frac{{}^{14}\text{C}}{{}^{12}\text{C}} = (1.94 \pm 0.09) \times 10^{-18} \text{ g / g}$$

- **²³²Th.** The concentration of ²³²Th was inferred from the measurement of the decays of its daughters through the tag on the delayed coincidences of ²¹²Bi(β)²¹²Po(α), with $\tau_{1/2}=0.30 \mu\text{s}$. The result is

$$[{}^{232}\text{Th}] = (4.4^{+1.5}_{-1.2}) \times 10^{-16} \text{ g / g}.$$

- **²³⁸U.** For ²³⁸U, the delayed coincidence tag is from the decays ²¹⁴Bi(β)²¹⁴Po(α), with $\tau_{1/2}=164 \mu\text{s}$. However, there were strong indications that the ²¹⁴Bi(β)²¹⁴Po(α) coincidence rate was not due to intrinsic ²³⁸U scintillator radioactivity, but rather diffusion of radon from the water into the inner vessel. This phenomenon was demonstrated by raising the Rn leveling the water and observing a positive linear correlation between the number of events arising from Rn in the water (via γ -rays) and the number of events which can only arise from Rn inside the vessel.

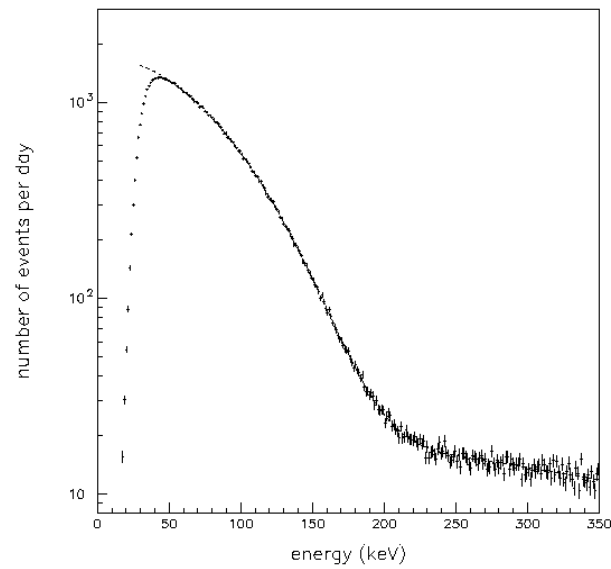


Figure 2.9 ^{14}C spectrum measured in CTF. The expected spectral shape from Monte Carlo simulations is superimposed on the data points.

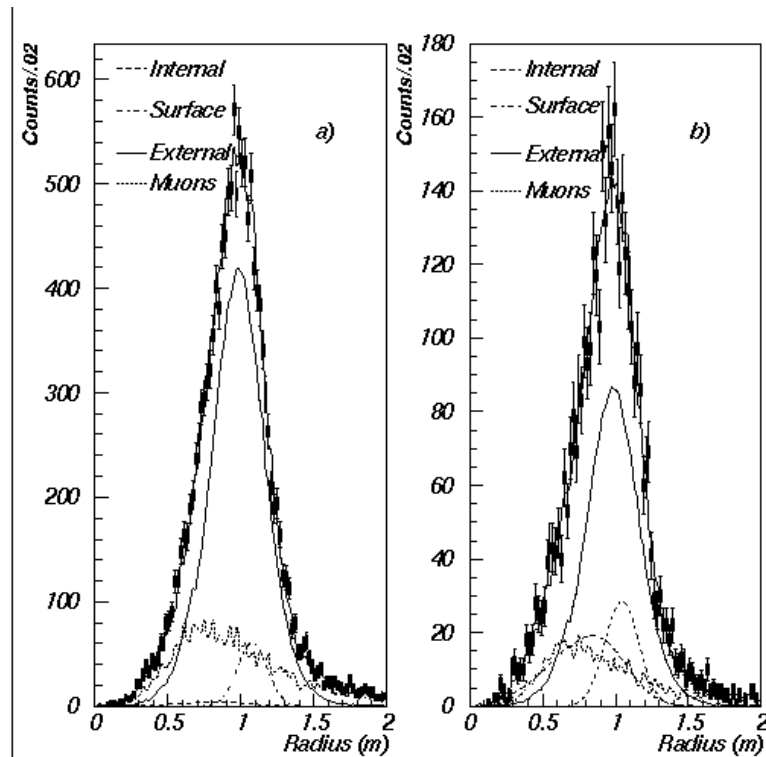


Figure 2.10 Radial distributions of the CTF data taken before (right) and after (left) the scintillator purification processes, and of the several types of expected contributions, obtained from Monte Carlo simulations.

The measured delayed coincidence counts due to intrinsic ^{238}U and diffused ^{222}Rn corresponds to an equivalent uranium concentration of

$$[^{238}\text{U}] = (3.5 \pm 1.3) \times 10^{-16} \text{ g / g} \quad \text{Eq. 2.4}$$

- **Purification.** The effect of the purification systems on the scintillator intrinsic contamination was studied by means of an analysis of the radial distributions of the single events. Figure 2.10 shows the radial distributions of the events position, obtained from the PMT time distributions by means of a reconstruction algorithm. The lines represent Monte Carlo simulations of the expected distributions for different classes of events: external, internal, muons and surface background. A fit of the data resulted an internal rate of 600 events/day before the purification and an upper limit of <30 events/day after the purification. As a comparison, the expected ^7Be neutrino signal in the 250 keV-800 keV energy window, is 2 events/day. The sensitivity of CTF was strongly limited by the external background, since the scintillator volume was too small for an adequate shielding of the external γ -rays.
- **a/b discrimination.** The ratio of the pulse tail integrated above 48 ns versus the total collected charge was used in CTF to discriminate between α and β events. At the energy of the ^{214}Po line – 751 keV, the efficiency of α rejection through pulse-shape discrimination is 97 %, with a β misidentification of 2.5 %. At lower energies, the α identification varies from 90 % to 97 %, with a β misidentification of 10 %.
- **Light propagation.** The main features of light propagation in a large scintillation detector were investigated taking advantage of the three-dimensional light collection in CTF. In particular, the investigation of the absorption and re-emission of light by the fluor (inelastic scattering) showed that this process affected 44 % of the detected light, with a corresponding increase of the effective scintillation decay time from 3.5 ns in small-scale laboratory measurements to 5.5 ns in CTF.

The CTF results demonstrated experimentally a series of important points on which the Borexino design is based. Organic liquid scintillators can be obtained with extremely low levels of radioactive impurities. The nylon vessel technique was successfully employed for containing the scintillator and the on-line purification demonstrated its effectiveness. The capabilities of the analysis methods of delayed coincidences, position reconstruction, and pulse-shape discrimination were demonstrated.

However, the high level of external background signalled the crucial need to control the activity of Radon in the buffer liquid. In order to reach this purpose, the design of Borexino incorporates an additional nylon vessel to serve as a Rn barrier.

2.4.3 CTF Upgrades

The CTF detector was upgraded in 1999 with the installation of new PMTs and two new nylon vessels, in which the outermost serves as a Rn barrier. After the CTF-II phase of tests with an alternative scintillator, the CTF-III phase will consist of a radioactivity screening campaign of the scintillator batches for Borexino.

2.5 Solar Neutrino Physics in Borexino

In this section, we discuss the potential measurements in Borexino, and their contribution for Solar Neutrino Physics, focusing on the main goal of the experiment, the detection of ^7Be solar neutrinos. Since this is a monoenergetic source, the possible measurements are essentially two: the average flux and time variations. The next sections will present the expected rates and time modulations of the signal in different neutrino oscillation scenarios.

The sensitivity of Borexino to other solar neutrino sources, like pp, pep and ^8B is limited, but might not be negligible, if the background rates are small enough. Even if with limited statistics with respect to experiments with larger masses, Supernova neutrinos and geological antineutrinos can be well identified above the background, due to distinctive coincidence signatures. For a discussion of the sensitivity of Borexino to non- ^7Be neutrino measurements, see references [33, 46].

2.5.1 Neutrino cross sections

The reaction used in Borexino to detect solar neutrinos is neutrino-electron elastic scattering:

$$\nu + e^- \rightarrow \nu + e^- \quad \text{Eq. 2.5}$$

The momentum transfer in the elastic scattering off protons or other nuclei is too low to produce charged particles with enough kinetic energy for useful detection. In addition, in the energy region of solar neutrinos (i.e., below 18 MeV) the cross section for inelastic scattering off nuclei is much lower.

The differential cross section $\sigma_\nu(t)$ for neutrino-electron elastic scattering was originally derived at first order by 't Hooft [⁶²]:

$$\mathbf{S}_n(q, t) = \mathbf{S}_0 \left[g_l^2 + g_r^2 \cdot \left(1 - \frac{t}{q} \right)^2 - g_l \cdot g_r \cdot \frac{m_e t}{q^2} \right] \quad \text{Eq. 2.6}$$

where t and q are the kinetic energies of the electron and the neutrino, respectively. The other quantities are

$$s_0 = \frac{2G_F^2 m_e^2}{p\hbar^4} = 88.1 \times 10^{-46} \text{ cm}^2$$

$$g_r = \sin^2 \theta_w = 0.23,$$

$$g_l = +\frac{1}{2} + \sin^2 \theta_w, \text{ for } \nu_e\text{-}e^- \text{ interactions,}$$

$$g_l = -\frac{1}{2} + \sin^2 \theta_w, \text{ for } \nu_\mu\text{-}e^- \text{ or } \nu_\tau\text{-}e^- \text{ interactions.}$$

where G_F is the Fermi constant of weak interactions, m_e is the mass of the electron at rest and θ_w is the Weinberg angle.

For energies of about 1 MeV the cross section for ν_μ and ν_τ is about five times smaller than for electron neutrinos. The scattering of ν_μ and ν_τ off electrons occurs only through neutral currents, while the scattering of electron neutrinos occurs through charged and neutral currents. Radiative corrections are not considered. These would modify the differential cross section based on the tree-level approximation by less than 2%.

For antineutrinos, g_l and g_r are exchanged. In addition, antineutrinos can be detected in Borexino via the classic Cowan-Reines inverse β^+ reaction:

$$\bar{\nu}_e + p \rightarrow e^+ + n \quad \text{Eq. 2.0.7}$$

The signature for this process is the delayed coincidence between the initial positron and the delayed 2.2 MeV neutron-proton capture γ -ray. This reaction may be useful to set limits on the antineutrino flux from the Sun or to detect antineutrinos emitted by the natural radioactivity in the Earth.

2.5.2 Interaction rates in different oscillation scenarios

The interaction rate for neutrino electron scattering is given by

$$R = N_e \int_0^{q_{\max}} \Phi_{\text{Earth}}(q) \left(P_{ee}(q) \int_0^{t_{\max}} s_e(q, t) dt + (1 - P_{ee}(q)) \int_0^{t_{\max}} s_{\mu\tau}(q, t) dt \right) dq \quad \text{Eq. 2.8}$$

where N_e is the number of electrons in the target, $\Phi_{\text{Earth}}(q)$ is the neutrino flux at the average Sun-Earth distance, $P_{ee}(q)$ is the electron neutrino survival probability, $\sigma_e(q,t)$ and $\sigma_{\mu,\tau}(q,t)$ are, respectively, the differential cross sections for electron neutrinos and for muon and tau neutrinos. The fluxes $\Phi_{\text{Earth}}(q)$ are taken from the BP2000 Standard Solar Model and their integrated values are listed in the second column of Table 2.8.

The electron neutrino survival probabilities $P_{ee}(q)$ depend on the Δm^2 and $\tan^2\theta$ parameters describing the considered neutrino oscillation mechanism. For the presently allowed solutions (see xxx) of oscillations in matter, SMA (Small Mixing Angle), LMA (Large Mixing Angle) and LOW (low mass), $P_{ee}(q)$ is plotted in Figure 2.11. Figure 2.12 shows the plot for the Vacuum solution.

There is an almost complete suppression of the ${}^7\text{Be}$ electron neutrinos (at 0.86 MeV) in the SMA solution, but since Borexino is also sensitive to muon and tau neutrinos via neutral currents elastic scattering, the neutrino interaction rate is not suppressed, but reduced by about a fifth with respect to the SSM rate.

The average survival probability in the LMA and LOW solution are of both of about 40 %, but due to MSW flavour regeneration in the Earth, there is a strong day-night asymmetry in the LOW solution.

The survival probability in the Vacuum solution is strongly dependent on the energy and on the particular value of Δm^2 within the allowed region, so an average rate prediction is not significative (it can vary from 30% to 80% of the SSM rate). The function represented in Figure 2.12 is the survival probability at low energies for one particular point ($\Delta m^2=6.0 \cdot 10^{-11} \text{ eV}^2$ and $\sin^2 2\theta=0.96$) inside the allowed parameter range of the Vacuum solution.

The expected event rates were calculated with the help of Monte Carlo simulations of the detector response and are shown in Table 2.8 in the cases of the Standard Model of electroweak interactions (i.e., with $P_{ee}(q)=1$) and the three matter oscillation solutions [⁶³],:

MSW Large Mixing Angle: $\Delta m^2 = 1.8 \cdot 10^{-5} \text{ eV}^2$, $\sin^2 2\theta = 0.76$;

MSW LOW: $\Delta m^2 = 7.9 \cdot 10^{-8} \text{ eV}^2$, $\sin^2 2\theta = 0.96$;

MSW Small Mixing Angle: $\Delta m^2 = 5.4 \cdot 10^{-6} \text{ eV}^2$, $\sin^2 2\theta = 6.0 \cdot 10^{-3}$;

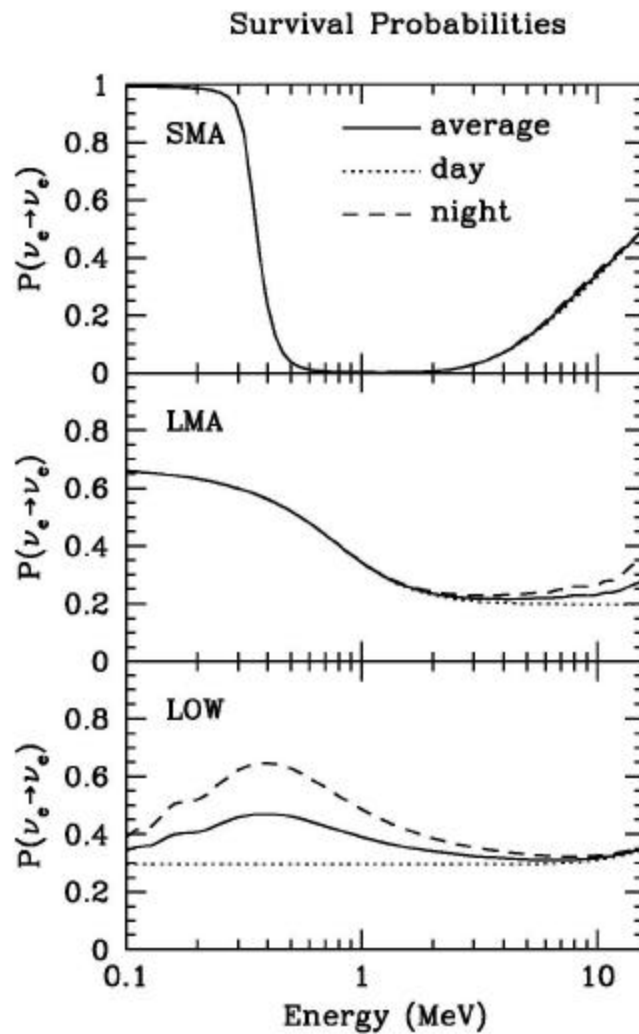


Figure 2.11 Electron neutrino survival probability for the SMA, LMA and LOW solutions.

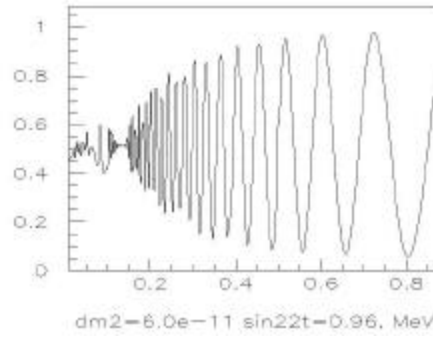


Figure 2.12 Electron neutrino survival probability for a particular point in the Vacuum oscillations allowed region.

Neutrino Source	Flux $10^{10} \text{ cm}^2 \text{ s}^{-1}$	Rates (events/day)			
		SSM	LMA	LOW	SMA
Pp	5.94 (+/-1%)	1.3	1.0	0.6	0.6
Pep	$1.40 \cdot 10^{-2}$ (+/-1.5%)	2.0	1.0	1.0	0.4
^7Be	0.482 (+/-10%)	45.9	26.1	25.2	9.7
^8B	$5.15 \cdot 10^{-4}$ (+20%/-16%)	0.10	0.04	0.05	0.05
^{13}N	$5.56 \cdot 10^{-2}$ (+21%/-17%)	3.9	2.1	2.1	0.8
^{15}O	$4.88 \cdot 10^{-2}$ (+25%/-19%)	5.0	2.6	2.6	1.0
^{17}F	$5.73 \cdot 10^{-4}$ (+/-25%)	0.06	0.03	0.03	0.01
Total		57	33	32	13

Table 2.8 Predicted solar neutrino event rates in Borexino for the Standard Model (no-oscillations) and for three neutrino oscillation solutions: LMA, LOW and SMA. The neutrino fluxes and their 1σ uncertainties are taken from the BP2000 Standard Solar Model. The rates are calculated for a fiducial mass of 100 t and in the energy window $250 \text{ keV} < E < 800 \text{ keV}$.

From the results presented in Table 2.8, we can see that the ^7Be flux is dominant on the neutrino window, but neutrinos from other sources, in particular from CNO cycle reactions, still contribute with about 20 % of the counts, and so must be taken into account in the analysis. Again, this consideration calls for a good spectral shape recognition.

Considering only the 10% error of the theoretically predicted ^7Be flux, the LMA and LOW solutions are indistinguishable on the basis of the rate alone, while the difference between the SSM and the LMA rates and between the LOW and SMA

rates are, respectively, 2.8σ and 4.3σ . This large separation between the predicted rates allows in principle for a good discrimination capability.

G.L.Fogli et al. from the University of Bari made a complete calculation of the expected ^7Be neutrino rate in Borexino, normalized to the SSM rate, in function of the Δm^2 and $\sin^2 2\theta$ oscillation parameters. Its results are plotted in Figure 2.13, along with the allowed regions for the LMA, SMA and LOW solutions (prior to the SNO results). This plot shows that, even taking into account the extension of the 99% C.L. allowed regions, the predicted rates for the LMA/LOW, SMA, and SSM solutions are significantly separated.

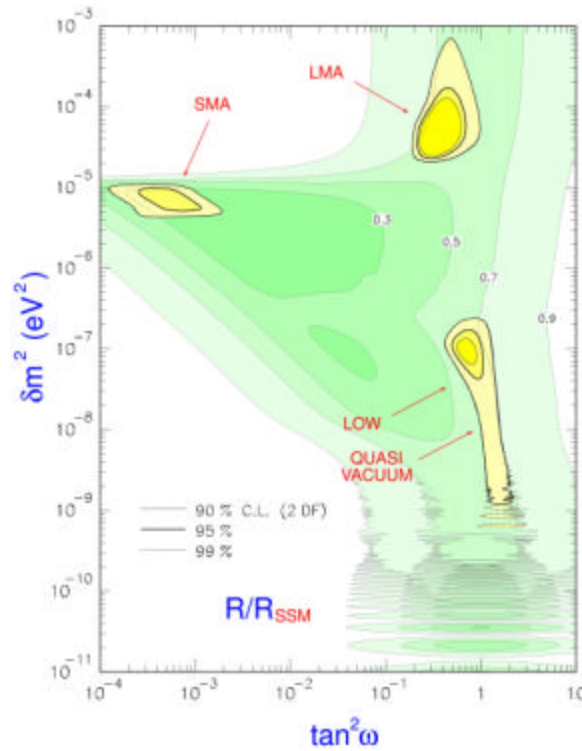


Figure 2.13 Confidence level contour plot of the solar neutrino problem solutions and the ^7Be neutrinos expected rate in Borexino, normalized to the SSM rate.

2.5.3 Time variations

In the previous section we have seen that the average rate measurement is a good variable to distinguish between the SMA and the other solutions at large mixing angle (LMA, LOW and Vacuum), but not to distinguish between these last three

solutions. However, for the LOW and Vacuum solutions, distinctive patterns of time variations of the neutrino flux are expected.

Figure 2.14 shows the annual variation of the ^7Be neutrino survival probability for the best fit point of the Vacuum oscillations allowed region (VO) and also for the HEE-VO solution, proposed by Berezhinsky et al.[⁶⁴] to explain the excess of high energy events observed in SuperKamiokande. The expected variations are significantly larger than the 7% yearly variation due to the $1/R^2$ effect, so the seasonal variation measurement gives Borexino a very good sensitivity to the Vacuum oscillations solution.

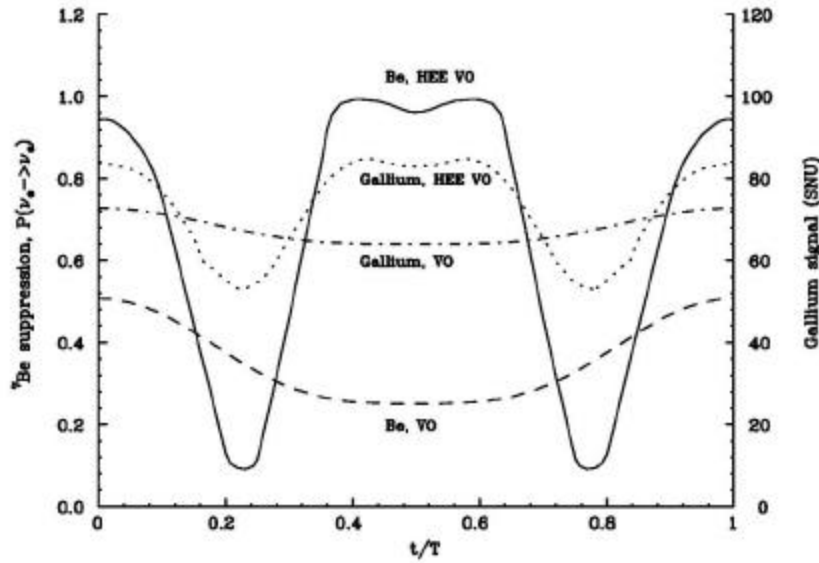


Figure 2.14 Expected annual variation of the ^7Be solar neutrino flux in the case of vacuum oscillations. Seasonal variation of the ^7Be neutrino survival probability and of the GNO gallium detector signal for the VO (Vacuum oscillation $\Delta m^2 = 6.5 \cdot 10^{-11} \text{ eV}^2$, $\sin^2 2\theta = 0.75$) and HEE-VO (High Energy Excess Vacuum Oscillations $\Delta m^2 = 4.2 \cdot 10^{-10} \text{ eV}^2$, $\sin^2 2\theta = 0.93$) solutions. T is 1 year. From [⁶⁵].

The high sensitivity to seasonal variations of the solar neutrino flux in Borexino can be appreciated in a different way, considering the Fourier analysis of the time dependence of the neutrino rates, by Fogli et al.[⁶⁶]. From the plots in Figure 2.15, we observe that, not only Borexino has a much higher sensitivity (of about 30 %) to deviations from ϵ (the Earth orbit eccentricity) of the first Fourier component of the neutrino rate time dependence than SuperK or SNO, but is also sensitive to the second and third Fourier components.

In the case of the LOW solution, a strong day-night asymmetry of the detected rate is expected in all the allowed region, due to the MSW flavour regeneration of electron neutrinos when crossing the Earth. Due to this so-called “day-night effect”, the Sun would effectively be brighter at night, at least for experiments sensitive based on charged current or elastic scattering interaction

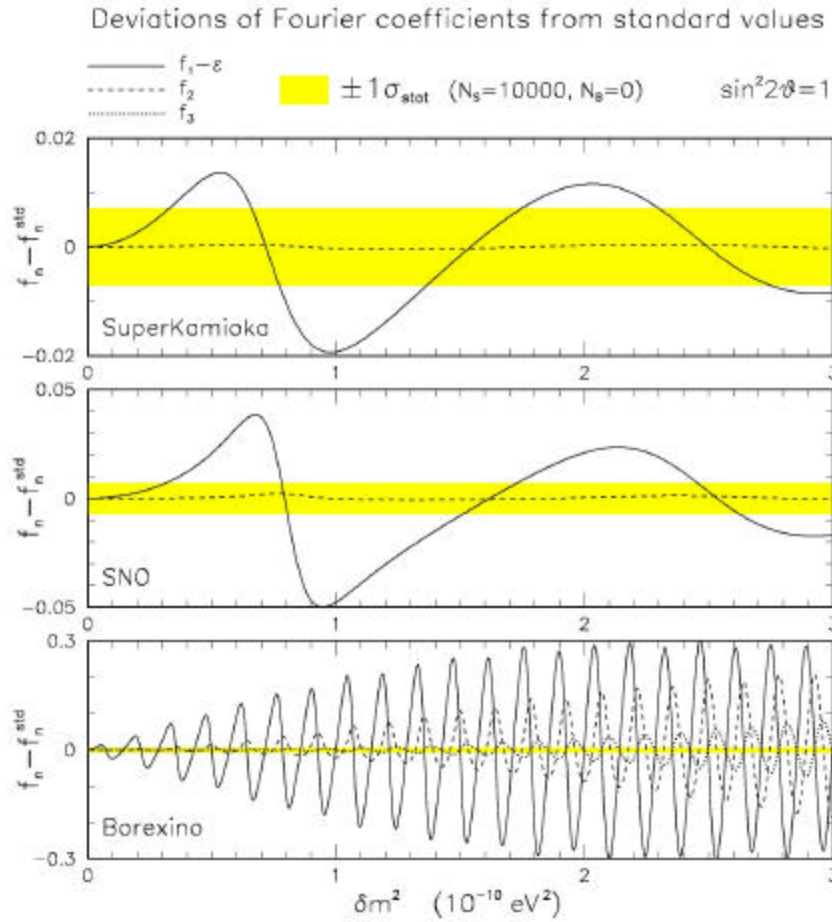


Figure 2.15 Deviation from standard of the Fourier components of the time dependence of the observable neutrino rates in the case of Vacuum oscillations. Maximal mixing is assumed. Compared sensitivity in SuperKamiokande, SNO and Borexino. Notice the different yy scale in each case. From ref. [66].

The day-night asymmetry is defined as

$$\frac{N - D}{N + D} \times 100 \quad \text{Eq. 2.0.9}$$

where N is the neutrino rate at night and D is the neutrino rate in the daytime.

Figure 2.16 shows the expected day-night asymmetry in function of the oscillation parameters. For the whole LOW region, allowed at 95 % C.L., the expected asymmetry is at least 5 %, so also in this case Borexino is well positioned to verify or reject this solution.

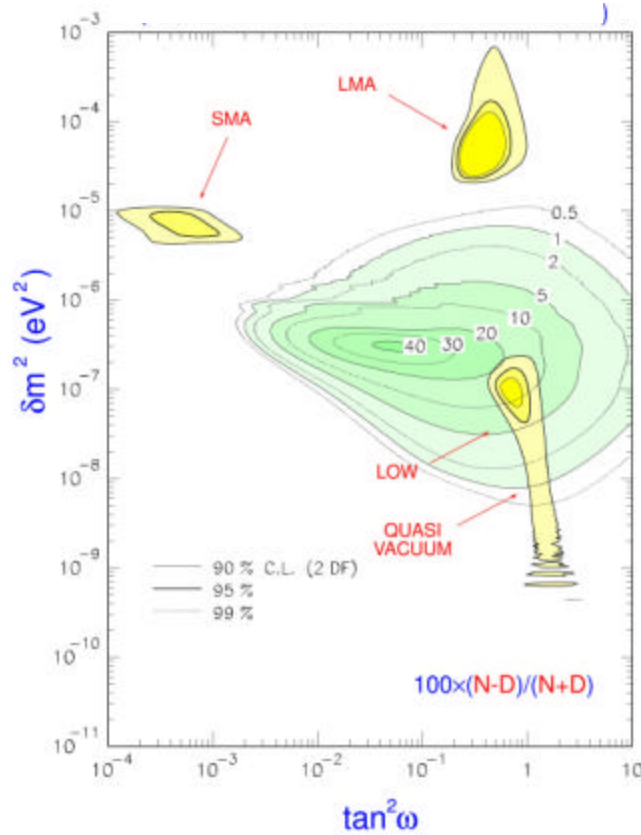
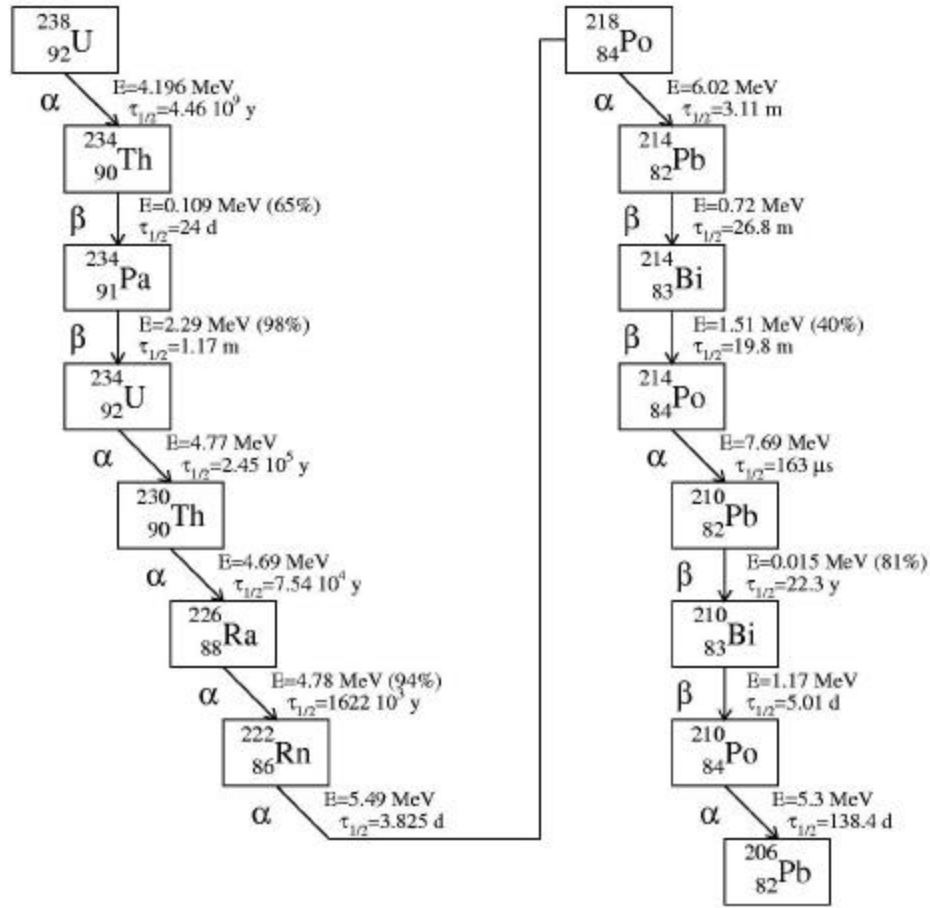


Figure 2.16 Confidence level contour plot of the solar neutrino problem solutions and the day-night asymmetry (in percentage) of the ^7Be neutrino rates in Borexino.

2.6 Background

With a count rate of about 50 events/day from solar neutrinos, the limiting factor to the Borexino sensitivity is not so much statistics as it is the signal-to-background (S/B) ratio. In order to have $S/B=1$, the background requirements are very stringent: the rate must not be higher than 0.5 events/day/ton or 5×10^{-8} Bq/kg in the energy range 250-800 keV.

Figure 2.17 Radioactive chain of ^{238}U .

It is natural to distinguish the background events between internal and external, i.e., the events that have its source inside and outside the scintillator volume, respectively, because the structure of the detector is designed to shield the inner the active scintillator volume from external radiation.

2.6.1 External background

2.6.1.1 Sources

As sources of external background, three kinds of natural penetrating radiation can be considered: gamma rays, neutrons and muons.

Cosmic muons are an intense external background source, but the muon veto system is designed to limit the residual rate to less than 0.5 events/day [33], so we will not consider this background in the present analysis. Neutrons are essentially produced in the rock surrounding the laboratory tunnel, and are stopped by the water buffer. A relevant rate of γ rays is emitted by most of the detector materials, such as the PMTs, the light concentrators, ancillary parts for

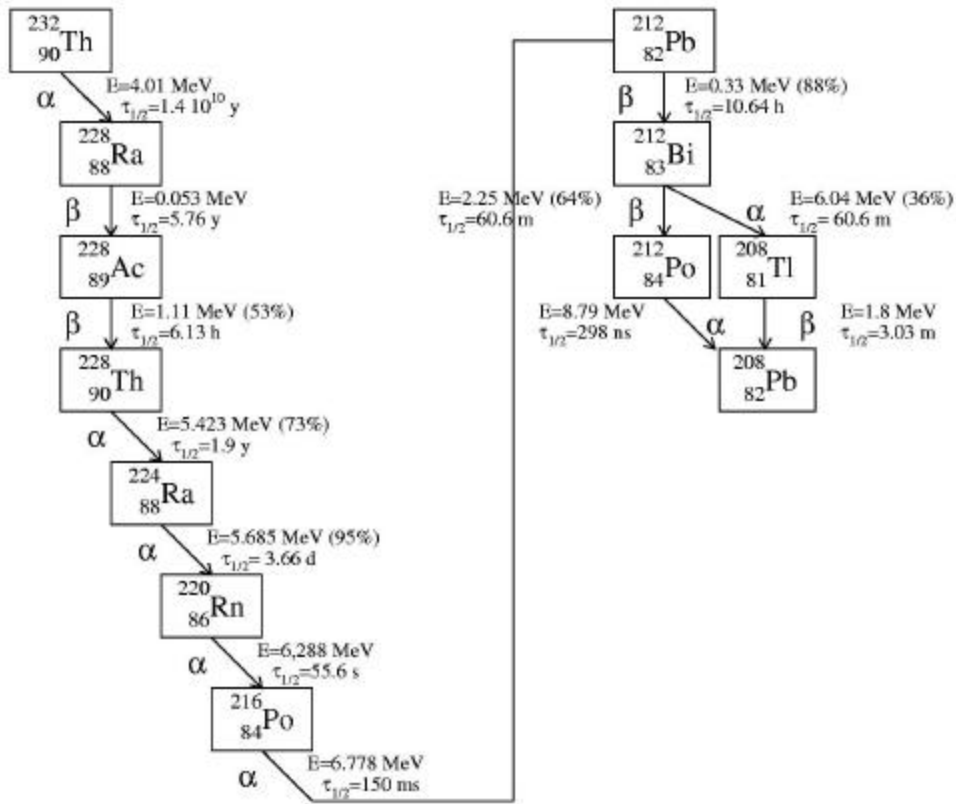


Figure 2.18 Radioactive chain of ^{232}Th .

the nylon vessels, the SSS, etc., that cannot be produced with the same radiopurity levels as the scintillator itself. So, the γ background will be described in more detail. Even if there is some contribution from ^{40}K , the main γ emitters are the isotopes from the ^{238}U and ^{232}Th chain.

The detailed structures of the radioactive decay chains of ^{238}U and ^{232}Th are shown in Figure 2.17 and Figure 2.18. The chains include 25 isotopes, of which 15 decay via α or $\alpha+\gamma$ emission and 11 via β or $\beta+\gamma$ emission (^{212}Bi of the ^{232}Th

chain presents both types of decays). The most relevant γ peaks are ^{208}Tl at 2.6 MeV and ^{228}Ac at 0.9 MeV in the ^{232}Th chain and the ^{214}Bi lines at 1.7 and 1.1 MeV in the ^{238}U chain.

Table 2.9 lists the content of radioactive impurities in the detector materials, the total mass employed, and the correspondent activity, considering only the γ -emitting decays.

Detector	^{238}U	^{232}Th	K_{nat}	Mass	Activity
Component	[g/g]	[g/g]	[g/g]	[g]	[g/d]
Nylon vessel	2×10^{-12}	4×10^{-12}	1×10^{-8}	3.2×10^4	0.5×10^3
IV support (nylon)	5×10^{-11}	2×10^{-12}	1×10^{-6}	2.1×10^4	1.0×10^4
OV support (steel)	1×10^{-9}	2×10^{-9}	7×10^{-8}	1.5×10^4	1.5×10^5
PC buffer	1×10^{-15}	1×10^{-15}	1×10^{-12}	1000 m ³	5.0×10^3
^{222}Rn in buffer		1 mBq/m ³		1000 m ³	2.2×10^5
Light Concentrators	1×10^{-8}	1.3×10^{-7}	6×10^{-6}	6×10^6	2.6×10^8
PMTs	3×10^{-8}	1×10^{-8}	2×10^{-5}	9×10^6	1.2×10^9
SSS	7×10^{-10}	3×10^{-9}	7×10^{-8}	7×10^7	1.1×10^9

Table 2.9 Content of radioactive impurities in the materials contributing to the external background in Borexino. All the quoted radiopurity values are results from measurements [54], except the values for the PC buffer, that are conservative assumptions.

The calculation of the expected activities is based on the assumption of secular equilibrium in the ^{238}U and ^{232}Th chains. The method used for the measurements, γ -ray spectroscopy with Ge detectors, is sensitive only to one, or two at most, isotopes of the Uranium and Thorium chains, so this assumption cannot be fully supported. However, the measured isotopes or the isotopes that must be in equilibrium with them because of a small half-life are the strongest emitters of the γ -rays with energies above 2 MeV, sufficient to penetrate deeply inside the detector. So the secular equilibrium assumption can be considered as a reasonable approximation when calculating the expected rates of external background γ events in the Borexino inner vessel.

The nylon vessel is made is extremely thin (125 μm) and is made with a very low radioactivity material, so it contributes much less than its auxiliary supports. In particular, the steel supports of the outer vessel, will cause a localized event distribution, since they are near the north and south poles of the Outer Vessel. For the PC buffer contamination, we assume a value ten times higher than the contamination of the active PC scintillator. Even in this conservative assumption, the radiopurity values are better than for the water produced in the purification plant (see Table 2.6). In fact, this was one of the reasons for choosing PC as the buffer material .

The PMTs are the detector component causing the highest γ activity, even if the chosen glass bulb has a particularly high radiopurity level (1/10 that of normal glass). The light concentrators are made from aluminium in order to resist the chemical aggression of PC and have a high contamination from ^{232}Th . They have a lower activity than the PMTs, but they are closer to the detector center, so the expected event rates in the scintillator volume will be comparable. The SSS is further away from the center so it contributes less than the PMTs.

2.6.1.2 Expected g rates in the scintillator

The calculation of the expected external background rates requires a detailed Monte Carlo propagation of the γ -rays from their origin to the active detector volume, i.e., the scintillator contained inside the inner vessel. In the case of the light concentrators, the PMTs and the Stainless Steel Sphere, the distances travelled (>2 m) are far higher than the average γ -ray attenuation length (40 cm at 1 MeV), so the event activity suffers a reduction of several orders of magnitude. For this reason, the propagation of each single γ -ray is a difficult way of obtaining an estimation of the event rate in the innermost regions of the detector (as well as a waste of computational resources). The strategy employed in these simulations consisted in dividing the detector in several spherical shells, the innermost one being the scintillator volume. When the generated γ -rays reach a shell border, their

energy and direction are registered and are the base for the next simulation of γ -rays propagation, with higher statistics.

The propagation of the γ -rays emitted by the impurities present in the several materials listed in Table 2.9 was simulated with the GENEB code and, in the case of light concentrators, PMTs and SSS, with its shell method extension. The resulting radial dependence of the external background is shown in Figure 2.19, compared with the neutrino signal. The expected rates are presented in Table 2.10, for the 250 keV-800 keV energy window and in four scintillator volumes. The radial distribution of the events and comparison of the expected rates with the SSM prediction of about 50 neutrino events per day in the 100 ton fiducial volume (1/3 of the rate in the whole scintillator volume) shows us that the external background has a very steep radial dependence, going from prohibitive in the whole scintillator volume to negligible values in the standard fiducial volume. The design value of the Borexino fiducial mass is indicatively fixed at 100 t, corresponding to a sphere with 3 m of radius. It can, in principle, be larger, and this would lead to a higher neutrino event rate. The final value will be defined on the basis of the actual external background rates that will be measured during data-taking.

The external background rates will depend not only on the materials radiopurity but also on the position resolution of the detector. The position is calculated by the reconstruction algorithm on the basis of the time information of the PMT signals. So, a good knowledge of the scintillator decay time and of the effects of light propagation on the event time distribution are essential for a good position resolution, as well as a good inter-PMT time equalization. In order to monitor these parameters, the detector includes calibration systems dedicated to the PMT equalization and to the measurement of the optical properties of the scintillator and buffer liquid. These systems are described in detail in Chapters 4 and 5.

An additional calibration system based on an external γ source will allow us to monitor the overall performance of the position reconstruction algorithm and to calculate the external background rejection efficiency in the final detector. This system is described in Chapter 5.

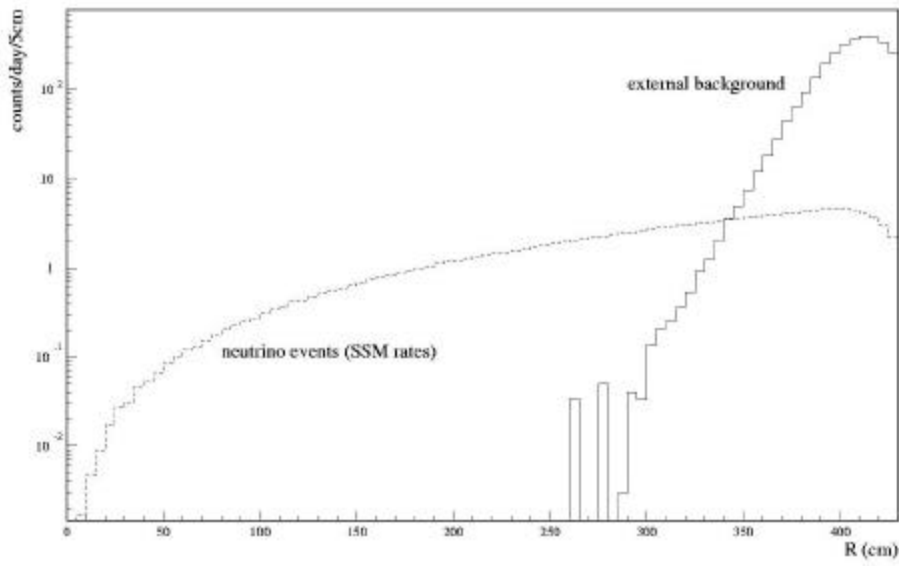


Figure 2.19 Radial dependence of the external background compared to the neutrino signal.

Detector component	Scintillator Volume			
	100t	160t	200 t	300 t
Nylon film	0.002	0.03	0.4	56
IV/OV support	0.016	0.91	9.1	955
Buffer	0.017	2.5	22	1453
Light Concentrators	0.054	2.3	18	896
PMTs	0.081	3.6	28	1294
SSS	0.005	1.6	12	496
Total (\pm stat. err.)	0.18 ± 0.05	11 ± 0.4	89 ± 1	5163 ± 8

Table 2.10 Expected rates of external γ background in neutrino energy windows, in three fiducial volumes (corresponding to 100 t and 160 t, 200 t) and in the whole scintillator volume (300 t). Values in events/day. Data for Nylon and IV support are from [46].

2.6.2 Internal background

As internal background, we consider all the background events that have its source inside the scintillator volume. These consist of β decays of ^{14}C , an ingradient part of the scintillator molecules, and α , β , γ decays of the radioactive impurities present as trace elements, in particular ^{238}U , ^{232}Th and ^{40}K . Even if it has a much lower activity (about 6×10^2 events/day, assuming a 10^{-16} g/g U and Th concentration) than external background, internal background is the major concern of the experiment because it is virtually unshieldable and undistinguishable from neutrino events on the basis of its reconstructed position.

As was seen in previous sections, the methods employed to keep the internal background under control are:

- Use of the CTF detector for ^{14}C quality control before filling Borexino;
- Purification of the scintillator, including distillation, water extraction, solid column purification, and nitrogen stripping.

The background from the residual impurities that remain after the application of these methods can be further reduced in the data analysis phase, as was shown in CTF. The next sections illustrate the use of the rejection methods and provide an estimate of the expected internal background levels.

2.6.2.1 Rejection methods

The ^{14}C isotope decays produce a continuous β spectrum with an endpoint at 167 keV. Since these β events are indistinguishable from low energy neutrino scattering events, the only way to reject the ^{14}C background is through an energy threshold cut. The ^{14}C event rate is several orders of magnitude higher than the neutrino rate, so the energy threshold is established at 5σ above the β spectrum endpoint, where σ is the energy resolution of the detector. The resolution is given by

$$\frac{s(E)}{E} = \frac{\sqrt{n(E)}}{n(E)} = \frac{1}{\sqrt{NE}} \quad \text{Eq. 2.0.10}$$

where $n(E)$ is the number of photoelectrons detected at energy E and N is the number of photoelectrons per MeV. From Monte Carlo simulations and comparisons with CTF data, we know that N is about 400, so

$$\sigma(E)/E = 13 \% \text{ at } 150 \text{ keV.} \quad \text{Eq. 2.11}$$

The energy threshold is then fixed at 250 keV, and, assuming a $^{14}\text{C}/^{12}\text{C}$ ratio of 10^{-18} (design value) this corresponds to a residual rate of 0.3 ev/day, including the effect of DAQ pile-up of two successive ^{14}C events.

The energies of the β particles are distributed from 0 to 2.2 MeV and the energies of the γ -rays go from 0 to 3.1 MeV. The α particles have energies from 4.0 MeV to 8.8 MeV, but, due to scintillation quenching, they produce light pulses with β -equivalent energies from 260 keV to 990 keV (see $Q(E)$ in Table 2.2).

With these energies, the internal background covers the whole ^7Be neutrino window ($250 \text{ keV} < E < 800 \text{ keV}$). The three methods used to reduce this background are the following:

- Pulse-shape discrimination;
- Delayed coincidences;
- Statistical cut.

The main rejection method for the background events from the radioactive decay chains of ^{238}U and ^{232}Th is Pulse-Shape Discrimination. Alpha particles have a higher ionization density than electrons or γ -rays, and this causes a higher quenching of the scintillation light. The effects of the light quenching are a lower β -equivalent energy and a larger scintillation decay time. The α quenching factor and the time distributions for α and β particle were shown in Chapter 2. The differences in the time distribution tails of α and β particles are used in order to discriminate between both types of particles. In CTF, simply using the tail-to-total ratio, an α identification efficiency of 90 % was reached, allowing a β -misidentification of 5 %. In Borexino, with the final electronics the whole time distribution can be taken into account and not only a threshold integral, so we expect better efficiencies.

The methods of the delayed coincidences and the statistical cut are based on the detailed structures of the radioactive decay chains of ^{238}U and ^{232}Th , shown in Figure 2.17 and Figure 2.18. Two Polonium isotopes, ^{214}Po ($\tau_{1/2}=163\ \mu\text{s}$) and ^{212}Po ($\tau_{1/2}=298\ \text{ns}$), have a half-life small enough so that its decay can be observed as a delayed coincidence with respect to the decay of their “fathers”, ^{214}Bi and ^{212}Bi , respectively. Once the correlated ^{214}Bi - ^{214}Po and ^{212}Bi - ^{212}Po events have been identified, the activities of these particular isotopes and of the chain segment with which they are in equilibrium are established. The isotopes of the ^{238}U chain in equilibrium with ^{214}Po are ^{222}Rn , ^{218}Po , ^{214}Pb and ^{214}Bi . In the ^{232}Th chain ^{224}Rn , ^{220}Rn , ^{216}Po , ^{212}Pb , ^{212}Bi and ^{208}Tl are in equilibrium with ^{212}Po . The knowledge of the activity of these isotopes allows us to statistically subtract the counts due to these events from the measured energy spectrum.

The ^{40}K isotope has an abundance of 0.0117 % in natural potassium and decays by two modes: via β^- with a probability of 89.3 % and an endpoint of 1311 keV; via electron capture with a probability of 10.7 % and the emission of a 1461 keV γ -ray from the first excited state of ^{40}Ar . Neither pulse-shape discrimination or the delayed coincidences method can be used to reject this background. A possible ^{40}K rejection method could be the spectral identification of the 1461 keV γ -ray and the statistical subtraction of the β^- counts in the neutrino window. However, this will ultimately depend on the rates of the other background sources in that energy window (in particular ^{234}Pa of the ^{238}U chain).

2.6.2.2 Expected rates

The estimation of the expected internal background rates is based on the design goals for the scintillator contamination levels:

- $10^{-16}\ \text{g/g}$ of ^{238}U
- $10^{-16}\ \text{g/g}$ of ^{232}Th
- $10^{-14}\ \text{g/g}$ of natural K

For ^{238}U and ^{232}Th , these levels are supported by the CTF results, but for natural K, they are only assumed, due to the lack of measurements with enough

sensitivity. In addition, secular equilibrium of the radioactive chains is assumed. The background events were simulated with the GENE and the tracking code and the results are listed in Table 2.11 and Table 2.12. The rates are referred to the energy window $250 \text{ keV} < E < 800 \text{ keV}$ (the “neutrino window”) and to the 100 t fiducial mass. The cut efficiencies are conservative assumptions based on the CTF experience

Isotope	Decay Type	Energy (keV)	Weight (%)	Rates (ev/day)			
				No Cuts	DC	PSD	SS
^{238}U	α	280	77	10.6	10.6	1.1	1.1
	$\alpha+\gamma$	278	23				
^{234}U	α	338	72	10.6	10.6	1.1	1.1
	$\alpha+\gamma$	386	28				
^{230}Th	α	330	76.3	10.6	10.6	1.1	1.1
	$\alpha+\gamma$	371	23.4				
^{226}Ra	α	339	94.5	10.6	10.6	1.1	1.1
	$\alpha+\gamma$	321	5.4				
^{222}Rn	α	417	99.9	10.6	10.6	1.1	0.05
^{218}Po	α	482	99.9	10.6	10.6	1.1	0.05
^{214}Po	α	746	99.99	3.2	0.2	0.02	0.02
^{210}Po	α	395	100	10.6	10.6	1.1	1.1
^{234}Th	β	-	-	0	0	0	0
	$\beta+\gamma$	-	-				
^{234}Pa	β	0-2290	98.6	3.9	3.9	3.9	3.9
	$\beta+\gamma$	760-2290	0.7				
^{214}Pb	β	0-1023	9.4	9.3	9.3	9.3	0.5
	$\beta+\gamma$	290-1023	40.7				
	$\beta+\gamma$	350-1023	47.3				
	$\beta+\gamma$	430-1023	2.5				
^{214}Bi	β	0-3230	19	0.5	0.02	0.02	0.02
^{210}Pb	β	-	-	0	0	0	0
	$\beta+\gamma$	-	-				
^{210}Bi	β	0-1116	100	6.4	6.4	6.4	6.4

Table 2.11 Expected internal background rates in Borexino due to the isotopes in the ^{238}U chain, assuming a contamination of 10^{-16} g/g . The rates are referred to a 100 t fiducial mass and the neutrino energy window. An efficiency of 95% is assumed for the Delayed Coincidences (DC) and Statistical Subtraction (SS) cuts. For the Pulse-Shape Discrimination (PSD) cut, an efficiency of 90% is assumed.

Isotope	Decay Type	Energy (keV)	Weight (%)	Rates (ev/day)			
				No Cuts	DC	PSD	SS
²³² Th	α	266	77	3.4	3.4	0.3	0.3
	$\alpha+\gamma$	330	23				
²²⁸ Th	α	409	72.7	3.5	3.5	0.4	0.4
	$\alpha+\gamma$	483	26.7				
²²⁴ Ra	α	440	94.5	3.5	3.5	0.4	0.02
	$\alpha+\gamma$	542	5.5				
²²⁰ Rn	α	519	99.9	3.5	3.5	0.4	0.02
	$\alpha+\gamma$	-	-				
²¹⁶ Po	α	590	99.9	3.5	3.5	0.4	0.02
	$\alpha+\gamma$	-	-				
²¹² Po	α	989	63	0	0	0	0
²¹² Bi	α	492	9.7	1.3	1.3	0.1	0.01
	$\alpha+\gamma$	527	25.2				
²²⁸ Ra	β	-	-	0	0	0	0
	$\beta+\gamma$	-	-				
²²⁸ Ac	β	0-2180	10	0.3	0.3	0.3	0.3
	$\beta+\gamma$	330-2180	9.6				
	$\beta+\gamma$	480-2180	6.7				
²¹² Pb	β	571	13	3.1	3.1	3.1	0.2
	$\beta+\gamma$	332-571	82				
	$\beta+\gamma$	155-571	5				
²¹² Bi	β	0-2251	40.3	0.8	0.04	0.04	0.04
	$\beta+\gamma$	700-2251	4.4				
²⁰⁸ Tl	β	-	-	0	0	0	0
	$\beta+\gamma$	-	-				

Table 2.12 Expected internal background rates in Borexino due to the isotopes in the ²³²Th chain, assuming a contamination of 10^{-16} g/g. The rates are referred to a 100 t fiducial mass and the energy window $250\text{keV} < E < 800\text{ keV}$. An efficiency of 95% is assumed for the Delayed Coincidences (DC) and Statistical Subtraction (SS) cuts. For the Pulse-Shape Discrimination (PSD) cut, an efficiency of 90% is assumed.

These rates due to the main sources of internal background in the neutrino window are summarized in Table 2.13. From these values, we can single out ^{238}U as the most important contaminant and Pulse-Shape Discrimination as the most effective analysis cut.

Source	Type	Rates (ev/day)			
		No Cuts	DC	PSD	SS
^{238}U chain	α	77.4	74.4	7.7	5.6
	β	20.1	19.6	19.6	10.8
^{232}Th chain	α	18.7	18.7	2.0	0.8
	β	4.2	3.4	3.4	0.5
^{40}K	β	1.5	1.5	1.5	1.5
Total		122	118	34	19

Table 2.13 Summary table for the internal background in the neutrino window.

Considering these values and a ^7Be neutrino rate of 46 ev/day (Table 2.8), and neglecting the external and the ^{14}C residual background in the fiducial volume, neutrino window, the signal-to-background ratio is

$$\frac{\text{Signal}}{\text{Background}} = \frac{46}{19} = 2.4 \quad \text{Eq. 2.12}$$

This value is the expression of the challenge faced by the experiment and calls for a very good recognition of the signal and background spectral shapes. This analysis is the subject of the last Chapter in this thesis.

Calibration of the Photomultipliers

The light pulses produced in the Borexino scintillator by all kinds of events, neutrino and background, are detected by the photomultipliers, so their performance has a direct influence on the position and energy resolution of the detector, as well as on the efficiency of the α background rejection through pulse-shape discrimination.

We have seen in Chapter 2 that the Borexino design is based on a shell structure that provides graded shielding against external radiation, the lowest background being at the center. After passive shielding buffer regions of water and quenched scintillator, the last, innermost shielding shell is a part of the active volume itself, so the background rejection is done through event position reconstruction and definition of a fiducial volume. Position resolution is important for an efficient background reduction and an accurate knowledge of the fiducial volume, for neutrino flux normalization. It is limited by the scintillator fluorescence decay time of 3.5 ns (effectively increased to 5.5 ns after the light propagation in large volumes, as shall be seen in Chapter 5), by the PMT transit time jitter of 1 ns and by the inter-PMT time equalization, i.e., the common definition of time t_0 . In order to keep the position resolution as good as possible given the decay time and jitter constraints, the PMT time equalization should be maintained at a subnanosecond level and checked on a regular basis.

The accuracy of the time measurement and calibration is important also for the alpha-beta discrimination, which is performed by observing the different fluorescence decay time distributions of alpha and beta scintillation events. These can be distorted by the time-of-flight differences that can be as large as 40 ns⁵ for photons originating far from the center and traveling in opposite directions. So,

⁵ Since the index of refraction of PC is 1.5, the speed of light is 20 cm/ns.

the pulse-shape discrimination analysis must be performed after the arrival time distribution has been corrected by subtracting the time-of-flight for each detected photon, estimated by means of the position reconstruction.

A good energy resolution, important for spectral shape recognition (Chapter 3), depends also on a good PMT charge calibration, since the energy is basically proportional to the number of detected photons. The charge calibration consists in determining the proportionality constant between the charge response of the PMT and the number of incident photons.

In this Chapter it is presented the PMT calibration system, a system for the time equalization and charge calibration of the photomultipliers. Section 3.1 reviews the basics of the performance of a photomultiplier tube, with special emphasis on the parameters relevant for single photon counting. Section 3.2 describes the system requirements and design. Sections 3.3 and 3.4 report the several tests that were done to verify the feasibility of the chosen method and the compliance with the constraints of the experiment. Finally, the quality control and installation of the final calibration system in Borexino is described in Section 3.5.

3.1 Low intensity light detection with photomultipliers

In this section an overview of the working principles and performance of the photomultipliers is presented, with specific focus on the parameters determining their sensitivity and resolution for the detection of low intensity scintillation light, i.e., in the single photoelectron counting regime [⁶⁷,⁶⁸].

Photomultipliers, often referred to also as phototubes or simply PMTs, are highly sensitive devices for the detection of low intensity light pulses, particularly used in nuclear radiation detection. The PMTs are essentially glass vacuum tubes that are partially covered on the inner surface by a photosensitive material and that have inside a chain of electrodes connected to high voltages.

In order to specify the main requirements of the Borexino PMTs and their calibration system, we describe the main components of a photomultiplier and their performance:

- *The photocathode.* The incident photons are absorbed by the photocathode, causing the emission of electrons by the photoelectric

effect, the usually called “photoelectrons” (p.e.). The photocathode material is usually based on the combination of bismuth or antimony with an alkali metal (typically cesium), which has semiconductive properties, so the photo-emission is due to the excitation of electrons from the valence band. A thin layer of the compound is deposited on the inner surface of the PMT bulb, where vacuum is made, so that the electrons can travel freely inside.

- *The dynode structure.* The potential applied between the cathode and the first electrode (or dynode) accelerates the photoelectrons. When the photoelectrons strike the first dynode, each one ejects further electrons (~ 3 to 5 , on average) by secondary emission. This electron multiplication process is repeated at subsequent dynodes, each of them at a higher potential than the preceding one, and results in a measurable current pulse at the last dynode, or anode. Typically, photomultipliers have 10 to 15 dynode stages and the total gain ranges from 10^5 to 10^8 .

3.1.1 Charge response

The fraction of incident photons that are converted into photo-electrons in the photocathode is the PMT quantum efficiency. We can represent its dependency on the photon wavelength by $E_{\text{cath}}(\lambda)$. The spectral quantum efficiency of the ETL9351 PMT, used in Borexino, was shown in Figure 2.2, in Chapter 2. If M is the average number of photons striking the photocathode and $I(\lambda)$ is their spectral intensity distribution, the average number of emitted electrons, μ , is given by:

$$\mu = M \frac{\int_0^{\infty} E_{\text{cath}}(I) I(I) dI}{\int_0^{\infty} I(I) dI} \quad \text{Eq. 3.1}$$

The emission of a low number of photo-electrons from the photocathode is determined by Poisson statistics, so the distribution function of the n electrons actually emitted is

$$P(n, m) = \frac{m^n e^{-m}}{n!} \quad \text{Eq. 3.2}$$

So, the PMT signal will be a superposition of contributions from 0, 1, 2, 3, ... p.e. emissions. The PMT response when no electron is released from the photocathode is the noise of the electron multiplication chain and is called the pedestal. It can be modelled with an exponential function, convoluted with a gaussian to take into account the resolution effect of the electronic noise. The anode pulse of an electron multiplier produced by a single electron released by the photocathode is called the single electron response (SER). Since the number of electrons at the anode is very large, its charge distribution is gaussian, and characterized by a mean charge x_1 and a standard deviation σ_1 . These parameters are directly connected to the gain of the electron multiplier and its spread. They depend on the details of the dynode structure and applied voltages.

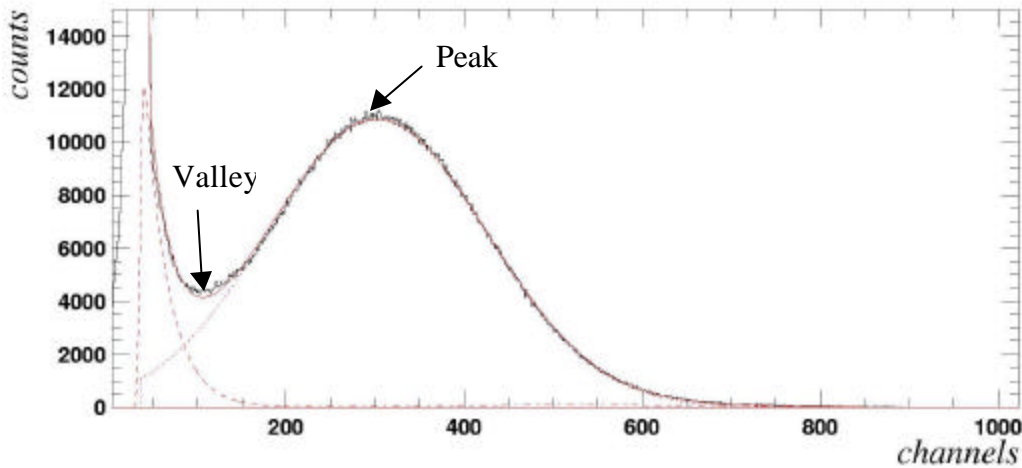


Figure 3.1 Single electron response of the ETL9351 PMT. The number of channels is proportional to the total charge of the pulses. From [68].

The charge spectrum shown in Figure 3.1 was obtained with a very low intensity light source, so that the average number of photoelectrons was $\mu=0.021$. The contribution of multiple-p.e. pulses can be written as

$$\frac{P(n > 1, m)}{P(n > 0, m)} = \frac{1 - e^{-m} - me^{-m}}{1 - e^{-m}} \quad \text{Eq. 3.3}$$

so, in the condition of $\mu=0.021$, it is 1 % and the pulse can be considered a very good approximation of an ideal SER. The spectrum is well described by the sum of an exponential for the pedestal and a single gaussian for the SER. The parameter that describes the separation between the SER (signal) and the pedestal (noise) is the peak-to-valley ratio, defined as the ratio between the count rate at the peak of the SER and the lowest count rate in the region between the signal and the pedestal (shown in Figure 3.1).

Within the linearity regime of the PMT the response to a n photo-electron pulse is also a gaussian with mean value x_n and standard deviation σ_n given by:

$$\begin{aligned} x_n &= n \cdot x_1 \\ \sigma_n &= \sqrt{n} \cdot \sigma_1 \end{aligned} \quad \text{Eq. 3.4}$$

For the Borexino PMTs, the linearity regime was verified to be valid up to illumination levels of about 100 p.e., much above the typical illumination levels in the experiment. In fact, the electronics dynamic range in Borexino is about 8 p.e. Therefore, the charge spectrum of a PMT can be modeled as a sum of gaussians, with parameters given by Eq. 3.4, and convoluted by the Poisson distribution. Figure 3.2 shows such a set of gaussians, used to describe the PMT response to an average illumination of 2 p.e

Generally, we measure x_n , the integrated charge of a PMT pulse, and want to know n , the number of photo-electrons that caused it. So the main task of the charge calibration is to supply the conversion factor, x_1 , which is the mean value of the single electron response.

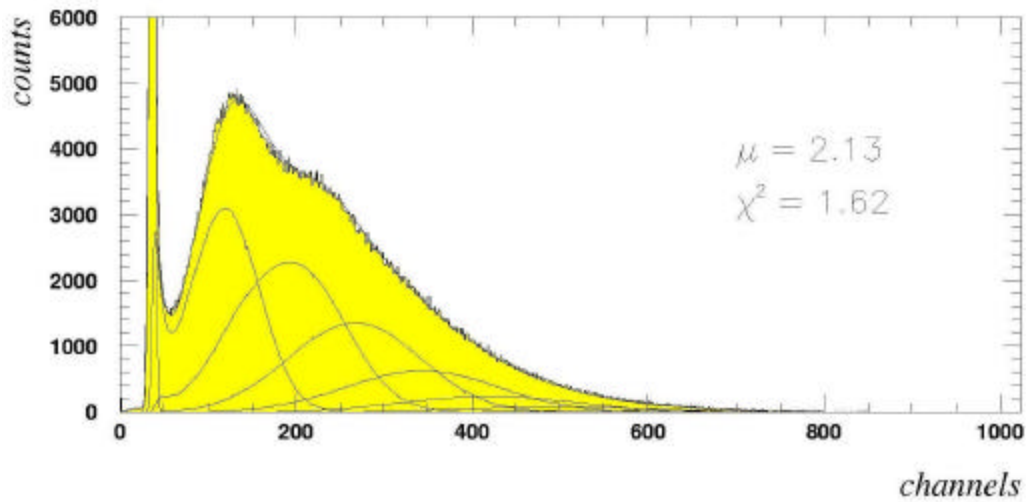


Figure 3.2 PMT response to an average of 2 photo-electrons. The set of gaussian functions used to fit the signal shape are also shown. The number of channels is proportional to the total charge collected at the PMT anode. From [68].

An important source of background to single photo-electron counting are the electrons spontaneously emitted by the photocathode due to thermal excitation. These pulses are present in the total absence of light, so they are called dark noise. In some PMTs, the charge response to the dark noise is very similar to the SER, and is often used to obtain the SER parameters. In the case of the ETL9351, however, it was demonstrated that the dark noise response has a large contribution from low amplitude pulses, making it unsuitable for a precise PMT calibration (see [68]). The contribution of the dark noise can be eliminated from the PMT data by triggering the acquisition electronics to the light pulse events. This can be done by using a triggered light source, such as a laser or, in its absence, requiring the coincidence of two or more PMTs. In order to keep the accidental dark noise contribution lower than 0.5 %, the minimum illumination level is 2% of a photo-electron, or $\mu = 0.02$ (for a typical dark noise rate of 2 kHz, and assuming a time gate of 100 ns for the acquisition).

3.1.2 Time resolution

The transit time of the electrons from the cathode to the anode varies according to the cathode–first dynode (D_1) configuration, the dynode structure and applied potentials. PMTs used in fast scintillation counting usually have transit times of

the order of 10-15 ns. The time position of the PMT response is defined as the time at which the leading edge reaches 50 % of the maximum value of the current pulse (using constant fraction discriminators). The shape of the SER pulse is gaussian and the rise time about 2-3 ns, but for pulses due to several photo-electrons, the rise time can be longer.

The most important parameter affecting the PMT resolution for time measurements is the spread of the transit time, commonly called time jitter. Several factors can affect the time jitter:

- There is a photocathode time spread caused by the difference in the transit time of electrons emitted from different parts of the cathode. This effect depends on the area of the cathode and on the electron optics of the cathode-D₁ configuration and it is in fact the main factor limiting the resolution of the large cathode PMTs used by large underground experiments, like Super-K, SNO and Borexino.
- There is a time spread due to the different initial velocities and directions of the photo-electrons. This can be decreased by reducing the thickness of the photo-sensitive layer, however causing some loss in the quantum efficiency, so a compromise is needed.
- Statistical fluctuations in the secondary electron multiplication.

In addition, the sensitivity to delayed photons may be limited by the formation of the after-pulses, that can occur up to several μ s after the main pulse. The photo-electrons may ionize any residual gases present inside the PMT bulb due to emanation from the dynodes. The positive ions are accelerated towards the cathode and produce further electrons when they strike. Then, these follow the electron multiplication chain, producing pulses at a delayed time with respect to the normal pulse.

3.1.3 The PMTs for Borexino.

For 1 MeV of deposited energy, 400 out of the total 2200 PMTs produce a signal, so the average number of photoelectrons per event per MeV is 0.18. So, according to the Poisson distribution, single photo-electron pulses are the most frequent,

with multiple p.e. pulses contributing only 10% of the total (excluding the pedestal).

In Borexino, the tail of the time distributions is used for alpha-beta discrimination, so a low fraction of after-pulses with respect to normal pulses is required. With 2.5 % after-pulsing, the ETL9351 PMT obeys this requirement.

Cathode diameter	19 cm
Cathode material	SbCsK
Peak quantum efficiency	32%
Gain	10^7
SER resolution σ_1/x_1	70 %
Peak-to-valley ratio	> 2.0
Transit time	15 ns
Transit time spread (jitter)	1 ns
Dark noise rate	1 kHz
After-pulses	2.5 %

Table 3.1 Properties of the ETL9351 photomultiplier.

3.2 System design

3.2.1 Requirements

In the design of the system to calibrate the time and charge response of the Borexino PMTs, the following requirements were taken into account:

- **Accuracy in time equalization.** The time spread due to inaccuracy of the inter-PMT equalization should not contribute to the time resolution of the Borexino detector more than the PMT jitter itself, which is 1 ns.
- **Accuracy in charge calibration.** The system must illuminate all 2200 PMTs at the single photoelectron level in order to measure the SER parameters of each PMT. If we require less than 1% contamination of the SER by multi-electron pulses, and by the dark noise random coincidences,

the illumination level should be, respectively, lower than $\mu=0.05$ p.e. and higher than $\mu=0.01$ p.e.

- **Linearity check.** The system must allow the use of higher illumination levels, in order to verify the linearity of the PMT response. The highest value is $\mu=8$ p.e., limited by the dynamic range of the electronics.
- **Acquisition rate.** In order to reduce the dead time of the experiment, the PMT calibration should be done at the fastest rate allowed by the DAQ system, 20 kHz at an illumination level of $\mu=0.05$ p.e., i.e., an average of 110 PMT hits per event.
- **Radiopurity.** Like all other detector components, the materials for the PMT calibration system should contribute as little as possible to the radioactive background. The requirement is a background level not higher than 1/10 of the PMT γ background.
- **Long-term reliability.** A useful lifetime of 10 years is required.
- **Operational convenience.** The system should allow a high level of automation, in order to facilitate its frequent use.

Requirement 1 calls for a fast light source and the choice was to use a diode laser. Requirements 2 and 3 call for a light transmission system that guarantees a low attenuation and a good uniformity of the illumination level to all PMTs.

Before adopting the definitive design for the light transmission system, several alternative methods were considered. The simplest solution would be a light diffuser in the center of the detector, illuminating simultaneously all PMTs but a permanent one would not be acceptable due its radioactivity, and a movable one would not allow the easiness of operation needed for frequent calibrations. These problems could in principle be solved by using several permanent light diffusers (as the system used in the LSND experiment [⁶⁹]) in the buffer region or light beams from optical fiber couplers in the Stainless Steel Sphere. Nevertheless a problem would remain: the light had to cross several meters in either just the buffer region or both the scintillator and buffer. The necessary geometrical

corrections to the light pulse arrival time would depend on the scintillator and diffuser material optical properties, such as index of refraction and attenuation length that can drift in time, thus compromising the accuracy of the calibration.

These considerations, and the experience gained with the PMT calibration system of the CTF detector, led to the definitive design, described in Section 3.2.3.

3.2.2 *The CTF experience*

The CTF detector, described in Section 2.3, is a prototype of Borexino, using 100 PMTs to collect the light produced in 4 tons of liquid scintillator. The system used to calibrate the CTF PMTs was based on a bundle of 100 quartz optical fibers coupled to each PMT. This system and its performance are presented shortly.

The fibers are illuminated by the light from a compact diode laser (Hamamatsu PLP-02) providing short pulses with a time width - 50 ps -, a wavelength of 410 nm, well matching the ETL9351 PMT quantum efficiency curve, and a peak power of 0.4 mW. The distribution of the laser beam to the 100 fibers was carried out using a divergent lens and a quartz light guide. The optical cables that went into the detector through a flange on top of the water tank consisted of the optical fiber itself, Kevlar strands for mechanical strength, all covered by a polyethylene coating. The fiber terminations were standard SMA connectors⁶ attached to the acrylic light concentrators, pointing towards each photocathode at a distance of 50 cm. The system provided more than enough light for the illumination of all PMTs. On the contrary, in order to reach the low level required for single photoelectron counting, attenuation filters had to be inserted in the optical path of the beam. The operation of the system allowed a frequent repetition of the calibration procedure, that was necessary for reasons of electronics stability.

The number of photomultipliers in Borexino is 20 times higher than in CTF, so the same method would not be applicable in a straightforward way. A CTF-like solution with a fiber for each PMT, all coupled to an external laser and entering the SSS in a single point, presents a major technical difficulty on the simultaneous

⁶ SMA connectors have threaded couplings, as opposed to ST connectors, another common standard for multimode fiber connections, where the coupling is made with a bayonet system.

coupling of a laser beam to 2200 fibers; furthermore the total mass of material, introduced by 2200 fibers of about 24 m each, would approach a level in which the radioactive contamination may be of concern.

3.2.3 Structure and components

The basic concept of the system is to distribute a fast light pulse to all the PMTs through the consecutive multiplexing of optical fiber bundles, as shown in Figure 3.3.

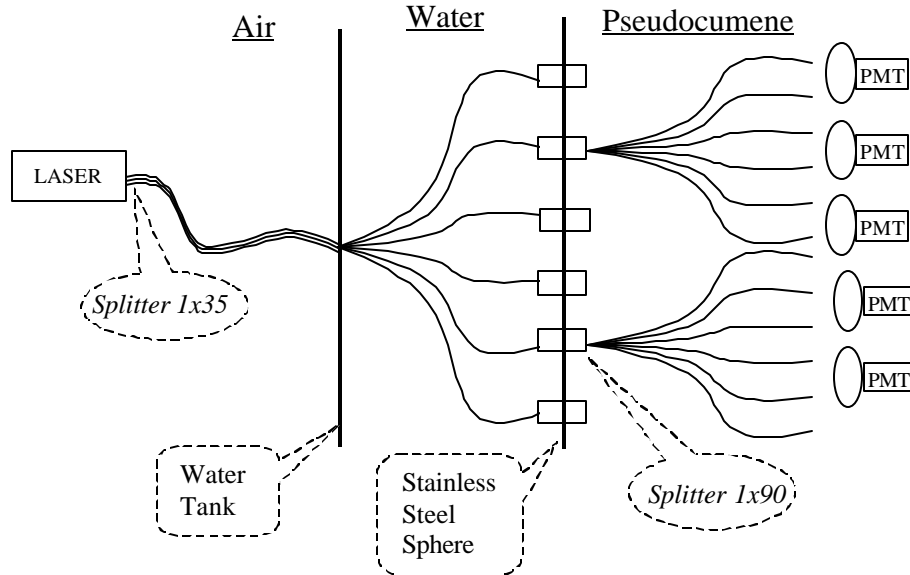


Figure 3.3 Scheme of the PMT calibration system for Borexino.

3.2.3.1 Light Source

The light source is a PicoQuant diode laser (Laser head model: LDH 400, Laser driver model: PDL 800-B, see [70] for more details) emitting a fast, 50 ps time width, light pulse at a wavelength of 394 nm, at which the photocathode quantum efficiency reaches 27 %. The maximum peak power is 400 mW, corresponding to 1.7×10^7 photons/pulse and the maximum repetition rate is 40 MHz. With these characteristics, we are able to take calibration data at the maximum rate allowed by the Borexino Data-Acquisition system.

The optical components associated with the coupling of the laser to the fiber bundle consist of a series of neutral density filters for attenuation and a lens that focuses the beam on the surface of a 2.5 mm diameter rigid quartz fiber, that distributes the light to the 35 fiber bundle. The lens is a 10x standard microscope lens. The focusing is necessary because the area of the laser spot (2×3.5 mm) is larger than the fiber core. The fiber is 10 cm long and its numerical aperture⁷ is lower than for the 35 fiber bundle, for a better optical transmission.

The light from this laser will also be used for the scintillator and buffer liquid monitoring system, that is described in the next Chapter. A splitting system was conceived in order to divert the laser beam towards a different set of fibers. The scheme for the optical assembly is illustrated in Figure 3.4.

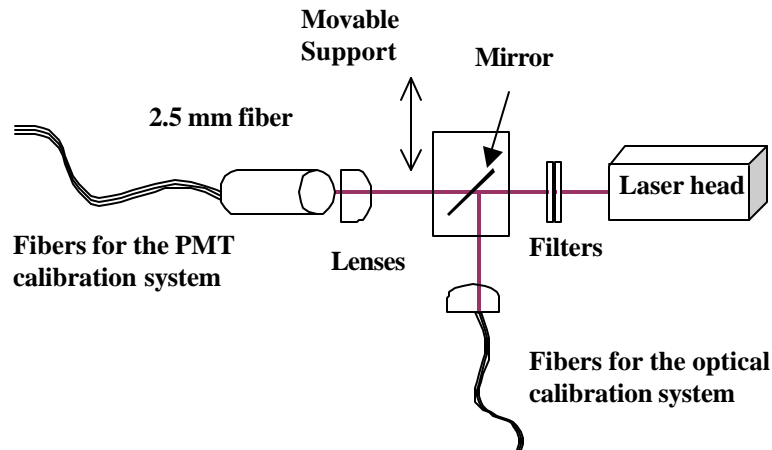


Figure 3.4 Laser and associated optics for fiber coupling.

The optical apparatus is mounted on a passive anti-vibration platform and enclosed by a light-proof stainless steel box. The laser head and the movable mirror support can be activated from outside the box.

3.2.3.2 External fibers

The laser beam illuminates the fiber bundle of the first splitting point through a focusing lens and an optical rod that makes it uniform and wide enough to cover

⁷ The sine of the aperture semi-angle of the light cone delivered by the fiber.

35 quartz fibers 40 m long. The diameters of the fiber core and cladding (layer of material with a lower index of refraction than the core, responsible for the total internal reflection that keeps the light inside the fiber) are, respectively, 300 μm and 325 μm . The fibers enter the detector through a single feed-through on top of the Water Tank mounted on an “organ pipe” flange. From that point, they form separate cables with Kevlar strands for mechanical resistance and a polyethylene coating, that go to their entry points on the SSS, chosen as the central position of each PMT cluster. There are 28 clusters of about 80 PMTs each, and, for mounting reasons, the PMTs mounted on the 3 m door require an extra fiber bundle, so there will be six spare external optical cables.

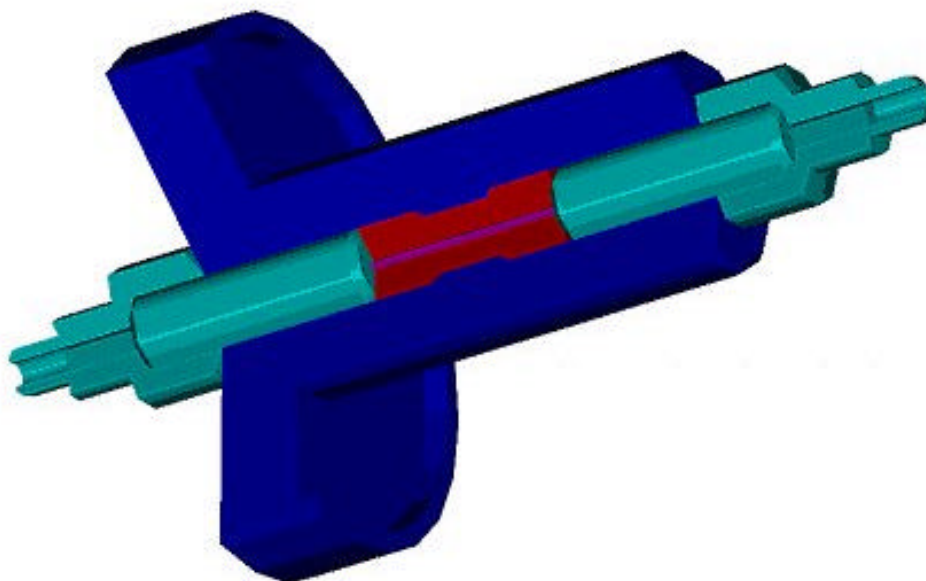


Figure 3.5 - Fiber feed-through for the SSS

3.2.3.3 Light-transmitting feedthrough

The most delicate part of the system is the feed-through on the Stainless Steel Sphere because it must split the light from 1 input to 90 output fibers as uniformly as possible, while maintaining a high level of tightness against liquid diffusion between both sides of the SSS. The feed-through and its internal components are illustrated in Figure 3.5. The technical drawing is included in the Appendix. The body and the connectors are made of electro-polished stainless steel; the sealing

with the stainless steel flange is accomplished through a Viton O-ring. The quartz fiber is 10 cm long, has a 1.5 mm diameter, and passes inside the connectors from the PC buffer to the water buffer side. The sealing against PC diffusion by capillarity near to the fiber is assured by filling the inner part of the feed-through with a PC-proof, quartz-steel adherent epoxy resin (shown in red).

3.2.3.4 Internal fibers

At this point the second step of the multiplexing chain is made by coupling the SSS feed-through to a bundle of 90 quartz fibers of 110 μm core diameter. A scheme of this coupling can be seen in Figure 3.6. Taking into account the packing ratio of circles on a plane $\left(\frac{P}{2\sqrt{3}} \cong 91\%\right)$, 90 closely packed fibers with a diameter of 120 μm (cladding) occupy an area of 1.12 mm^2 . The section of the 1.5 mm diameter fiber in the feed-through is 1.76 mm^2 , so a tolerance of 50% for a non-optimal packing of the fiber bundle is assured.

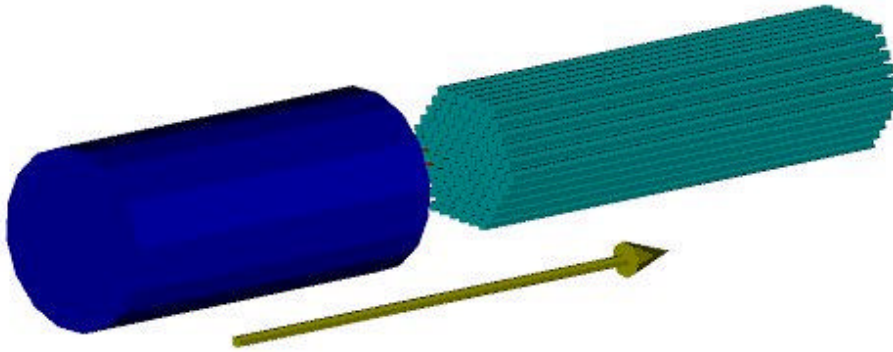


Figure 3.6 Optical coupling of the 90-fiber bundle.

Both internal and external fibers, as well as the lens and clad rod used at the beginning of the optical path, have a quartz core in order to optimize the light transmission efficiency in the ultraviolet wavelength region. While the cladding of the external fibers can be made of plastic, the strong chemical reactivity of Pseudocumene determines the choice of quartz for the cladding of the internal

fibers. This is one of the reasons for using Teflon (and not polyethylene) for the coating of the internal cable. The other is that measurements, done in the collaboration, show that Teflon has a very low rate of Radon emanation. The end-tip of the fiber is inserted in a metal cylinder to facilitate its polishing. A Teflon support (shown in Figure 3.7), attached to the light concentrator, points the fiber termination in the direction of the photocathode, at a distance of 20 cm. For the internal muon veto PMTs, that do not have light concentrators, the fiber support is attached to a steel bracket that keeps the fiber tip at the same distance from the photocathode as for all the other PMTs.

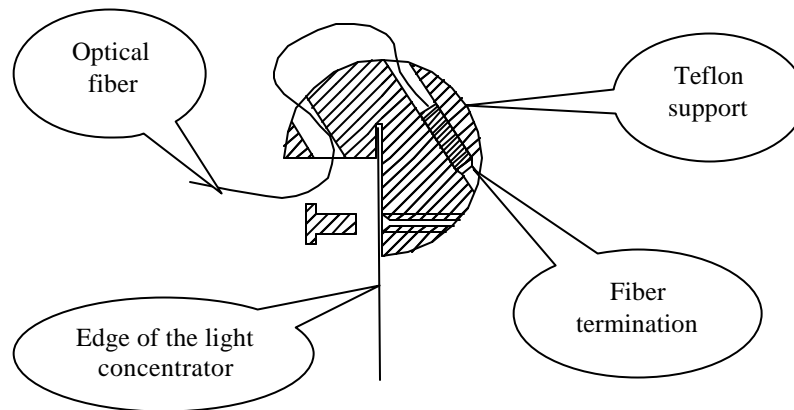


Figure 3.7 Support for PMT calibration fiber.

3.3 Preliminary feasibility tests

3.3.1 *Light transmission in the fiber multiplexing chain*

A prototype of the light transmission chain was built, having the goal of measuring the light attenuation that can be realistically expected from a system based on the consecutive multiplexing of optical fiber bundles. It is made of a smaller number of shorter fibers, but it is based on the same structure of the general system:

1. Quartz fiber of 1 mm core diameter, 40 cm length and 0.35 numerical aperture. It served to enlarge the light beam so that it can illuminate the fiber bundle that follows.
2. Multiplexing bundle with 5 quartz-plastic (core-cladding) fibers. All five fibers had different core diameters and lengths: (\varnothing 600 μm , 2 m); (\varnothing 300 μm , 1 m); (\varnothing 300 μm , 5 m); (\varnothing 200 μm , 1 m); (\varnothing 200 μm , 5 m).
3. Stainless steel feed-through with 1 mm quartz fiber inside.
4. Multiplexing bundle with 3 fibers of 110 μm core diameter and 3.5 m length.

The light transmission of the fibers multiplexing chain is the fraction of the input light intensity that arrives to one termination.

.

The transmission of the single parts and of the whole chain was measured with a white lamp as light source and a photodiode-based power meter as light detector. The connections between the light source, the fibers and the power meter were done through standard SMA couplings.

Since the operating wavelength for the definitive system is 394 nm, in order to check the validity of the attenuation measurements in the right wavelength region, we repeated the measurement of part 2 with a Hammamatsu PLP-02 diode laser as the light source emitting at 410 nm and an ETL9351 PMT as light detector.

3.3.1.1 Results

The transmission results are presented as the ratio of light power detected at the output of each part of the chain with respect to the output of the preceding one. Since we did not have the final laser and associated optics, we could not measure the transmission of Part 1. The transmission measurements of part 2, that is, the 5-fiber splitter, are shown in Table 3.2. We quote an average transmission for the \varnothing 200 μm fibers. They have very close transmission values so no conclusion can be drawn on length-dependent attenuation.

Fiber	Lamp/Photodiode	Laser/PMT
Ø 600 µm	24±1 %	23±1.5 %
Ø 300 µm	7.9±0.7%	6.5±0.9 %
Ø 200 µm	3.5±0.5 %	2.6±0.7 %

Table 3.2 Transmission of the 5-fiber splitter prototype (part2) measured both with lamp/photodiode and laser/PMT.

The differences between the values measured with lamp/photodiode and with the PMT/laser are compatible within the errors. If we consider the measurement with the largest uncertainty (200 µm fiber), we can give an upper limit of 20 % for the difference between the attenuation of white light and the attenuation of 410 nm light in short fibers (< 5 m). Measured only with lamp/photodiode, the transmission of the feed-through (Part 3) is 75 ± 3 (%), and the transmission of the 3 fibers of the last splitter in the chain (Part 4) is 1 ± 0.3 (%).

3.3.1.2 Implications for Borexino

The main factor contributing to the transmission T of the whole chain is expected to be purely a geometrical efficiency, i.e., the area ratio of the fibers in the multiplexing junctions, but we take into account also the losses due to imperfect couplings and attenuation in the fiber material. We can write T as the product of the transmission of each individual part in the chain T_1, \dots, T_4 :

$$T = T_1 T_2 T_3 T_4 \quad \text{Eq. 3.5}$$

The 1 mm fiber in the feed-through has a larger diameter than any fiber in Part 2, so there are no geometrical losses, and we can simply have $T_3 = 75\%$. T_1 was not measured, but we will assume $T_1 \sim T_3$. In Part 2 we consider only the 300 mm diameter fiber, the same as in the definitive design for Borexino.

For Parts 2 and 4 (the multiplexing bundles), we separate the geometrical efficiency from the transmission factor L due to other losses:

$$T_2 = \left(\frac{D_2}{D_1} \right)^2 L_2 \quad T_4 = \left(\frac{D_4}{D_3} \right)^2 L_4 \quad \text{Eq. 3. 6}$$

where D_i , with $i=1, \dots, 4$ are the fiber core diameters.

Since we have $D_1 = D_3 = 1 \text{ mm}$, $D_2 = 0.3 \text{ mm}$, $D_4 = 0.11 \text{ mm}$, and $T_2 = 6.5 \%$, $T_4 = 1 \%$, we obtain $L_2 = 72 \%$ and $L_4 = 83 \%$.

In Borexino, the diameters of the optical rods that stand immediately before the splitters (Parts 1 and 3) are larger in order to accommodate a higher number of fibers, so $D_1 = 2.5 \text{ mm}$ and $D_3 = 1.5 \text{ mm}$. Even with a 2.5 mm diameter fiber, it would not be possible to illuminate 35 fibers with a $600 \text{ }\mu\text{m}$ diameter. So, for Borexino we chose the 300 mm fiber for Part 2. Using Eq. 3. 6, we can estimate the values for T_2 and T_4 :

- $T_2 = 1.0 \%$
- $T_4 = 0.45 \%$,

Assuming the coupling losses in the definitive Parts 1 and 3 are the same as measured with the 1 mm fiber, we can now estimate T for the definitive system:

$$T \approx 2 \times 10^{-5} \quad \text{Eq. 3. 7}$$

This number can be used to estimate the average light intensity expected at the end of the chain. The number of photons emitted in each laser pulse is given by

$$N_{ph} = \frac{P \times \Delta t \times I}{hc} \cong 5 \times P(mW) \times \Delta t(ps) \times I(nm) \quad \text{Eq. 3.8}$$

where P is the laser power, Δt the pulse width and λ the wavelength. Replacing the numerical values for the Hamamatsu PLP-02 laser ($P=0.4 \text{ mW}$, $\Delta t=(40 \text{ ps})/2$, $\lambda=410 \sim \text{nm}$), in which we assume the shape of the time pulse to be triangular, we have $N_{ph}=16400$ photons per pulse. If we now use the value of T and take into account the PMT quantum efficiency of 25% , the illumination level provided by

the system coupled to the Hamamatsu laser is expected to be equivalent to $\mu = 0.08$, or 8 % photoelectrons (p.e.) per pulse.

Even if the transmission in the laser/fiber coupling would be smaller than the assumed value of 75 %, we can reasonably expect to provide light above the limit of 1 % p.e., as required for the measurement of the single electron response. However, the study of the PMT response at higher illumination levels, in order to verify the charge linearity, would not be possible. This led us to use a new laser for Borexino, to replace the Hamamatsu PLP-02. The definitive laser, already referred to in Subsection 3.2.3.1, has a wavelength of 394 nm, a pulse width of 50 ps, and a high peak power of 400 mW. So, for normal SER calibration, we will use the laser at a fraction of its power, but there will be also the possibility of calibrating the PMTs in the whole dynamic range of the electronics, up to 8 p.e.

3.3.2 Compliance of the materials with the standards of the experiment

During the design phase, several tests were performed to guarantee the compliance of the system with the general requirements of the experiment in terms of radiopurity and chemical compatibility. The radioactivity of the fibers, Kevlar, Teflon and the epoxy resin were measured using gamma spectroscopy, and the results are shown in Table 3.3.

	^{238}U (g/g)	^{232}Th (g/g)	nat-K
Quartz fibers	$(4.1 \pm 0.2) \cdot 10^{-8}$	$(4.1 \pm 0.2) \cdot 10^{-8}$	$(4.0 \pm 0.2) \cdot 10^{-5}$
Kevlar	$(3.5 \pm 0.6) \cdot 10^{-8}$	$< 3.4 \cdot 10^{-8}$	$< 2.8 \cdot 10^{-5}$
Teflon	$(2.3 \pm 0.3) \cdot 10^{-9}$	$< 1.4 \cdot 10^{-9}$	$< 2 \cdot 10^{-6}$
PMT glass	$(6.6 \pm 1.9) \cdot 10^{-8}$	$(3.2 \pm 0.3) \cdot 10^{-8}$	$(1.6 \pm 0.4) \cdot 10^{-5}$

Table 3.3 Radioactivity of the materials used in the optical fiber cable, compared to the PMT glass. Data from [71].

The radioactivity levels of the fiber material are comparable or lower than the values for the PMT glass. Since the fibers have a much lower total mass (50 g) than the PMTs, the external background we expect from them is negligible.

The high chemical reactivity of Pseudocumene can have two kinds of consequences: damage to the materials it is in contact with and formation of optical impurities that decrease the buffer liquid attenuation length (untreated mu-metal and some kinds of steel were found to cause this effect). All the materials for the internal optical cable have passed the accelerated ageing tests immersed in Pseudocumene and no effect on the Pseudocumene transparency was detected [⁷²]. Moreover, in Borexino, the surface-to-volume ratio of the materials is much smaller than in the test samples so, any possible effect is expected to be further reduced.

The Helium leak rate was measured at the level of 10^{-9} mbar l s^{-1} , three orders of magnitude better than the general requirement for the Stainless Steel Sphere

3.4 Complete prototype test

The second prototype of the fiber chain reproduces exactly the full-scale system, both in terms of type and length of the fibers and materials for the cable and feed-through, and was installed in the Two-Liquid Test Tank, an operating environment as close as possible to Borexino.

3.4.1 *The Two-Liquid Test Tank*

The Two-Liquid Test Tank (TLTT) consists of two concentric cylindrical tanks with, respectively, 2.7 m and 3.7 m diameter and 1.3 m height. The inner tank is filled with 7 tons of pseudocumene and the outer region with 6 tons of ultra-pure water. Photomultipliers, complete with mu-metal shielding and fiber optics supports, are mounted in 49 of the 54 holes of the inner wall, with the body of the PMT immersed in Pseudocumene and the connector and cable inside water. The remaining five holes are used for the feedthroughs of the two fiber systems prototypes: three for the PMT calibration and two for the PC transparency monitoring (next Chapter). A scheme of the TLTT is shown in Figure 3.8.

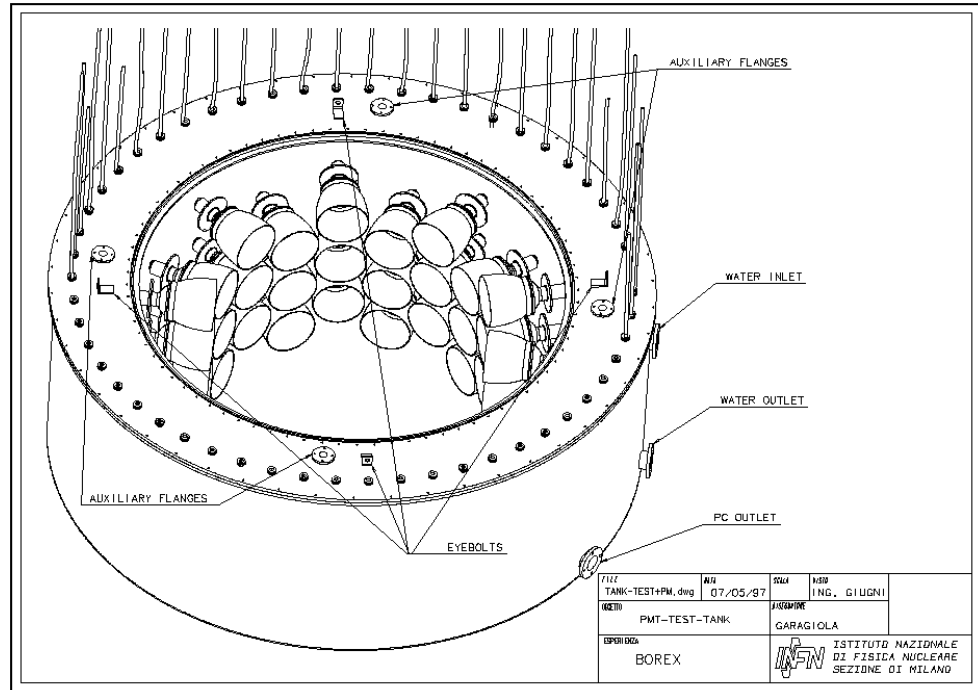


Figure 3.8 Scheme of the Two-Liquid Test Tank

The main goal of the TLTT was to test the performance of a significant number of PMTs in realistic environmental conditions, *i.e.*, immersed in pseudocumene, with the cable and connector in water. The most important technical aspect of the PMT construction under study with this test was the sealing and its resistance to the chemical aggression of pseudocumene over large periods of time.

Due to its large scale and working conditions similar to those of Borexino, the TLTT naturally became a facility to test other aspects of the Borexino design, in particular, the calibration systems using optical fibers. In addition to the system for PMT calibration, a prototype of the PC transparency monitoring system was also installed and tested in the TLTT (see Chapter 5).

The TLTT is made of stainless steel and its surface was treated with pickling and passivation, like the Borexino Stainless Steel Sphere (SSS). Although not in a clean-room environment, the PMTs, the fibers and the tank surface were carefully cleaned before the filling, which was done with a constant nitrogen blanket.

3.4.2 The fiber system

Following the structure and design principles of the general Borexino PMT calibration system, the tests in the Two-Liquid Test Tank make use of a laser, its associated optics and a two-stage multiplex optical fiber distribution system. The laser and the first stage of the optical fiber system are shown in Figure 3.9 a) and Figure 3.9 b).

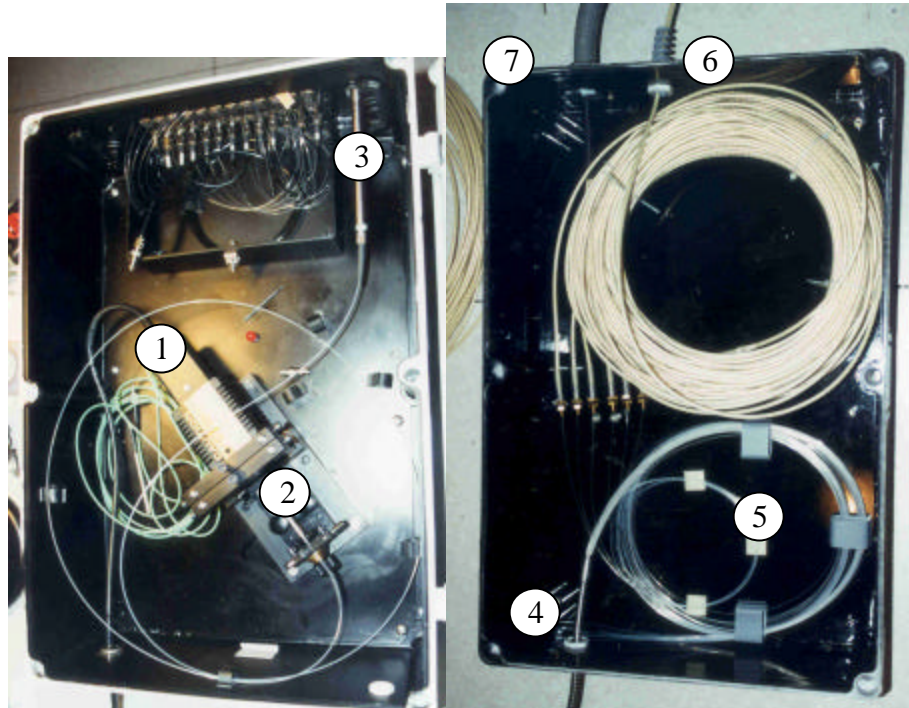


Figure 3.9 a) Laser and associated optics in light-proof box; b) First stage of optical fiber multiplex distribution system. 1-Laser; 2-Filters and lens; 3-GRIN rod; 4-Entry point of the 35 fiber bundle; 5-29 short fibers; 6-4 long fibers going into the TLTT; 7-2 long fibers staying in the counting room.

The laser (1) is a Hamamatsu PLP-02 diode laser emitting at 410 nm with a peak power of 0.4 mW and a pulse width of 50 ps. At 410 nm, the photocathode quantum efficiency of the ETL9351 PMT is high, about 25 %. Since the PMTs have a transit time jitter of 1 ns, the pulse width of the laser is quite sufficiently narrow for its calibration. From the results of the preliminary prototype tests, a peak power of 0.4 nW is expected to supply enough light at the end of the fiber chain (previous section). If the laser power was too high in order to reach the single photoelectron illumination level, after the laser, two filters (2) can be used

to reduce the beam intensity. A 10x microscope type lens is then used to focus the beam on the surface of a 600 μm fiber that can be connected to a graded refraction index - GRIN - rod that acts as a lens, creating a wide, uniform beam to illuminate the next fiber bundle. The rod has a diameter of 2.5 mm and a length of 10 cm and can be seen in Figure 3.9 a) with number 3. Alternatively, the 600 μm fiber may be connected to another fiber distribution system going into a dark room for PMT tests, that can be seen on the left of the GRIN rod.

Following the fiber multiplexing concept illustrated in Figure 3.6, a bundle of 35 fibers with 300 μm core is connected to the GRIN rod. In order to keep the light-tightness of the system, the first 1m segment of the 35 fiber bundle is protected by metallic tubing entering a light-proof box through point (4). For the purpose of illuminating the 49 PMTs in the TLTT, we use only three fibers out of the 35 fiber bundle. In order to test the light transmission efficiency and uniformity of the 1 to 35 fiber splitting it is not necessary that the fibers have the whole length of the full-scale system (40 m), so 29 fibers in this bundle are short (1.5 m) and bare, that is, without any cabling and connector. The 29 bare fibers are kept inside the box (5). Two additional fibers have the full-scale length, a lightproof cabling and a standard SMA connector, but do not go into the Tank, allowing us to test the whole fiber chain independently of the TLTT measurements. A single cable containing four fibers (one of them is spare), leaves the box through point (7) and enters the TLTT through one of the PMT ports (which can be seen in Figure 3.8, with cables coming out), using a feed-through built with the same design as the full-scale system. Inside the water buffer region, the four fibers are cabled independently with a polyethylene coating.

Three stainless steel feed-throughs following the design illustrated in Figure 3.5 and shown in detail in the Appendix are mounted in the internal wall of the TLTT, separating the water buffer region from the Pseudocumene region. Each one is coupled to a 300 μm fiber on the outside and to a bundle of 110 μm fibers on the inside.



Figure 3.10 The TLTT just before filling.

The water-PC sealing is implemented with a stainless steel gasket (O-ring) between the wall flange and the feed-through, like in the original sealing design for the PMTs. Grounding problems led to a change in the design and the use of Viton gaskets in the PMT sealing. Of course the problem does not exist for the optical fiber feed-throughs, but, for simplicity and uniformity of installation, the full-scale system calibration feed-throughs will also be sealed with Viton gaskets. Four fiber bundles were built according to the full-scale design, both in terms of fiber type (110 μm core diameter, quartz core, quartz cladding, teftzel buffer), cabling (Kevlar, Teflon), terminations and length (6 m). The three bundles with 28 fibers each were installed in the TLTT and the last one, having 90 fibers (as in full-scale), completed the full fiber chain that remained available for tests outside the tank. The fibers inside the TLTT were pointed to the photocathode of each PMT using an earlier version of the fiber support shown in Figure 3.7.

The photo in Figure 3.10 presents a general view of the inner part of the TLTT. On the second column from the right can be seen one of the PMT calibration feed-throughs, and one of the 30 fiber bundles. The PMTs were mounted without the light concentrators – the cones around them are the mu-metal magnetic field shield – so the fiber supports were mounted on stainless steel brackets.

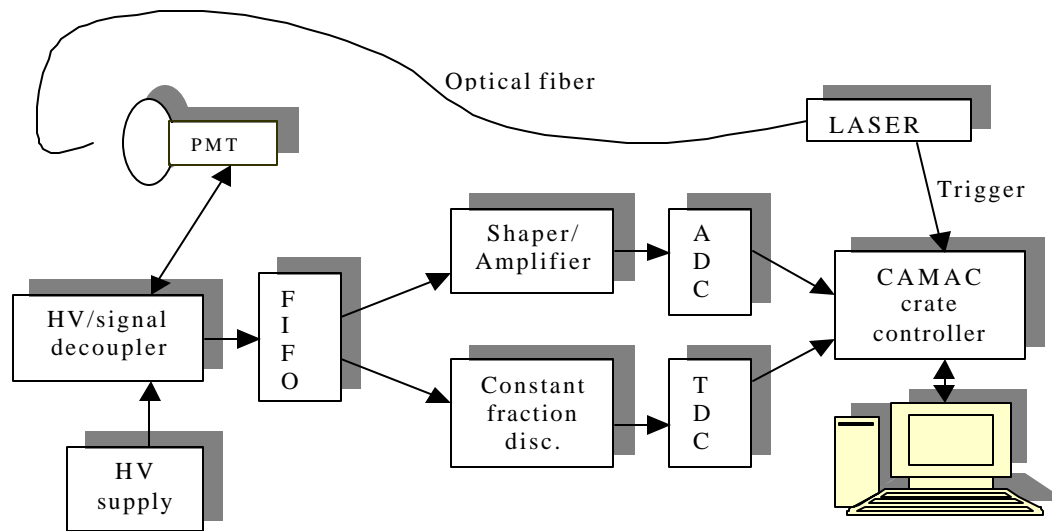


Figure 3.11 Scheme of the electronics and DAQ of the TLTT

Each bundle covered a region with 16 PMTs, so 3×12 fibers were spare. In order to eliminate the contribution from the light carried by these fibers, their termination was inserted in holes drilled on the surface of the feed-through, and fixed with small Viton O-rings.

3.4.3 Electronics and DAQ

For this test, only minor adjustments were done to the existing Electronics and Data Acquisition (DAQ) setup used regularly by the PMT working group. The logical scheme of the setup is shown in Figure 3.11. The PMT is connected to the front-end electronics through a single cable carrying both the signal and the high voltage, so the first module is a capacitive decoupler. Two 24 channels power supplies were used, so one of the 49 installed PMTs was off. Not enough digital channels were available, so the 48 PMTs were divided in two groups with 24 PMTs each. The DAQ program allowed the alternative data-taking of both groups in succession without changing the wiring. Additional time delay was introduced in the laser trigger line due to the longer fiber length. The existing DAQ program stored the data exclusively as a series of 48 histograms - one for the ADC and one for the TDC for each PMT - losing any correlation between the time and charge signal. The program was modified to write the data on a matrix (ntuple) with 2×24

columns and one row per event, in order to do a more complete analysis, on an event-by-event basis. Each event corresponds to a laser pulse in which at least one PMT gave signal. Since ntuples occupy more space than histograms, the data corresponding to a run was stored in cd-rom format.

3.4.4 Data analysis

The goals of the data analysis of the TLTT are to obtain the charge and time calibration parameters for all the PMTs. The time calibration parameters consist on the time differences between the responses of all the PMTs to a common and simultaneous light pulse. In order to have a common time reference for all the PMTs, the data must always be corrected according to these time shifts. Since there is a slight correlation between the charge and the PMT pulse rise time, an accurate time calibration should be done at the typical illumination level of the experiment. For Borexino, this is the single photoelectron level.

The charge calibration consists in finding the conversion factor between the measured ADC channel number and the number of photoelectrons detected. The mean (or centroid, if we fit it) of the SER peak is the calibration parameter. It is obtained by illuminating the PMT with a very weak light source, so that the SER peak is clearly dominant with respect to the multi-photoelectron peaks in the ADC spectrum. The requirement (see Section 3.2.1) is an illumination level between 1 % p.e. and 5 % p.e., in order to reduce the contribution of dark noise and multi-electron pulses to less than 1 %.

3.4.4.1 Time Calibration

The correspondence between time and the TDC channel number is 20.48 channels/ns since the TDC has 2048 channels and is set for a range of a 100 ns. The analysis code of the calibration data of the TLTT was written in C++ and uses the routines and the environment of the CERN-developed ROOT analysis software package. The program allows a semi-automatic procedure for the histogram fits and the calibration parameter extraction.

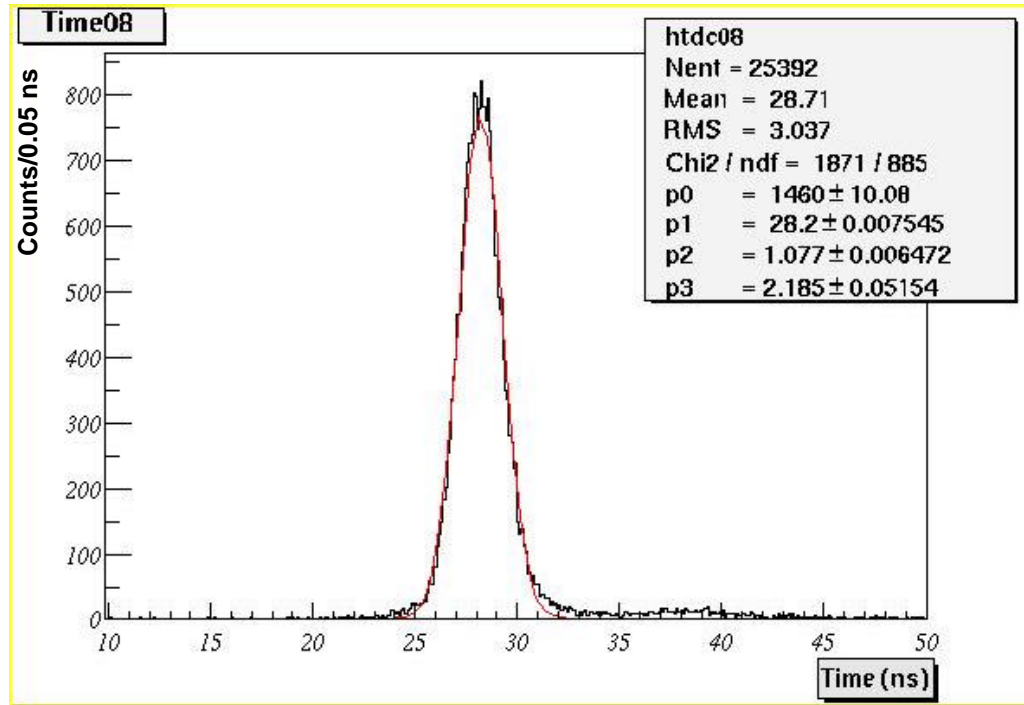


Figure 3.12 Typical time distribution for the PMTs illuminated with the calibration system. The smooth curve is the result of a gaussian fit to the data.

Figure 3.12 shows a typical time distribution histogram obtained from a data ntuple; the region below 10 ns is not shown in order to eliminate the large peak in the channels near zero due to laser triggers that did not cause any TDC signal. The region between 50-100ns contains only constant background at the level of a few counts per bin. All the channels show a similar behaviour: a sharp central peak, a constant, low background, uncorrelated with the laser trigger and a much smaller peak at about 10 ns from the first one. Since the speed of light in Pseudocumene is 20 cm/ns, the diameter of the TLTT is 2.7 m and the length of a PMT is 35 cm, this second peak is interpreted as resulting from reflections of the light coming from the fiber of the opposite PMT on its glass window. This last peak is well separated and with a much lower intensity so this phenomenon does not interfere with the calibration.

The time histograms of all channels were fit with the sum of a gaussian and a constant to take into account the background, using the same starting values for the fit parameters. The procedure was semi-automatic in the sense that, when the

convergence failed, the starting values of the minimization parameters were changed individually to more suitable values.

The result for each data run was a calibration table with the mean values and the standard deviations (hereafter called time resolution) of the time distributions of all channels. These are shown in the histograms of Figure 3.13 for a typical calibration run.

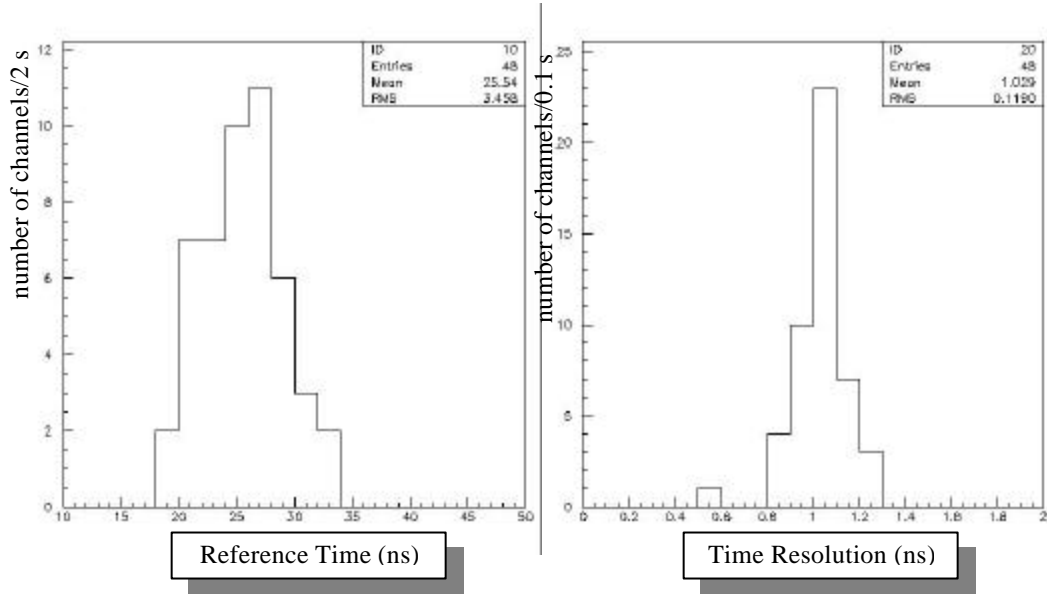


Figure 3.13 (a) Reference time distribution of all channels before equalization. (b) Time resolution.

From the reference time distribution, it can be seen that, before equalization, the systematic error on the time measurement can be up to 15 ns. The time resolution is about 1 ns for all channels, the same as the nominal time jitter of the PMTs, which means that the time spread due to the laser and fibers system is negligible, as expected. Since the statistical error on the reference time determination can be as low as desired and, conservatively assuming a low precision of 1 cm on the fiber length differences, the maximum systematic error is 0.05 ns. So, after equalization, the time measurement accuracy is dominated by the single-channel resolution, or PMT time jitter of 1 ns.

3.4.4.2 Charge calibration

A typical charge spectrum from a calibration run is shown in Figure 3.14, where the bins below channel 50 are not shown because of the very high number of counts in the pedestal, the spectral region corresponding to the low charge pulses from dynode background.

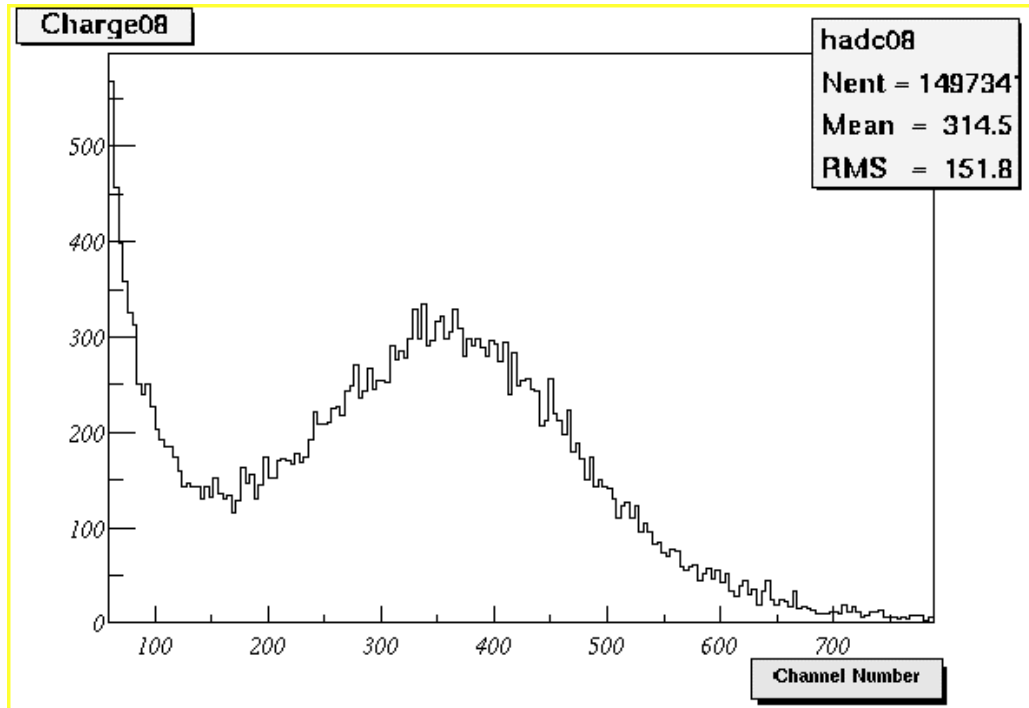


Figure 3.14 Typical single photoelectron charge spectrum of a PMT illuminated with the calibration system.

In order to estimate the value of μ , the illumination level, most methods require a precise estimation of the number of counts in the pedestal and a global fit of the charge spectrum with an adequate function. In order to simplify the automated analysis of a large number of channels, an alternative method was used in the TLTT, allowing for a simultaneously simple and precise calculation of μ .

Using the Poisson distribution, (see Eq. 3.2) we can write:

$$m = \ln \left(\frac{1}{1 - P(n \geq 1)} \right) \quad \text{Eq. 3.9}$$

where $P(n=1)$ is the probability of having at least one p.e. emitted from the photocathode. The total number of light pulses was precisely determined because

the DAQ system added a count to a single bin in the long-range TDC histogram for every laser trigger so,

$$P(n \geq 1) = \frac{\text{Counts above the pedestal}}{\text{Total laser triggers}} \quad \text{Eq. 3.10}$$

To eliminate the pedestal from the analysis, instead of a threshold cut on the charge spectrum, we selected the events lying in the time spectrum peak. Figure 3.15 shows the charge spectrum of the events for which the time measurement lies within three standard deviations of the peak centroid.

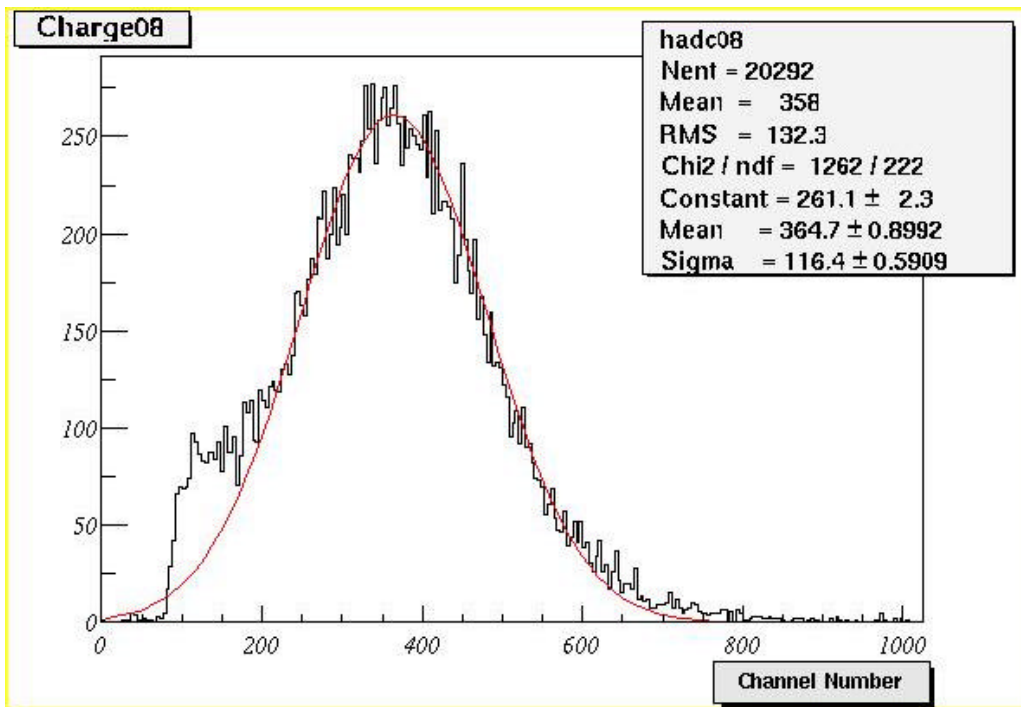


Figure 3.15 PMT charge spectrum after selection of the laser events. The red curve is the result of a gaussian fit to the data.

Using this method, μ was calculated for every channel and the average result was 1.5 %. It is a low illumination level, but still within the region required for the SER calibration. There is a reasonable agreement between this average value and what we expected from the preliminary prototype tests, that was an illumination level higher than 1 % with a maximum of 8 %.

At this point, the charge calibration parameter, *i.e.*, the average channel number for one photoelectron signal was calculated for all channels with a simple gaussian fit, since we have eliminated the pedestal and the contribution from pulses with a more than one photoelectron was negligible.

3.5 Comissioning of the final system

The production and commissioning of the final system for Borexino, now installed and ready for operation in Borexino, were organized in the following way. All stainless steel and Teflon parts were produced by Avimatic, a precision mechanics company, according to the Milano technical drawings (see Appendix). Fiberlan, a company specialized in optical fiber systems, contributed to the system design and carried out the fiber mounting for all the feed-throughs and bundles, as well as the installation of the laser distribution box. We carried out the quality control of the system, its cleaning and installation, as well as the final commissioning tests.

3.5.1 *Quality control of the feed-throughs*

The quality control of the 29 feed-throughs includes leak-checking and optical tests.

All feed-throughs were leak-checked before and after the installation on the SSS. The first leak-check was done with helium and the second one with argon, because the PMT glass sealing is permeable to helium. The helium leak rate of all the installed feed-throughs was better or equal than 4×10^{-9} mbar $l\ s^{-1}$ (sensitivity limit), while the requirement is 1×10^{-6} mbar $l\ s^{-1}$.

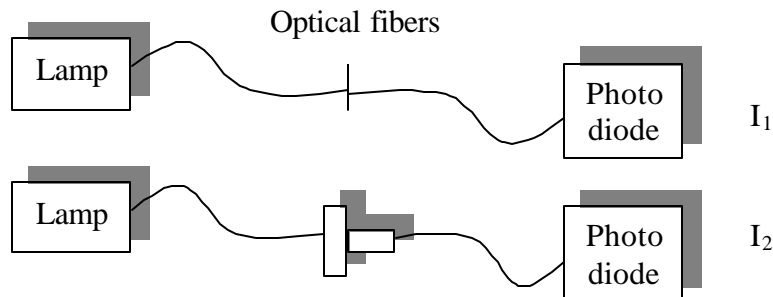


Figure 3.16 Measurement of the light transmittance of the feed-throughs.

The optical transmittance of the feed-throughs was measured with a white lamp and a photodiode, according to the setup shown in Figure 3.16. The core of both the input (from the lamp) and the output (to the photodiode) fibers have 1.5 mm diameter, just like the fiber mounted on the feed-through, so there is no geometrical loss. The losses can be due to the gap in the coupling and some numerical aperture losses. Bulk attenuation in quartz is unlikely, due to the small length. The average transmittance is $77 \pm 4 \%$.

3.5.2 *Quality control of the fiber bundles*

Figure 3.17 shows a photo of a feed-through and of an illuminated 90 fiber bundle. Every fiber was checked for light transmission with a lamp and a photodiode, using the same setup used for the feed-throughs and shown in Figure 3.16. This measurement is used to reject broken or partially damaged fibers and to select the best 80 fibers of each bundle. Only these will be actually used, since we have 10 spare fibers per each 90 fiber bundle.

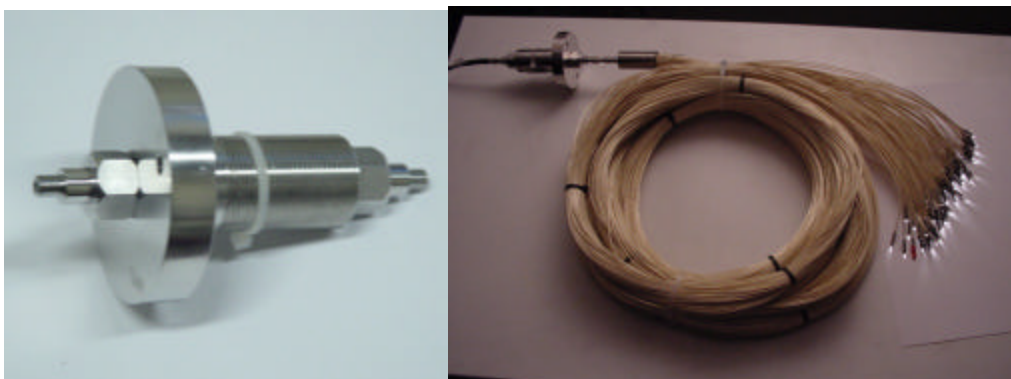


Figure 3.17 Feed-through and optical fiber bundle for PMT calibration.

Since the laser is powerful enough and will have to be filtered, the average transmission of the fiber chain is not a huge concern. However, since we require all PMTs to be illuminated at the single photoelectron level, a good uniformity is required. The absolute illumination level can be adjusted with neutral filters on the laser beam path, but nevertheless we require that all PMTs should be illuminated

with a light intensity between 1 % p.e. and 5 % p.e., so the transmission of the worst fibers should not be lower than a fifth of that for the best channels.

This was the criterion for rejecting damaged fibers, and their number was always below 10, the number of spares.

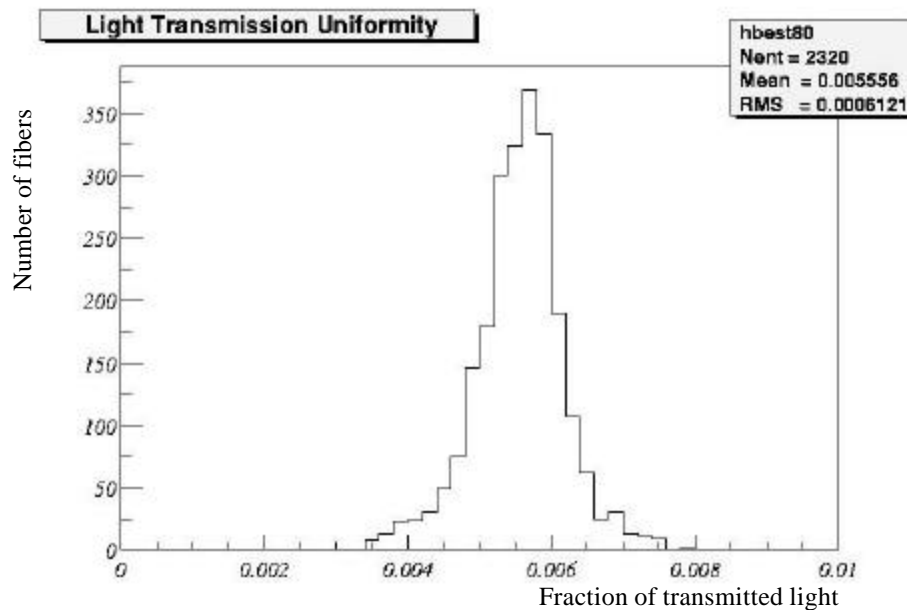


Figure 3.18 Distribution of the fraction of transmitted light by each fiber, with respect to the intensity of the light incident on the feed-through. Only the best 80 fibers (out of 90) of each bundle are taken into account.

Figure 3.18 shows a plot of the light transmission of the best 80 fibers of each bundle. The average is 5.5×10^{-3} and the standard deviation is 12 %. The sole geometrical efficiency for the light transmission is 5.9×10^{-3} , so the fiber coupling originates a small loss. The uniformity is also good, and the ratio between the transmission of the worst and best channels is about 0.5, safely above the requirement of 0.2.

3.5.3 Cleanliness

The fiber cleaning procedure consisted in 2 steps: immersion in purified water and hand-cleaning with isopropyl alcohol. The immersion in ultra-pure water from the Borexino water purification system served as a rough pre-cleaning in which essentially small particles and dust were eliminated. After that, the fibers were cleaned one-by-one, with clean-room tissues embedded with isopropyl alcohol, in

order to eliminate grease residues from hand contact. The chemical compatibility of isopropyl alcohol with Pseudocumene was checked by our collaborators at the University of Perugia. A photo of the cleaning procedure is shown in Figure 3.19. All the work was done in a class 100 clean-room environment and the fibers were spreaded in large tables in order to minimize the mechanical stress.



Figure 3.19 Cleaning two optical fiber bundles in the Borexino underground clean-room facilities.

The cleanliness level was checked by measuring with a microscope the dust content of ultra-pure water that was put in contact with $1/6$ of the surface of a fiber bundle. The cleanliness level of the fibers surface was found to be within the Borexino standards at the same level of the PMTs.

3.5.4 Installation

The items that compose the PMT calibration system must be installed in three different regions of the detector. The optical feed-throughs and internal fibers are located inside the Stainless Steel Sphere; the external fibers, inside the Water

Tank; and the laser box, outside the Water Tank, near the external flange from where the external fibers come out.

The priority was given to the installation of the feed-throughs and internal fibers in order to follow the schedule of the PMT installation, and also because this is the most time-consuming operation. Figure 3.20 shows the inside of the Borexino detector during the internal fibers installation.

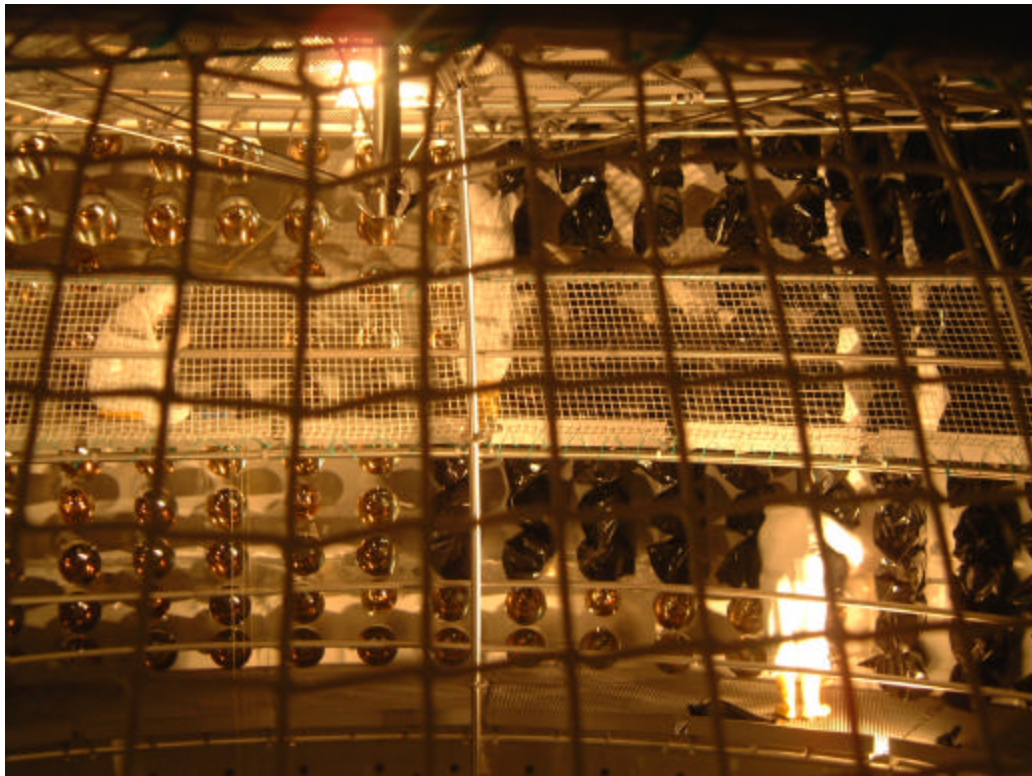


Figure 3.20 Installation of the fiber bundles on clusters 3 and 4 on the upper hemisphere. The center of cluster 4, from where the fibers are distributed, can be seen on the upper left corner of the photo.

On the upper left quadrant of the figure, it is visible the center of a fiber bundle, from where the fibers come out radially in order to reach all the 80 PMTs of each cluster. In order to maintain as much as possible the cleanliness of the detector, for the whole period of installations inside the SSS, each PMT is covered with a plastic bag. During the fiber installation, the bag was temporarily removed just for the minimum amount of time necessary.

Special care was employed for handling the fibers, but inevitable mechanical stresses during the installation of the bundle in the detector can cause some fibers to break. Since the Teflon coating is transparent, when the fiber is illuminated the damage is clearly visible because light comes out from the breaking point. This allowed us to use a lamp to permanently monitor each fiber during the installation and substitute any broken fibers. On average, one fiber per bundle was broken during the installation. The broken and spare fibers were collected in a single bundle and their light emission was suppressed by inserting their termination in a drilled Teflon plate. All the fibers were re-checked after the installation, and special care was taken to avoid tight curvatures of the fiber, with radius below 1 cm, in order to assure that the transmission properties measured in the quality control phases are valid for the start of the data-taking.

The laser and all its associated optical components were mounted in the anti-vibration platform inside the light-proof box, according to the design described in Subsection 3.2.3.1. A photo of the system is shown in Figure 3.21. On the center of the platform we can see the mirror on its movable support, activated by the automatic driver shown on center-top. The rod in the left is the 2.5 mm fiber that will illuminate the 35 fiber bundle (not shown). Next to it there is a focusing lens and filter supports. On the bottom of the figure we have the three fibers for the optical calibration system and the respective coupling lens. Finally, on the right, there are two laser heads. On top, the Picoquant laser that will be used in the normal operation of the system. In the center, there is a He-Ne laser that was used for the preliminary alignment adjustments instead of the definitive laser because it emits visible light. After the final installation of the laser box on top of the Borexino Water Tank in the Gran Sasso laboratory, the last alignment will be done with the Picoquant laser in position and with a photodiode for light detection. As soon as the external fibers are installed, the system is ready for data-taking.

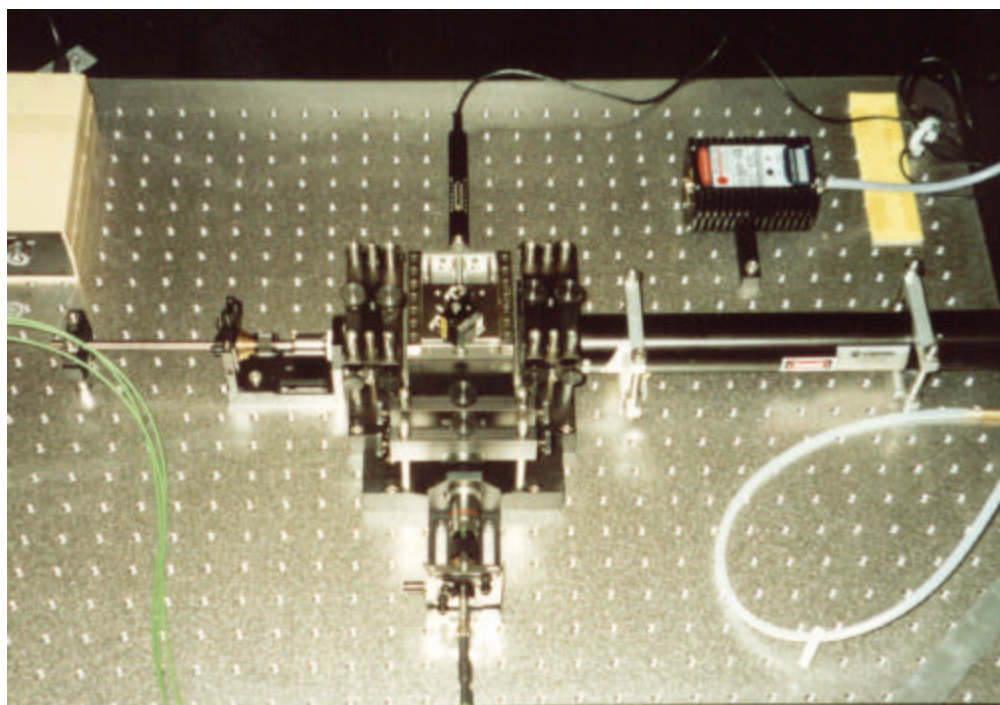


Figure 3.21 Laser and associated optical components mounted on an anti-vibration platform inside a light-proof box.

Optical Calibration of the Scintillator and Buffer Fluid

4.1 Overview

This chapter describes the systems of the scintillator and buffer liquid. The goal of these systems is to measure and monitor the stability in time of different parameters concerning the production and the propagation of scintillation light in the Borexino detector. Together with the detection of light, already addressed in Chapter 4, concerning the calibration of the PMTs, these are the three fundamental processes determining the signal quality in the experiment.

The systems for the optical calibration were designed with the following general goals:

- Monitor on-line the properties and response of the scintillator, eliminating possible systematic errors due to sampling and handling procedures.
- Avoid the use in Borexino of results extrapolated from small scale laboratory experiments. Standard methods for the optical analysis of liquids have low sensitivity to scattering lengths above 2-3 m, but this range is still important in a detector where light travels, in average, over distances of about 6 m.
- Avoid the risk of introducing radioactive contaminants in the scintillator during calibration and monitoring operations. Since Borexino has the most stringent radiopurity requests for a large volume underground detector, the insertion of radioactive sources in the inner vessel is a very critical

operation and should not be performed as often as necessary for an optimal monitoring of the detector.

- Disentangle the several underlying effects of light propagation in a large volume liquid scintillator. Light propagation in the scintillator and buffer liquid is affected by several competing phenomena, such as scattering in the solvent, absorption/reemission in the solute, absorption or scattering in impurities. A simple measurement of the overall response of the detector that does not distinguish them supplies an incomplete model of the detector.

The design is focused on the use of light sources based on the coupling of optical fibers to lasers, cross-checking and combining the results from different configurations of light wavelengths and fiber locations.

According to the region of the detector where they will be installed, and the processes they will investigate, we can distinguish two subsystems:

- Internal system. A fiber inserted inside the inner vessel volume will excite the scintillator with ultraviolet light in order to study both the scintillation mechanisms and the overall detector response.
- External system. Several fibers mounted on the Stainless Steel Sphere will send light beams across the scintillator and buffer liquid in order to study the photon absorption and scattering.

The Section dedicated to each subsystem includes a review of the Physics of light production and propagation in a liquid scintillator and how it affects the resolution of Borexino, as well as the description of the system design and the experimental tests performed. In the last section we present the results of Monte Carlo simulations of the expected performance of the external systems.

4.2 Internal system

4.2.1 Goals and requirements

The system is essentially a low contamination risk calibration source, consisting of an ultraviolet laser connected to the scintillator region through an optical fiber. The basic idea behind it is that the scintillator absorbs the ultraviolet radiation and re-emits it according to its own wavelength spectrum. It was shown [73] that if the excitation wavelength matches the solute absorption band, the emission spectrum is the same when the scintillator is excited by charged particles. For such a calibration source to be useful in Borexino, at the least the main component of the scintillation decay time must also be the same. The demonstration of this fact was the main goal of the laboratory tests described in Section 4.2.4.

The light source will be used for position calibration, relative energy calibration and for studies of the absorption-reemission effect.

As a position source, the internal fiber system can be used in the following ways:

- Applying the reconstruction algorithm to the time distributions of events collected with the source in several locations inside the inner vessel and compare the reconstructed positions with the nominal ones.
- Use the time distribution obtained when the source is at the center of the detector as an experimental probability density function (Section 3.2.3) for the reconstruction algorithm.

An absolute energy calibration of the detector is impossible with this system but it can be used to do relative measurements of light collection in function of position. For an absolute calibration, radioactive sources are needed, as will be described in Section 6.2. Monte Carlo simulations of the light propagation in Borexino predict a difference of 4 % between the number of collected photo-electrons per MeV in the center and in the external regions ($r = 4\text{m}$) of the inner vessel. The detector geometry and the shape of the light concentrators favor a uniform light collection from all the inner vessel volume.

This small disuniformity is explained by a large volume effect in the light propagation because, in average, light produced in the outer regions of the inner vessel suffers less absorption by the PPO than light produced in the center.

In order to achieve these goals, the following requirements must be fulfilled:

- The time distributions of the light source events must be very similar to the “true” distributions due to β particles. In particular,
 - The scintillation decay times must be the same;
 - The laser must be fast and the dispersion in the fiber must be small, so that their combined time spread can be lower than 1 ns, the PMT time jitter.
- The light pulse should have a good uniformity, or else the comparison between events obtained in different positions has little meaning. The goal is to have a light source non-uniformity similar to the one caused by the blank regions in the pmt distribution, on the poles, that amount to 1%.

4.2.2 Scintillation light production

Organic liquid scintillators are characterized by the following properties:

- The absolute scintillation efficiency S , the fraction of incident particle energy converted into fluorescence photons;
- The response L to different ionizing radiations. The light quenching depends on the specific ionization density of different particles.
- The scintillation emission spectrum;
- The light absorption spectrum;
- The scintillation decay time of the fast component;
- The slow scintillation component and the dependence of the pulse shape on the nature of the incident radiation.

These properties are determined by the structure of the π electron levels which are delocalized orbitals, usually classified according to the free-electron model. σ orbitals are responsible for the molecular carbon bonds and the excitation or

ionization of these electrons leads, respectively, to non-radiative energy dissipation or to molecular damage, ultimately causing the light quenching.

It is convenient to divide the scintillation processes in two stages:

- The primary processes correspond to the transfer of energy from the ionizing radiation to the excitation energy of the solvent molecules.
- The secondary processes correspond to the radiative or non-radiative relaxation of the excited molecules.

4.2.2.1 Excitation by charged particles

In binary scintillators, the concentration of the solutes is normally small, of about a few g/l, so that their direct excitation can be neglected. We shall consider only excitation and ionization of the π -electrons of the solvent molecules, since other kinds of processes do not lead to scintillation. Figure 4.1 shows the π -electron energy levels of an organic molecule.

Electrons can be excited directly to the vibrational sub-levels of the singlet states and their, but direct transitions to the excited triplet states are spin-forbidden. Molecules in excited triplet states are produced by π -electron ionization followed by ion recombination. On simple statistical grounds, the recombination into triplet states is dominant with respect to singlet states. An additional way to populate the triplet states is through S_1 - T_1 transitions, involving spin-orbit couplings. Generally, the non radiative, spin reversal transitions are called “inter-system crossings”. The emission of fluorescence light corresponds to radiative transitions between S_1 and S_0 . In statistical terms, these transitions are uncorrelated events, so the intensity of the fluorescence emission decays exponentially with time t according to

$$I = I_0 e^{-t/\tau}$$

where I_0 and I are the intensities at $t=0$ and t respectively and τ is the fluorescence decay time. Since the period of molecular vibrations, typically of 10^{-12} s, is much smaller than decay time of S_1 , typically 10^{-8} - 10^{-9} s, the molecules reach thermal equilibrium before the emission which then happens only from S_{10} . Therefore the fluorescence spectrum is determined only by the vibrational sub-levels of the

ground state, while the absorption spectrum is determined by the sub-levels of the excited singlet states.

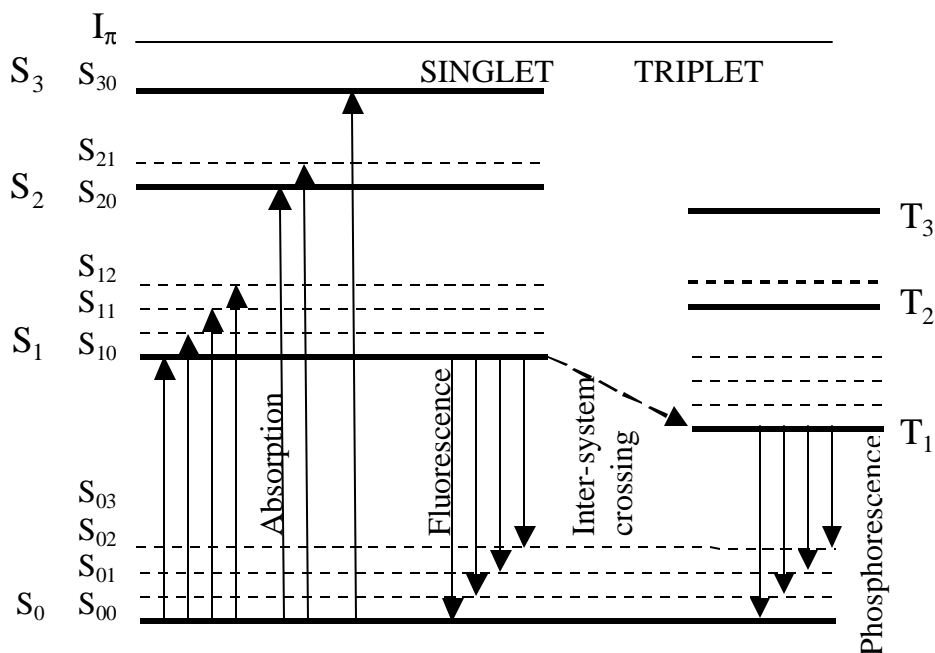


Figure 4.1 π -electronic levels of an organic molecule. S_0 is the ground state. S_1, S_2, S_3 are excited singlet states. T_1, T_2, T_3 are excited triplet states. $S_{00}, S_{01} \dots S_{10}, S_{11}$, etc. are the vibrational sub-levels. I_π is the π ionization energy. From reference [45].

Since it is spin-forbidden, the radiative transition from T_1 to S_0 , that is called phosphorescence, can happen only with a much longer time constant of 10^{-4} s. Therefore it is not observed in liquid scintillators because the energy is dissipated faster through thermal processes.

Excited triplet states contribute to the scintillation mechanism by delayed fluorescence, which consists on thermally activated inter-system crossings from T_1 to S_1 , followed by the normal fluorescence emission. Since the radiative transition is still from S_{10} to S_0 , the delayed fluorescence spectrum is the same for the fluorescence emission. However, the decay time is increased by the characteristic times involved in the thermal activation and spin-orbit coupling. The slow decay time component due to the delayed fluorescence is not exponential, but is well-described by a sum of exponentials with different time constants.

The relative weight of fast and slow decay time components depends on the ionization density of the charged particle. High ionization densities favor ionization and recombination into triplet states over direct singlet excitation. This is why the slow decay time components have larger weights for alpha particles than for beta excitation. The weights and time constants of the four exponential that describe the time distributions for the Borexino scintillator were shown in Table 2.1, in Chapter 2.

After the primary processes of excitation, ionization, ion recombination and inter-system crossing, non-radiative relaxation (quenching) and fluorescence compete for the energy of the excited molecules. Usually, solutes are added to the liquid scintillator in order to:

- Increase its fluorescence quantum efficiency, defined as fraction of excited molecules that decay radiatively;
- Reduce the scintillation decay time, thus improving the time resolution of the scintillation detector;
- Shift the emission spectrum to higher wavelengths, away from the solute absorption bands, and towards a better match with the PMT quantum efficiency.

Compound	Decay time (ns)
PC	28 ns
PPO	1.6 ns
PC+PPO (1.5 g/l)	3.5 ns in laboratory 5.5 ns in CTF

Table 4.1 Decay times (fast component) of PC and PPO.

The solute is chosen so that its first excited singlet state has a lower energy than S_1 , the first excited singlet state of the solvent molecules. In liquid scintillators, where molecular collisions are more important than for solids, the energy migration from the solvent to the solute happens primarily through non-radiative

processes, that are faster than the radiative lifetime of S_1 . The excitation energy migrates through neighboring solvent molecules until it is “trapped” by a solute molecule, since its first excited state has a lower energy. In this way, the processes that lead to energy migration to the solute molecules cause the suppression of the direct fluorescence from the solvent. So, even if at the normal solute concentrations of a few g/l, the direct excitation of the solute molecules by charged particles is negligible, all the scintillation light is emitted with the characteristic spectrum of the solute.

The fast component of the scintillation decay times of PC and PPO, isolated or combined are shown in Table 4.1. We recall that the slow components, presented in Table 2.1, are referred to the PC+PPO mixture.

The different decay times observed in the laboratory and in CTF are mainly due to the effect of absorption and re-emission, or inelastic scattering, that is due to the partial overlap of the emission and absorption spectra of the scintillator solute. These spectra are shown in Figure 4.2 for the PPO solute, used in Borexino. Part of the emitted photons with lower wavelengths are absorbed by PPO, causing a transition to the first excited singlet state (directly or following thermal relaxation of higher excited levels). The excited state can decay radiatively so, even if the photon is absorbed, there is a high probability, given by the PPO quantum efficiency of 80 %, that it is not completely lost.

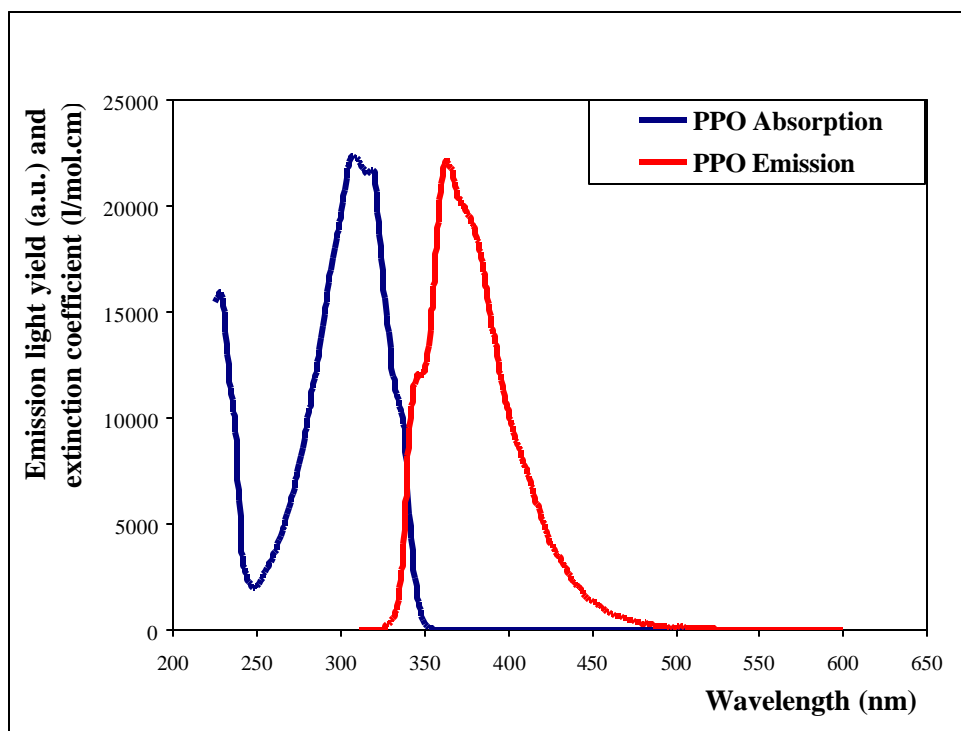


Figure 4.2 Emission and absorption spectra of PPO.

However, considering the radiative lifetime of the PPO molecule and the fact that the direction of the re-emitted photon is totally random, there is an effective increase on the decay time of the scintillation pulse. The overlap region is small, so the effect is negligible for laboratory-size samples. However, the CTF results showed that in large volume detectors, low extinction coefficients become significative. Tests made with a partially obscured light source inside (see references [37,⁷⁴]) the detector showed that about 44 % of the detected light had suffered at least one inelastic scattering, justifying the increase in decay time from 3.5 ns in laboratory samples to 5.5 ns in a large volume.

The effect is therefore significant and it must be taken into account in the reconstruction algorithm, but its mechanism is not yet fully understood. It is usually assumed that the spectrum of the emissions following absorptions in the long wavelength tail of the solute absorption band is the same as for absorptions in the main absorption band, but there is no actual evidence for this in the literature.

4.2.2.2 Excitation with ultraviolet light

The scintillator can also be excited with light matching its absorption bands, that are normally in the ultraviolet. We can distinguish two different responses, according to the spectral region of the excitation light:

1. The region where the solvent is transparent, but the solute absorbs, so that its fluorescence is excited directly. In PPO, this region partially overlaps its emission spectrum, causing inelastic scattering.
2. The region where solvent absorption is dominant, so that the solute fluorescence is excited indirectly by energy transfer from the solvent.

In case 1 the decay time is given just by the radiative lifetime of the solute first excited state. In case 2, the excitation energy must follow the same processes that happen in the singlet levels excitation by charged particles. i.e.:

- Direct excitation of the singlet states of the solvent;
- Energy migration to a solute molecule;
- Fluorescence of the solute molecule.

Therefore, the decay time in case 2 should be the same as the fast component of the charged particle scintillation pulse. In both cases we do not expect the excitation of the triplet states, and delayed fluorescence should not take place. Therefore, the time distribution consists of a simple exponential in which the time constant is simply the main fluorescence decay time, without any of the slow component tails.

4.2.3 System design

The internal system has three main components:

- The lasers and their associated optics;
- The fibers for the light transmission;
- The insertion mechanism and the location system.

4.2.3.1 Lasers

Two lasers will be used: the first emits at 266 nm, within the absorptions bands of PC, and the second at 355 nm, within the overlap region between absorption and emission spectra of PPO (Figure 2.2).

The technical properties of the two diode lasers are summarized in Table 4.2.

Laser Properties	NanoUV 266	NanoUV355
Wavelength	266 nm	355 nm
Pulse width	0.43 ns	0.43 ns
Peak power	2.75 mW	2.80 mW
Repetition rate	7.1 kHz	11.5 kHz
Stability (short-term/long-term)	< 0.2% / 1% (σ)	< 0.2% / 1% (σ)

Table 4.2 Technical properties of the lasers.

The two lasers have a low pulse time width, smaller than the PMT time jitter, allowing for a good time resolution. The average energy per pulse is sufficiently high to tolerate a high attenuation through the fiber.

The light from the 266 nm laser will be used for the position and energy calibration measurements, since the fluorescence emission following its absorption is expected to have the decay time characteristic of a charged particle excitation, except for the slow components. The absence of the slow components does not reduce the significance of the measurement, because for position reconstruction only the prompt signals are used.

The light from the 355 nm laser will be used to study the inelastic scattering in PPO in large volumes, in order to optimize the model for this process that is used in the Monte Carlo simulations. The joint analysis of the time distributions of events obtained with the 355 nm and the 266 nm laser can isolate the re-emission component of the scintillation decay time from the primary fluorescence component.

4.2.3.2 Fibers

In order to cause the least possible spread to the short laser pulse width we use a thin step-index fiber with small mode dispersion. For a core diameter of 50 μm , the time dispersion is estimated to be 1.4 ns for the total fiber length of 20 m. The transmission of 266 nm light poses two problems that require a special care in the design of the fiber termination:

The contamination of the 266 nm pulse with light of higher wavelength can induce a different regime of scintillator response, thus falsifying the measurement. If part of the pulse arriving to the scintillator has wavelengths above 310 nm, the decay time profile of the re-emitted light will have a faster component from the fluorescence following direct solute absorption. From our preliminary tests, we have indications that this phenomenon does take place (see next sections). To avoid this difficulty, a small custom-made low-pass filter is included in the fiber termination.

We expect that a source based on the absorption/reemission of laser pulses should exhibit a very good illumination homogeneity, since the re-emitted scintillation light is, in principle uniform. However, 266 nm light arriving to the tip of a fiber immersed in pseudocumene is immediately absorbed in a few tenths of microns, so the subsequently re-emitted fluorescence pulse comes from a practically point-like region. So, a large fraction of the re-emitted light should be channeled back into the fiber itself, causing a shadow effect, in which large detector regions would not be illuminated directly by light from the primary emission point but only from secondary absorption/re-emission or scattering processes. To overcome this, the fiber is inserted in a sealed spherical quartz vial, so that light from the fiber travels a few mm in air and quartz before reaching the scintillator.

The design of the fiber termination is shown in Figure 4.3. In order to have a good optical coupling with the low-pass filter, the fiber is mounted on a stainless steel cylindrical support and placed inside the quartz tube. The epoxy sealing prevents the scintillator to infiltrate into the small air gap between the fiber and the quartz sphere.

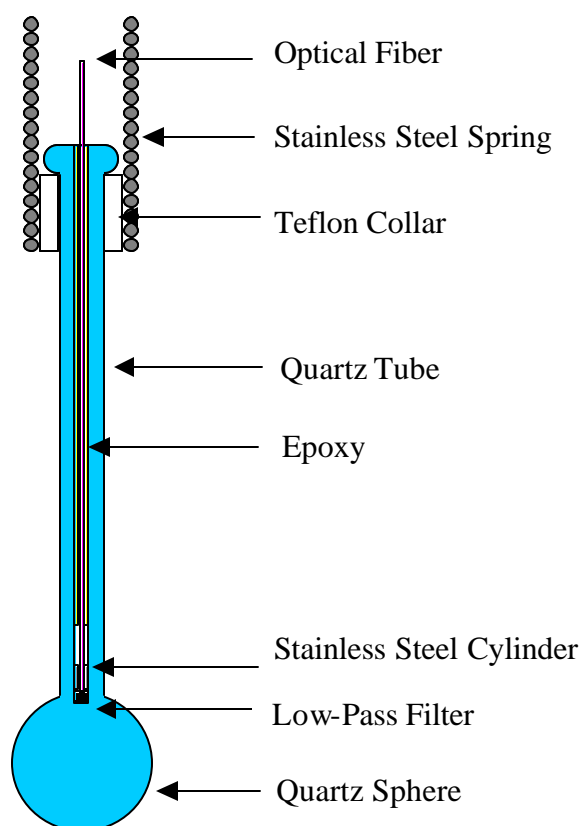


Figure 4.3 Schematic view of the internal system fiber termination.

The diameter of the quartz sphere is 2 cm, enough to reduce to about 1 % the solid angle determined by the 3 mm diameter filter in the position of absorption and re-emission of the light pulse. For 355 nm light, the absorption length in PPO is 1.5 cm, so the shadow effect is minimal and the fiber tip can be simply immersed in the scintillator.

The fiber is inserted and moved in the inner vessel by means of a rod mechanism operated from within a class 10 clean-room, where the lasers and all the apparatus will be installed. The source position is independently monitored thanks by means of digital cameras installed on the Stainless Steel Sphere and diodes attached close to the fiber tip. Both these systems were developed by our collaborators at Virginia Tech for radioactive source insertion and will be described in Chapter 6.

4.2.4 Experimental tests

4.2.4.1 Overview

The goals of this test were the following:

- Verify that the time dispersion of the laser pulse due to the propagation in the fiber (the modal dispersion) is small enough to allow the measurement of decay times of few nanoseconds.
- Investigate a possible partial conversion of ultraviolet light into higher wavelengths due to fluorescence in the fiber, and the effectiveness of filters to prevent it from reaching the scintillator.
- Verify that ultraviolet radiation with a wavelength of 266 nm is absorbed and reemitted by the scintillator, producing light pulses in which the decay time is equal to the time constant of the first exponential component of the time distribution obtained with excitation by ionizing particles, i.e., 3.5 ns.
- Observe the direct excitation of the solute, PPO, by measuring the response of the scintillator to incident ultraviolet light with a wavelength of 355 nm, for which PC is transparent. The expected scintillation decay time is 1.6 ns.

4.2.4.2 Description of the experimental setup

A laboratory was prepared in Milano for the study of the response of the PC+PPO scintillator to excitation with ultraviolet laser pulses. The scintillator consisting of PC and PPO at the concentration of 1.5 g/l was contained in a quartz vial placed inside a light-proof box, as shown in Figure 4.4.

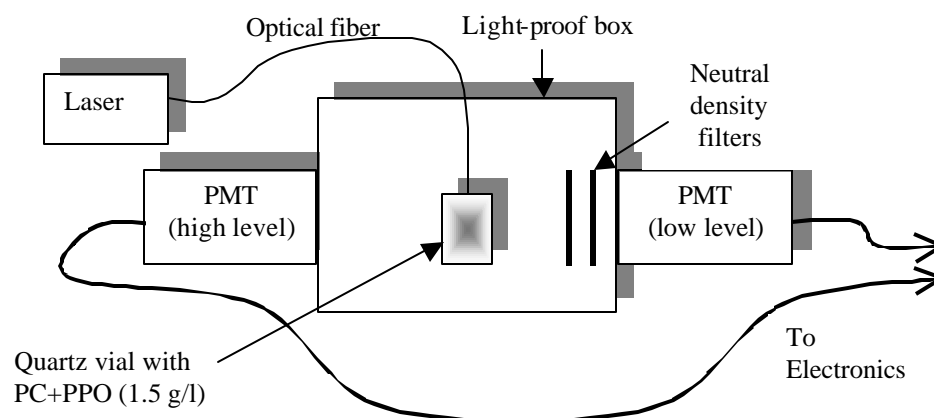


Figure 4.4 Scheme of the setup for the measurement of the scintillator response to excitation with ultraviolet laser pulse.

An optical fiber coming from the laser entered the box and its tip could be immersed in the scintillator. Alternatively, the fiber could be placed out of the vial, with an optical filter between its tip and the scintillator. Both PMTs were placed in light-proof cans connected to the main box and facing the center. Neutral density filters were placed in front of the cathode of one PMT, called low level PMT, the other one being the high level PMT. Both PMTs were connected to high voltage and an electronics chain based on the NIM and CAMAC standards. A photo of the experimental apparatus is shown in Figure 4.5.

We used the same scintillator that will be used for Borexino, made of pseudocumene as solvent and PPO as solute, at a concentration of 1.5 g/l. Before each use, the scintillator was saturated with nitrogen in order to remove oxygen.

The same diode lasers for the final configuration in Borexino were used. Their technical characteristics were reported in Table 4.2



Figure 4.5 Photo of the experimental setup for the study of the scintillator response to laser excitation. From left to right: computer for remote-control of the lasers, laser boxes, electronics, light-proof metal box with two PMTs, and computer for data acquisition.

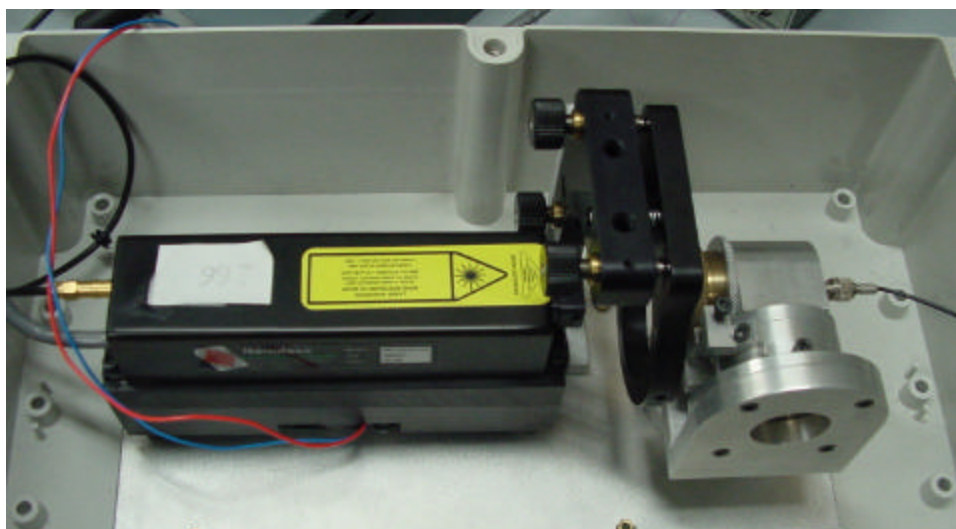


Figure 4.6 Laser head (266 nm), cooling vent, filter support, and fiber coupling system inside a light-proof box.

Figure 4.6 shows one of the lasers inside a light-proof box, a support for filters and the connection for optical fiber, that consists of a micrometric rotation stage with a quartz lens focused on the surface of an optical fiber.

The optical fiber is made of high OH pure fused silica in order to have a good transmission at low wavelengths. Due to its small core diameter (50 μm), its nominal modal dispersion is lower than 0.8 ns/10 m. The fiber was covered by a black PVC coating and the tip to be immersed in the scintillator was “bare”, i.e. without any connector. The other tip had a standard SMA connector that allowed it to be connected to one of the two lasers. The tip could be directly immersed in the scintillator or could be coupled through an interferential filter that selects only a band of 266 \pm 3 nm.

The PMTs used in this test were the model Philips XP2262B 2'' and their characteristics are listed in Table 4.3. This is not the same PMT used in Borexino, but its time jitter and dark noise are the same.

Photocathode diameter	44 mm
Dynode	CuBe, Linear focused
Supply voltage, gain	1850 V, 3×10^7
Quantum efficiency at 400 nm	25 %
SER resolution	70 %
Dark noise	1 kHz
Anode pulse rise time	2.3 ns
Transit time	31 ns
Time jitter	1 ns

Table 4.3 Properties of the Philips XP2262B 2'' PMT used in the test.

In order to measure correctly the shape of the scintillation pulse, the illumination intensity at the low level PMT must be of the order of a single photoelectron. To reach this level a set of neutral density filters was placed between the scintillator vial and the PMT. No filters were placed in front of the high level PMT, in order

to have a large number of photons hitting the photocathode. In this way, the pulse leading edge was determined by the prompt scintillation photons and was independent of the scintillation decay time. This signal was used to give a trigger in coincidence with the scintillation event in order to reject the dark noise and supply a reference for the time measurement.

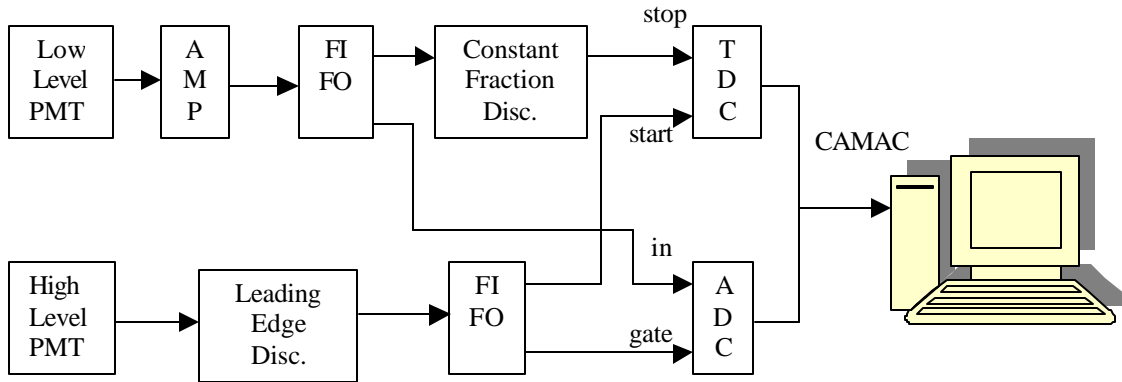


Figure 4.7 Scheme of the electronics chain.

A diagram of the front-end electronics and the Data Acquisition (DAQ) is presented in Figure 4.7. The threshold of the leading edge discriminator to which the high level PMT is connected is set in such a way that rejects the low amplitude dark noise pulses. The signal from the discriminator is then used to open a gate of 80 ns in the Analog-to-Digital Converter (ADC) and to provide the “start” reference to the Time-to-Digital Converter (TDC). The signal from the low level PMT is linearly amplified and sent to the ADC and to the constant fraction discriminator that provides the “stop” for the TDC. The ADC and TDC are read by a CAMAC crate controller connected to a computer running the DAQ code.

4.2.4.3 Experimental results

The measurements were made in four steps:

1. Obtain the single photo-electron illumination of the low level PMT. We checked the PMT charge spectrum after each successive increase of the filter attenuation.

2. Excite the degassed scintillator with 266 nm ultraviolet light, using the “bare” fiber tip immersed in it.
3. Excite the degassed scintillator with 266 nm ultraviolet light, placing an interferential filter between the fiber and the scintillator.
4. Excite the degassed scintillator with 355 nm ultraviolet light, using the “bare” fiber tip immersed in it.

The charge spectra of the low level PMT obtained with both lasers after step 1 are shown in Figure 4.8. From the position of the valley and the nearly gaussian shape of the main peak we can roughly estimate an upper limit of 4 % for the percentage of multi-electron pulses with respect to the SER peak.

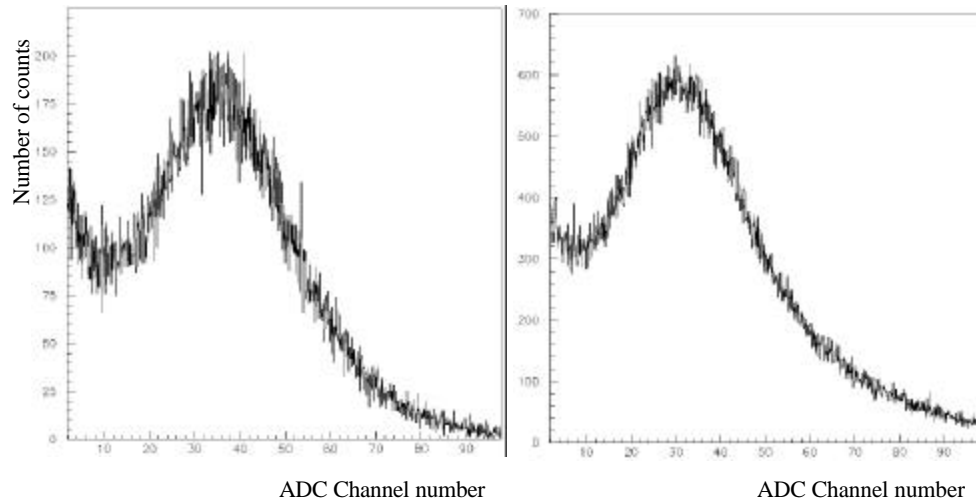


Figure 4.8 Charge spectra of the low level PMT when the scintillator is excited by 266 nm (left) and 355 nm (right). The ADC channel number is proportional to the collected charge.

The time distributions obtained in steps 3 and 4 are shown in Figure 4.9. The function that was used to fit the time distributions is the convolution of an exponential, giving the scintillation decay time τ , and a gaussian, giving the system resolution σ :

$$f(t) = N \int_0^{+\infty} e^{-\frac{x}{\tau}} e^{-\frac{(x-t)^2}{2\sigma^2}} dx \quad \text{Eq. 4.1}$$

The $\chi^2/\text{d.f.}$ of the experimental distribution fits was about 1.0 and the resulting parameters are listed in Table 4.4

Wavelength (nm)	Filter	Standard deviation of the gaussian component	Time constant of the exponential component
266	no	1.2 ± 0.1 ns	2.5 ± 0.1 ns
266	yes	1.2 ± 0.1 ns	3.5 ± 0.1 ns
355	no	1.2 ± 0.1 ns	1.6 ± 0.1 ns

Table 4.4 Results of the time distribution analysis.

These results deserve several comments:

- The gaussian component of the time distribution was 1.2 ns, a confirmation that the system had a good enough time resolution for fast scintillation pulses. We can estimate the fiber time dispersion Δt_{fiber} by using the following relation

$$\sigma^2 = \Delta t_{\text{PMT}}^2 + \Delta t_{\text{laser}}^2 + \Delta t_{\text{fiber}}^2 \quad \text{Eq. 4.2}$$

where σ is the time resolution, Δt_{PMT} is the PMT time jitter and the laser pulse time width. Since $\Delta t_{\text{PMT}} = 1$ ns and $\Delta t_{\text{laser}} = 0.43$ ns, we get $\Delta t_{\text{fiber}} = 0.5$ ns. The value, measured with a 12 m fiber is actually two times better than the dispersion of 0.8 ns/10 m, quoted by the supplier.

- The fact that no indication was found for additional exponential tails is in good agreement with other similar measurements in the literature and with the theory of energy migration in liquid scintillators. Tails arise in the time distribution of scintillation pulses due to the excitation of triplet states. The triplet states can be populated in the molecular collisions that happen in the path of an ionizing particle. Their radiative transitions to the ground state take longer times, since they require the collision of two triplet-excited molecules and the formation of a singlet excited one. However, since the absorption transitions from the ground state to the triplet states

are spin-forbidden, these states will not be populated when the scintillator is excited with UV light.

- The decay time of the scintillator in response to excitation by 355 nm is the decay time of PPO alone, in good agreement with the prediction of direct solute excitation.
- The decay time of the scintillator in response to excitation by 266 nm is the same as the fast component of beta particle excitation (3.5 ns), as long as the filter is used. This confirms the prediction of indirect excitation of the solute, through non-radiative energy migration from the solvent excited molecules, when there is only excitation with light below 310 nm.
- The lower time found without the filter indicates the possible presence of light with a wavelength above the PC absorption band, but within the PPO absorption. The actual time distribution would then be a sum of gaussian and two exponentials, one with a decay time of 3.5 ns, due to the absorption of 266 nm by the PC, and the other with a decay time of 1.6 ns, due to absorption of the higher wavelength light directly by the PPO. The limited detector resolution makes it hard to distinguish between two superimposed exponentials with similar decay times, so the result is a single exponential fit with a time constant in between the two values.

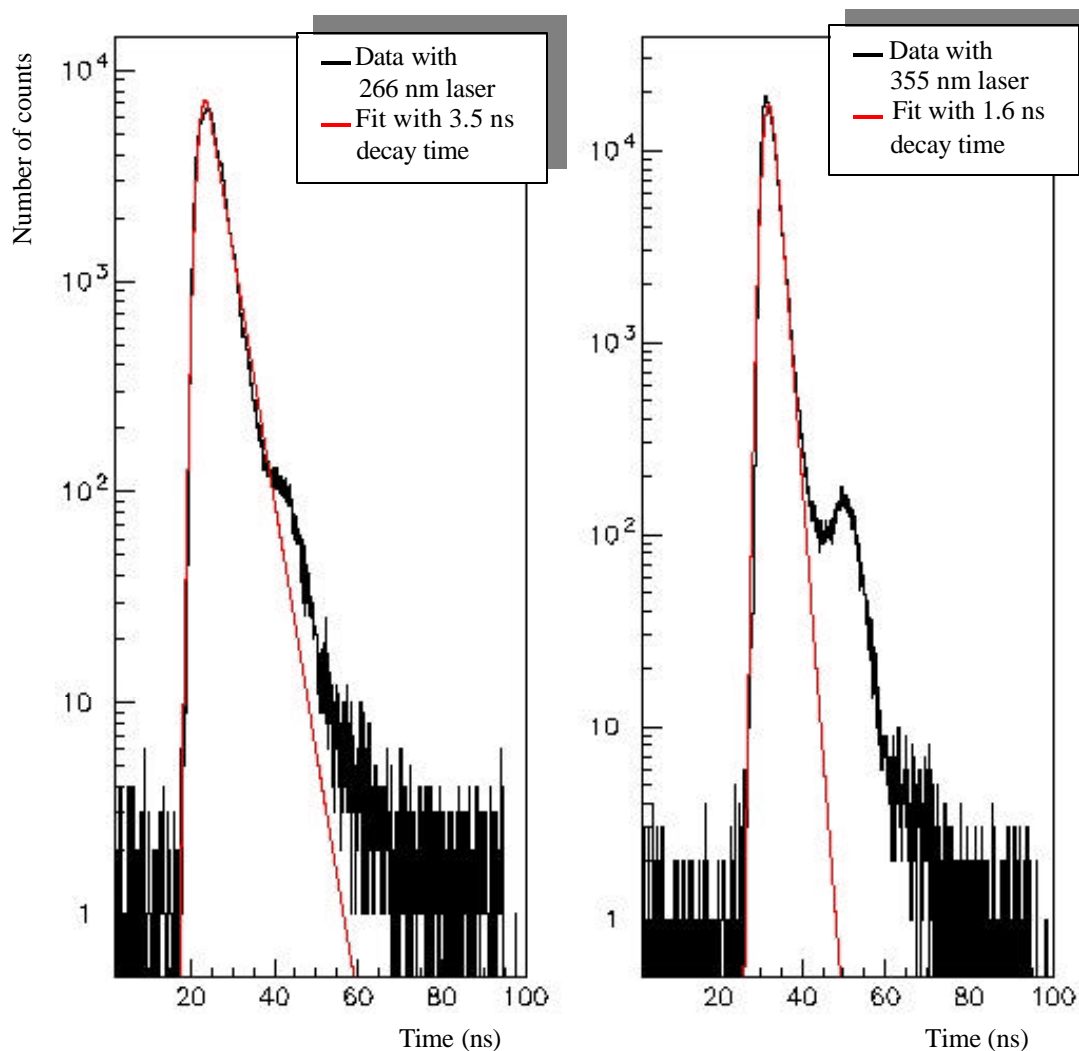


Figure 4.9 Time spectra of the scintillation pulses obtained by exciting the scintillator with 266 nm (left) and 355 nm (right) ultraviolet light.

4.3 External systems

The goal of the external systems is to monitor the stability of the scintillator and buffer liquid in what concerns their optical transparency, i.e., the processes affecting the propagation of light.

The key point is the use of a wavelength different from the one that is used with the internal system, so that different regimes of the scintillator response can be studied in an independent way.

4.3.1 Light propagation in PC+PPO

Light transmission is usually described by the attenuation length Λ , defined by:

$$\Lambda = -\frac{d}{\ln(I/I_0)} \quad \text{Eq. 4.3}$$

where I/I_0 is the fraction of transmitted light after traveling a distance d in the material. Even if the light may not be lost, but just scattered we shall use the term attenuation length in the general sense of an “interaction length” and distinguish between absorption length and scattering length when necessary to avoid ambiguity.

Light attenuation measurements are often presented in function of the molar decadic extinction coefficient ϵ , related to Λ through

$$\epsilon = \frac{\ln(10)}{\Lambda c} \quad \text{Eq. 4.4}$$

where c is the concentration.

The extinction coefficients for light transmission in PC, PPO and DMP were measured by the collaboration using spectrophotometric methods [75, 76] and the results are shown in Figure 4.10 in function of the attenuation length.

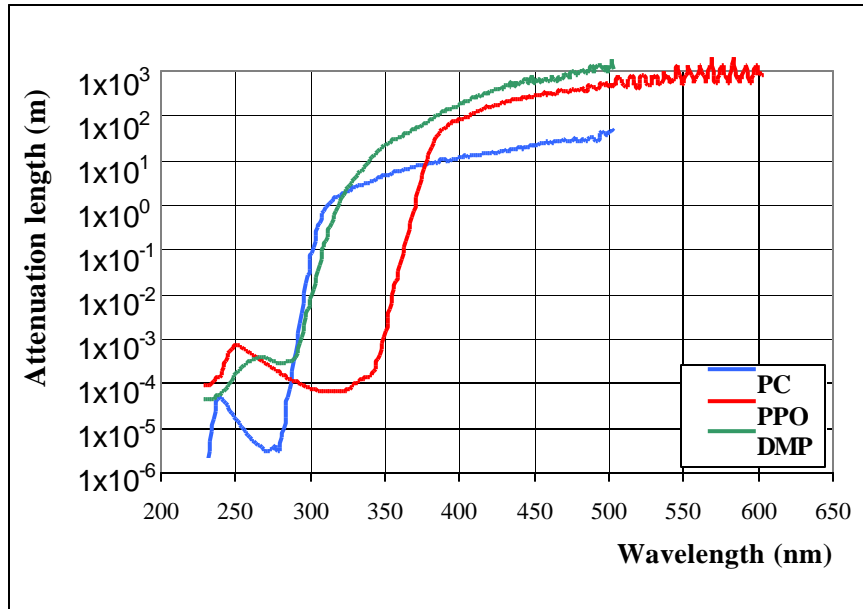


Figure 4.10 Optical attenuation length of PC, PPO and DMP.

Within the main absorption band of each compound, the absorption is too strong to allow the measurement with the pure PC or with the PPO and DMP at the nominal concentrations of 1.5 g/l and 5 g/l, respectively. Ciclohexane, that has the same absorbance as water down to 230 nm, was used to prepare diluted PC solutions for the measurements up to 290 nm. The same procedure was applied to the PPO and DMP measurements in the wavelength region of their absorption bands. Conversely, in the longer wavelength region, the attenuation lengths are too high to be measured accurately in 1 cm spectrophotometer cells, so the solute attenuation was measured with concentrated solutions. This process, however, cannot be applied to the solvent, that was measured at 100% concentration.

From the plot in Figure 4.10 we can distinguish two dominant light propagation regimes in the wavelength region of the PC+PPO emission spectrum:

- Absorption (and re-emission) by PPO molecules, up to 375 nm.
- Scattering by PC molecules, above 375 nm.

Inelastic scattering was considered in the previous section. The net effect of the cascade of inelastic scattering processes suffered by the fluorescence light is a spectral shift from lower to higher wavelengths. This happens within a short distance from the scintillation point, with respect to the dimensions of the detector. Only a small fraction of the light is absorbed by PPO beyond 1 m from its emission point. In consequence, for most of its path from emission to detection, scintillation light has a wavelength for which the only dominant process is elastic scattering. In the buffer region, it is the only process, since there is no PPO and the attenuation by DMP is negligible.

Measurements done by the collaboration [76] roughly show a λ^{-4} dependence of the extinction coefficients and confirm that the scattered light has the same wavelength as the incident beam. This indicates that the dominant process affecting light transmission in PC in the long wavelength region is elastic scattering.

The elastic scattering of light happens through the Rayleigh mechanism, i.e., the formation of induced molecular dipoles in a medium where light is passing. The induced dipoles oscillate and emit electromagnetic radiation in a very short timescale (10^{-15} s), with the same wavelength and in a direction correlated to the original photon. Through theoretical calculations, one can obtain an expression for the ratio of the intensity of scattered light to the intensity of incident light [77]. For our purposes, it is enough to consider:

$$\frac{I}{I_0} \propto \frac{1 + \cos^2 \theta}{\lambda^4} \quad \text{Eq. 4.5}$$

where λ is the wavelength and θ is the angle between the incident and scattered directions.

This scenario assumes that the scintillator is a simple binary mixture. The presence of impurities can decrease the transparency of the scintillator or buffer liquid if they have absorption bands above 350 nm, or if they are not completely soluble and form scattering centers. Materials such as stainless steel, aluminium or mu-metal will be in contact with the buffer liquid of Borexino. Studies performed in the Borexino collaboration showed that, after some time in contact with these materials, there is some degradation of the PC transparency. All the tests were made with laboratory samples, in which the surface-volume ratio is very large when compared to Borexino. The expected consequences for Borexino are negligible if the degradation effect is proportional to the surface-volume ratio, but this has not been demonstrated.

Elastic scattering increases the average path travelled by the photons, increasing their arrival time. This causes an increase of the time distribution tails and therefore, a reduction of the α – β pulse-shape discrimination efficiency.

4.3.2 *Monitoring strategy*

The main goal of the external systems is the monitoring of the stability of the scintillator and buffer liquid transparency for what concerns elastic scattering. Absorption without reemission is not strongly addressed since it does not affect the time distribution of the detected photons and its effect can be monitored through the monitoring of the light collection efficiency.

The strategy of the monitoring system is to use the 4π light collection capability of Borexino to measure separately the scattered and transmitted light, using collimated beams coming from optical fibers, instead of uniform light sources.

Two fiber configurations will be used, each with different advantages: light transmission feedthroughs fixed at the SSS, sending light diametrically through the whole detector and light transmission feedthroughs sending light obliquely only through the buffer region. The design of each of these subsystems is described in Sections 4.3.3 and 4.3.4. In particular, the tests described in Section 4.3.3.2 showed a good capability in isolating the backscattered light. The wide angle light coming from the fibers was focused with a lens and collimated with pin-holes, in order to obtain narrow beams with angles between 2° and 6° . Section 4.3.4.2 described the measurements of the angular distributions of the different light beams that will be used in the final system.

The primary light source is the 394 nm diode laser used in the system for the calibration of the photomultipliers. At this wavelength, interaction with the PPO molecules is negligible, so the Rayleigh scattering in PC is expected to be the dominant process, with an interaction length of about 5 m. The technical characteristics of the laser are summarized in Section 3.2.3.1.

A secondary light source will be the 355 nm laser, also used with the internal system. The scattering length of PC at 355 nm is about 2.5 m. Only the buffer liquid can be monitored at this wavelength due to the PPO absorption. In fact, after the absorption –reemission processes in the scintillator, the 355 nm light coming out of the inner vessel is reduced to negligible levels. Nevertheless, monitoring the buffer transparency at low wavelengths supplies complementary information to the measurements on the main spectral region.

A common patch panel will allow the manual connection of both lasers to both fiber subsystems.

4.3.3 *Radial beams system*

4.3.3.1 Design

This system will produce light beams sent from the SSS in the direction of the center of the detector. The PMTs mounted on the opposite side of the Sphere within the aperture angle of the beam will be illuminated primarily with the light transmitted through 8.5 m of scintillator and 4.8 m of buffer liquid. All other PMTs will be illuminated with scattered light, but the ones that will have a higher count rate are the ones near the axis of light propagation, since at 0° and 180° the cross section for Rayleigh scattering is the double of the cross section at 90° (Eq. 4.5). Since the PMTs at 0° will measure both direct and scattered light, we expect that the best way to isolate the scattered light is with the PMTs that are located near the origin of the beam, that should see only backscattered light. We also expect reflections, but at a definite time, so they should be easy to eliminate. Section 4.3.5 presents result of Monte Carlo simulations showing the expected time distributions of the collected light.

The radial beams subsystem consists of 12 modules composed of a quartz fiber and a light-transmitting feed-through. The fiber carries the laser pulse from the patch panel outside the detector to the feed-through mounted on the SSS.

The type of fiber used is the same as for the external part of the PMT calibration system: 300 μm core diameter, 40 m length, black PVC coating. On the side of the patch panel, the fiber has a ST connector (bayonet coupling), that allows a good repeatability of the connection. On the side of the SSS, the fiber will always remain fixed, so the connector can be SMA (threaded coupling).

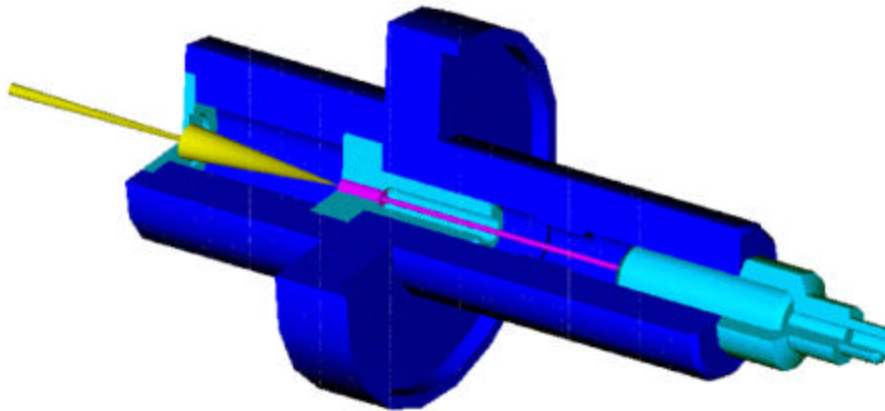


Figure 4.11 Schematic view of the feed-through of the radial system for scintillator optical monitoring.

The design of the feed-through is also based on the one used for the PMT calibration system, shown schematically in Figure 4.2. The radial system feed-through must not only transmit light to the inside of the SSS, but it also should focus and collimate the light beam, so the fiber is terminated by a small lens and there is also a pin-hole support attached. The technical drawing of the apparatus can be found in the Appendix and a schematic view is shown in Figure 4.11.

The stainless steel parts are shown in dark and light blue and the optical parts (fiber and lens) in purple. The yellow cones represent the transmission of light through the pin-hole.



Figure 4.12 Prototype of the radial beam feed-throughs. The parts in white are in Teflon, but in the definitive version, they are made of electropolished stainless steel.

The light transmission inside the feed-through is assured by a segment of 300 μm fiber, the same as outside. For beam focusing we use a **Graded Refraction INdex** (GRIN) lens. This is a 3 mm diameter, 1 cm long quartz cylinder in which the refraction index decreases continuously from the axis to the surface. It has the advantage that a reasonable focusing can be obtained just by putting it in direct contact with fiber. The absence of air gaps was a requirement in order to maintain a good mechanical tightness. The pin-hole has a fixed diameter of 0.5 mm, and is placed at a distance of 30 mm from the GRIN lens. The pin-hole support is made of stainless steel and was designed to avoid the trapping of air bubbles during the filling operations, regardless of its vertical orientation.

4.3.3.2 Experimental test in the TLTT

The Two-Liquid Test Tank, already described in Section 4.4.1, provided good conditions for a test of the radial beam system:

1. The large volume of the tank itself – 7 m³ – allowed us to study the propagation of the light beams traveling over distances of 2.5 m in pseudocumene.
2. The tank has 50 PMTs installed on the wall of a cylindrical tank, so we can detect light scattered from 0 to 180 degrees.
3. The tank is also used for the PMT calibration system test, so the PMTs can be calibrated in time and energy.

Description of the setup

The radial beams system for the TLTT consists of two light-transmitting feed-throughs connected by optical fibers to a diode laser. The laser is the same that was used for the test of the PMT calibration system, a diode laser emitting at 410 nm with a time width of 40 ps. The fibers are of the same type of the external fibers for the definitive system, i.e., quartz fibers with a core diameter of 300 μm . They have 28 m of length and are covered by a thick black PVC coating. The fibers enter in the external tank through individual flanges with the same type fittings used for the PMT cables. We have a single fiber for each feed-through, so they cannot be connected simultaneously to the laser.

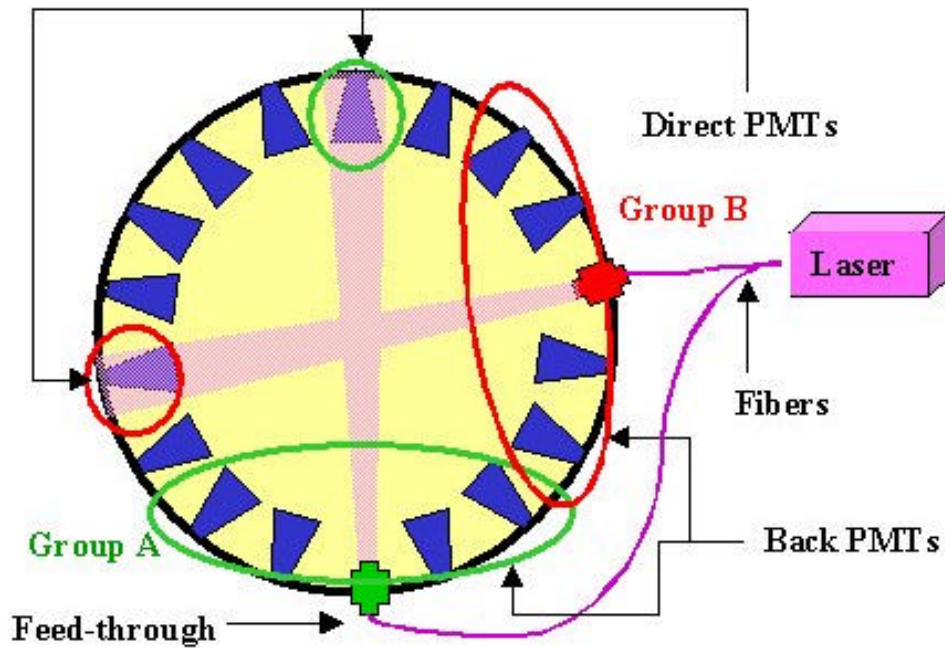


Figure 4.13 Schematic view of the experimental setup of the radial system test in the TLTT.

The feed-throughs are an early version of the definitive design shown in Figure 4.11 and Figure 4.12, that does not have any pin-hole, so the beam comes out directly from the GRIN lens. Before the installation, a measurement of the radial beams aperture was made in air with a white lamp. The beam presented a uniform illumination and we found a semi-aperture angle of $6 \pm 0.5^\circ$. For the definitive system, more precise measurements were done later (see Section 4.3.4.3).

A diagram of the relative positions of the radial beams feed-throughs in the TLTT is shown in Figure 4.13. There are 54 holes in the TLTT wall, organized in 18 columns with 3 holes each. The radial beam feed-throughs, shown in red and green, and the feed-throughs for the PMT calibration system, not shown in the figure, occupy five of these holes. The remaining 49 holes are occupied with PMTs, represented in blue.

The aperture angle of the radial beams was enough to illuminate directly two PMTs mounted on the diametrically opposite column. These PMTs are referred to

as direct PMTs. The two PMTs mounted on the same column as the feed-through and the PMTs on the four adjacent columns are referred to as back PMTs. The angular positions of the back PMTs with respect to the beam axis are 20° and 40° . In order to distinguish between both feed-throughs and their respective direct and back PMTs, we call them group A and group B. The angle between the beam axes of both groups is 100° . In this way, as can be seen from the figure, the groups are completely redundant, since there is no superposition of direct and back PMTs from each other.

Data-taking

The electronics and data—acquisition setup was the same that was used for the PMT calibration system test, already described in Section 3.4.3. As was described then, the DAQ system had only 24 channels, so two consecutive runs had to be made in order to take data from the 48 PMTs. The data-taking was simplified by including the direct and back PMTs of each group in the same 24-channel run.

Each run consisted of data-taking with the PMT calibration system and both radial beams feed-throughs. A total of five runs were made, from December 1999 to April 2000. The first run was done before the filling with pseudocumene (PC), with the tank full of nitrogen. The following three runs were done with the tank filled with 7 m^3 of PC, as arrived from the production plant, without any further processing. In April 2000, the tank was emptied in order to visually inspect the status of the PMTs after 4 months of immersion in PC and to repair a PMT cable. The PC was kept in stainless steel storage tanks for two weeks and then put back again into the TLTT. The last run was performed immediately after the tank was refilled. At the time of each run, a sample of PC was taken from the tank and sent for spectrophotometric analysis by our collaborators in the University of Perugia.

Data analysis

In order to obtain the relevant time spectra, the first steps of the data analysis were the following:

1. The raw calibration data was analyzed in the way described in Chapter 3 in order to obtain the PMT calibration parameters. The time calibration parameters are the reference time and the time jitter for each channel. The charge calibration parameters are the average and the standard deviation of the single electron response (SER) of each PMT, expressed in terms of ADC channel number.
2. Correction of the raw data according to the calibration parameters. The reference time was subtracted from the measured time and the measured charge was divided by the SER average, in order to obtain time measurements with a common reference and light intensity measurements expressed in photoelectrons.
3. The histograms of the time spectra of the 2 direct PMTs and of the 15 back PMTs of each group were added.

The time distributions of the direct and back PMTs for the nitrogen run are shown in Figure 4.14. The time distributions of the remaining PMTs do not present sharp spectral features and were not used in the following analysis.

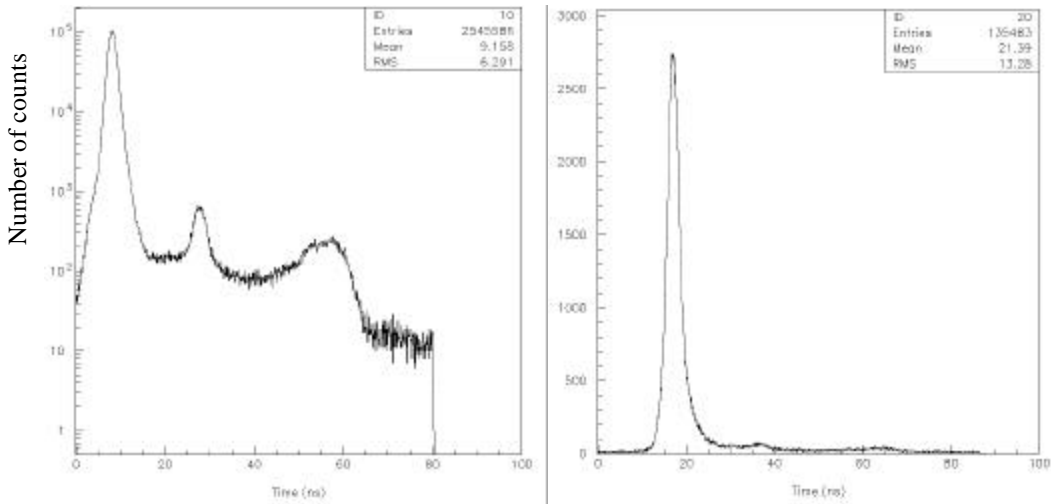


Figure 4.14 Time spectra of the direct (left) and back (right) PMTs obtained with the tank filled with nitrogen.

On the direct spectrum we can distinguish the largest peak, at $t_{d1}=8$ ns, and two smaller peaks, at $t_{d2}=27$ ns and $t_{d3}=55$ ns. The back spectrum has a large peak at $t_{b1}=17$ ns and a smaller one at $t_{b2}=37$ ns.

The first peak of the direct spectrum is caused by light that traveled directly from the feedthrough to the photocathode, without any interactions, so it is called the direct peak. The first peak of the back spectrum is interpreted as due to a reflection of the light sent from the feedthrough on the opposite wall of the tank. This is sustained by the fact that the time difference to the direct peak corresponds to the time-of-flight of light crossing the whole tank diameter:

$$t_{b1} - t_{d1} = \frac{1}{c} D_{TLTT} = 9 \text{ ns} \quad \text{Eq. 4.6}$$

In a similar way, we can interpret the second peak of the direct spectrum and of the back spectrum as due, respectively, to two and three successive reflections on opposite sides of the tank. In these cases, we have

$$t_{d2} - t_{b1} = t_{b2} - t_{d2} = 10 \text{ ns} \quad \text{Eq. 4.7}$$

a higher value than the one for the first reflection. This indicates that after the second and third reflections, the light has changed slightly its direction, possibly due to a non-specular reflection, and now travels over a distance longer than the tank diameter.

The last peak of the direct spectrum is an instrumental feature of the PMT, present also in the calibration spectra and other previous tests⁸.

The reflectivity of stainless steel after pickling and passivation, the surface treatment applied to the TLTT walls and the Borexino Stainless Steel Sphere, was measured by the collaboration^[78]. Most of the light, 37 %, suffers diffuse reflection, but 3 % is reflected back at angles lower than 7° . The intensity ratio of the reflected and direct peaks can be estimated at about 2.5 %, in agreement with this value of the specular reflectivity of the TLTT walls. In fact, the diffuse

⁸ This is attributed to the so called “late pulses”, due to photoelectrons reflected on the first dynode and re-accelerated back again by the electric field.

reflection component should not contribute significantly to the first reflection peak, since the light travels in different directions and so the distribution of its time of detection should be very broad. In addition, diffuse light will more likely be deflected towards the region behind the PMTs and towards the tank floor or upper cover, decreasing its detection probability.

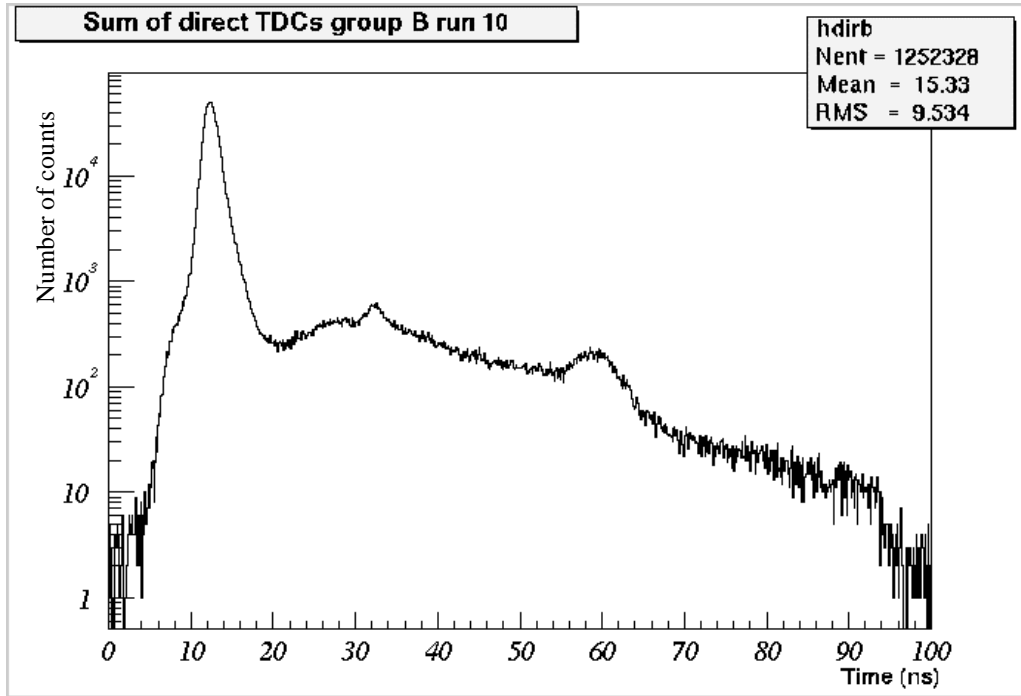


Figure 4.15 Time spectrum of the direct PMTs for a typical run with PC.

The time distributions for the first Pseudocumene run are shown in Figure 4.15 and Figure 4.16. The same reflection peak structure is maintained, with the direct peak at $t_{d1}=13$ ns and the first reflection peak in the back PMT distribution, at $t_{b2}=27$ ns. This time difference corresponds to the time-of-flight in the tank, taking into account the PC refractive index of 1.5. The time distance from the direct peak to the second reflection peak, at $t_{d2}=33$ ns, now corresponds to the time-of-flight of photons that are reflected in the PMT photocathode, instead of in the tank wall:

$$t_{d2} - t_{d1} = 2 \frac{n_{PC}}{c} (D_{TLIT} - 2L_{PMT}) = 20ns \quad \text{Eq. 4.8}$$

where L_{PMT} is the length of a photomultiplier, from the wall to the photocathode. In PC, the semi-aperture angle of the beams is 4° , instead of the 6° measured in air and the beam is more tightly focused on the surface of the opposite PMT. So, it illuminates less wall surface than if it propagates in nitrogen.

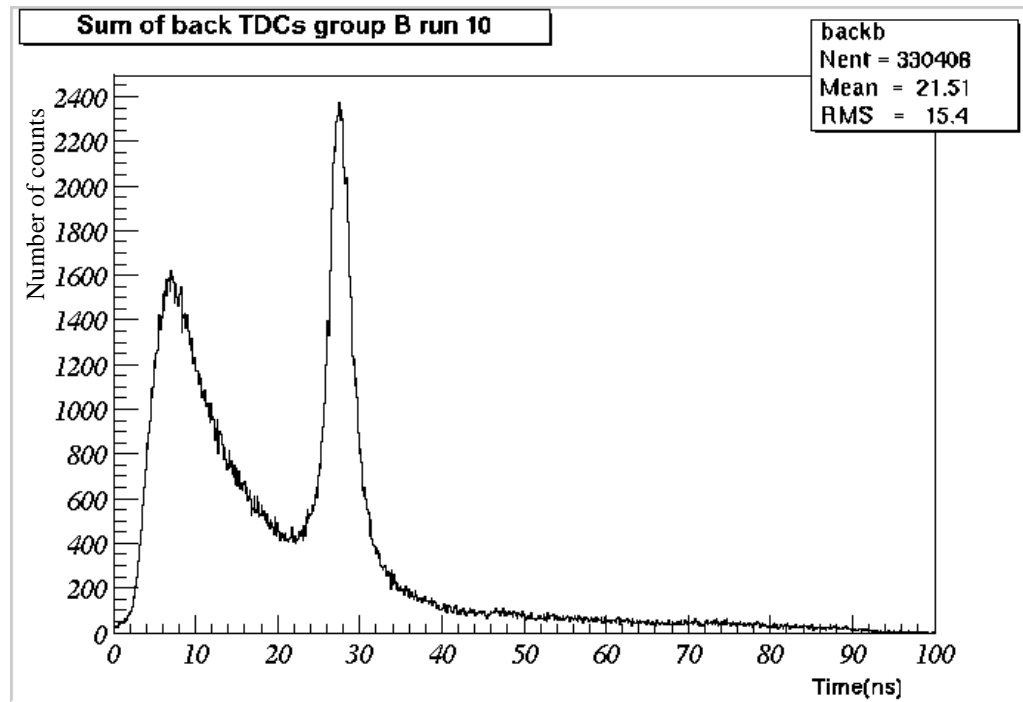


Figure 4.16 Time spectrum of the back PMTs for a typical PC run.

However, the most relevant feature of the time spectra obtained in PC is the backscattering peak that can be seen in Figure 4.16, clearly distinguished from the reflection peak. This feature is present at short times, before the reflection peak, so it can only be due to the light interaction with the PC, and this interaction must be elastic scattering, since the wavelength of 410 nm is far above the PC absorption bands.

This plot shows that the backscattering peak is at least as high as the reflection peak, clearly demonstrating the importance of elastic scattering in large scintillation detectors.

A quantitative analysis of the spectra was performed by integrating the light intensity corresponding to each peak. Since the data were stored in n-tuples, we know the number of photoelectrons corresponding to each PMT hit shown in the time spectra. The limits for integration of the direct and reflected peaks were $[\langle t \rangle - 2s, \langle t \rangle + 2s]$, calculated through gaussian fits. For the backscattering feature, we simply integrated from 0 ns up to 20 ns. Instead of just adding the bins in the time spectra, which would be equivalent to assume that every hit produced charge 1, we added the number of p.e., calculated from the ADC measurements and the PMT charge calibration, corresponding to each peak in the time distribution. This procedure eliminates the systematic error of counting the multiple-PMT hits as single. In the measurement of the direct peak integral, this error would be of about 10 %, since the average number of p.e. per detected event was 1.1.

We performed the same analysis for the four PC runs, using the same integration limits for the peaks. The three integral values of direct, reflected and backscattered light were combined in the ratios of Backscattered-to-Reflected (Back/Ref) and Backscattered-to-Direct (Back/Dir), listed in Table 4.5.

Run	Attenuation Length (m)	Back/Ref ($\pm 0.7\%$ stat.)	Back/Dir ($\pm 0.3\%$ stat.)
December 1999	7.3	2.04	0.110
January 2000	7.6	1.94	0.110
March 2000	8.0	2.01	0.113
Tank emptied and refilled			
April 2000	5.7	2.30	0.119

Table 4.5 Values of the Backscattered-to-Reflected and Backscattered-to-Direct ratios measured at different periods, compared with the attenuation length measured by spectrophotometry by our collaborators at Perugia University.

The second column lists the results of the spectrophotometric analysis of the samples sent to our collaborators in the University of Perugia. According to these

results, the transparency of the PC remained relatively stable during the first four months of data-taking. Also in this period, both the Back/Ref and Back/Dir parameters were stable, within differences of $\pm 3\%$ from the average value, respectively, 2.00 and 0.111.

However, after the tank was emptied and refilled in April, the parameter showed significant increases, of 8 % for Back/Dir, and 15 % for Back/Ref. These increases were clear signs that the transparency of the PC had decreased as a result of the temporary storage in external tanks, that probably contained optical contaminants. This fact was supported by the spectrophotometric analysis, that showed a decrease of the attenuation length, from an average of 7.6 m to 5.7 m.

In conclusion, these tests demonstrated that the method proposed for the radial beams system is capable of:

- a good separation between the spectral features due to interaction in PC and reflections on the detector walls,
- a good sensitivity to the stability or variation of the PC transparency.

4.3.4 Oblique beams system

4.3.4.1 Goals and requirements

Since the light beams from the radial system feed-throughs cross both the scintillator and the buffer liquid, an independent tool is needed in order to distinguish the scattering in each region. The goal of the oblique system is to monitor the stability of the transparency of the buffer liquid only.

However, the geometry of Borexino places two constraints to the propagation and detection of light beams in the buffer region.

1. Any beam originated in the SSS either will cross the inner vessel or be blocked by the PMTs and light concentrators, since they are tightly packed on the SSS surface.
2. The shape of the light concentrators is designed in order to reflect back any photons arriving with an incidence angle (with respect to the radial

direction in that point) larger than 44° , which is the maximum incidence angle from any photon originated in the inner vessel. It is defined as the angle at which a straight-line tangent to the inner vessel crosses a sphere tangent to the concentrators edge.

In order to obey the first constraint, the origin of the light beam must be moved away from the SSS and placed at least at about the same distance from the center as the light concentrators edge. As targets for the light beams, only PMTs without light concentrators were chosen.

The analysis of the PC transparency with the radial beams system is based essentially on the detection of backscattered light, since it is easily separable from direct and reflected light. Due to the geometrical constraints listed above, the application of this method to the beams crossing the buffer liquid would be far from straightforward, so the analysis of the PC transparency with the oblique beams will be based essentially on the detection of the direct light.

On the basis of these considerations, we can express the following requirements of the oblique beams system:

- The beams must not cross the inner vessel nor be blocked by light concentrators.
- The target PMTs cannot have light concentrators. This implies that the target is a single PMT, because the no-concentrator PMTs are distributed uniformly on the SSS surface.
- The oblique beams should cross a wide range of distances. The distribution of the detected light intensity in function of the distance is the basis for the calculation of the PC attenuation length.
- In order to have redundancy of information, the system should have more than a single beam crossing the same distances. This can allow us a better control over the factors limiting the sensitivity of the measurement: different illuminations, different PMT quantum efficiencies.
- In order to increase the sensitivity to direct light, the contribution of scattered light to the total intensity detected by the target PMTs should be

minimized. For this purpose, the oblique beams are focused and collimated.

4.3.4.2 Design

The oblique beams subsystem consists of 19 modules composed of:

1. A quartz fiber that carries the light from the laser to a feed-through mounted on the SSS, identical to the radial system fibers.
2. A feed-through for light transmission mounted on the SSS that does not contain any GRIN lens or pin-hole. Its design is the same as the PMT calibration feed-through, just with a thinner fiber, of 300 μm core diameter.
3. A second fiber, that is identical to the preceding one, but is just 1 m long and has a PC-proof Teflon coating. On one end, the fiber is coupled to the feed-through by means of an SMA connector and on the other end its tip is glued to a connector directly in contact with a GRIN lens.
4. A mechanical system to support the GRIN lens fiber termination and point it in the direction of one of the chosen PMTs.

Additionally, there is a reference module composed of a quartz fiber, a light-transmitting feed-through with a 1 mm fiber inside and a 20 fiber bundle, similar to the PMT calibration system bundles, but with 20 m long fibers. The fibers of this bundle will be connected directly to each target PMT, providing a measurement of the reference intensity in order to normalize the intensity detected with the other modules.

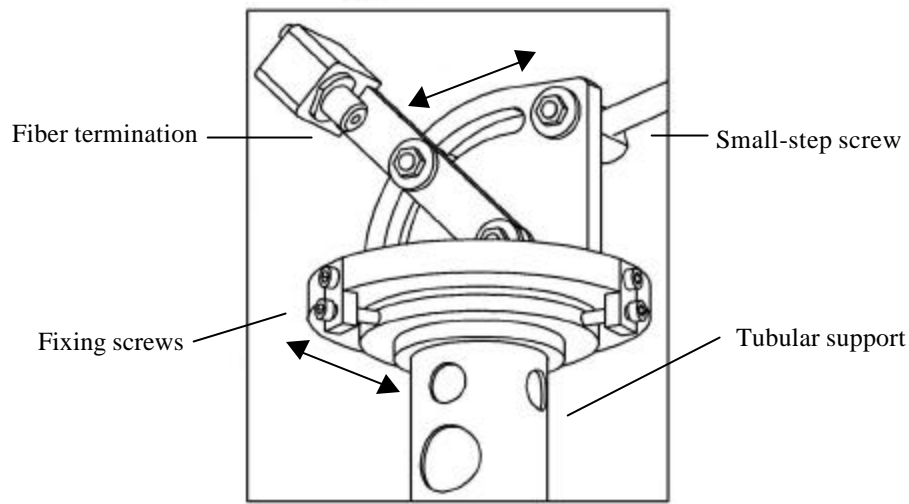


Figure 4.17 Detail of the fiber pointing system. The arrows indicate the direction of rotation.

Pointing system

Figure 4.17 shows a detail of the pointing system, supported at 45 cm from the SSS by a tubular structure, providing a very good stability against flexion and vibration. Figure 4.18 shows a photograph of a complete module, already installed in the detector and surrounded by four PMTs, one of which (upper left corner) does not have the light concentrator. The complete mechanical drawings for the pointing system can be found in [79]. The orientation of the module with respect to the absolute detector coordinates is not known in advance, since the orientation of the flange cannot be predefined. So, in order to set the correct direction after the installation inside the detector, the pointing mechanism allows the arm that holds the fiber termination to move with two angular degrees of freedom. By combining parts in stainless steel and Teflon, the system has very smooth and precise movement capability. The movement along the θ coordinate has a precision of about 0.1° , guaranteed by means of a small step thread precision mechanism.



Figure 4.18 Photo of one of the oblique system pointing modules, already installed in the Borexino detector, surrounded by PMTs.

Position of the modules

The criterion for the choice of the positions of the oblique beams modules and the target PMTs was to allow the widest possible range of distances between them. The maximum distance for an unblocked optical is 9.3 m, dictated by the radius of the inner vessel. The minimum distance depends on the light blocking by the neighboring concentrators, since the target photocathodes are farther away from the center than the concentrator's edge. The interferences of the light concentrators with the oblique beams were checked using the map containing the positions of all the 2214 PMTs to be installed on the Stainless Steel Sphere, as well as the position of the 156 flanges available for calibrations hardware. For nearly all the available target PMTs, the minimum distance to avoid blocking was 5.5 m. However, in some particular cases, the PMT distribution in the SSS

presents vacant PMT positions near no-concentrator PMTs. These positions either cannot be filled due to interference with the SSS support legs or are occupied with the feed-throughs for the PMT calibration system. So the light blocking for the PMTs near these positions is reduced and the minimal distance between beam module and target PMT can be as low as 2.0 m.

Fiber termination

The criterion for the fiber termination design was to minimize the contribution of scattered light to the total light detected in the target PMTs, while maximizing the direct light collection. Therefore the light beam should cover the whole target photocathode surface, but not much more than that.

So the fiber termination, shown schematically in Figure 4.19, focuses the beam with the GRIN lens and also collimates it with pin-holes, in order to obtain the best aperture angles for each distance.

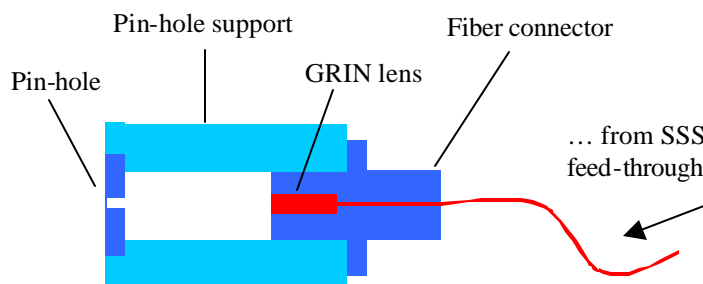


Figure 4.19 Fiber termination with GRIN lens.

During the detector filling, air or water bubbles can remain trapped inside the fiber termination distorting the light beam because PC has a different refractive index. The mechanical design of the fiber connector and the pin-hole support took this into account by including grooves that allow the complete filling of the beam path with PC, in any possible orientation of the fiber termination.

The distance between the GRIN lens and the pin-hole can be 9 mm or 33 mm, with the use of an additional spacer between the fiber connector and the pin-hole support. Pin-holes of several diameters can be used, according to the aperture

angle that is needed for each distance. The aperture angle of the beam is determined by the photocathode diameter, D_{PMT} , at each given distance, L_{target} , plus a tolerance $Tol=0.6^\circ$, to take into account the pointing inaccuracy:

$$\alpha = \arctan\left(\frac{D_{PMT}}{L_{target}}\right) + Tol \quad \text{Eq. 4.9}$$

Table 4.6 shows the chosen distances and the best aperture angles for the 19 oblique beams.

Distance (m)	Angle ($^\circ$)	Number of modules
2.0	6.0	3
2.5	5.0	2
2.9	4.4	2
4.1	3.2	4
5.7	2.5	4
7.9	2.0	4

Table 4.6 Target distances and aperture angles of the oblique beams.

The choice of the best pin-hole diameter in order to obtain these angles, and the test measurements to verify them are the subject of the next Subsection.

4.3.4.3 Light beam profiles

In order to obtain the aperture angles listed in Table 4.6 the typical pin-hole diameter is about 1 mm, so the GRIN lens cannot be considered to be a point-like light source, since its diameter is 3 mm. If we consider the GRIN lens a uniform, extended light source, after passing through a pin-hole, the produced beam will have a central zone of full illumination and a twilight zone of decreasing intensity. We can define the twilight zone as the set of points that can be connected with a straight line to some, but not all of the points in the light source, as is shown schematically in Figure 4.20.

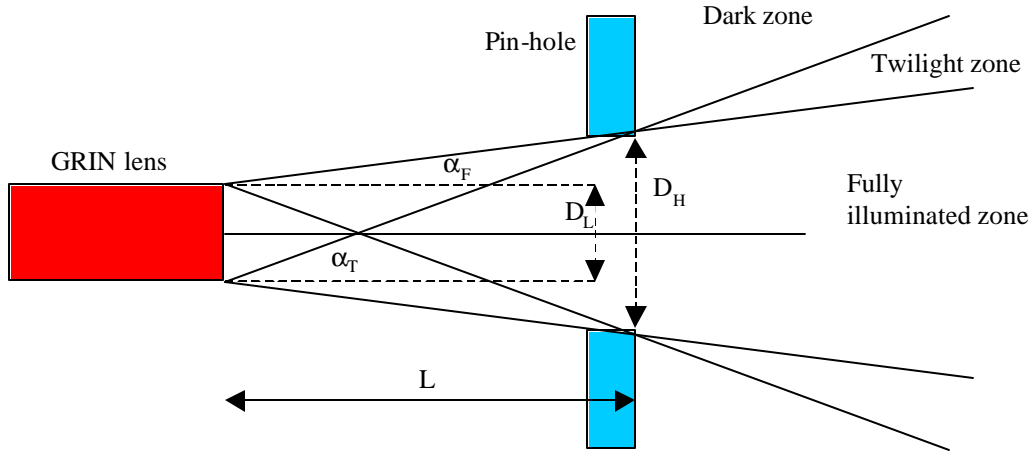


Figure 4.20 Schematic diagram for the calculation of the aperture angles for the fully illuminated and twilight zones of the collimated light beam.

The aperture angles of the fully illuminated and the twilight zones, respectively α_F and α_T , can be written as

$$\begin{aligned} \alpha_F &= \arctan\left(\frac{D_H - D_L}{2 \cdot L}\right) \\ \alpha_T &= \arctan\left(\frac{D_H + D_L}{2 \cdot L}\right) \end{aligned} \quad \text{Eq. 4.10}$$

where D_H is the pin-hole diameter and D_L is the diameter of the GRIN lens, or better, of its illuminated section, that is smaller – 1 mm. The distance L between the lens and the pin-hole includes the pin-hole plate thickness.

In order to verify these assumptions, we prepared a setup for the measurement of the angular profiles of the light beams. This setup is schematically represented in Figure 4.21.

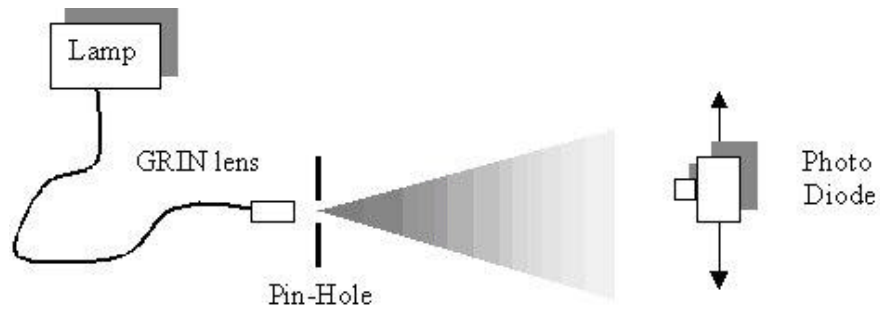


Figure 4.21 Setup for the measurement of the beam profiles.

The fiber/lens module was illuminated with a white lamp and several pin-holes of different diameters, from 0.5 mm to 2.0 mm, were used in the fiber termination. The pin-hole support spacer allowed us to use two lens-hole distances, $L=10\text{mm}$ and $L=32\text{ mm}$. The distance between the lens and the photodiode was 0.5 m or 1.0 m, depending on the use or not of the spacer. The photodiode was mounted on a rail, movable along a horizontal direction perpendicular to the beam axis. The accuracy of the movement was of 1.5 mm, so the angular resolution is 0.1° for the measurements with the spacer (done at a 1 m distance and 0.2° for the measurements without the spacer (done at 0.5 m).

Figure 4.22 shows the measured angular distribution of the light beam obtained with the radial feed-through, with and without any pin-hole. The Full Widths at Half Maximum (FWHM) for these distributions are, respectively, $2.8 \pm 0.1^\circ$ and $10.3 \pm 0.2^\circ$.

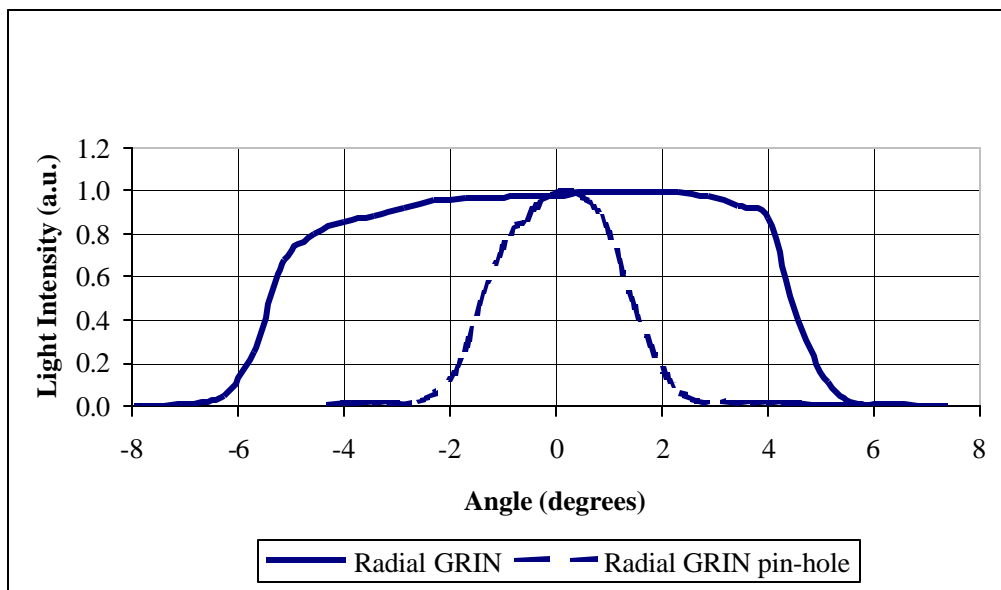


Figure 4.22 Angular distribution of the light from the GRIN lens coupled to a 300 μm fiber, with and without a pin-hole.

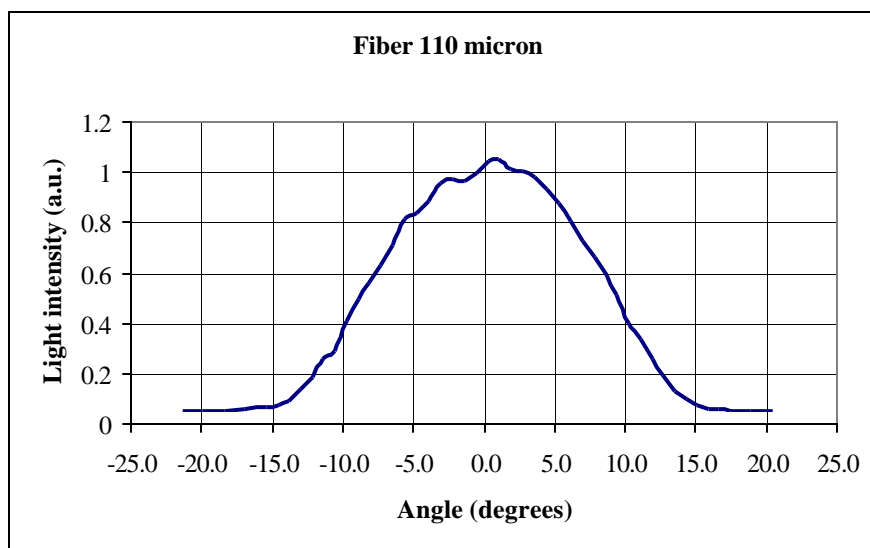


Figure 4.23 Angular distribution of the light from the 110 μm diameter quartz fiber.

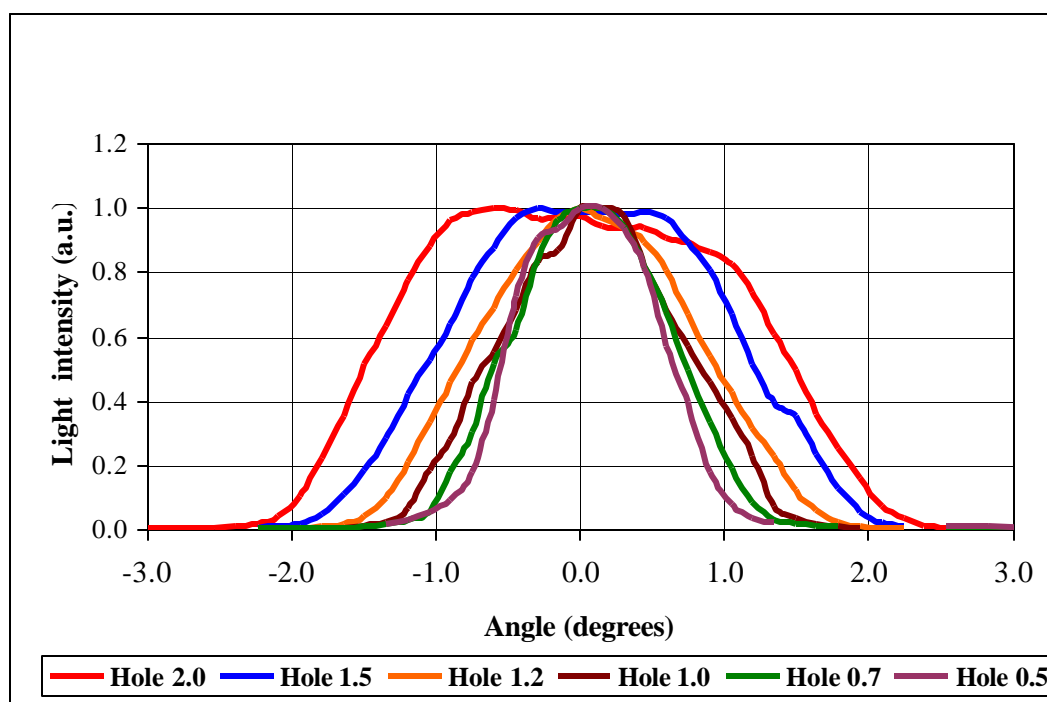


Figure 4.24 Angular distribution of the light from the GRIN lens coupled to a 300 μm fiber, with several pin-holes at a distance of 32 mm (using the spacer).

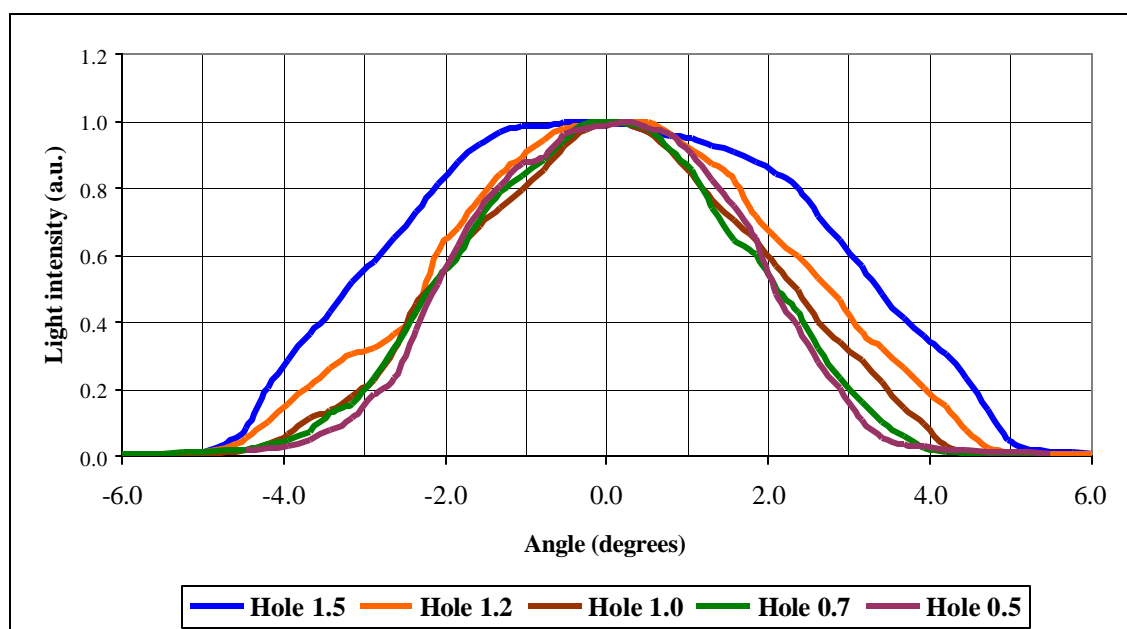


Figure 4.25 Angular distribution of the light from the GRIN lens coupled to a 300 μm fiber, with several pin-holes at a distance of 9 mm (without using the spacer).

For comparison, in Figure 4.23 is shown the angular distribution of the beam from a 110 μm fiber, without a GRIN lens, presenting a width of $7.2 \pm 0.3^\circ$. These distributions show that the effect of the lens is not only to focus the beam, but also to make the intensity distribution more uniform. Figure 4.24 and Figure 4.25 show the results of the measurements done with the oblique system terminations. Since the distributions present a large twilight zone, we consider the FWHM as the aperture angle. These values are listed in Table 4.7, as well as the angle calculated on the basis of Eq. 4.10. For $D_H > D_L$, the calculated angle is $\alpha_F + \alpha_T$, and for $D_H < D_L$, it is simply α_T .

	Diameter (mm)	Measured Angle ($^\circ$)	Calculated Angle ($^\circ$)
Spacer (L=32 mm)	0.5	1.2 \pm 0.1	1.3
	0.7	1.4 \pm 0.1	1.5
	1.0	1.5 \pm 0.1	1.7
	1.2	1.8 \pm 0.1	2.1
	1.5	2.3 \pm 0.1	2.6
	2.0	3.0 \pm 0.1	3.5
No Spacer (L=10 mm)	0.5	4.2 \pm 0.2	3.9
	0.7	4.3 \pm 0.2	4.4
	1.0	4.6 \pm 0.2	5.2
	1.2	5.0 \pm 0.2	6.3
	1.5	6.6 \pm 0.2	7.9

Table 4.7 Measured and calculated angles of the oblique beams.

We consider this a satisfactory result given the simplicity of the beam formation model. The calculated angles are slightly overestimated with respect to the measured values with a maximum discrepancy of 20 %. We interpret this discrepancy as due to the fact that we considered the GRIN lens as a perfectly uniform source, while it would be more realistic to assume a dependence of the emitted intensity on the position on the lens surface. Nevertheless, if we consider not the absolute value, but ratios of beam angles, the difference is at maximum 6 %. In practice, these are the relevant parameters, since the analysis method is based on the relative comparison between the light intensities at the different distances. On the basis of these results, we chose the pin-hole diameter for each distance, listed in Table 4.8.

Distance (m)	Angle ($^{\circ}$)	Spacer	Pin-hole Diameter (mm)
2.0	6.0	No	1.5
2.5	5.0	No	1.2
2.9	4.4	No	1.0
4.1	3.2	Yes	2.0
5.7	2.5	Yes	1.5
7.9	2.0	Yes	1.2

Table 4.8 Chosen values of the pin-holes diameter in order to obtain the required beam angles.

4.3.5 Monte Carlo simulations of the expected performance

The response of the detector to light beams coming from the radial and oblique system was studied by means of Monte Carlo (MC) simulations, using the Borexino photon tracking code (Section 3.2.2), and an additional routine for the generation of light beams with a fixed axis and aperture angle.

The MC simulations of the light beam propagation were used both in the early design phase of the calibration systems in order to explore the possibilities of different beam configurations and later, in order to develop an analysis method for the oblique system and to estimate its sensitivity to the buffer liquid attenuation length.

4.3.5.1 Simulation of the radial beams

Before defining the radial beam design as it was described in Section 4.3.3.1, we studied the possibility of using the internal fiber system to produce diametral beams crossing large sections of the scintillator. The plots presented in Figure 4.26 and Figure 4.27 are the summed time distributions of the upper and lower hemisphere PMTs, resulting from downward pointing beams, symmetric with respect to the z axis. The line colors refer to three different starting points of the beam (fiber tip positions): center of the detector, $z = 0$ m (blue) and near the inner vessel, at $z = +4$ m (red) and $z = -4$ m (black). The simulations results represented by the dotted line do not consider any kind of reflections on the Stainless Steel Sphere, while for the simulations shown with the solid line, 50 % specular reflectivity was assumed. In order to consider a worst-case scenario, we made the

very conservative assumption of 50% specular reflectivity. The measured reflectivity of the SSS, with a pickling and passivation surface treatment, is 5 % specular reflectivity and 35 % diffusion. The diffuse reflection has a much lower impact on the time distributions, since many photons remain “trapped” behind the light concentrators (from MC simulations).

The most well-defined features on the lower hemisphere time distribution are the direct peaks (on the left side in Figure 4.27) and the second reflection peaks (on the right side), separated by a distance of 140 ns, the time-of-flight for optical photons to cross two detector diameters.

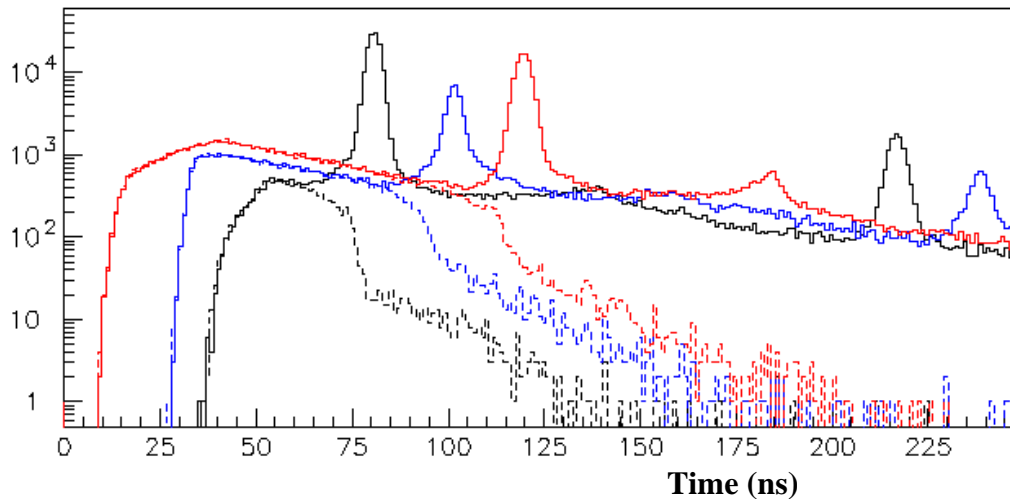


Figure 4.26 - Time spectra of the upper hemisphere PMTs in response to a downward pointing laser beam.

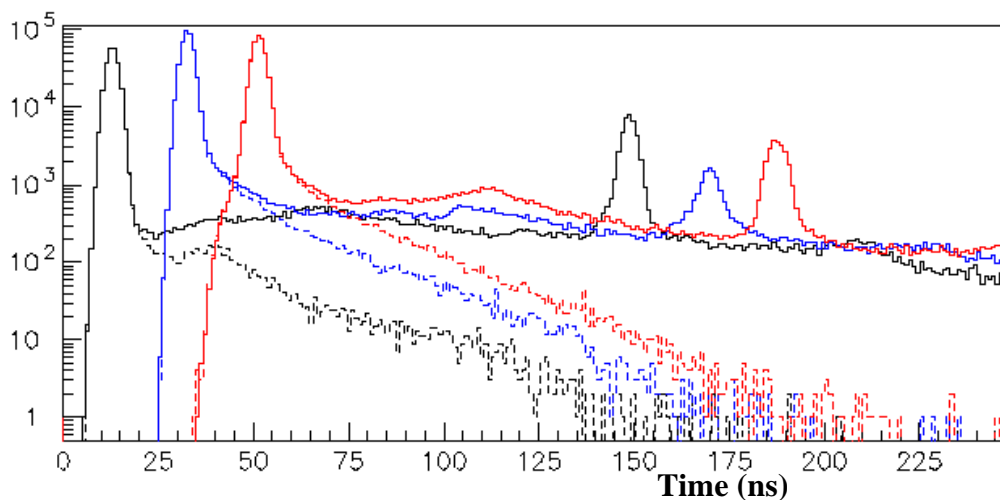


Figure 4.27 - Time spectra of the lower hemisphere PMTs in response to a downward pointing laser beam.

On the upper hemisphere, the comparison between the solid (with reflections) and the dotted (without reflections) curves, shows that the first reflection peak and the backscattering feature (in the left side of Figure 4.26) are also well defined, so that a simple time interval cut can separate both features. This separation is much more evident in the case $z = +4$ m (red line) with respect to $z = -4$ m, since the distance to the SSS is larger, and so the reflection peak is well delayed with respect to the backscattering feature.

This last result has proven the feasibility of detecting the backscattered light, separating it from the reflection background. Using time cuts, we can obtain ratios between backscattered and direct light, or between backscattered and reflected light providing reference monitoring parameters. If the beams are fixed to a single distance, the parameters do not allow the direct calculation of the attenuation length, but we can use any change on their value as a warning that more refined analyses are needed.

Since the operation of the internal fiber system presents a limited, but not negligible, risk of scintillator contamination, the radial system was designed with fixed beam positions. On the basis of this design, we prepared the test in the TLTT that confirmed experimentally the good identification of the backscattering feature and the validity of the Backscattered/Direct and Backscattered/Reflected ratios as transparency stability parameters. In fact, even if referred to different conditions (Borexino and TLTT), the simulated time distributions (Figure 4.26 and Figure 4.27) are qualitatively similar to the measured ones (Figure 4.15 and Figure 4.16).

4.3.5.2 Simulation of the oblique beams

The propagation in the detector of the light beams produced by the oblique system was simulated. The main beam parameters - target distances and aperture angles - are taken from Table 4.6. Within the beam aperture angle, a uniform emission intensity was assumed, and no emission at all outside that angle. Since the light sources will be lasers, only monochromatic beams were simulated, so the transparency of the PC can be described by a single parameter, Λ , the elastic scattering attenuation length. We considered several values of Λ , from 2 m to 5 m,

in steps of 50 cm. The attenuation lengths of PC for $\lambda=394$ nm and $\lambda=355$ nm are, respectively, $\Lambda=5$ m and $\Lambda=2.5$ m, as measured by spectrophotometric methods with small samples.

As any attenuation phenomenon, we expect the monochromatic light intensity $I(x, \Lambda)$ at distance x from the source to have an exponential distribution in function of distance. However, since elastic scattered photons can be detected by the target PMTs and the fraction of beam solid angle determined by the PMT varies with distance, the intensity function should include a geometrical efficiency, ϵ_G and a scattered photon fraction efficiency, ϵ_S . So, we have

$$I(x, \Lambda) = I_0 \cdot e_G(x) \cdot (1 - e_S(x, \Lambda)) \cdot e^{-\frac{x}{\Lambda}} \quad \text{Eq. 4.11}$$

where I_0 is the intensity of the light beam at $x=0$ (origin).

The geometrical efficiency is the fraction of direct light that actually hits the photocathode. In theory, this can be calculated as the fraction of solid angle determined by the PMT surface, taking into account the beam aperture, the distance and the incidence angle. In practice, the beam aperture is not a well-defined parameter, because the angular distribution of the beam light is very spreaded. Our approach is to measure directly the values of $\epsilon_G(x)$ for the six fiber-PMT distances by means of a series of pre-calibration measurements during the early detector runs with nitrogen and water. In both these cases $\Lambda = \infty$, so the geometrical efficiencies are obtained from the measured intensities after a correction for the PC refractive index. In this Monte Carlo analysis, in order to obtain $\epsilon_G(x)$, the elastic scattering was “turned off”.

On the other hand, the fraction of scattered photons $\epsilon_S(x, \Lambda)$ depends on Λ and so, cannot be “calibrated”. Figure 4.28 shows the fraction of detected photons that suffered one or more elastic scattering processes along their path towards the target PMT, for attenuation lengths that vary from 2 m up to 5 m.

We can see that there is a strong dependence of the scattered fraction on the attenuation length, but the most relevant result is that the dependence on the target

distance is very weak. Along the whole range of distances from 2.0 m to 7.9 m, the fraction of scattered light presents only small increases, from 1 % to 4 %. We interpret these small variations as due to the fact that the accumulated scattering probability increases with distance x according to $1 - e^{-\frac{x}{\Lambda}}$, but this effect is counter-balanced by the higher acceptance of the PMTs at short distances. In addition, we have selected the aperture angles of the beams in function of the distance, in order to illuminate a spot not much larger than the pmt photocathode surface. So, from the total scattered light, the fraction that is actually detected is smaller at large distances.

Now, if we assume that $\epsilon_s(x, \Lambda)$ does not depend on x , after correcting for the geometrical efficiency $I(x, \Lambda)$ depends on x only through the exponential factor, all the other factors being normalization constants.

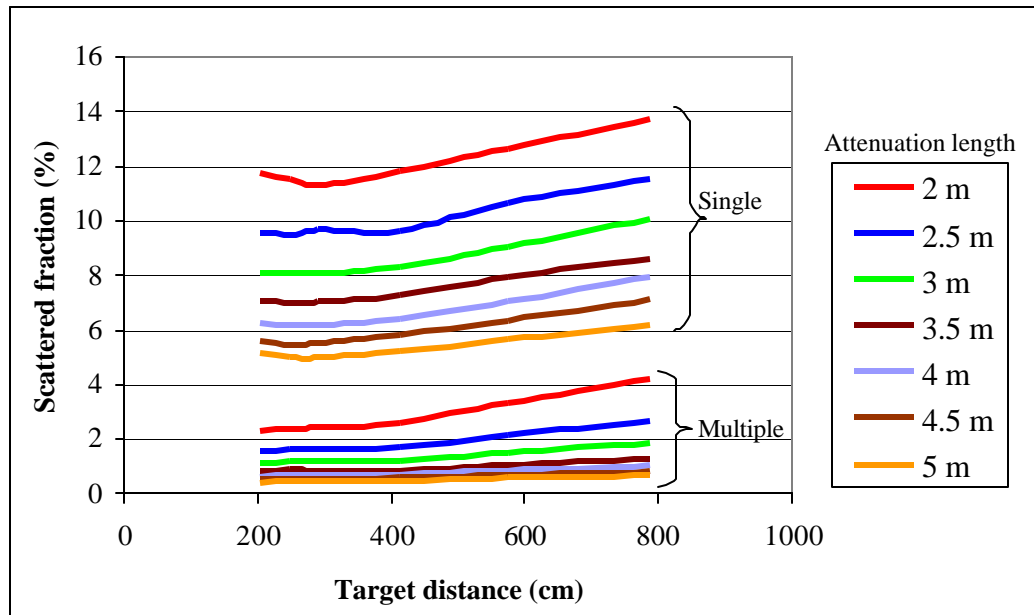


Figure 4.28 Fraction of detected photons that suffered one (single) or more (multiple) elastic scattering processes on their path from the oblique module to the target. Results from Monte Carlo simulations.

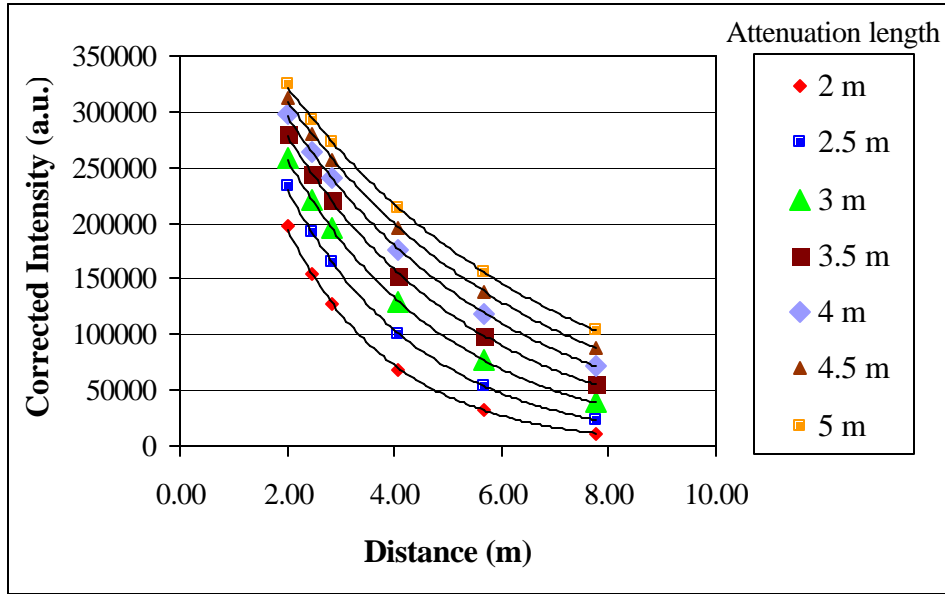


Figure 4.29 Intensity of detected light in function of the target distance, for several nominal attenuation lengths. The intensity is corrected for the geometrical efficiency. The lines correspond to exponential functions fit to the simulation results using the least squares method.

This is shown in Figure 4.29, that represents the values of detected intensity corrected for the geometrical efficiency, in function of the target distance. No correction for the scattered fraction was applied. The simulated data sets corresponding to the different nominal attenuation lengths were fitted with exponential functions using the least squares method. The value of $\chi^2/\text{d.f.}$ was 1 for all data sets and the attenuation length was obtained from the fit with an error of 2 % with respect to the nominal value given as input to the simulation. The situation will clearly be more complex in Borexino. Nevertheless, these fits confirm that, due to the right choice of beam apertures, the dependence of the scattered fraction on the distance is weak enough so that we can neglect it, strongly simplifying the analysis method.

Calibrations with radioactive sources

In order to complete the panorama of the Calibration and Monitoring efforts for Borexino, this Chapter presents the goals and design of the systems for the calibration with radioactive sources. In the same way as for the optical calibration systems, these systems are distinguished between internal and external:

- The internal source system carries out the insertion of radioactive sources in the Inner Vessel, as well as the internal fiber for optical monitoring. This system was developed by our collaborators at the Virginia Tech University.
- The external source system allows high activity γ sources to be positioned at the level of the PMTs. This system was developed in collaboration with Virginia Tech. We carried out the initial feasibility studies with Monte Carlo simulations of the expected signal from the source, the selection and procurement of the source itself, while Virginia Tech was responsible for the design, production and installation of the insertion hardware design.

The use of radioactive sources in the Borexino calibration is complementary to the optical methods, in order to obtain several important parameters, such as the absolute energy calibration, α/β discrimination efficiency, and the radial profile of external γ showers. The calibration and monitoring operations will be scheduled in succession according to the radioactive contamination risk of each method, each step being carried out only if the desired accuracy was not obtained with the preceding ones. Naturally, the calibration with internal radioactive sources, and in particular, long-lived ones, is the last step in the operational schedule.

In addition, a check of the overall neutrino detection efficiency is possible by using a high intensity neutrino source. A ^{51}Cr source ($^{51}\text{Cr} + e^- \rightarrow ^{51}\text{V} + \nu_e$) has a

half-life of 27.7 days and produces monoenergetic neutrinos in the energy range of ^7Be neutrinos: 0.75 MeV (90 %) and 0.43 MeV (10 %). A source with an activity of 1.7 MCi, comparable to the one used in the performance tests of the GALLEX experiment [⁸⁰], would produce about 900 counts in a month of data-taking [⁸¹], comparable to the solar neutrino rate. Confirmation of the Borexino results through the source measurement would be particularly relevant in the case of the Small Mixing Angle solution, where the expected rate is low (10 events/day). Procurement and activation of the ^{51}Cr source is under study by the Heidelberg group.

5.1 Internal sources

Calibrations with radioactive sources inserted in the active scintillator volume (internal sources) are planned in Borexino in order to measure as reliably as possible the differences in energy scale between the different particle types – α , β and γ - and the particle identification efficiencies at different energies. Following the experience of CTF, source calibration will also supply important data for position resolution and energy uniformity studies, now as a complement to the internal laser measurements.

5.1.1 Types of sources

Radioactive sources consisting of a quartz vial containing Radon-loaded scintillator were used successfully in CTF [⁸²], demonstrating its advantages:

- Direct contact between the nuclide and the scintillator, necessary for a reliable α and/or β energy calibration;
- Emission of both α and β particles from the source, allowing for an absolute calibration of the particle discrimination efficiency;
- ^{222}Rn , with a 3.8 days half-life, is sufficiently long-lived to permit it to be used over a period of days, yet it decays away quickly enough that it doesn't pose a risk for long-term contamination;
- The delayed coincidence between the decays of ^{214}Bi and ^{214}Po , short-lived ^{222}Rn daughters, allows a good identification of the

source signal from the detector background, even with a low activity. Typical initial activities of the CTF sources were 1 Bq. For these reasons, a source based on ^{222}Rn is the main option also for Borexino, but additional isotopes will be considered.

The long-lived isotopes from the initial segments of the ^{238}U and ^{232}Th chains would supply excellent calibration points for low energy α identification efficiency but the use of sources based on these isotopes in Borexino is still an open option.

Sources based on Phosphorus or Sulfur would allow a direct γ/β quenching efficiency measurement. The possibility to have them in a chemical form compatible and soluble in the Borexino scintillator is under study.

5.1.2 Insertion and positioning mechanisms

In order to guarantee its cleanliness, the insertion process will be done inside a class 10 clean room built for this purpose on top of the Water Tank. For radiopurity reasons, no fixed supports can be attached inside the IV and the access tube must be small (7.66 cm diameter) to limit the quantity of ancillary parts material. Due to these constraints, it is difficult to know the position of the tip of a 4 m long arm with a precision better than 5 cm, the requirement for an accurate position calibration. The adopted solution consisted in determining the source position with a separate location system, independent from the insertion and positioning system.

The positioning system is made from a set of hollow stainless steel rods with small negative buoyancy in PC. Once attached to one another and inserted in the detector, a hinge mechanism operated by a nylon string allows the arm to bend at 90 degrees. With such a method, the positions available for calibration will be situated in coaxial cylinders. As an additional safety measure against IV damage, both the radioactive sources and the optical fiber terminations will be mounted on a spring attached to the tip of the rod.

In order to ensure the best cleanliness, the source insertion hardware is kept in the clean room inside an insulated glove box filled with high-purity nitrogen. Since the IV is kept at an overhead pressure of about 2 m of PC in order to avoid scintillator contamination in case of small IV leaks, the source and the insertion hardware must pass through a pressurized chamber. A sliding seal with Viton O-rings allows the communication between the storage glove box and the pressurized insertion chamber.

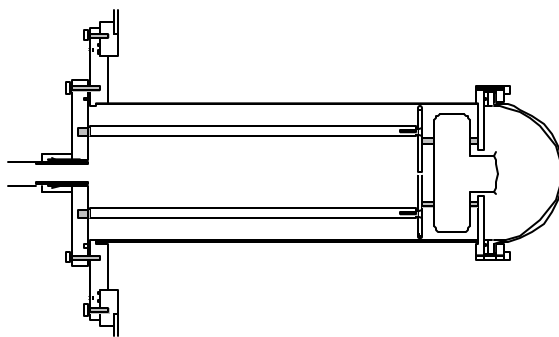


Figure 5.1 CCD camera mounting system.

The location system consists of a set of six digital photographic cameras (CCDs) mounted on the stainless steel sphere and a light-emitting diode (LED) mounted near the source, at the tip of the insertion rod. Combining the images obtained with at least two of the CCD cameras, all three coordinates of the source position can be found. Redundancy in the number of cameras is needed due to the shadowing of the diode light by the insertion arm in some positions and also to tolerate possible failures. The positions for CCDs have been chosen as the points in the sphere that intersect three straight lines forming an orthogonal set of axis and, in particular, those that stay in two horizontal planes.

In order to observe all points inside the IV, the camera must be able to collect light with an angle of incidence up to 43 degrees. To overcome the problem of loss of angular acceptance of the camera due to the different index of refraction of PC, the camera case window is spherical. Actually, the distance from the CCD to the window is calculated so that light coming from the whole region inside the 11 m diameter Outer Vessel can be observed. Figure 5.1 represents a scheme of the

CCD mounting system, where it is shown the half-spherical window that allows for a wide-angle coverage and a significant distance from the SSS, in order to avoid the shadow from the nearby PMTs.

The radioactivity of the cameras and windows material has been measured [⁸³] at LNGS using gamma spectroscopy and the results are reported in Table 5.1. Considering that the CCDs are placed at approximately the same distance from the IV as the PMTs, we compare these values with PMT activity. From the Table, we can see that the ²³⁸U and ²³²Th activity of the cameras is negligible with respect to the PMTs, but the ⁴⁰K activity is not. However, the ⁴⁰K rate accounts for just 5% of the total PMT external background rate, so the contribution of the cameras to the total external background can be estimated in 7 % of PMT contribution, a tolerable value.

	²³⁸ U [Bq]	²³² Th [Bq]	⁴⁰ K [Bq]
Cameras	1.3+/-0.2	2.0+/-0.2	6.0+/-1.5
Lenses	0.20+/- 0.02	0.16+/- 0.04	44+/-3
Glass window	3.0+/-0.6	0.5+/-0.1	970+/- 150
Sum	4.5+/-0.7	2.7+/-0.3	1020+/- 151
Total (Sum x 6)	26 Bq	16.2 Bq	6.1 kBq
PMTs	3 kBq	450 Bq	4.2 kBq

Table 5.1 Radioactivity content of the positioning cameras and associated components. The activities are referred to a single piece. In the two bottom lines we compare the total activity of the 6 cameras with the activity of the 2200 PMTs.

In order to avoid long-term damage to the PMTs by turning them on and off frequently, they will be kept on while the source is inserted and located, so the diode light should be as weak as possible and in a wavelength range as far away from the photocathode sensitive region as possible. Infrared diodes would have been the right choice, but pseudocumene has strong absorption bands in the

infrared [⁸⁴], so a standard red diode was chosen. The response of the PMTs to a weak red diode pulse was tested both at LNGS and Virginia Tech. The PMT desaturated less than 1 s after the diode was turned off, and no changes were observed in the quantum efficiency, in the transit time jitter or in the amount of afterpulses. So, at least for short term exposures, PMTs do not suffer any damages from the use of red diodes inside the detector.

5.2 External source monitoring

The calibrations with an internal radioactive source imply a certain risk of contamination that is not negligible in a detector such as Borexino, that has the highest radiopurity standards. As a complementary method to the internal sources, the collaboration suggested the use of γ -emitting sources located outside the sensitive detector volume in order to calibrate the detector without any contamination risks.

Since the radiation must cross some meters of passive shielding material (the buffer liquid), the isotope should be a γ -emitter, and the source activity was expected to be high, with respect to any source that could be used for the internal calibrations. The determination of the necessary activity was done by Monte Carlo simulation of the γ shower propagation in the detector.

It was soon realized that the energy and position distribution of the events produced by an external γ source would closely resemble the external background distributions, so the focus of the source measurements became the monitoring of the position reconstruction and external background rejection efficiency.

So, the goals of the external source calibration can be summarized as follows:

- Determine the position reconstruction efficiency by comparing the measured radial distribution of the events with the Monte Carlo predictions.
- Monitor the stability of the position reconstruction cut by periodically measuring the event rate with different radial cuts. If the detector is stable,

the difference in event rate should be exactly predicted by the source half-life.

- Supply an energy calibration point.

The monitoring of the position reconstruction efficiency is particularly important for the evaluation of the amount of residual external background events that are mis-reconstructed and tail into the fiducial volume. A realistic evaluation of this number can be done only with this type of source.

The stability-monitoring of the fiducial volume cut is important to check the validity of the solar neutrino signal time variation measurements. Time variations are the signature for neutrino oscillations in the LOW and Vacuum solutions, but also for the solar origin of the signal. In fact, due to the Earth orbit eccentricity, a yearly variation of 7% is expected. In order to guarantee a good sensitivity to this variation, we require a precision of 1% or better on the determination of the number of counts in each periodical calibration measurement. So the source activity should be high enough to produce at least 10000 calibration events in a short time period, no longer than a day, and the definition of “calibration events” should be such to allow a signal/noise rate of at least 100.

5.2.1 Monte Carlo simulations of the expected performance

The external sources will be located at over 2m from the scintillator volume, that correspond to more than 5 interaction lengths for γ -rays with energies of 2-3 MeV. So the γ detection efficiency, that is, the fraction of emitted γ -rays that reaches the scintillator and produces useful calibration events, is expected to be very small.

The feasibility of the method depends on whether it is possible to obtain a significant event rate with a standard source, small enough to be inserted in a straightforward way. This question was addressed by performing Monte Carlo simulations of the propagation of the γ showers in the detector.

After verifying that the detection efficiency for γ -rays with energies below 2 MeV was too small for a practical measurement, we verified that the only standard, long-lived source with a high energy γ decay was ^{228}Th [49]. The half-life of ^{228}Th

is 1.9 years and, since it belongs to the radioactive chain of ^{232}Th , the detailed list of the decays of its daughters can be found in xxx and xxx, in Chapter 2. For our purposes, the important decay is that of ^{208}Tl , that emits a 2.6 MeV γ -ray. All other isotopes produces α and β particles, that are blocked by the source shielding, and low energy γ -rays, that do not reach the scintillator. A fraction of the β particles can produce Bremsstrahlung photons, but their energy and rate are small with respect to the 2.6 MeV γ -rays from ^{208}Tl .

From the Monte Carlo simulations of the propagation of the ^{208}Tl γ -rays, we obtained the position and energy distributions shown in Figure 5.2 and Figure 5.3. The results were normalized for an equivalent ^{228}Th activity of 200 μCi , the highest activity that we could find in a commercially available source. The γ -source radial position was assumed to be at 635 cm from the center, the same distance as the edge of the light concentrators.

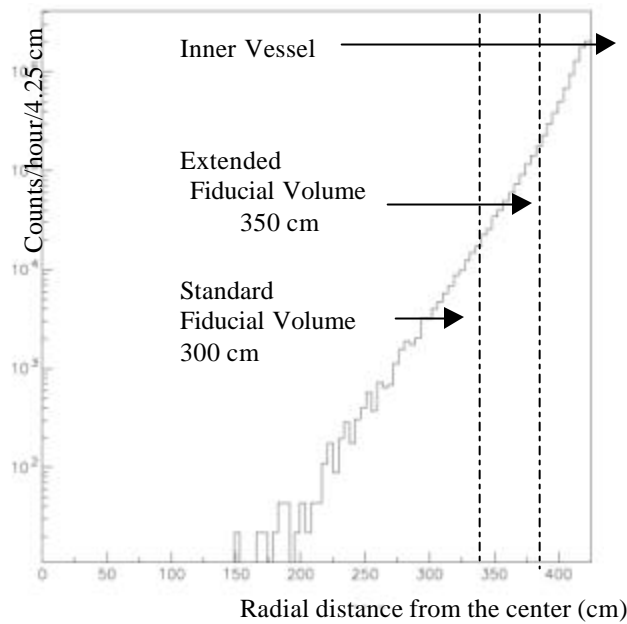


Figure 5.2 Radial distribution of the simulated events from a 200 μCi Th source placed at 635 cm from the center.

As expected, the radial distribution has a strong variation, with the overwhelming majority of events concentrated in the outer regions of the scintillator volume, just

like for the external background (the radial distribution of the external background was shown in Figure 2.19). However, the number of counts/hour in the inner most regions is far from negligible.

The energy distribution presents large variations according to the detector region selected. In the whole scintillator volume (solid line), there is a continuous distribution on all energies, from 0 to 2.6 MeV, while in the 350 cm fiducial volume, the low energy events have been strongly reduced. In both cases, the 2.6 MeV γ peak is in evidence and the edge of the spectrum is well defined, so this point can be used for energy calibration.

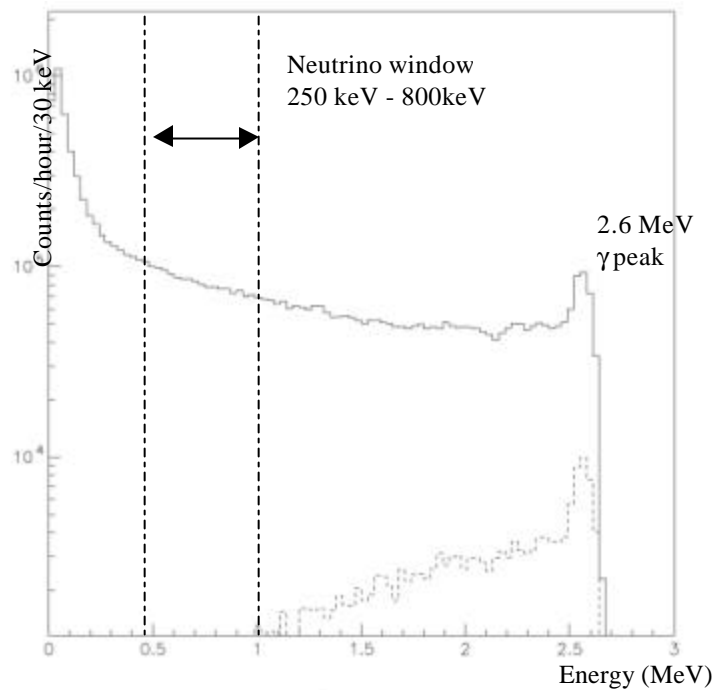


Figure 5.3 Energy distribution of the simulated events from a 200 μCi Th source placed at 635 cm from the center. The solid line refers to the events in all the scintillator volume, and the broken line to events deposited in the extended fiducial volume, at a radius lower than 350 cm.

Table 5.2 presents a summary of the count rates obtained in the standard ($R < 3.0$ m) and extended ($R < 3.5$ m) fiducial volumes, in the energy windows of $250 \text{ keV} < E < 800 \text{ keV}$ and $800 \text{ keV} < E < 3 \text{ MeV}$. The signal-to-noise ratio is calculated considering the total rates of neutrino signal, internal and external background as noise for the source calibration.

Detector	250 keV < E < 800 keV		800 keV < E < 3 MeV	
Region	Rate (events/hour)	S/N	Rate (events/hour)	S/N
R < 3.5 m	180	14	5900	$1.3 \cdot 10^4$
R < 3.0 m	4	0.5	670	500

Table 5.2 Predicted rates (in events/hour) and signal-to-noise (S/N) ratio in different detector regions and energy windows for a 200 μCi ^{228}Th source located at 635 cm from the center (near the PMTs).

From these results, we can see that only the high energy events can allows us a signal-to-noise ratio higher than 100. In this case, in the standard fiducial volume, we need about 15 hours to accumulate a 10 000 events, for a 1 % statistical error. In the extended fiducial volume, this period is shortened to 2 hours, allowing a stability check between day and night rates.

5.2.2 Design of the insertion system

The design of the external source insertion system was guided by the following requirements:

- The source should be located as close as possible to the scintillator volume, in order to minimize the required source activity.
- The source must be inserted and extracted without opening the scintillator containment system, i.e., the Nylon Vessels and the Stainless Steel Sphere. In this way, any risk of scintillator contamination is eliminated.
- Several positions in the different detector regions should be available, for redundancy cross-checks.
- The exact source position must be unambiguously known.

In the final design, the sources will be located in 16 positions of the detector, all at the distance of 635 cm from the center of the detector, and the handling operations are performed from the top of the External Tank. A schematic diagram of one of

the 16 modules of the insertion system is shown in Figure 5.4. A stainless steel insertion tube, shown in Figure 5.5, is mounted on the SSS, and protrudes 50 cm towards the inside of the detector. The innermost end of the tube is closed. A semi-flexible tube, made of polyethylene, connects the open end of the stainless steel tube to the external feed-through, across the water buffer region. The tube will be filled with mineral oil, in order to prevent it from collapsing due to the water pressure. The entrance point for the source is the external feed-through, mounted on a flange on the top of the External Tank, accessible by a walkway. The source is pushed into the tubes by a flexible metallic tape until it reaches the closed end of the stainless steel tube. The source container is metallic, so there is an electrical contact when the source is in position. A reservoir coupled to the external feed-through collects the excess of mineral oil displaced by the source and tape insertion.

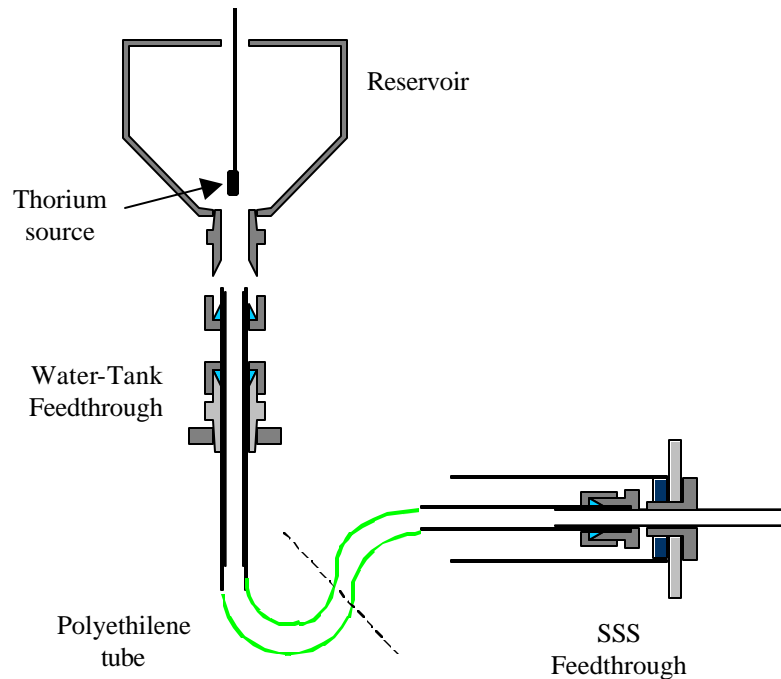


Figure 5.4 Diagram of the external source insertion mechanism.

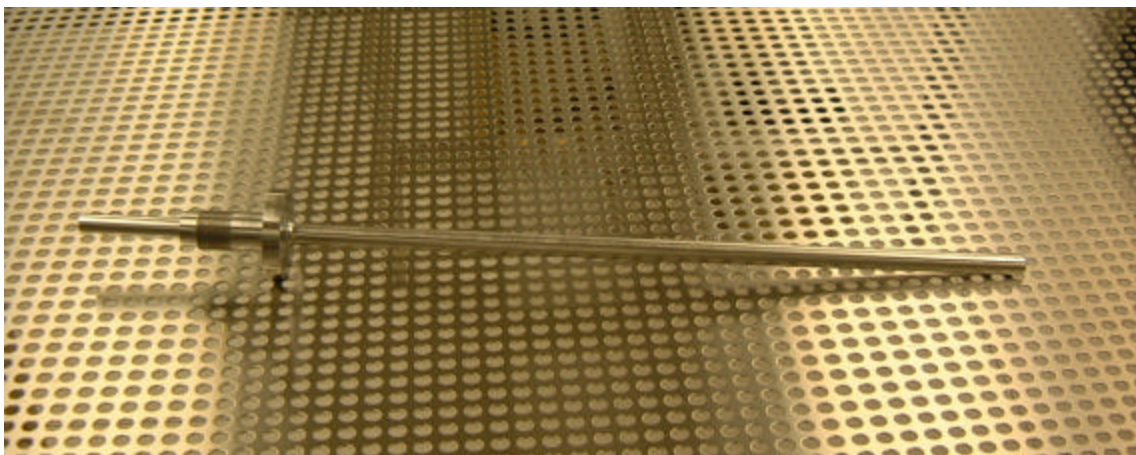


Figure 5.5 Stainless steel tube for the external source insertion. The piece on the left is the feed-through that is inserted and sealed in the SSS hole. The tube length, from the feed-through to the closed end on the right, is 50 cm.

The 16 locations for the insertion modules were chosen along a detector meridian, that is, lying on vertical plane that contains the center. In this way, possible up-down asymmetries of the detector efficiency can be monitored.

Sensitivity of Borexino to ^7Be Neutrinos

In this Chapter we discuss the sensitivity of Borexino to the ^7Be solar neutrinos, by studying the energy spectrum analysis with analytic functions to describe both the neutrino and the background distributions. The expected neutrino and background energy spectra are generated by means of Monte Carlo simulations, and considers different experimental conditions, in terms of scintillator radiopurity and detector efficiency. Different ^7Be neutrino rates were also considered, according to the neutrino oscillation probabilities predicted by the presently allowed scenarios. The flexible approach made possible by this method allowed a better estimation of the errors than in previous analysis methods.

6.1.1 General Approach

Considering the different types of background in the future analysis of the Borexino experiment, we can distinguish the following successive steps when passing from raw data to the ^7Be neutrino flux.

1. Rejection of the muon events. The muon veto system will use PMT time distributions, the ratio of no-concentrator to concentrator PMT hits and the coincidence between inner and outer detector signals in order to reduce the residual rate to less than 0.5 events/day in the neutrino window ($250 \text{ keV} < E < 800 \text{ keV}$).
2. Rejection of external background through position reconstruction. About 0.2 residual events/day are expected in the 100 ton fiducial volume.
3. Rejection of the ^{14}C background by establishing an energy threshold of 250 keV. Less than 0.5 residual events/day are expected.

4. Assuming a scintillator contamination of 10^{-16} g/g of ^{238}U and ^{232}Th , the internal background in the neutrino window is reduced from 120 ev/day to 20 ev/day by applying the following cuts:
 - a. Delayed Coincidences;
 - b. Pulse-Shape discrimination;
 - c. Statistical subtraction.
5. Fit to the energy spectrum in order to separate the ^7Be neutrino signal from the residual background counts and from the signal due to other neutrino sources.

The criterion followed in this sequence is to reject first the events originated outside the scintillator volume, and then the internal background that can be easily identified in the energy spectrum (^{14}C). The most critical steps in the analysis are the internal background cuts, because they have a limited efficiency and the fit to the energy spectrum, that requires a good knowledge of the spectral shapes of the several components. The ^{14}C content of the liquid scintillator will be screened in CTF prior to the filling and the muon events are monitored by a dedicated system. An independent monitoring of the position reconstruction efficiency and external background rejection will be performed with an external γ source (see Chapter 6). Therefore, the expected residual counts due to ^{14}C , muons and external background are much less than the residual internal background counts, so they will be neglected in order to simplify our approach to the study of the sensitivity of the neutrino signal measurement.

In order to identify the neutrino signal on the basis of the “Compton-like” edge recognition in the energy spectrum, our strategy is to complement the detailed description of all the expected shapes with a flexible approach that allows the method to better adapt itself to unexpected and not easily reproducible effects. The method is based in a description of the ^7Be neutrino recoil electron spectrum and that of the several background contributions by the theoretical shapes, appropriately convoluted with a gaussian function in order to take into account the detector resolution. Such a method allows extra degrees of freedom in the description of the signal, because, besides the weight of each component, there

can be other free fit parameters, such as the energy scale, the resolution and parameters relevant to the equilibrium of the ${}^{238}\text{U}$ and ${}^{232}\text{Th}$ chain. This approach is complementary of, and does not replace, a Monte-Carlo based analysis. It should be particularly adapted during the calibration and early phases of the data-taking, in order to quantify possible sources of systematic errors.

6.1.2 Neutrino energy spectrum

The function that reproduces the energy spectrum of the recoil electrons scattered by ${}^7\text{Be}$ solar neutrinos (${}^7\text{Be}$ neutrino function, for short) is the convolution between the differential cross section $\sigma_v(t)$ for ν -e elastic scattering (Eq. 2.6) and a gaussian describing the detector resolution, normalized to the total expected counts:

$$f(x) = A \int_{-\infty}^{+\infty} \frac{1}{\sqrt{2p} s_{res}} \exp\left(-\frac{(x-t)^2}{2s_{res}^2}\right) \cdot s_n(t) dt \quad \text{Eq. 6.1}$$

A is the signal amplitude (total number of counts), x and t are the kinetic energy variables and $\sigma_v(t)$ is normalized and evaluated at the neutrino energy $q=0.866$ MeV. When integrating, the dependence of the resolution σ_{res} on the energy variable t must be taken in to account. Since

$$\frac{s_{res}(t)}{t} = \frac{\sqrt{n}}{n} \quad \text{Eq. 6.2}$$

where n is the number of detected photoelectrons, we get

$$s_{res}(t) = \frac{t}{\sqrt{n}} = \frac{t}{\sqrt{t \cdot N}} = \sqrt{\frac{t}{N}} \quad \text{Eq. 6.3}$$

where N is the number of photoelectron per MeV.

In the future data analysis, the N will be obtained from the calibrations and used to convert the information of total measured charge into event energy. However, since the detector resolution depends strongly on N, we prefer to leave it as a free parameter in the analysis (the future calibration information can be used as a bound to the fit). So, in order to avoid converting the data with a number that is

simultaneously an adjustable fit parameter, the data spectrum is left in photoelectrons. This requires that we replace x by x/N in Eq. 6.1.

Since in the real situation of the detector, the energy resolution may have some deviations from the ideal function of Eq. 6.3, in some cases it is useful to arbitrarily consider two different photoelectron scales: one responsible by the energy resolution, N_R , and another, responsible by the energy scale itself N_S . This option allows an easier adjustment of the function shape to possible small deviations from an ideal gaussian resolution, without affecting the energy scale definition (this is not always necessary and both these parameters can be constrained). After these manipulations, the function can be written as,

$$f(x) = A \int \sqrt{\frac{N_R}{2\pi \cdot t}} \exp\left(-\frac{N_R (x/N_S - t)^2}{t}\right) \cdot s_n(t) dt \quad \text{Eq. 6.4}$$

The function is then determined by three parameters: the amplitude (total number of events), normalized with respect to the whole energy spectrum, the energy scale N_S , and N_R , the resolution parameter, both expressed in photoelectrons per MeV. The spectra are fit in a fixed range of number of photoelectrons, from 100 to 325 p.e., corresponding roughly to the 250 keV-800 keV energy window. The variations of N are usually small enough not to change significantly the correspondence between the p.e. range and the energy window.

Before applying the function to a global fit, we tested its validity through a fit of the Monte Carlo spectrum of the ^7Be neutrino signal only. One year of data-taking was simulated. In the Standard Solar Model (SSM) scenario, 46 events/day in the neutrino window are expected, corresponding to 25550 neutrino events in one year in the whole energy range. The fit procedure is carried out by minimization with the least squares method, using the MINUIT software package[85]. The simulated spectrum and the fit function are shown in Figure 6.1. The nominal neutrino amplitude was found within an error lower than 1 %, and the ratio of χ^2 over degrees of freedom ($\chi^2/\text{d.f.}$) was about 1, demonstrating that the analytical

model is essentially correct and capable of describing at least the known effects included in the Monte Carlo simulation.

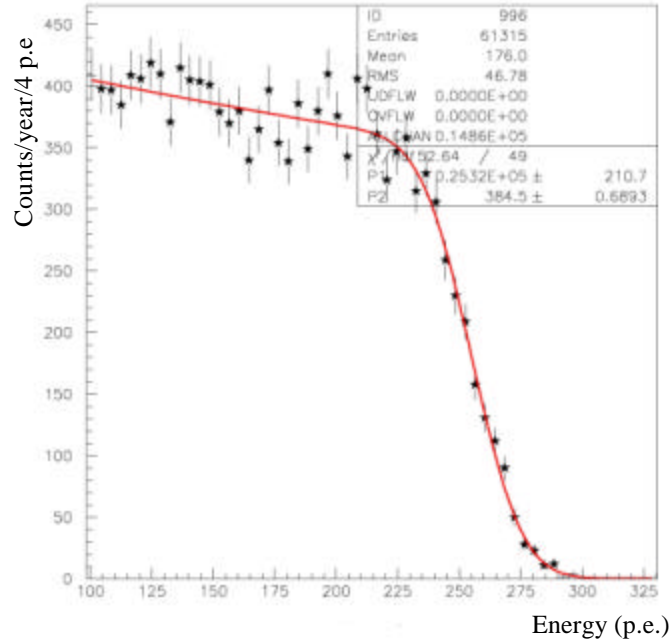


Figure 6.1 MC simulated spectrum (points) and fit function (line) of the ^7Be neutrino signal.

In the Borexino neutrino window, there is also a small, but not negligible, contribution from solar neutrinos of the CNO cycle. These sources produce a continuous spectrum so they have no sharp spectral features in the neutrino window. For this reason, and for the expected low number of counts, as an exception to our analytical approach, we modelled this contribution with a straight line fitted to the Monte Carlo spectrum, both shown in Figure 6.2.

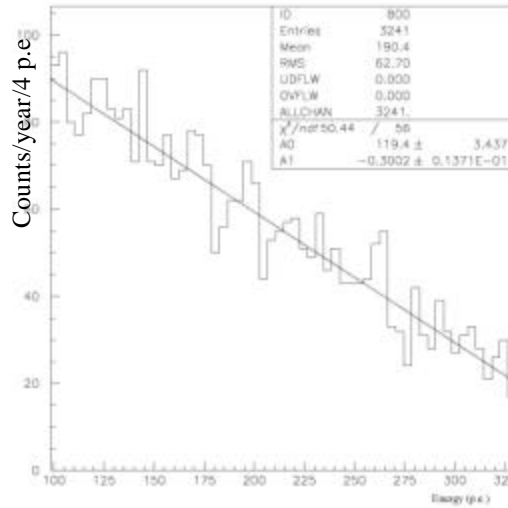


Figure 6.2 Monte Carlo simulation of the recoil electron spectrum due to CNO solar neutrinos. One year statistics. The straight line is the result of a least squares fit.

6.1.3 Background description

The internal background consists of α and $\alpha+\gamma$ events, that produce a discrete spectrum, and β or $\beta+\gamma$ events, that produce a continuous spectrum. The model function for α decays is a simple gaussian, centered on the sum of the β -equivalent “quenched” energy of the specific α particle and the eventual contributions from the γ -rays. For the β decays, we use the theoretical shape of the β^- spectrum, including the corrections for Coulomb screening due to the high Z of the atoms in the ^{238}U and ^{232}Th chain. The function is shifted by $\sum E_\gamma$ if there are contributions from γ -rays and, just like for the neutrino function, it is convoluted with the detector resolution. The model functions for α and β decays are shown in Figure 6.3.

From these functions, the spectrum of the decay of each isotope in the ^{238}U and ^{232}Th chains is built as a weighted sum of all its decay modes with a relative weight above 0.5 %. The relative weights and energies of these decays are listed in Table 2.11 and Table 2.12.

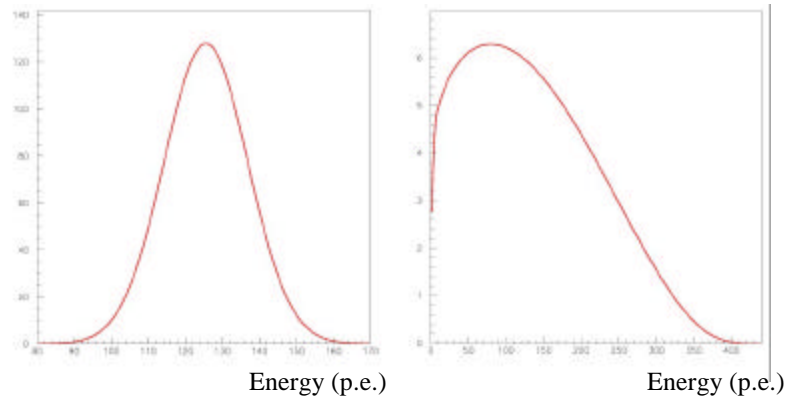


Figure 6.3 Fit functions for the α and β components of the background spectrum.

The design goal for the scintillator radiopurity is 10^{-16} g/g of ^{238}U and ^{232}Th and, since the scintillator is made from oil deposits that have millions of years, it is usually assumed that the radioactive chains are in secular equilibrium, i.e., that all the isotopes have the same activity. Several considerations indicate that actually the equilibrium may be broken, and we specifically discuss the implications of this problem in Subsection 6.2.2.1. If not stated otherwise, secular equilibrium is assumed in all the remaining analyses, which means that the relative weights of all the decays in each chain are constrained with respect to the first isotope, and the total number of counts is given by a single free amplitude.

Figure 6.4 shows the simulated Uranium and Thorium background spectra fitted by the respective analytical functions. In these cases the ratio of χ^2 over the degrees of freedom ($\chi^2/\text{d.f.}$) was good but not so low as for the neutrino function. We interpret this fact as due to the difficulty in finding the best value for the resolution, given the superposition of a large number of gaussians in these spectra. However, the spectral recognition is still good, since the nominal amplitudes are found with very small errors, of 0.5% and 1.1 % respectively, showing that also the background functions are detailed enough to take all the relevant effects into account.

We neglected the background contribution from ^{40}K , since the count rate would be only 3 % of the ^7Be neutrino signal, assuming a contamination near the design goal of 10^{-14} g/g (of K_{nat}).

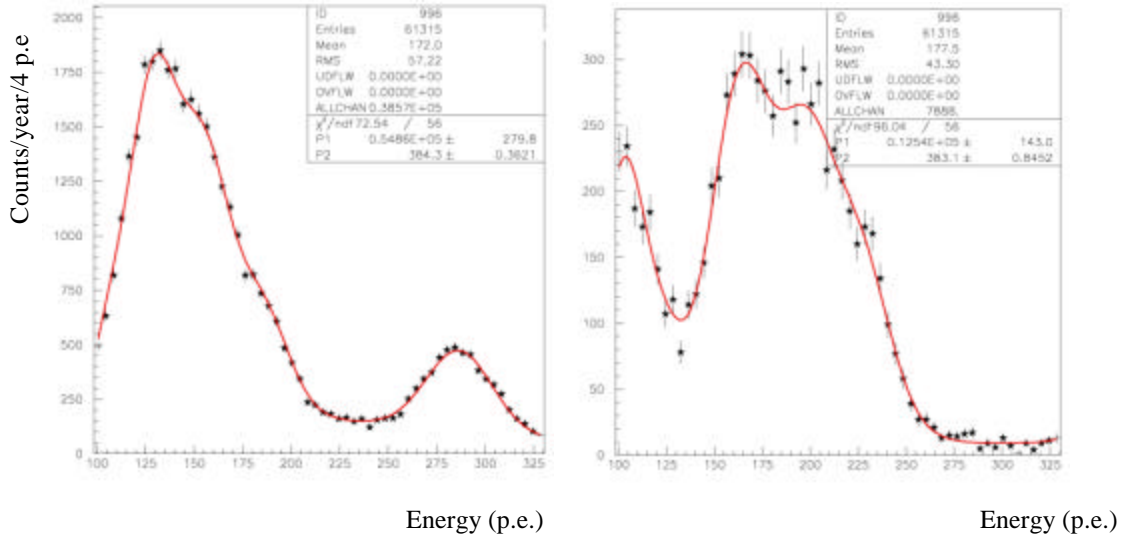


Figure 6.4 Fit of the U and Th chains background. 1 year statistics.

6.2 Sensitivity of the ^7Be neutrino energy spectrum fit

In this section we estimate the expected sensitivity of the ^7Be neutrino flux measurement in Borexino by means of the energy spectrum analysis method we presented in the previous sections. The simulated data consist of the ^7Be and CNO neutrino signals and the background from the ^{238}U and ^{232}Th chains. As we mentioned earlier, we neglect residual background counts from ^{14}C decays, muons, external γ and ^{40}K events. All the spectra refer to one year statistics. The parameters for the evaluation of the detector sensitivity are the relative error used to identify the ^7Be neutrino component of the spectrum, its relative discrepancy with respect to the nominal value used in the data simulation, and the $\chi^2/\text{d.f.}$ of the global fit.

After studying the effect of the application of the internal background fits in Section 6.2.1, we estimate the sensitivity of the neutrino measurement in different oscillation scenarios, and its dependency on the intrinsic scintillator contamination. Finally, in Section 6.2.2, we focus on the effects of possible distortions of the background shape, a problem in which the detector calibrations will play a determinant role.

6.2.1 *Global fits*

The global spectrum is the sum of the simulated energy (photoelectron) histograms of the different components. The global fit function is the sum of the neutrino and background functions described above, in which the energy scale and energy resolution parameters are the same for all components. The free parameters in the fit are the amplitudes for the ^7Be and CNO neutrinos, the amplitudes for the U and Th background and, optionally, the energy scale and energy resolution parameters.

The global fits of the simulated data without considering the internal background cuts are shown in Figure 6.5 and Figure 6.6. The contribution of CNO neutrinos is considered only in the second case.

Even with such a disfavourable signal/noise ratio, in both cases there is a reasonable recognition of the general spectral shapes, since the $\chi^2/\text{d.f.}$ is 1.2. The ^7Be neutrino flux is identified with an error of 6 %. It is interesting to note the role of the energy resolution parameter (P5) in facilitating the adaptation of the function shape to different conditions: when we consider also the CNO contribution that has no particular features, the energy scale parameter (P4) remains exactly the same, while the resolution is slightly adjusted from 382 p.e to 379 p.e.

For the study of the energy spectrum fit after the internal background cuts we reduced both the simulated data counts and the relative weights in the fit function assuming the standard cut efficiencies (obtained from CTF results): 90 % for pulse-shape discrimination (PSD) and 95% for delayed coincidences (DC) and statistical subtraction (SS). No energy or position dependency of the efficiencies was assumed.

The resulting fit is shown in Figure 6.7, where the ^7Be signal contribution (blue) is now clearly visible as the predominant one. The error of the ^7Be neutrino amplitude is decreases from 6.1% to 2.3% after the application of the cuts, a direct consequence of the signal/background ratio increasing from 0.35 to 1.6.

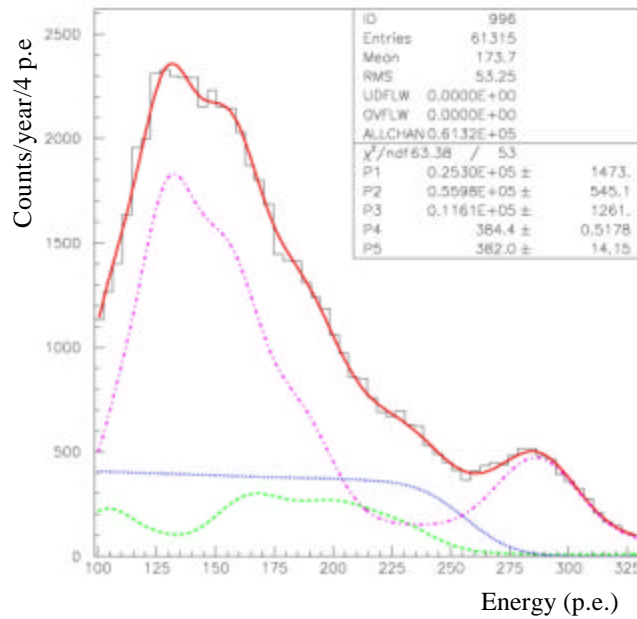


Figure 6.5 Global fit of the ^7Be neutrino signal, the U and Th chain. Without internal background cuts. The plot shows the MC simulated spectrum (histogram), the global fit function (red line), the ^7Be neutrino component (blue), and the ^{238}U (magenta) and the ^{232}Th (green) components.

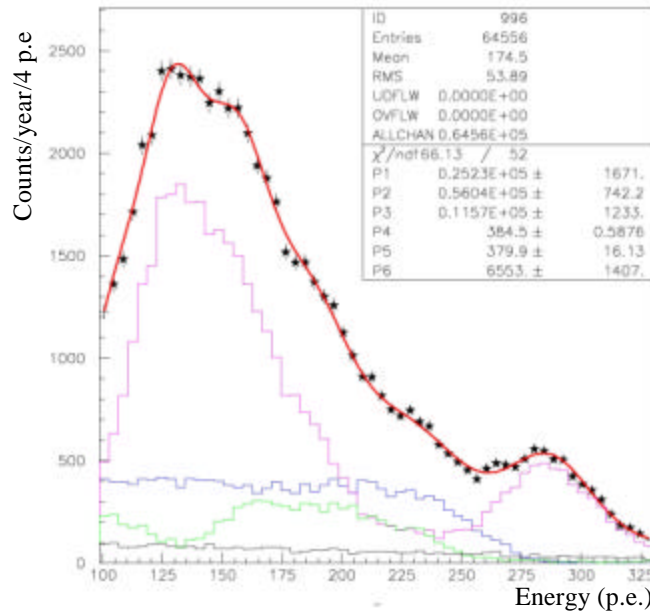


Figure 6.6 Global fit of the ^7Be neutrino signal, the U and Th chain backgrounds and the CNO neutrinos contribution. No internal background cuts were applied. The plot shows the MC simulated spectrum (stars), the global fit function (red line), the ^7Be neutrino component (blue), the CNO neutrinos component (black) and the ^{238}U (magenta) and the ^{232}Th (green) components.

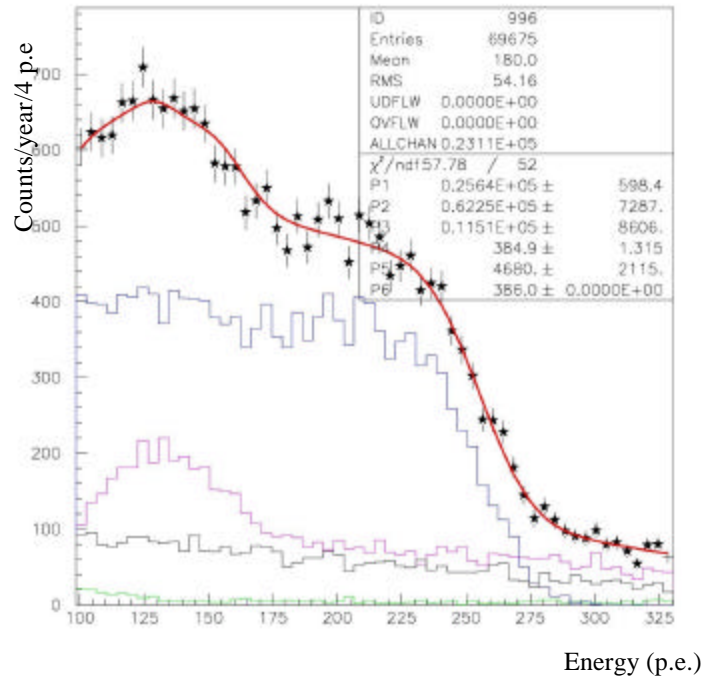


Figure 6.7 Global fit of the ^7Be neutrino signal, the U and Th chain backgrounds and the CNO neutrinos contribution. The three internal background cuts (PSD, DC and SS) were applied. The plot shows the MC simulated spectrum (stars), the global fit function (red line), the ^7Be neutrino component (blue), the CNO neutrinos component (black) and the ^{238}U (magenta) and the ^{232}Th (green) components.

However, the uncertainty for the determination of the background components increased, as shown in Table 6.1, and the energy resolution parameter had to be constrained, in order to obtain the fit convergence. For U and Th the increase in the error is higher than what is expected just from the reduction in statistics. This fact must then be interpreted also as due to the loss of the spectral features that help the fit procedure to better recognize the different components.

Spectral Component	Error on the amplitude determination	
	Before IB cuts	After IB cuts
^7Be	6%	2.3%
U	1.3 %	12%
Th	11%	75%
CNO	22%	45%

Table 6.1 Error on the amplitude determination of the different spectral components, before and after the application of the internal background (IB) cuts.

6.2.2 *Signal/Background issues*

In this section we study different situations in which the Signal-to-Background ratio (S/B) in Borexino is different from the value

$$\frac{S}{B} = \frac{46}{19} = 2.4, \quad \text{Eq. 6.5}$$

expected if the ^7Be neutrino rate is the SSM predicted value, with no oscillations, and the intrinsic scintillator contamination is 10^{-16} g/g:

- Secular equilibrium breaking. If the activities of the different isotopes in the ^{238}U and ^{232}Th chains are not in equilibrium, the expected energy spectrum changes, and so does the ^7Be signal identification.
- Intrinsic scintillator contamination. We discuss how the sensitivity changes from higher ($10 \times$) to lower values ($1/10 \times$) of the internal background.
- Neutrino oscillations. In all the neutrino oscillation solutions to the Solar Neutrino Problem, the expected ^7Be signal rate is lower than the SSM prediction of 46 events/day (going from 10 events/day in the SMA solution to 26 events/day in the LMA or LOW solutions). We calculate the expected sensitivity for each of these solutions.

6.2.2.1 **Secular equilibrium breaking**

In a first approximation, the radioactive chains of U and Th are assumed to be in secular equilibrium, so the amplitudes of the background spectra are usually described by a single parameter, the concentration of the first isotope, ^{238}U or ^{232}Th . However, even if the scintillator is made from oil deposits that have millions of years, under some conditions the secular equilibrium may be broken. In the most conservative approach, only those segments of the chains in which the isotopes have half-lives of about some days or lower should be considered in equilibrium. A more realistic approach should be guided by the following considerations:

- Radon is a very volatile, so its concentration in the scintillator can vary in the several phases of the experiment. Radon contamination may happen during transport and filling of the detector, or during the data-taking itself, by emanation from the nylon vessel. In the first case, equilibrium with the rest of the chains is reached again soon, since the lifetime of ^{222}Rn is about 5 days, but its long-lived daughter ^{210}Pb , remains in the scintillator. In the former case, that of emanation, there is a permanent source and so the equilibrium breaking remains.
- The purification systems can have different extraction efficiencies for different isotopes, according to their chemical properties. Large deviations from the secular equilibrium can be produced if the purification efficiency are different for the long-lived isotopes, in particular U, Th and Ra.

The study of the consequences of secular equilibrium breaking can be done in a simple way with the analytical approach, just by leaving the amplitudes of some chain segments as free parameters, while constraining others. The conservative approach would leave too many free parameters and the energy spectrum fit is simply not possible, so we chose to investigate the most probable scenario: secular equilibrium breaking at the level of Radon. Now each of the radioactive chains of U and Th are divided in two segments, each described by its own independent amplitude. In the U chain, the first segment includes the isotopes from ^{238}U to ^{226}Ra and the second segment from ^{222}Rn to ^{206}Pb . In the Th chain, the first segment includes the isotopes from ^{232}Th to ^{224}Ra and the second from ^{220}Rn to ^{208}Pb .

The simulated background shown in Figure 6.8 assumes the double of the equilibrium contribution from the second segment of both chains, U and Th. The fit indicates some difficulties due to the increase of the number of degrees of freedom, since the $\chi^2/\text{d.f.}$ is 2.7, but the neutrino signal and all the other contributions are identified within the errors (4% for the ^7Be signal, < 2% for both segments of the ^{238}U chain, 13 % and 4 % for the first and second segments of the ^{232}Th chain, respectively, and 25% for the small CNO contribution).

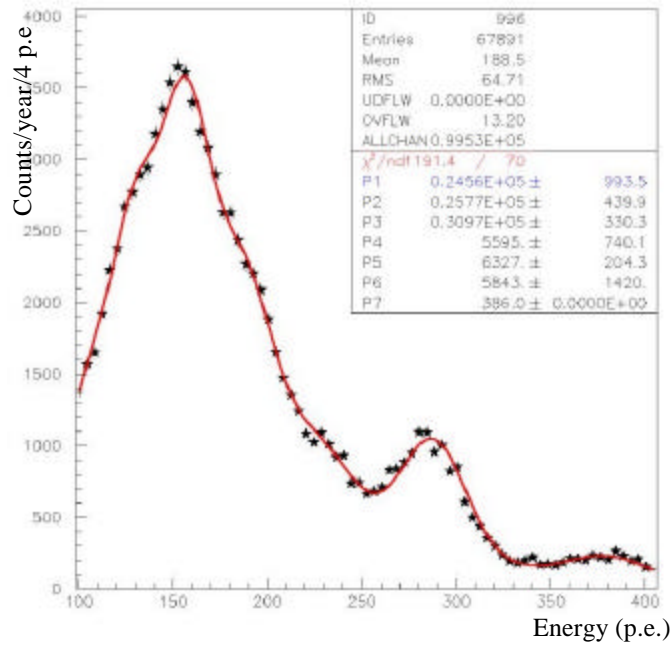


Figure 6.8 Global fit of the ^7Be neutrino signal, the U and Th chain backgrounds and the CNO neutrinos contribution. A higher contribution from the Radon segment of the chains is simulated and the secular equilibrium of the radioactive chains is NOT assumed in the fit. No internal background cuts were applied.

In order to investigate the limit of sensitivity of the energy fit, we produced a series of simulated data spectra in which the weight of each chain segment was increased from 1 to 3. For simplicity, the weight of each segment is the same for the U and Th chains. In the fit, however, no constraint is assumed, so there are four degrees of freedom to describe the U and Th background.

The value of $\chi^2/\text{d.f.}$ for the resulting fits is shown in Figure 6.9, for the range of variation of the weights of segment 1 (U/Th –Ra) and segment 2 (Rn-Pb) of the radioactive chains. No internal background cuts were applied. From this distribution, we can see that the χ^2 parameter grows much faster with the increase of the weight of the first segment than with the weight of second segment. So, we can say that the energy spectrum fit is more tolerant to an increase of the second segment than to an increase of the first segment.

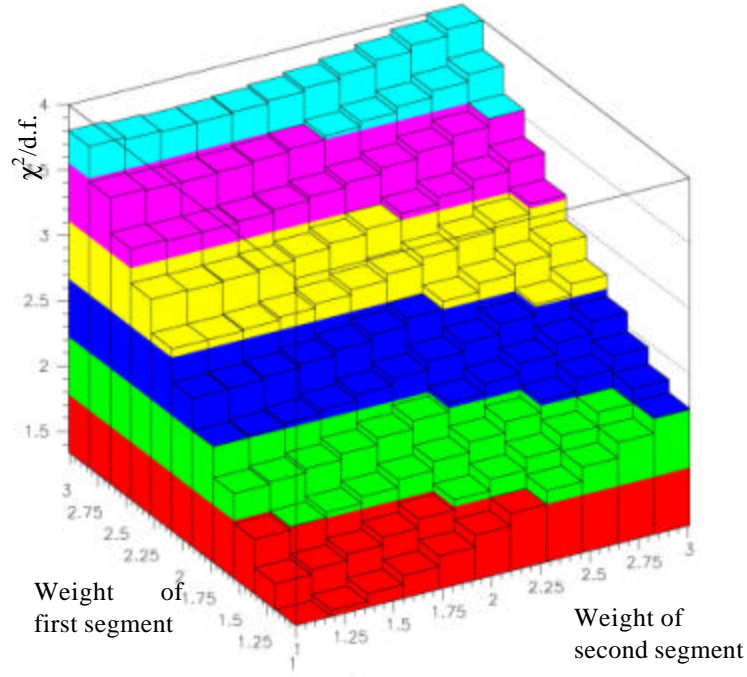


Figure 6.9 Distribution of the $\chi^2/\text{d.f.}$ for the energy spectrum global fits, depending on the weight given to the first and second segments of the radioactive chains of U and Th. The reference weight corresponds to 10^{-16} g/g scintillator contamination.

This result is interpreted in the following way. From the isotope lists of Table 2.11 and Table 2.12, we observe that the first segment of the U and Th chains includes several superimposed low energy α decays, while the second segment has an isolated high energy α peak (from ^{214}Po in the U chain and from ^{212}Po in the Th chain). The single high energy peak can be easily identified, while the superimposed low energy peaks lose their distinctive features, needed for a good recognition by the fit procedure.

6.2.2.2 Scintillator radiopurity and neutrino oscillation solutions

The measurement of the average ^7Be neutrino rate has a strong potential for the discrimination of the oscillation solution with different mixing angles. For the other oscillation solutions (LOW and Vacuum), that differ mainly in the Δm^2 parameter, a strong signature is supplied by the expected time variations.

In fact, as can be seen from Table 2.8, the expected rates for the LMA, SMA and SSM (no-oscillation) are very different. These large differences are due to the low energy of the ^7Be neutrinos, since the largest variations of the ν_e survival probability in the several oscillation scenarios are expected below 1 MeV. In addition, the monoenergetic characteristic of ^7Be neutrinos eliminates the need of averaging the survival probability over a large spectral region.

We investigated the sensitivity of Borexino to the LMA and SMA solutions in 20 different background conditions, assuming a U and Th scintillator contamination 10 times worse and 10 times better than the design goal of 10^{-16} g/g. In all the simulated spectra, the weights of the first and second segments of the U and Th chains are equal, i.e., we consider that the chains are in secular equilibrium. However, we do not assume this in the fit function, the weights of both segments are left as free parameters.

The dependence of the goodness-of-fit parameter, $\chi^2/\text{d.f.}$, is shown in Figure 6.10 and Figure 6.11 that refer, respectively, to the analysis without and with internal background cuts. It is interesting to note that, in both cases, the largest differences between the different oscillation solutions are found when the background is lower than 1×10^{-16} g/g, and we interpret this as due to the larger relative weight of the contribution from CNO neutrinos, which is strongly reduced in the SMA and LMA solutions, with respect to the SSM.

Above 10^{-16} g/g, the χ^2 rises strongly with the background, indicating the intrinsic limit of a low signal-to-background ratio. Figure 6.12 and Figure 6.13 show the errors on the ^7Be neutrino amplitude defined as the fit error (sigma) and as the discrepancy with respect to the nominal value. The comparison between these two values is used as an estimator of the quality of the spectral fit: if the discrepancy is lower than the fit error, we have a reliable estimation of the uncertainties. Above this limit, the fit is still sensitive and the measurement is possible, but the estimation of the error will be more difficult, since the fit procedure itself starts to suffer from systematic effects that prevent it from adapting the correct shapes.

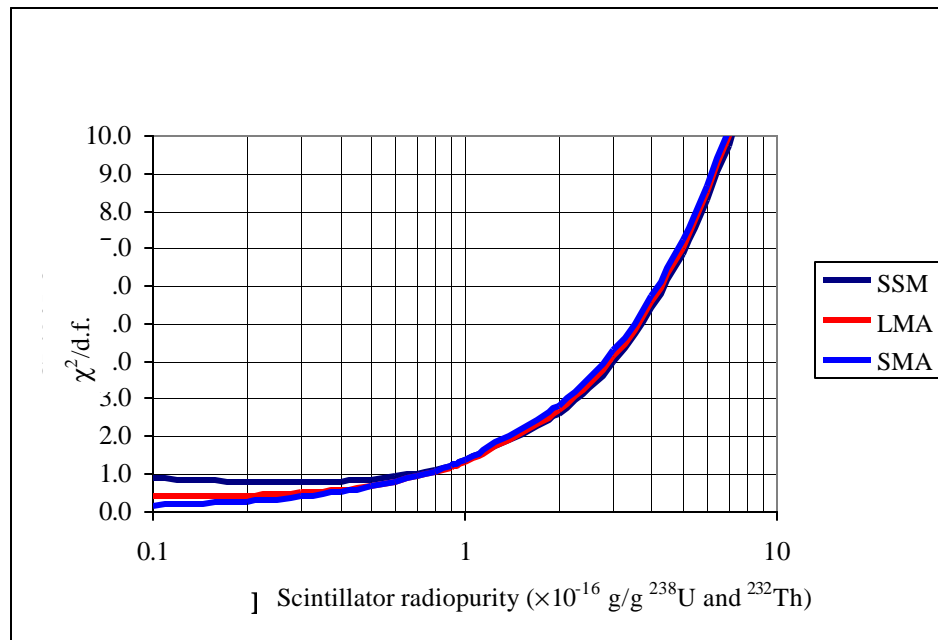


Figure 6.10 $\chi^2/\text{d.f.}$ for the global fit. No internal background cuts applied.

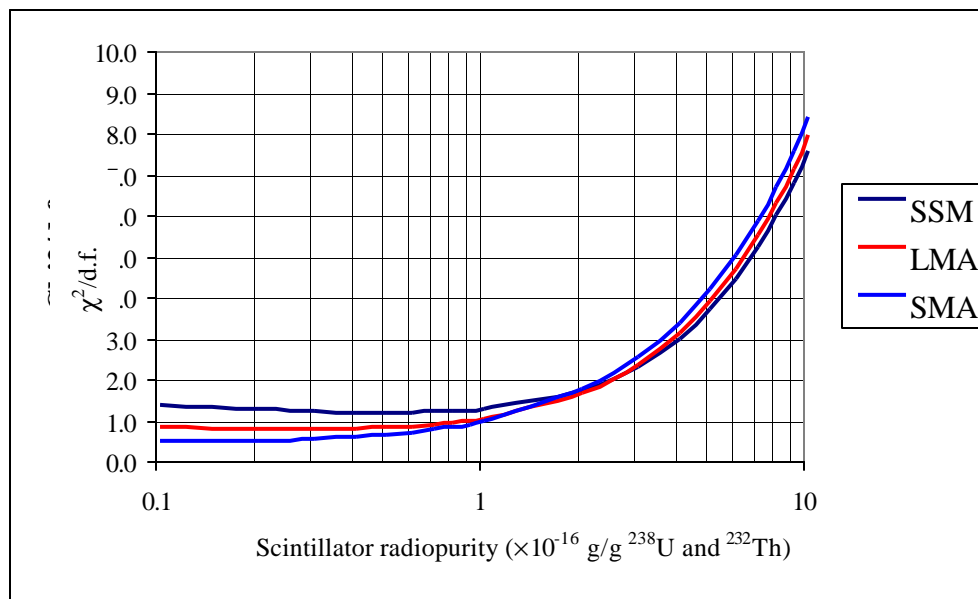


Figure 6.11 $\chi^2/\text{d.f.}$ of the global fit. After internal background cuts.

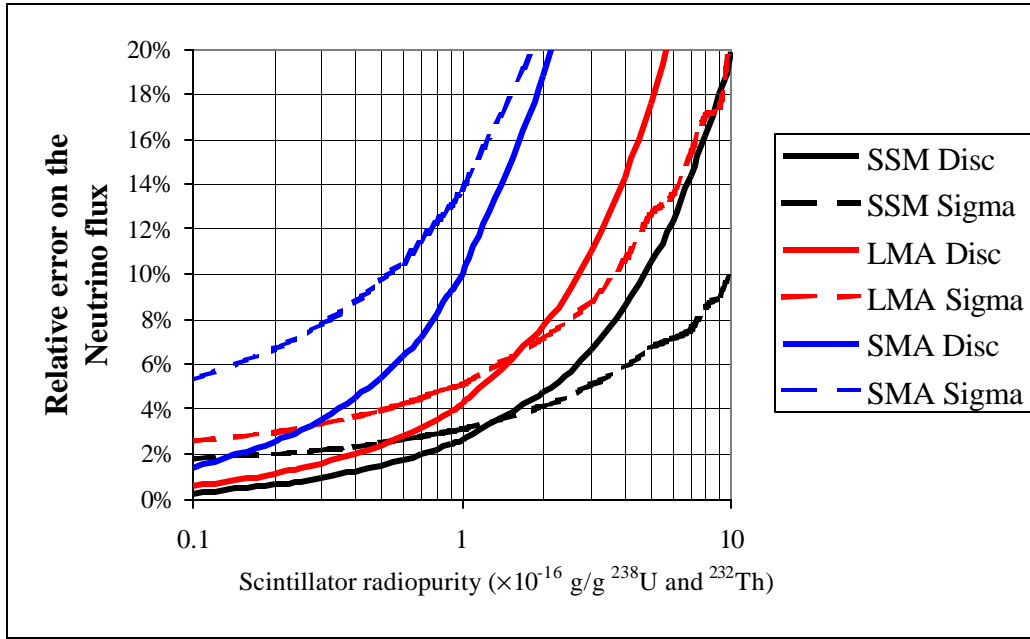


Figure 6.12 Uncertainties on the ^7Be neutrino rate: discrepancy from the nominal value and fit error (sigma). Neutrino rates for SSM and two oscillation solutions SMA and LMA. Without internal background cuts.

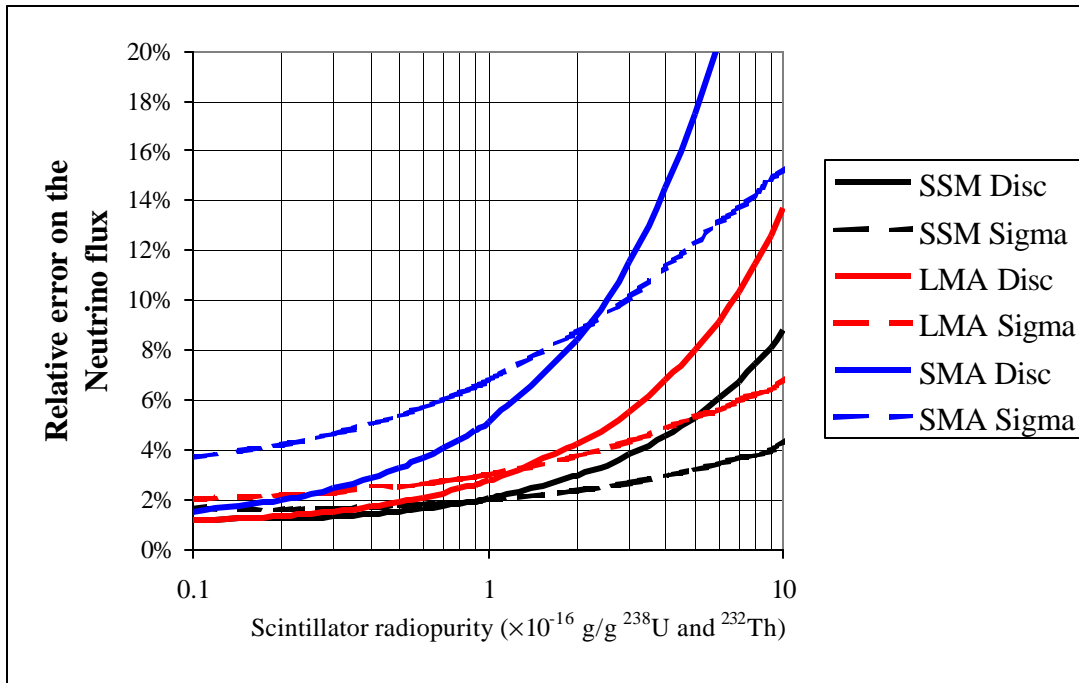


Figure 6.13 Uncertainties on the ^7Be neutrino rate: discrepancy from the nominal value and fit error (sigma). Neutrino rates for SSM and two oscillation solutions SMA and LMA. After internal background cuts.

From the plots, this limit is at about 2×10^{-16} g/g of scintillator contamination in all the situations. The sensitivity to the different oscillation solutions can be appreciated from the errors on the ^7Be neutrino signal identification in this background condition.

	Without cuts	With cuts
SSM	46+/-3	46+/-2
LMA	26+/-2	26+/-1
SMA	10+/-2	10+/-1

Table 6.2 Events rates and uncertainties on the ^7Be neutrino signal identification in the background condition 2×10^{-16} g/g.

The results shown in Table 6.2 shows that the application of the internal background fits does not make the analysis more tolerant to a higher background, but reduces the errors on the neutrino amplitude. In fact, if the cuts are applied, the errors in the rate determination are equal or lower than the theoretical uncertainty in the ^7Be flux prediction of 10 %.

6.2.3 Calibration issues

In the last section, we saw that the application of the IB cuts leads to a worse recognition of the background features. The ^7Be signal was well identified because we fitted the spectrum with the correct background shapes, assuming in the fit function the exact cut efficiencies used in the simulated data. In this section we will examine two effects that can lead to spectral distortions - a poor knowledge of the cut efficiency and β/γ energy quenching - and the role of the calibrations systems in correcting these distortions.

6.2.3.1 PC transparency and Pulse-Shape discrimination

The recognition of the residual background spectral shape requires a good knowledge of the internal background cuts efficiency, because the relative weights of the different decay modes of the U and Th chains must be corrected after the application of these cuts.

We focused our analysis on the pulse-shape discrimination cut because it has the largest impact on the background reduction (see Table 2.13) and, since it is based on the shape of the time distributions, we expect it to depend significantly on the scintillator optical properties. In the case of the delayed coincidences (and the derived statistical subtraction), the characteristic time correlation allows a direct calculation of this efficiency from the data and this efficiency depends mainly on the electronics dead time and the total background rate, so any changes are easily identified.

Monte Carlo simulations

We carried out a series of Monte Carlo simulations in order to evaluate the variation of the pulse-shape cut efficiency with the elastic scattering length of pseudocumene. The time distributions of typical α - β events in the neutrino window, the decays of ^{214}Bi and ^{214}Po , were generated considering the standard spectrum of the elastic scattering attenuation length (shown in Chapter 4) and in five conditions of distortion in which the attenuation length was decreased by 5 %, 10%, 15%, 20% and 25%. The α rejection method is based on the tail-to-total parameter, i.e., the ratio of photons detected above 33 ns to the total number of photons. Events with large tail-to-total ratios, above a certain threshold, are considered as α events. A decrease of the elastic scattering length increases the time-of-flight of the detected photons. This leads to larger tails in the time distributions that mask the differences between α and β scintillation pulses.

If the attenuation length degradation is noticed by the calibrations systems and it is not very large (<20%), this effect can be corrected by using a different tail-to-total threshold. However, if the effect is not corrected, large degradations of the identification efficiency are produced, as it is shown by the results in Table 6.3.

Attenuation length discrepancy (%)	α identification efficiency (%)
0	89
5	83
10	76
15	70
20	62
25	54

Table 6.3 Efficiency of the α identification with the pulse-shape method, according to the distortion of the elastic scattering attenuation length.

The impact of the attenuation length distortion on the energy spectrum fit and on the neutrino identification was evaluated by generating different simulated spectra for which the efficiency is given in Table 6.3. The fit, however, was always done with the same function, and the efficiency assumed to be 90 %. In this way, we can estimate the response of the analysis procedure to an unknown variation of the α rejection efficiency.

Results

For the spectra corresponding to 10% distortion or more, the fit convergence is very difficult, with a $\chi^2/\text{d.f.}$ above 2 and unphysical (negative) amplitudes of the CNO and Th contributions. For the spectrum corresponding to a 5 % distortion, shown in Figure 6.14, the $\chi^2/\text{d.f.}$ is lower, at 1.2 , and only the CNO amplitude is negative, but the ^7Be neutrino amplitude presents a 4σ discrepancy with respect to the nominal value.

We recall that these results are far worse than the simple fit without any internal background cut, for which the error on the neutrino signal was 6 %.

If the statistical subtraction is not considered, the signal-to-noise ratio is lower, but the function finds more spectral features that allow it a better spectral recognition. In this fit, shown in Figure 6.15, all the components have physical amplitudes, and the neutrino amplitude, in particular, is found with an error of 3.2 % and a discrepancy of 0.25σ .

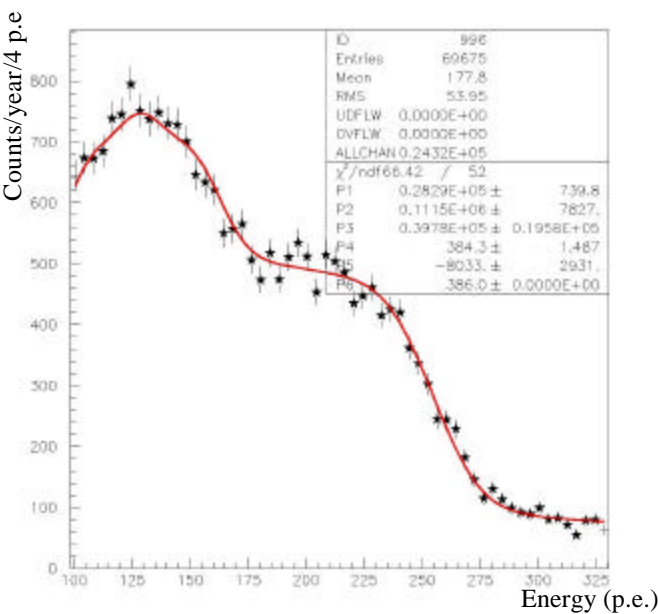


Figure 6.14 Global fit assuming an α/β discrimination efficiency corresponding to a 5% attenuation length distortion. The distortion is NOT assumed in the fit function.

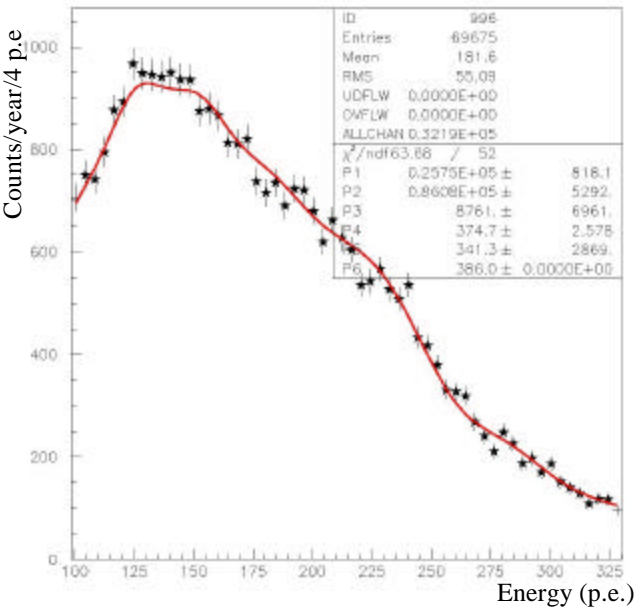


Figure 6.15 Global fit assuming an α/β discrimination efficiency corresponding to a 5% attenuation length distortion. The distortion is NOT assumed in the fit function. The statistical subtraction is not applied.

These results show the importance of a correct model of the background shapes in Borexino. Even in a relatively favorable condition, with a good signal-to-background ratio, a small spectral distortion leads to large discrepancies in the neutrino identification.

Efficiency calibration

So, above a maximum tolerance level of 5 % attenuation length distortion, corresponding to a 6 % efficiency variation, the pulse-shape discrimination method must not be applied without a correction of the threshold and efficiency.

The efficiency of pulse-shape discrimination, must be calculated from a well-known α - β data sample, that can be the Bi-Po events identified with the delayed coincidences. The use of the Bi-Po coincidences to calibrate the α - β discrimination efficiency has the advantage of allowing a continuous monitoring, but on the other hand these events are uniformly distributed on the whole scintillator volume and the efficiency calculation must rely on a possibly biased position reconstruction. An alternative method is the use of radioactive sources positioned inside the inner vessel (used in CTF). These allow for a high statistics measurement in the center and possibly the study of the energy dependency of the efficiency, by using different sources.

Once the α - β discrimination efficiency is measured with a source calibration, its stability must be monitored in a regular basis. The optical calibration systems are an effective way of monitoring the PC transparency, the direct cause of α - β efficiency degradation.

These results indicate that the neutrino analysis requires an attenuation length uncertainty not larger than 5 %. From the Monte Carlo simulations of the expected performance of the optical calibration systems, the goal of such an accuracy seems feasible but, even if in the real condition of Borexino these results should be considered only in a qualitative way, they illustrate the impact of a particular calibration system in the final analysis and in the evaluation of the neutrino measurement systematic error.

6.2.3.2 Energy scale correction for b/g quenching

The goal of this study is to find a simple, analytical approximation to the energy spectrum distortions due to the β/γ ionization quenching effect.

Ionization quenching on α particles was extensively studied by the collaboration in small scintillator samples and in CTF. Its effect is known and was summarized in Chapter 2, so we expect no spectral distortions derived from it.

The mechanism of ionization quenching for electrons is not so well known. Empirically, the phenomenon was described by Birks using the following expression for the specific fluorescence emission:

$$\frac{dL}{dx} = \frac{S \cdot \frac{dE}{dx}}{1 + K_b \frac{dE}{dx}} \quad \text{Eq. 6.6}$$

where $\frac{dE}{dx}$ is the specific ionization, S is the scintillation efficiency (typically about 10^4 photons/MeV) and K_b is usually known as the Birks parameter. Typically, the Birks parameter is small enough so that, for relativistic particles, that have a small $\frac{dE}{dx}$, the denominator in Eq. 6.6 is close to 1 and, integrating over x , we have simply the commonly assumed linear behavior of the scintillation fluorescence:

$$L = S \cdot E \quad \text{Eq. 6.7}$$

The measurements reported in [86] indicate a value of the Birks parameter for pseudocumene equal to 1.48×10^{-2} cm/MeV. The numerical integration of Eq. 6.6 with this value indicates that the region where the linear approximation is valid is above 100 keV. It was noted [87] that, even if the fluorescence-energy linearity is valid above the 250 keV threshold for single electrons, significant distortion effects can be produced in γ events, since a large fraction of their energy deposits are low energy electrons.

We examined the consequences of this effective γ quenching spectral distortion by including the Birks empirical formula in the Monte Carlo GENEB simulation code. For each electron energy, we use the Bethe-Bloch expression for $\frac{dE}{dx}$ in order to integrate Eq. 6.6 and obtain L . The resulting energy spectra for the U and Th background are shown in Figure 6.16, compared with the Monte Carlo simulation in which no β quenching is considered.

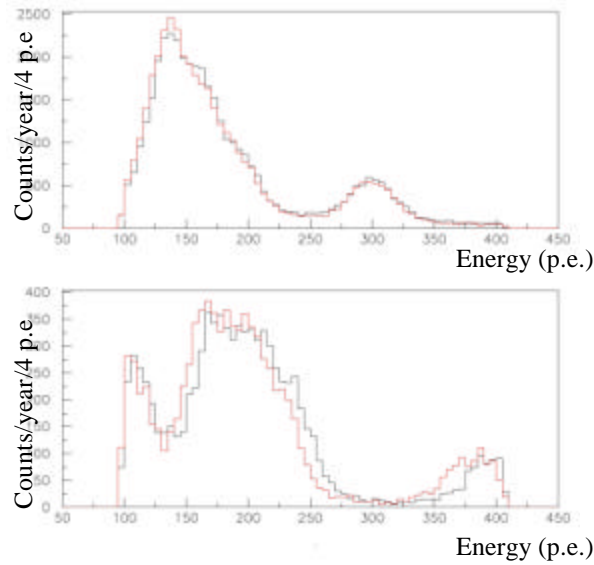


Figure 6.16 Energy spectra of the U (top) and Th (bottom) background with (red) and without (black) β/γ quenching.

The spectral distortions are clear and consistent, not only at low energies, but in all the energy spectrum, in particular for the Th background. If these distortions are not taken into account in the analysis function, and the cuts are not applied, the fit simply does not converge, indicating a total inadequacy of the assumed background shapes. If the cuts are applied (Figure 6.17), the identification of the several components is very poor: a 12 % discrepancy of the ^7Be signal from the nominal value ($> 6 \sigma$) and a negative, unphysical, contribution from the CNO neutrinos

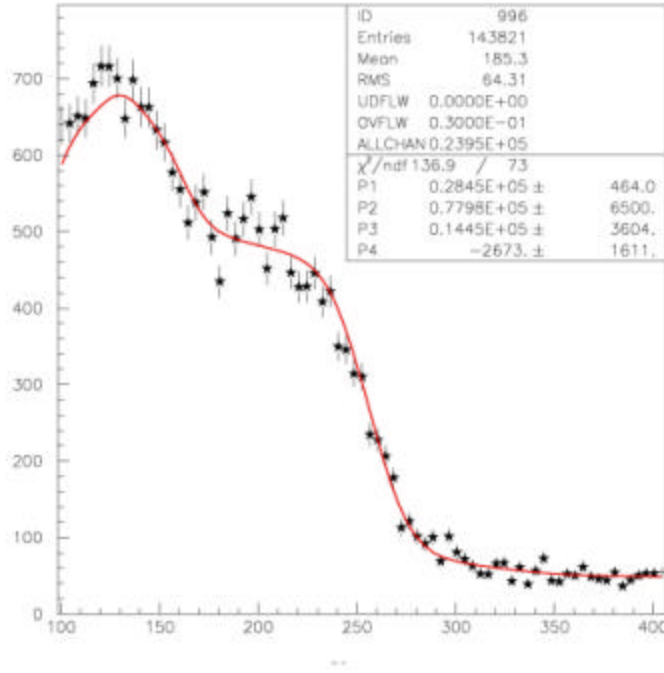


Figure 6.17 Global fit with cuts and without gamma scale correction.

In order to obtain an analytical correction of the ionization quenching distortions, we simulated the quenched response of the Borexino scintillator to γ -rays with several energies, from 20 keV up to 2.4 MeV. The result is shown in Figure 6.18 in terms of the “quenched” energy E_q (i.e., the actually produced scintillation light expressed in equivalent energy) in function of the nominal γ -ray energy. For the three points in the ^7Be neutrino energy window, 250 keV, 500 keV and 750 keV, the quenched energy discrepancy is, respectively, 28%, 16% and 12%. Since the plot is well described by a straight line above the neutrino window threshold, we will approximate the $E_q(E)$ dependency by the following broken line:

$$E_q = 0.96 \cdot E - 60 \text{ keV} \quad \text{for } E > 240 \text{ keV}$$

$$E_q = 0.70 \cdot E \quad \text{for } E < 240 \text{ keV}$$

The parameters for the function above 240 keV are obtained from a least squares fit to the simulated data, and below 240 keV the parameters are determined by a continuity constraint.

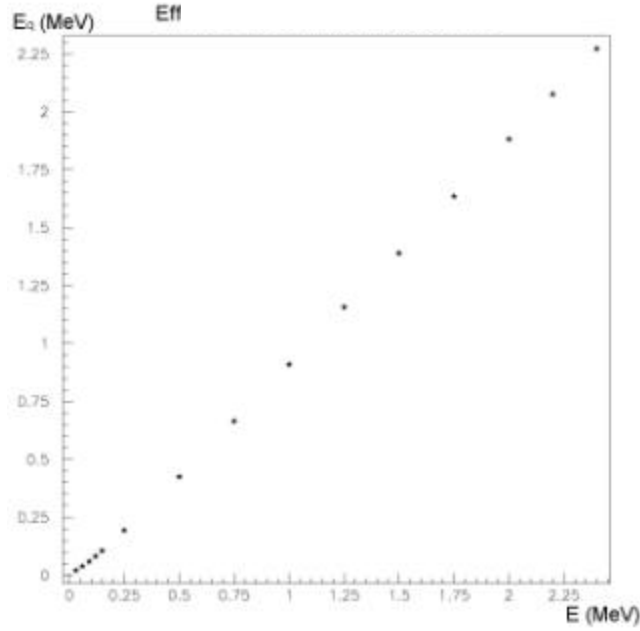


Figure 6.18 Effect of the ionization quenching on the total deposited energy by γ -rays in pseudocumene. Monte Carlo simulation using the Birks semi-empirical formula (Eq. 6.6) and $K_B = 1.48 \times 10^{-2} \text{ cm/MeV}$.

We now introduce this energy scale correction in all the γ components of the global fit function. The quality of the fit, shown in Figure 6.19, is still not satisfactory, since the $\chi^2/\text{d.f.}$ is about 3, the Th component is overestimated by 15 % and the CNO component in practice is not determined (60 % underestimation). In fact, the regions where the function is not able to describe the spectrum are clearly visible in the plot, near 190 p.e. and 270 p.e. However, there is convergence and the neutrino signal is underestimated only by 4 % (1.4σ).

The situation improves when the internal background cuts are applied (Figure 6.20), since the $\chi^2/\text{d.f.}$ reaches 1 and the error on the neutrino signal reaches 2 %. In fact, in this situation, the statistical weight of the residual distortion of the γ components was much reduced, in particular by the statistical cut.

These results tell us that even if the γ energy scale correction with the broken line is still a crude approximation and there is room for future improvement of this model, it is already a step in the right direction.

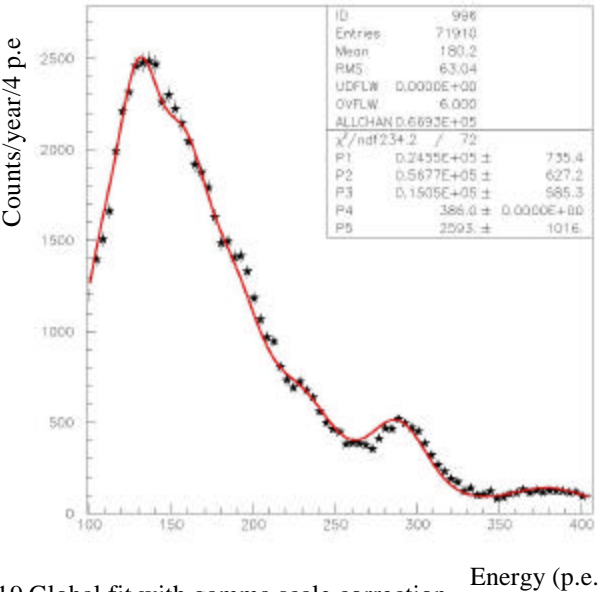


Figure 6.19 Global fit with gamma scale correction.

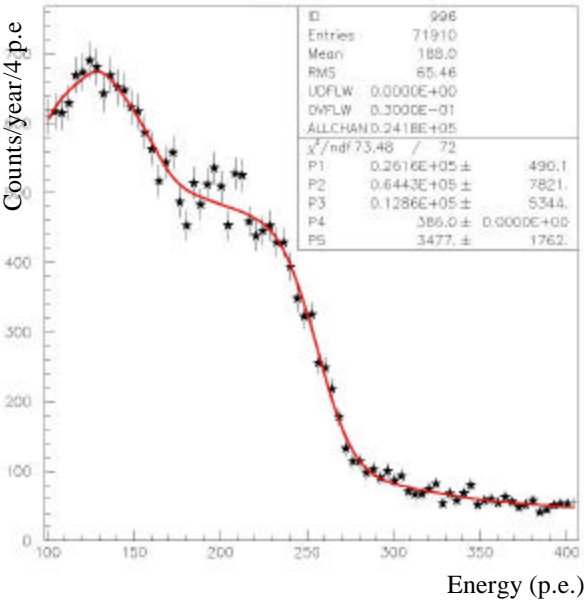


Figure 6.20 Global fit with cuts and gamma scale correction.

In this analysis, the parameters of the broken line were obtained from the Monte Carlo simulations in which we used K_β as the only input parameter describing the ionization quenching phenomenon. In the future analysis of Borexino, the γ energy scale correction should be obtained with the actual detector data in the calibrations phase. This could be done by using β and γ sources inside the scintillator and fitting the energy spectrum with an analytical function with the broken line parameters left free.

6.3 Conclusions

The results presented in this Chapter are used in order to estimate the potential of Borexino to discriminate among the presently allowed oscillation solutions for the Solar Neutrino Problem. The ratio between measured and predicted rate must be added in quadrature to the 10 % uncertainty of the ^7Be neutrino flux, as predicted by the BP2000 Solar Standard Model. In addition, the extension of the allowed range on the expected elastic scattering rate of ^7Be neutrinos for the different MSW oscillation solutions should also be taken into account.

The predicted ranges of ^7Be flux have been calculated by Bahcall, Krastev and Smirnov [88], based on the 99 % confidence level contour of the allowed oscillation solutions⁹:

$$\begin{aligned} \frac{R_{Be}(SMA)}{R_{Be}(BP98)} &= 0.23^{+0.24}_{-0.01} \\ \frac{R_{Be}(LMA)}{R_{Be}(BP98)} &= 0.59^{+0.15}_{-0.18} \end{aligned} \quad \text{Eq. 6.8}$$

We choose to estimate the discriminating potential of Borexino between the LMA and SMA solutions by asking the following questions:

“If the SMA solution is correct, by how many standard deviations is Borexino able to exclude the LMA solution? And vice-versa?”

⁹ These calculations are prior to the SNO results and the values are referred to the BP98 solar model.

This number is given by the difference between the rate expected in the best fit point (0.23) of the SMA region, and the lower limit (0.41) of the LMA allowed range, divided by the combined theoretical and experimental errors. Using the worst case uncertainties (without cuts) for the SMA and LMA measurements in Table 6.2, the value of the “exclusion potential” for the LMA solution, if SMA is correct, is

$$\frac{R_{\text{lower}}(LMA) - R_{\text{best}}(SMA)}{\sqrt{s_{\text{exp}}^2 + s_{\text{th}}^2}} = 3.8s \quad \text{Eq. 6.9}$$

and the exclusion potential for SMA, if LMA is correct, is

$$\frac{R_{\text{best}}(LMA) - R_{\text{upper}}(SMA)}{\sqrt{s_{\text{exp}}^2 + s_{\text{th}}^2}} = 1.3s \quad \text{Eq. 6.10}$$

The potential for a complete exclusion of SMA is small because the allowed range is large. However, the recent results from SNO have further reduced the SMA allowed region, so a further restriction of the ^7Be elastic scattering range is also expected. In addition, the best fit point is in the lower extreme of this range, so a measurement of the ^7Be rate close to the LMA predicted value will exclude a large fraction of the allowed range anyway, as long as the error is small.

The general underlying assumptions behind this estimation of the Borexino sensitivity are a good knowledge of the light propagation mechanisms in the large volume liquid scintillator and an overall stability of the detected rates vs. fiducial volume vs. energy, at the level of 1%, that should be monitored through the use of the optical and external source calibration systems. Moreover, the specific requirements must be considered:

- Negligible residual external background. In order to achieve this, the position reconstruction efficiency cut must be such to reduce this rate to 0.5 events/day in the fiducial volume, neutrino window. This requires a time calibration of the PMTs with an accuracy of 0.5 ns, a reliable measurement (20%) of the effective scintillation decay time, with internal

optical calibration, and an overall check of the external background rejection efficiency.

- Precise knowledge of the internal background rejection efficiency. The efficiency of α/β particle discrimination is strongly related to the external optical properties of the scintillator/buffer liquid. The optical calibration systems will be sensitive to variations of the attenuation length of the order of 5 %, within the requirements for the ^7Be identification.
- Accurate knowledge of the energy spectrum shapes of neutrino signal and background. An accuracy of a few % at 660 keV, the ^7Be “Compton edge”, in the determination of the energy calibration parameter is required for the different types of ionizing particles (α , β , γ), by means of internal radioactive sources.

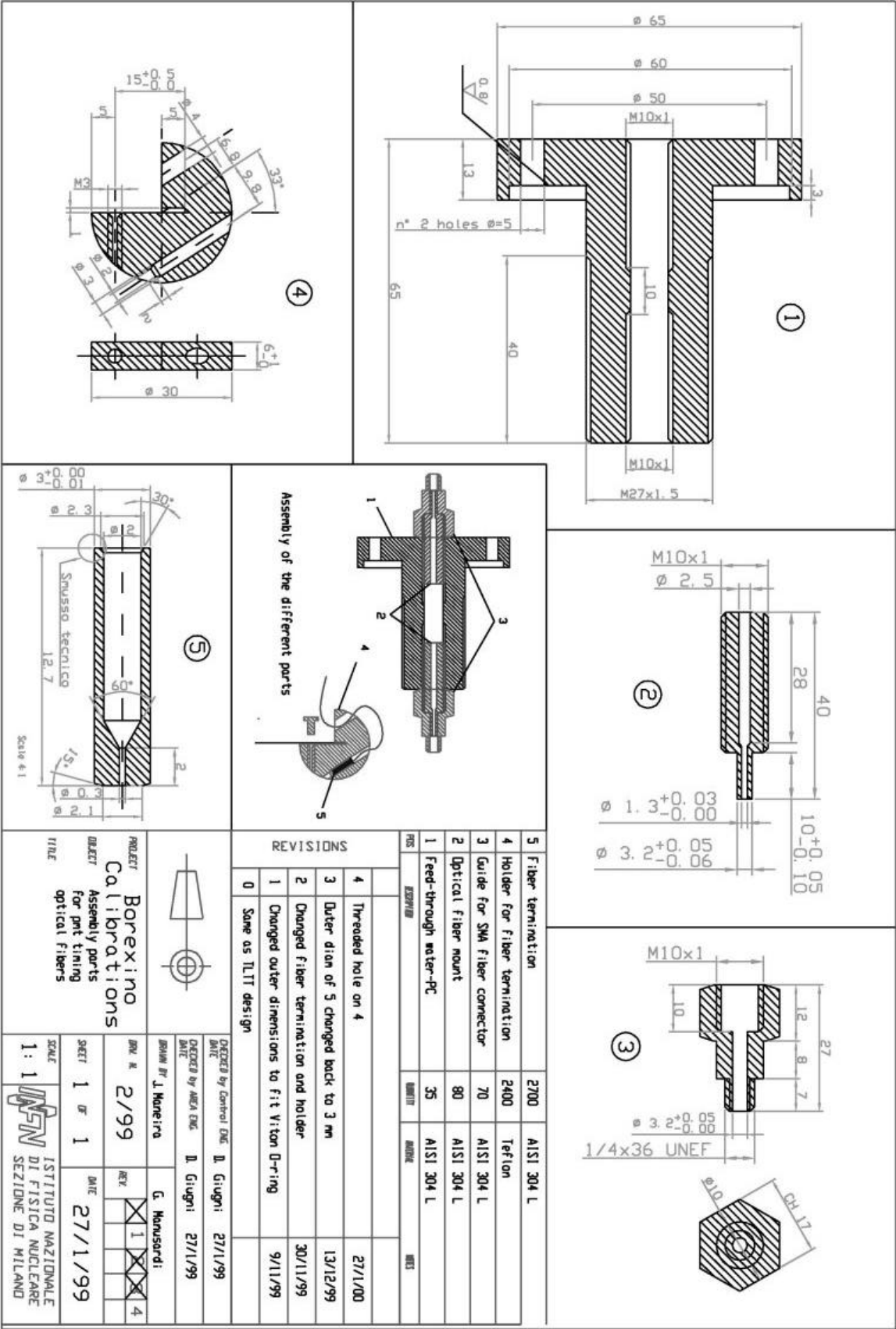
The work presented in this thesis consisted of the design, tests and installation in the final detector of the systems that address each of the critical issues, and in the establishment of the level of accuracy necessary to meet the requirements through a complete analysis method. The results obtained showed the paramount importance of the detector calibration strategy for the Borexino Physics program.

Appendix

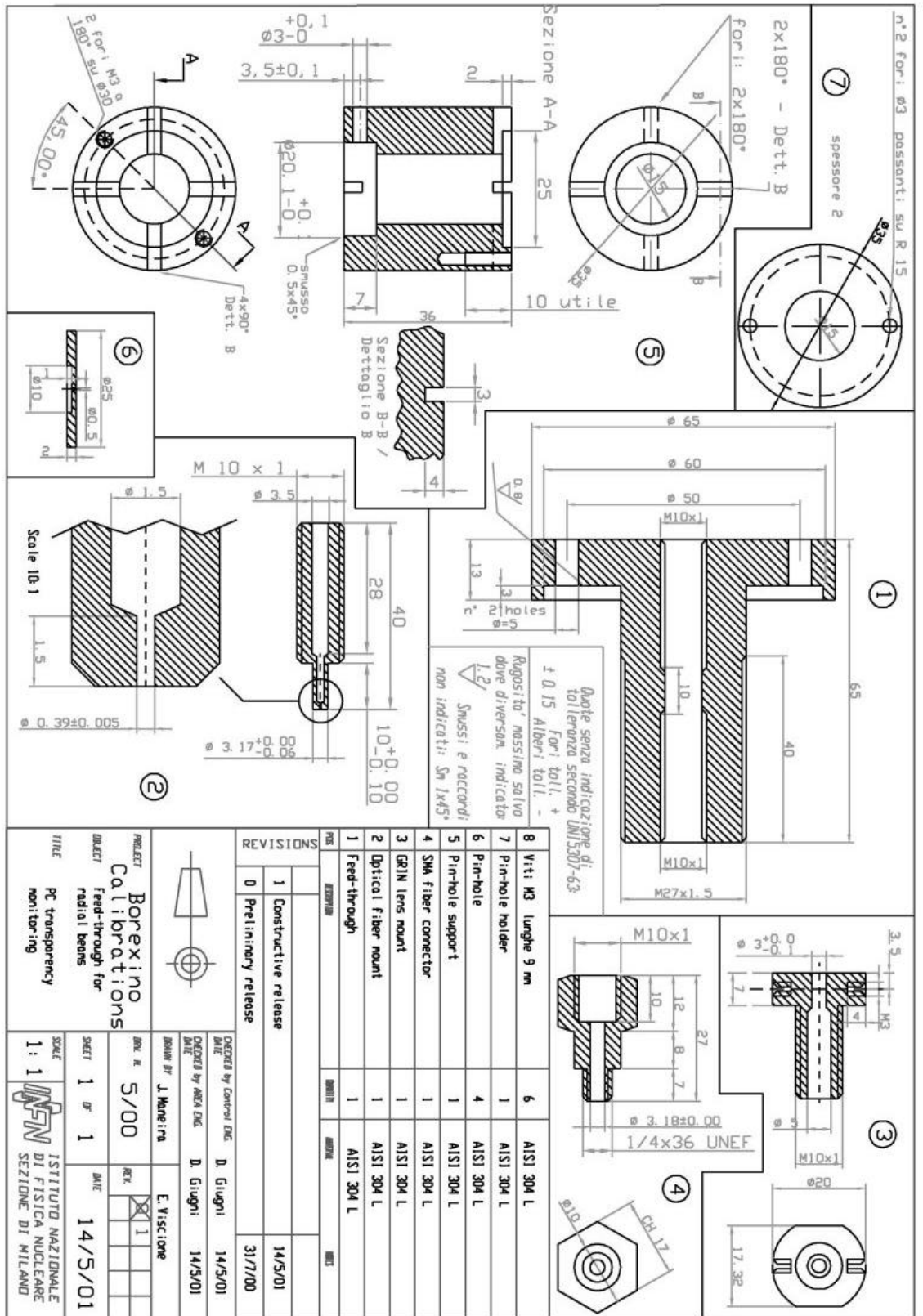
Drawing 1 - Technical drawing of the SSS feedthrough for the PMT calibration system.

Drawing 2 - Technical drawing of the SSS radial feedthrough for the optical calibration system.

Drawing 1



Drawing 2



Acknowledgements

I wish to thank Prof. Gianpaolo Bellini for the hospitality, the opportunity of doing research in Solar Neutrinos and for giving me his trust and support, without which this work would not have been possible.

The contribution of Dr. Sandra Malvezzi was invaluable, supplying the guidelines and strategy of this work, as well as constant help, advice and encouragement. For this, and the friendship, it's difficult to thank her enough.

A special word of gratitude goes to Prof. Amélia Maio, whose constant support, encouragement, and constructive criticism made 2200 km seem like “just next door”.

I thank Barbara Caccianiga for all the help and dedication to the team work. Thanks also to Danilo Giugni for his help in many aspects of the mechanical design. For his precious advice, enriching collaboration and hospitality during my visit to Virginia Tech, I express my gratitude also to Prof. Bruce Vogelaar.

Many thanks also to the several people who I had the pleasure of working with throughout these years: Davide Franco, Augusto Brigatti, Piero Inzani, Lino Miramonti, and the whole Milan group of the Borexino experiment, as well as Giorgio Manusardi, Sergei Sukhotin, Igor Machoulin and Oleg Smirnov.

I acknowledge the support of the Fundação para a Ciência e a Tecnologia through the Ph.D. grant PRAXISXXI/BD/11274/97, and the hospitality of the Milan section of the Istituto Nazionale di Fisica Nucleare.

References

- [1] H.A. Bethe, *Phys. Rev.* **55** (1939) 434
- [2] J.N. Bahcall, *Neutrino Astrophysics*, Cambridge University Press (1989)
- [3] LUNA collaboration (R. Bonetti *et al.*), “First measurement of the He-3(He-3,2p)He-4 cross section down to the lower edge of the solar Gamow peak.”, *Phys. Rev. Lett.* **82** (1999) 5205-5208
- [4] J.N. Bahcall, M.H. Pinsonneault, *Rev. Mod. Phys.* **64** (1992) 885
- [5] J.N. Bahcall, S.Basu, and M.H. Pinsonneault, “Solar Models: current epoch and time dependences, neutrinos, and helioseismological properties”, accepted in *ApJ*, e-print astro-ph/0010346
- [6] F.Reines and W.R. Kropp, “Limits on Solar Neutrino flux and elastic scattering”, *Phys. Rev. Lett.* **12** (1964) 457-459, reprinted in [10].
- [7] F.Reines *et al.*, *Phys. Rev. C* **7** (1973) 1564
- [8] F.Reines, R.M. Woods, *Phys. Rev. Lett.* **14** (1965) 20
- [9] T.L. Jenkins, *A proposed experiment for detection of solar neutrinos*, Case Western Reserve Univ. Report COO-818-62 (1962)
- [10] J.N. Bahcall, R. Davis, Jr., P. Parker, A. Smirnov, R. Ulrich (editors), *Solar Neutrinos – The First Thirty Years*, Addison-Wesley, 1995, p. 79
- [11] R. Davis, Jr., D.S. Harmer, and K.C. Hoffman, “Search for Neutrinos from the Sun”, *Phys. Rev. Lett.* **20** (1968) 1205-1209
- [12] B.T. Cleveland, T. Daily, R. Davis, Jr. *et al.*, *Astrophys. J.* **496** (1998) 505
- [13] SAGE collaboration (J. N. Abdurashitov *et al.*), “Measurement of the Solar Neutrino capture rate by SAGE and implications for neutrino oscillations in vacuum”, *Phys. Rev. Lett.* **83**, (1999) 4686-4689, astro-ph/9907131
- [14] GALLEX Collaboration (W. Hampel *et al.*), “GALLEX Solar Neutrino observations: results for GALLEX IV”, *Phys.Lett.B* **447** (1999) 127-133
- [15] GNO Collaboration (M. Altmann *et al.*), “GNO Solar Neutrino observations: results for GNO I”, *Phys.Lett.B* **490** (2000) 16-26, hep-ex/0006034
- [16] Kamiokande Collaboration (Y. Fukuda *et al.*), “Solar Neutrino data covering solar cycle 22”, *Phys.Rev.Lett.* **77** (1996) 1683
- [17] “Solar B-8 and hep neutrino measurements from 1258 days of SuperKamiokande data”, SuperKamiokande Collaboration (S. Fukuda *et al.*). Mar 2001. 7pp. Submitted to *Phys.Rev.Lett.* e-Print Archive: hep-ex/0103032
- [18] SNO Collaboration (McDonald *et al.*), “The Sudbury Neutrino Observatory”, *Nucl. Inst. Meth.A* **449**, 172 (2000)

-
- [19] SNO Collaboration, (MacDonald et al.), “Measurement of the rate of $\nu_e + d \rightarrow p + p + e^-$ interactions produced by ^8B neutrinos at the Sudbury Neutrino Observatory”, *Phys. Rev. Lett.* **87** (2001) 071301, nucl-ex/0106015
- [20] <http://www.sns.ias.edu/~jnb/>
- [21] S. Bludman, N. Hata, P. Langacker, “Astrophysical solutions are incompatible with the Solar Neutrino data”, *Phys. Rev. D* **49** (1994) 3622-3625
- [22] V.N. Gribov, B.M. Pontecorvo, “Neutrino Astronomy and lepton charge”, *Phys. Lett. B* **28** (1969) 493-496, reprinted in [10]
- [23] S.P. Mikheyev, A.Y. Smirnov, “Resonance enhancement of oscillations in matter and Solar Neutrino spectroscopy”, *Sov. Jour. Nucl. Phys.* **42** (1985) 913-917, reprinted in [10]
- [24] S.P. Mikheyev, A.Y. Smirnov, “Neutrino oscillations in a variable density medium and ν -bursts due to the gravitational collapse of stars”, *Sov. Phys. JETP* **64** (1986) 4-7, reprinted in [10]
- [25] L. Wolfenstein, “Neutrino Oscillations in matter”, *Phys. Rev. D* **17** (1978) 2369-2374, reprinted in [10]
- [26] B. Kayser, “Neutrino mass, mixing, and oscillation”, to appear in the Proceedings of TASI2000, the Theoretical Advanced Study Institute in Elementary Particle Physics held in Boulder, Colorado in June 2000
- [27] H. Bethe, “Possible explanation of the Solar Neutrino puzzle”, *Phys. Rev. Lett.* **56** (1986) 1305-1308
- [28] J.N. Bahcall, “How many sigmas is the solar neutrino effect?”, to be published in *Phys. Rev. C*, hep-ph/0108147
- [29] G.L. Fogli, E. Lisi, D. Montanino, A. Palazzo, “Model-dependent and independent implications of the first Sudbury Neutrino Observatory results”, *Phys. Rev. D* **64** (2001) 093007, hep-ph/0106247
- [30] P.I. Krastev, A.Yu. Smirnov, “Global analysis with SNO: toward the solution of the Solar Neutrino Problem”, Aug. 2001, hep-ph/0108177
- [31] J.N. Bahcall, M.C. Gonzalez-Garcia, C. Peña-Garay, “Global analysis of solar neutrino oscillations including SNO CC measurement”, *JHEP* **8** (2001) 14, hep-ph/0106258
- [32] Super-Kamiokande Collaboration (Y. Fukuda et al.), “Evidence for oscillation of atmospheric neutrinos”, *Phys. Rev. Lett.* **81** (1998) 1562-1567
- [33] Borexino Collaboration (G. Alimonti et al.), “The Science and technology of Borexino : a real time detector for low energy solar neutrinos”, *Astrop. Phys.* **16** (2001) 205-234, hep-ex/0012030
- [34] Borexino Collaboration (G. Alimonti et al.), “A large scale low background liquid scintillator detector: the Counting Test Facility”, *Nucl. Inst. Meth. A* **406** (1998) 411
- [35] Borexino Collaboration (G. Alimonti et al.), “Measurement of the C-14 abundance in a low-background liquid scintillator”, *Phys. Lett. B* **422** (1998) 349

-
- [³⁶] Borexino Collaboration (G.Alimonti et al.), "Ultra-low background measurements in a large volume underground detector", *Astropart. Phys.* **8** (1998) 141
- [³⁷] Borexino Collaboration (G.Alimonti et al.), "Light propagation in a large volume liquid scintillator", *Nucl. Inst. Meth. A*, **440** (2000), 360
- [³⁸] Borexino Collaboration (C. Arpesella et al.), *Borexino at Gran Sasso: Proposal for a real time detector for low energy solar neutrinos*, G. Bellini, M. Campanella, D.Giugni and R. S. Raghavan, Editors, INFN Milano (1991)
- [³⁹] R. S. Raghavan et al., *Design Concepts for Borex*, ATT Bell Labs memo 11131-880114-02 (1988)
- [⁴⁰] R. S. Raghavan et al, ATT Bell Technical Report 11121-901129-63 (1990)
- [⁴¹] F. Masetti et al., *J. Luminescence*, **68** (1996), 15
- [⁴²] J. B. Benziger et al., *Nucl. Inst. Meth. A*, **417** (1998), 278
- [⁴³] M. Johnson et al., *Nucl. Inst. Meth. A*, **333** (1993), 553
- [⁴⁴] M. Johnson, *Scintillator Purification and Study of Light Propagation in a Large Liquid Scintillation Detector*, Ph.D. Thesis, Princeton University (1998)
- [⁴⁵] J. B. Birks, *The Theory and Practice of Scintillation Counting*, Pergamon Press (1974)
- [⁴⁶] L. Cadonati, *The Borexino Solar Neutrino Experiment and its Scintillator Containment Vessel*, Ph.D. Thesis, Princeton University, January 2001
- [⁴⁷] N. Darnton, "Adsorption properties of activated charcoal", Borexino internal report, April 1997
- [⁴⁸] A. Pocar, "Radon filtering from air", Borexino internal report, October 1999
- [⁴⁹] J. Maneira, *Contribution to the Study of Backgrounds and Stability-Monitoring in the Borexino Solar Neutrino Detector*, M.Sc. Thesis, Lisbon University, November 1997
- [⁵⁰] J. Maneira, "On the need for a quencher in the Borexino PC buffer", Borexino internal report, September 2000
- [⁵¹] M. Chen, F. Masetti, G. Testera, "Quenching of undesired fluorescence in a liquid scintillator particle detector", *Nucl. Inst. Meth. A*, **420** (1999), 189
- [⁵²] M.E. Moorhead, *Reflectors in Cherenkov detectors*, Ph.D. thesis, Oxford University (1992)
- [⁵³] M. Balata et al, "The water purification system for the low background Counting Test Facility of the Borexino experiment at Gran Sasso", *Nucl. Inst. Meth A* **370** (1996), 605
- [⁵⁴] Borexino collaboration, "Measurements of extremely low radioactivity levels in BOREXINO", submitted to *Astrop. Phys.* (September 17, 2001), hep-ex/0109031
- [⁵⁵] G.Heusser et al., *Appl. Rad. Isot.* **52** (2000), 691
- [⁵⁶] V. Lagomarsino, G. Testera, *Nucl. Inst Meth. A* **430** (1999) 435
- [⁵⁷] S. Bonetti et al., *Nucl Inst. Meth. A*, **329** (1993), 314
- [⁵⁸] S. Bonetti, B. Caccianiga, M. Giammarchi, J. Maneira, "GENEB: Generation of Neutrinos and Background", Borexino internal report, October 1997

-
- [⁵⁹] C.M. Lederer, V.S. Shirley (editors), *Table of Isotopes*, seventh Edition, John Wiley and Sons(1978)
- [⁶⁰] W.R Nelson *et al.*, “The EGS4 code system”, Technical report, SLAC-265 UC-32 (E/I/A), (1985)
- [⁶¹] I. Manno, “Tracking”, Borexino internal report, September 1997
- [⁶²] G. ‘t Hooft, Phys. Lett. B 37, 195 (1971), reprinted in [10]
- [⁶³] J.N. Bahcall, P.I. Krastev, A. Smirnov, “Where do we stand with solar neutrino oscillations?”, *Phys Rev. D* **58** (1998) 096016, hep-ph/9807216
- [⁶⁴] V. Berezinsky, G.Fiorentini, M. Lissia, “Vacuum Oscillations and excess of high energy solar neutrino events observed in Super kamiokande”, *Astrop. Phys* **12** (2000) 299
- [⁶⁵] V. Berezinsky, G.Fiorentini, M. Lissia, “Vacuum Oscillations and excess of high energy solar neutrino events observed in Super kamiokande”, *Astrop. Phys* **12** (2000) 299
- [⁶⁶] G.L. Fogli, E. Lisi, D. Montanino. “Fourier analysis of real-time, high-statistics” solar neutrino observations”, *Phys. Rev. D* **56** (1997) 4374
- [⁶⁷] J.B. Birks, *The theory and practice of scintillation counting*, Pergamon (1968)
- [⁶⁸] G. Rannucci, O. Smirnov, A. Ianni, R. Dossi, “Methods for precise photoelectron counting with photomultipliers”, *Nucl. Inst..Meth. A*, **451** (2000), 623
- [⁶⁹] Highland, V. L. *et al*, The LSND timing calibration system, NIMA
- [⁷⁰] http://www.picoquant.com/_lightsources.htm
- [⁷¹] Borexino collaboration, “Measurements of extremely low radioactivity levels in Borexino”, submitted to Astroparticle Physics, 17 September 2001, hep-ex/0109031
- [⁷²] Masetti, F. (Perugia), private communication, 1999
- [⁷³] Birks, J.B., *Photophysics of Aromatic Molecules*, Wiley-Interscience, London, 1970
- [⁷⁴] J. Benziger, F.P. Calaprice, M. Chen, N. Darnton, M. Johnson, F. Loeser, C. Stoia, R.B. Vogelaar, “A Rn-222 source for low-background liquid scintillation detectors”, *Nucl. Inst. Meth. A* **414** (1998), 459
- [⁷⁵] F. Elisei, F. Gatti, A. Goretti, T. Hagner, F. Masetti, U. Mazzucato, G. Ranucci, S. Schoenert, G. Testera, P. Ullucci, S. Vitale, “Measurements of liquid scintillator properties for the Borexino detector”, *Nucl. Inst. Meth. A* **400** (1997), 53
- [⁷⁶] Johnson, M. C., “Scintillator purification and study of light propagation in a large liquid scintillation detector”, Ph.D. dissertation, Dept. of Chemical Engineering, Princeton University, 1998
- [⁷⁷] Tanford, C., *Physical Chemistry of Macromolecules*, John Wiley & Sons, Inc., New York 1961
- [⁷⁸] Cadonati L., private communication, July 1998
- [⁷⁹] Borexino technical drawings database at

-
- http://sgicad1.mi.infn.it/cgi-bin/wrap.db/giugni/Borexino/AREA_1/Calibration
- [⁸⁰] GALLEX Collaboration, *Nucl. Inst & Meth. A* **378** (1996) 233
- [⁸¹] A.Ianni, D. Montanino, “The ^{51}Cr and ^{90}Sr sources in Borexino as tools for neutrino magnetic moment searches”, *Astrop. Phys.* **10** (1999) 331-338
- [⁸²] J. Benziger, F.P. Calaprice, M. Chen, N. Darnton, F. Loeser, M. Johnson, C. Stoia, R.B. Vogelaar, “A ^{222}Rn Source for Low-background Liquid Scintillation Detectors”, *Nucl. Inst. Meth. A* **414** (1998) 459
- [⁸³] G. Heusser, M. Laubenstein, LNGS, private communication, January 2001
- [⁸⁴] F.Masetti, Perugia University, private communication, February 2001
- [85] F. James, MINUIT minimization package reference manual, Version 94.1, Computing and Networks Division, CERN
- [86] M. Peron, *Étude de la réponse lumineuse des scintillateurs liquides à des électrons monoenergetiques de basse energie*, Thèse pour le grade de docteur: Université de Paris-Sud Centre d’Orsay (1995)
- [87] S. Bonetti, O. Donghi, C. Salvo, G. Testera, “Ionization quenching: effects on electron and gamma detection in Borexino and CTF”, Borexino internal report, October 1998
- [88] J.N. Bahcall, P.I. Krastev, and A.Yu. Smirnov, “Where do we stand with solar neutrino oscillations ? ”, *Phys. Rev. D* **58** (1998), 96016